Normandie Université

UNIVERSITÉ CAEN NORMANDIE

THÈSE

Pour obtenir le diplôme de doctorat

Spécialité **GENIE CIVIL**

Préparée au sein de l'**Université de Caen Normandie**

Quantification of carbon uptake in recycled aggregate concrete

Présentée et soutenue par

GUESSOUM MERIEM

Thèse soutenue le 13/01/2026

devant le jury composé de :

MME KHADRAOUI-MEHIR FOUZIA	Chercheur HDR - BUILDERS ECOLE D'INGENIEURS CAEN	Directeur de thèse
M. CHATEIGNER DANIEL	Professeur des universités - UCN - Université de Caen Normandie	Co-directeur de thèse
M. LAFHAJ ZOUBEIR	Professeur des universités - Ecole centrale de Lille	Président du jury
M. BECQUART FREDERIC	Maître de conférences - ECOLE D'INGENIEURS DES MINES DE DOUAI	Membre du jury
M. BOUTOUIL MOHAMED	Directeur de recherche - BUILDERS ECOLE D'INGENIEURS CAEN	Membre du jury
M. EL MOUSTAPHA BOUHA	Enseignant chercheur - BUILDERS ECOLE D'INGENIEURS CAEN	Membre du jury
M. TOUATI KARIM	Maître de conférences - EPF - Engineering School	Membre du jury
MME BELAYACHI NAIMA	Professeur des universités - Université d'Orléans	Rapporteur du jury

Thèse dirigée par **KHADRAOUI-MEHIR FOUZIA** (Ecole d'ingénieurs - Builders For Society) et **CHATEIGNER DANIEL** (Laboratoire de cristallographie et sciences des materiaux (Caen))

ED 591 PSIME

Builders Lab

يَرْفَعِ اللَّهُ الَّذِينَ آمَنُوا مِنكُمْ وَالَّذِينَ أُوتُوا الْعِلْمَ دَرَجَاتٍ وَاللَّهُ بِمَا تَعْمَلُونَ خَبِيرٌ

سورة المجادلة (الآية 11)

أَخِي لَنْ تَنَالَ العلمَ إلَّا بستةٍ سأُنبيك عن تفصيلِها ببيانِ

ذكاءٌ وحرصٌ واجتهادٌ وبُلغةٌ وصحبةُ أستاذٍ وطولُ زمانِ[1]

للإمام محمد بن إدريس الشافعي (٢٠٤هـ) رحمه الله

[1] Excerpt from a poem by Imam Al-Shafi'i, which may be translated as follows: *"My brother, knowledge is not attained except through six virtues: intelligence, devotion, perseverance, means to pursue, the guidance of a teacher, and patience over time."*

Acknowledgment

Many people have played a role in this long journey through my PhD at Builders Ecole d'Igénieurs, Caen. I would like to sincerely thank everyone who has, in one way or another, contributed to this thesis or supported me over these past three years.

First and foremost, I would like to express my sincere gratitude to the members of my thesis jury. I extend my warmest thanks to Ms. Naima BELAYACHI and Mr. Zoubeir LAFHAJ for accepting to serve as rapporteurs for this work and for their careful review and constructive remarks, which helped improve the quality of this thesis. I am also grateful to Mr. Frédéric BECQUART, Mr. Karim TOUATI, and Mr. Mohamed BOUTOUIL for serving as examiners and for their relevant questions and comments, which contributed to deepening the reflection on this research.

Words are hardly enough to express my gratitude to my supervision team. I would like to sincerely thank Ms. Fouzia KHADRAOUI-MEHIR**,** my thesis director, for her trust, support, and constant availability throughout this journey. My heartfelt thanks go to Mr. Daniel CHATEIGNIER, my co-supervisor. Every significant and insightful aspect of this thesis bears the mark of his expertise and mentorship. *Daniel, you are one of the most inspiring people I've had the privilege to meet*. My warm thanks also go to Mr. Bouha El-Moustapha for his steady guidance and encouragement.

I would also like to thank Stéphanie GASCOIN for guiding me through the SEM analysis of my concrete, making the exploration of its microstructure feel like an exciting journey into another dimension, and for her patience throughout the process.

I gratefully acknowledge the European Synchrotron Radiation Facility (ESRF) for the provision of synchrotron radiation facilities and Momentum Transfer for facilitating the measurements. Jakub Drnec is thanked for assistance and support in using beamline ID31. The measurement setup was developed with funding from the European Union's Horizon 2020 research and innovation program under the STREAMLINE project (grant agreement ID 870313). Measurements performed as part of the MatScatNet project were supported by OSCARS through the European Commission's Horizon Europe Research and Innovation Program under grant agreement No. 101129751.

I would like to express my sincere thanks to Mr. Mohammed Zelloufi for guiding me during my first steps in the laboratory, for the stimulating scientific exchanges, and for his valued friendship.

Special thanks to my fellow PhD colleagues, Imane GHARBAGE, Lally GARRIGUE, Asmahan TALEB-AHMED, and Alexiane PHAN, for their support, encouragement, and the enjoyable moments shared during our research journey. I would also like to wish Fatima Zahra ZINI, Yasmine LADJIMI, Anas AZHAR, Khalid FDAL, Shaswat Kumar DAS, and Ali OBEID a great experience in their research.

A heartfelt thanks to the little “family” I’ve been fortunate to have in Caen, both to those who are still here and to those who have moved on: Selma BELLAR, Adem BENNANI, and Yasmine LADJIMI. Mohammed ZELLOUFI, you are also very much a part of this family.

Finally, I would like to express my sincere gratitude to my dear brothers and to the sister whom life has brought into my life, for always supporting me and believing in me. To my beloved parents, thank you for being so proud of me. I am deeply grateful and proud of such humble and wonderful people who raised me, shaped my character, and provided a home that values hard work and the pursuit of knowledge.

Table of contents

Abstract

Intending to mitigate emissions from the construction industry, this doctoral research aims to evaluate the CO_2 storage capacity of different self-compacting concrete (SCC) mixtures incorporating alternative raw materials, particularly the use of scallop shell powder (SSP) as a substitute for limestone powder (LS) in the binder and recycled coarse aggregates (RCA) to replace natural coarse aggregates (NCA). For this purpose, carbonation curing was adopted as the protocol to store CO_2 in the SCC mixtures.

The experimental approach began with the characterization of the raw materials to understand the mineralogical and physical properties of both the conventional constituents and their substitutes. The goal of this characterization was to identify the primary differences between the comparative materials, anticipate their behavior in fresh and hardened SCC, and assess their potential influence on CO_2 storage.

Building on the raw material characterization, four SCC mix designs were then developed and cured under optimal environmental conditions for microstructural development, which is water (standard) curing. This investigation aimed to assess the fresh and hardened properties of the mixes, ensuring that the incorporation of SSP and RCA could provide stable rheology and sufficient strength before exploring their potential for CO_2 storage. These substitutions improved the stability of fresh SCC with only a moderate impact on hardened properties. RCA caused an 8% to 11% reduction in compressive strength at 28 days, depending on the mix design. SSP, although achieving higher strength development up to 28 days, showed a moderate decrease in strength at 90 days. These effects were attributed to the intrinsic characteristics of each precursor.

The next step focused on evaluating the carbonation behavior of the SCC mixes, with the aim of identifying the key factors controlling their CO_2 uptake. To achieve this, a carbonation curing protocol was carefully developed, starting with a preconditioning step to remove part of the free water, and followed by the precise selection of environmental conditions in the carbonation chamber. This approach was designed to maximize CO_2 storage while ensuring the best possible performance of the SCC. Overall, the specimens containing RCA and SSP demonstrated higher CO_2 compared to their counterparts with NCA and LS. While the type of precursors and coarse aggregates influenced water retention during preconditioning, their overall impact was limited. Instead, the interplay between hydration and carbonation processes largely determined the extent and efficiency of CO_2 uptake.

The final step of the experimental approach comprises two main sections. The first section aimed to evaluate the effect of carbonation curing on the physical and mechanical properties of SCC, as well as the microstructural changes. Carbonation curing improved the studied properties across all specimens, although the extent of the improvement was not primarily dependent on the $CaCO_3$ content. The C-S-H remaining after carbonation also played a crucial role in preserving microstructural cohesion.

SEM analysis further highlighted that the spatial distribution of the precipitated $CaCO_3$ significantly contributed to matrix densification, refining the pore structure and enhancing mechanical performance. The second section aimed to validate carbonation curing as a valuable alternative to standard curing by primarily comparing the physical and mechanical properties of SCC specimens under each curing regime. The main difference observed across all specimens was in the time required by each SCC mix' specimens to recover from the preconditioning step and reach the same properties as those achieved through standard curing. In this regard, LS-based specimens outperformed SSP-based specimens, demonstrating faster recovery and achieving properties comparable to their standard-cured counterparts after 7 days of curing.

Keywords: Self-compacting concrete; Limestone powder; Scallop shell powder; Recycled coarse concrete aggregates; Carbonation curing; Fresh and hardened properties; CO_2 uptake; Thermogravimetric analysis; X-ray diffraction, Rietveld refinement; mass loss; Scanning Electron Microscopy; Mercury Intrusion Porosimetry.

Résumé

Dans le but de réduire les émissions du secteur de la construction, cette thèse doctorale vise à évaluer la capacité de stockage du CO_2 de différents mélanges de béton autoplaçant (BAP) incorporant des matières premières alternatives, notamment de la poudre de coquille Saint-Jacques (SSP) en remplacement de la poudre de calcaire (LS) dans le liant, et des agrégats grossiers recyclés (RCA) en remplacement des agrégats grossiers naturels (NCA). Pour ce faire, le durcissement par carbonatation a été adopté comme protocole de stockage du CO_2 dans les mélanges SCC.

L'approche expérimentale a débuté par la caractérisation des matières premières, dans le but de comprendre les propriétés minéralogiques et physiques des constituants conventionnels ainsi que de leurs substituts. Cette étape visait à identifier les principales différences entre les matériaux, à anticiper leur comportement dans le béton autoplaçant, tant à l'état frais qu'à l'état durci, et à évaluer leur influence potentielle sur le stockage du CO_2.

Sur la base de la caractérisation des matières premières, quatre formulations BAP ont ensuite été développées et durcies dans des conditions environnementales optimales pour le développement microstructural, à savoir un durcissement standard à l'eau. Cette étape visait à évaluer les propriétés à l'état frais et durci des mélanges, afin de garantir que l'incorporation de SSP et de RCA conférait une rhéologie stable et une résistance mécanique suffisante avant d'explorer leur potentiel pour le stockage du CO_2. Ces substitutions ont amélioré la stabilité du SCC frais, tout en n'affectant que modérément les propriétés durcies. L'utilisation de RCA a entraîné une réduction de 8% à 11% de la résistance à la compression à 28 jours, selon la formulation du mélange. Quant au SSP, bien qu'il ait permis un développement de résistance supérieur jusqu'à 28 jours, il a entraîné une diminution modérée de la résistance à 90 jours. Ces effets ont été attribués aux caractéristiques intrinsèques de chaque précurseur.

L'étape suivante a été consacrée à l'étude du comportement des BAP durcis lors de la carbonatation, dans le but d'identifier les principaux facteurs influençant leur absorption de CO_2. Pour ce faire, un protocole de cure à la carbonatation a été soigneusement élaboré, débutant par une étape de pré-conditionnement visant à éliminer une partie de l'eau libre, suivie de la sélection précise des conditions environnementales dans la chambre de carbonatation. Cette approche visait à maximiser le stockage de CO_2 tout en assurant les meilleures performances possibles du BAP. Dans l'ensemble, les échantillons contenant des RCA et du SSP ont montré une absorption de CO_2 plus élevée que celle de leurs homologues à base de NCA et de LS. Bien que le type de précurseurs et d'agrégats grossiers ait influencé la rétention d'eau lors du préconditionnement, leur impact global est resté limité. En revanche, l'interaction entre les processus d'hydratation et de carbonatation a été le principal déterminant de l'étendue et de l'efficacité de l'absorption de CO_2.

La dernière étape de l'approche expérimentale s'est articulée en deux volets principaux. Le premier avait pour objectif d'évaluer l'effet du durcissement par carbonatation sur les propriétés physiques et mécaniques du SCC, ainsi que sur les modifications microstructurales induites. De manière générale, le durcissement par carbonatation a amélioré les propriétés étudiées pour l'ensemble des échantillons. Toutefois, l'ampleur de ces améliorations ne dépendait pas uniquement de la teneur en $CaCO_3$ formée ; la fraction de C-S-H préservée après carbonatation a également joué un rôle essentiel dans le maintien de la cohésion microstructurale. Par ailleurs, les observations au MEB ont mis en évidence que la distribution spatiale des précipitations de $CaCO_3$ contribuait fortement à la densification de la matrice, favorisant l'affinement de la porosité et l'amélioration des performances mécaniques. Le second volet visait à valider le durcissement par carbonatation comme une alternative pertinente au durcissement standard, en comparant principalement les propriétés physiques et mécaniques des échantillons selon chaque régime de cure. La principale différence observée entre les formulations concernait le temps requis pour compenser l'effet du préconditionnement et atteindre des propriétés équivalentes à celles obtenues sous cure standard. À cet égard, les échantillons à base de LS ont montré une meilleure performance que ceux à base de SSP, en retrouvant plus rapidement des propriétés comparables à leurs homologues durcis à l'eau, et ce dès 7 jours de cure.

Mots-clés: Béton autoplaçant (BAP); Filler calcaire; Poudre de coquille de coquille Saint-Jacques; Granulats grossiers recyclés; Durcissement par carbonatation; Propriétés à l'état frais et durci; Stockage de CO_2; Analyse thermogravimétrique; Diffraction des rayons X; Affinement de Rietveld; Perte de masse; Microscopie électronique à balayage; Porosimétrie au mercure.

List of Figures

List of Tables

List of abbreviations and symbols

CCSU	Carbone Capture, Storage, and Utilization
GWP	Global Warming Potential
CO_2	Carbon dioxide
H_2CO_3	Carbonic Acid
$CaCO_3$	Calcium carbonate
HCO_3^-	Hydrogencarbonate (bicarbonate) ion
CO_3^{2-}	Carbonate ion
K_{sp}	Solubility product
SCC	Self-Consolidating or Self-Compacting Concrete
SCM	Supplementary Cementitious Materials
SSP	Scallop shell powder (*P. maximus*)
RCA	Recycled coarse concrete aggregates
NCA	Natural coarse aggregates
PCS	Polycarboxylate superplasticizer
ITZ	Interfacial transition zone
OPC	Ordinary Portland Cement
CHFA	Carbonated High Calcium Fly Ash
HFA	High calcium Fly Ash
FA	Fly Ash
GGBS	Ground Granulated Blast-furnace Slag
XRD	X-Ray Diffraction
SEM	Scanning Electron Microscopy
TGA	Thermogravimetric analysis
MIP	Mercury Intrusion Porosimetry

General introduction

Behind every ton of cement, every cubic meter of concrete, and every building humans construct lies a hidden cost, one only the planet can pay for: ***"CO_2 emissions"***. Unfortunately, this is not just a current problem; it is a challenge that has been growing for decades and will shape the future if left unaddressed. The situation becomes even more worrying when we examine the numbers. In 2022, CO_2 emissions reached 297.5 million tons (Mt) in France, 5.11 billion tons (Bt) in Europe, and 37.15 Bt worldwide. Over time, these emissions have driven global warming, causing the world to deviate from the 1.5 °C target for 2030 and reach 2.4 °C instead [1]. In the worst-case scenario, the mean global surface temperature could potentially rise by up to 8 °C by 2100 [2], causing further long-term changes in the climate system that pose a global concern [3].

Of course, these emissions do not occur naturally; they are driven by industrial activities, a significant portion of which is associated with the construction industry. The industry is projected to account for more than 52% of global emissions by 2050 [4]. A significant proportion of these emissions originates from cement production, especially from the calcination of limestone and the energy-intensive clinkerization process, which requires temperatures above 1450 °C and relies heavily on fossil fuel consumption [5]. China alone generates 16.4 Bt of CO_2 from the cement industry, making it by far the largest cement producer and CO_2 emitter, although other countries collectively also contribute significantly to global CO_2 emissions.

Given this pressing need to curb emissions, the construction sector is under growing pressure to adopt effective mitigation strategies. The implementation of carbon capture, storage, and utilization technologies (CCSU) in the sector represents an effective means of transforming carbon waste into valuable resources [6,7]. Consequently, these technologies have become a key strategy adopted by the European Union to achieve net-zero emissions by 2050.

CCSU in the construction sector primarily targets cement and concrete production, where captured CO_2 is used to produce carbonated cement-based materials (such as aggregates and concrete) or during curing and preparation processes. Within these approaches, referred to as ex-situ carbonation, carbonation curing, particularly the most suitable for Self-Compacting Concrete (SCC), has attracted growing attention in recent decades due to its effectiveness in accelerating material hardening, improving durability, and offering a pathway for permanent CO_2 storage. Therefore, the present research focuses on the application of carbonation curing to SCC, intending to evaluate the CO_2 storage potential of different SCC mix designs.

However, despite recognition of its potential for CO_2 storage and utilization, and the growing interest in precast applications for low-carbon SCC, several knowledge gaps remain, which form the focus of this doctoral research. These include: (i) limited data on SCC's CO_2 uptake; (ii) the unclear impact of the pre-conditioning step, particularly when elevated temperatures are required before CO_2

exposure, on compressive strength loss and the curing time needed to recover it; (iii) the limited understanding of the chemical factors influencing CO_2 uptake.

In line with our approach to mitigating atmospheric CO_2, we prioritize sustainability when selecting raw materials for our SCC mixes. Traditionally, limestone (LS) composes up to 30% of the binder by mass, and natural coarse aggregates (NCA) account for up to 35% of the SCC volume. Together, these materials contribute to the approximately 360 Mt of natural aggregates extracted annually in France [8]. Instead, we opted for alternative materials such as scallop shell powder (SSP) and recycled concrete aggregates (RCA). These alternatives, although sharing similarities with the conventional materials, also provide the opportunity to valorize these secondary resources in concrete production. Each year, over 10 million tons of mollusk shells waste are generated, mainly from Pacific oysters (*Crassostrea gigas*), king scallops (*Pecten maximus*), and blue mussels (*Mytilus edulis*) [9]. In parallel, the French construction sector produces around 227.5 million tons of waste annually, 49% of which comes from demolition [10].

Accordingly, the research aims to: (i) assess the CO_2 storage potential of four SCC mixes with different precursors, including NCA, RCA, LS, and SSP; (ii) adapt the carbonation curing protocol to optimize CO_2 uptake; (iii) estimate the CO_2 uptake in the carbonated concrete and identify the key parameters influencing it and (iv) evaluate the impact of carbonation curing on the physical, mechanical, and microstructural properties of SCC.

To systematically address the research objectives and knowledge gaps identified above, the present doctoral research is structured around five complementary chapters:

The state of the art is addressed in the **first chapter**, which provides a synthesis of the literature relevant to this research topic. The opening section examines SCC, covering its fundamental fresh-state properties, hardened-state properties, and the performance of SCC incorporating selected materials, including both conventional aggregates and their alternative substitutes. The discussion then turns to carbonation pathways in general, followed by a more detailed focus on carbonation curing and its implementation at the laboratory scale. Particular attention is given to the carbonation chemistry of cement-based materials, from the initial dissolution of CO_2 to the formation of final carbonation products. In addition, measurement methods and approaches for assessing CO_2 storage are reviewed. The chapter concludes with an overview of the changes in the physical properties of cement-based materials induced by carbonation, the challenges associated with concrete carbonation mechanisms, and the potential environmental benefits of ex-situ carbonation technologies.

The **second chapter** first introduces the materials used in SCC formulation with their detailed characterization. It then describes the mix design proportions, sample preparation, and the different curing regimes adopted in this study. Finally, the chapter outlines the experimental procedures, including

characterization of raw materials, SCC characterization, methods for estimating CO_2, and microstructural analysis.

The **third chapter** presents an experimental investigation of the rheological behavior, hardened properties, and microstructural characteristics of SCC mix designs under standard (water) curing. The objective of this investigation is to establish a comprehensive understanding of SCC performance under optimal curing, along with the effects of RCA and SSP on the evaluated properties.

The **fourth chapter** focuses on the experimental investigation of CO_2 uptake in SCC specimens subjected to carbonation curing, with the primary objective of evaluating the potential of the mixes to permanently store the absorbed CO_2. To enable a reliable estimation of the net CO_2 uptake, parallel investigations were also carried out on specimens cured under sealed (CO_2-free) conditions, providing a reference for comparison.

Finally, the **fifth chapter** synthesizes the experimental findings through two complementary investigations. The first examines the influence of the carbonation curing protocol on the physical, mechanical, and microstructural modifications induced by this curing regime, with sealed-cured specimens serving as a reference to quantify the extent of these alterations. The second evaluates the viability of carbonation curing as a sustainable alternative to standard curing, focusing on its ability to ensure satisfactory physical and mechanical performance while simultaneously contributing to permanent CO_2 storage.

Chapter I

State of knowledge and bibliographic synthesis

1 Introduction

Cement-based materials have the potential to serve as significant carbon sinks by mineralizing carbon dioxide (CO_2) into calcium carbonate ($CaCO_3$), making them a promising solution for CO_2 sequestration. The process through which CO_2 is stored is generally referred to as carbonation, with terms like ex-situ carbonation, accelerated carbonation, or terms that describe the specific stage or method by which carbonation is applied. Whichever ex-situ carbonation method is used to store CO_2, it generally enhances the chemical and physical properties of carbonated concrete products, thereby promoting the reuse of CO_2 in various construction applications. However, reinforced concrete is an exception, as the pH drop induced by carbonation is detrimental to its durability. Therefore, this type of concrete falls outside the scope of this research.

By examining the literature, this chapter aims to provide a comprehensive theoretical review of the ex-situ carbonation pathway as part of Carbon Capture Storage and Utilization (CCSU) technologies, focusing on their application in the construction industry. Found on the principal aspects surrounding the ex-situ carbonation pathway adopted in our research, the chapter provides a background for assessing the CO_2 storage potential of the considered materials to identify the main factors influencing the carbonation process and explore the resulting micro and macro-scale changes in the carbonated material. Before delving into details on these aspects, a description of the fundamental characteristics of the material intended to serve as a CO_2 sink is presented.

Therefore, the chapter begins with an overview of Self-Compacting Concrete (SCC), highlighting the main reasons behind selecting this candidate for CO_2 storage. The section covers its key rheological and hardened properties, as the material's conception constitutes a fundamental parameter in determining how the SCC will interact with CO_2 and how the CO_2 storage or uptake influences its microstructure and mechanical behavior.

The subsequent section introduces the ex-situ carbonation pathway applied to cement-based materials in earlier and current research and how researchers generally customize the procedures in a laboratory setting based on the material conception, the suitability of the pathway with the material, the final carbonation product, and the intended application. Based on this analysis, the most suitable path for SCC and its intended application is approved. A significant portion of this section is dedicated to exploring the interaction of CO_2 with the concrete matrix, which involves a complex mechanism of physicochemical reactions, and to the factors affecting its occurrence and the carbonation product chemistry. The section further summarizes measurement methods used to estimate CO_2 absorption by materials to elicit our estimation method for assessing the CO_2 absorption capacity of SCC. It further points out the properties changing within the cement-based material induced by the carbonation,

particularly regarding compressive strength, pore system evolution, and microstructural alteration. The section then ended with highlighting the environmental assets of carbonation technologies.

Finally, the chapter is concluded with a synthesis of the key findings and insights discussed, highlighting the rationale behind the chosen pathway and its relevance to our research objectives. This reflection also outlines the gaps and opportunities that guided our experimental choices.

2 Self-compacting concrete

As an innovative construction material, SCC, also known as Self-consolidating concrete, was developed in the 80s by Japanese researchers (K. Ozawa and K. Maekawa) at the University of Tokyo [11]. The development of such concrete was driven by the need to improve the casting process for structures with densely reinforced formwork and optimize work efficiency by reducing on-site labor and accelerating construction timelines [12–14]. The first introduction of SCC to the research community happened at the 2nd East Asia and Pacific Conference on Civil Engineering and Construction in January 1989 in Chiang Mai, Thailand [15]. However, it was at the fourth CANMET-ACI international conference, held in Istanbul in May 1992, where the SCC caught the world's attention [16]. This conference was the turning point in the rapid spread and adoption of this innovative concrete technology worldwide.

SCC refers to a new type of high-performance concrete mixture distinguished from Conventional Vibrated Concretes (CVC) mainly by its fresh state properties resulting from a specific formulation. The latter must reconcile two a priori contradictory properties, including good stability to segregation and high fluidity. The exceptional flowability of this concrete allows it to consolidate under its own weight without requiring external vibration [17], which reduces noise from and on the construction site. Given these characteristics, SCC is nowadays extensively used in the construction industry. The market store of SSC in different applications also demonstrates a significant increase due to the enhanced productivity, efficiency, and overall construction quality that it can provide [18].

However, the formulation of SCC is not as simple as that of CVC. SCC must maintain satisfactory stability and perfect homogeneity while remaining fluid. Fluid concrete requires more than a simple addition of water; such manipulation leads to segregation phenomena, resulting in a drop in concrete performance. It's a question of finding the optimal composition between the various constituents and guaranteeing the absence of segregation and bleeding [14]. To prevent these potential issues, the SCC must maintain high flowability when it is being cast and high viscosity when it is at rest. Here comes the interest behind the use of superplasticizer (SP), which is precisely to provide control of the flow behavior of SCC and concrete in general, especially when the adjustment of the SP is much simpler than modifying formulation parameters. In this way, it is possible, including, but not limited to,

counteracting the variation of sand or filler in a concrete mix so that the rheological characteristics remain unchanged compared to the control concrete. Meanwhile, the stability of SCC against segregation is achievable by using a generous amount of fine materials, viscosity-modifying agents, or selecting appropriate sand and aggregate content [19].

2.1 Distinctive Components of Self-Compacting Concrete

SCC is made from the same fundamental raw materials as CVC (cement, fine and coarse aggregate, and mixing water), along with mineral additions and admixtures. These components are also present in other concrete, but with different proportions. This section is dedicated primarily to the SCC's distinctive components, while the principal raw materials are mentioned throughout the subsequent sections.

2.1.1 Admixtures

The admixtures are chemical products, often synthetic polymers with a high molecular weight. They can be added to the concrete during the mixing phase or before its conception at doses of less than 4% of the weight of cement to enhance one or more target characteristics in the fresh and/or hardened state [19]. However, their incorporation must conform to NF EN 934-2 [20]. The admixtures include, among others, water-reducing admixtures (superplasticizers (SP) and plasticizers), set-controlling admixtures (accelerators and retarders), and air-entraining admixtures. However, this research specifically focuses on using SP and set accelerators.

a) Superplasticizer

The SP, also called superfluidizers or superfluidifiers, belongs to the water-reducing admixtures category [21]. It is typically used in concrete to maintain its workability when reducing the water/cement (w/c) ratio or increasing its workability when the w/c ratio remains the same [19]. The SP can reduce water content by up to 30% compared to other admixtures of the same category, thereby increasing the strength and reducing the porosity and permeability of the concrete [22]. The SP admixtures are categorized into four groups (Figure I-1). Each group product is unique by the molecular weight of its backbone, the chemical changes it has undergone, or the presence of other chemical substances within the backbone [23,24].

Among various types of SP, such as Naphthalene-based Superplasticizer (NS), and Air-entraining Superplasticizer (AS), the Poly Carboxylate-based Superplasticizer (PCS), so-called last generation, was found to be the most preferred for the precast industry, for its best fluidity, its ability to retain concrete slump without prolonging its setting times at low dosages, and its capacity to achieve a strength of 40 MPa within 8–20 hours. It’s also recognized for its ability to develop High-Performance

Concrete (HPC), Ultra-High Performance Concrete (UHPC), and Ultra-High Performance Fiber-Reinforced Concrete (UHPFRC), besides SCC [24].

Moreover, the PCS can be synthesized in various chemical compositions by varying the backbone length, the content of ionic groups, the length, amount, and type of side chains, and the molar ratio of different monomers and macromonomers, consequently leading to differences in the performances of cement-based materials [25,26]. It was reported that the high content of the carboxylic group (–COO−) in the PCS accelerates its adsorption on the surface of cement particles, which optimizes the initial dispersion, but results in poor slump retention [27]. The PCS possessing a high grafting density or long side chain demonstrates a dispersion effect on cement particles. One with a shorter side chain exhibits a proportional increase in the retardation effect on cement hydration. It is worth mentioning that the SP, in all types, is not a miraculous product. Improper dosage, composition, or application leads to segregation and bleeding. Thus, the optimum recommended SP dosage range falls between 1% and 2% of the binder [28].

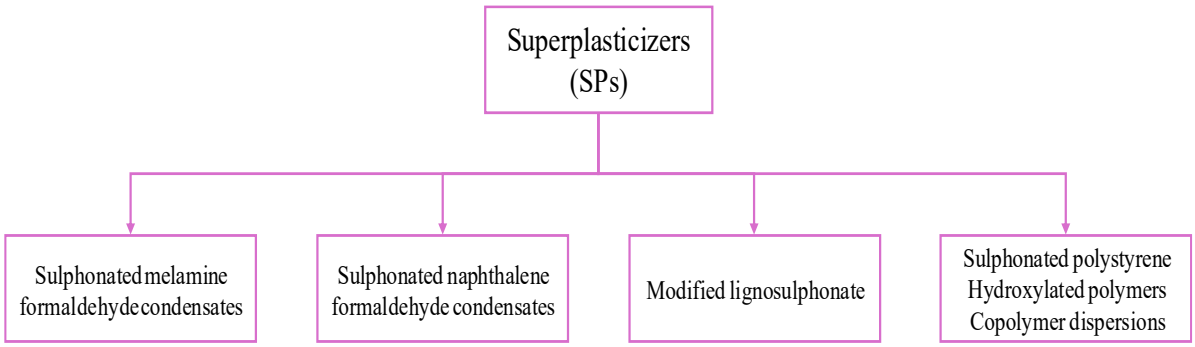

Figure I-1: Classification of SPs [29].

- **Superplasticizer's acting mechanism**

The acting mechanism of SP involves the adsorption of negatively charged functional groups, such as the carboxylic group (–COO−) in the case of PCS, onto cement particles. This imparts a negative charge to the cement grain surfaces, reducing or eliminating the attractive interparticle forces (Van der Waals). Consequently, the cement particles, which tend to agglomerate, repel each other and maintain an ultrathin film of water due to electrostatic repulsion (zeta potential), thus preventing flocculation.

Additionally, the electrolyte available within the aqueous medium forms an electrochemical double layer (repulsive interparticle forces) around the cement grains, neutralizing the electrostatic potential and stabilizing the dispersion [30]. PCS, in particular, provides further steric hindrance that prevents close contact between particles, reducing the magnitude of the attractive forces [21].

Following the acting mechanism of SP, the trapped water between the cement particles is released. The latter then serves to fluidify the concrete. Figure I-2 illustrates the acting mechanism of the PCS admixture [23].

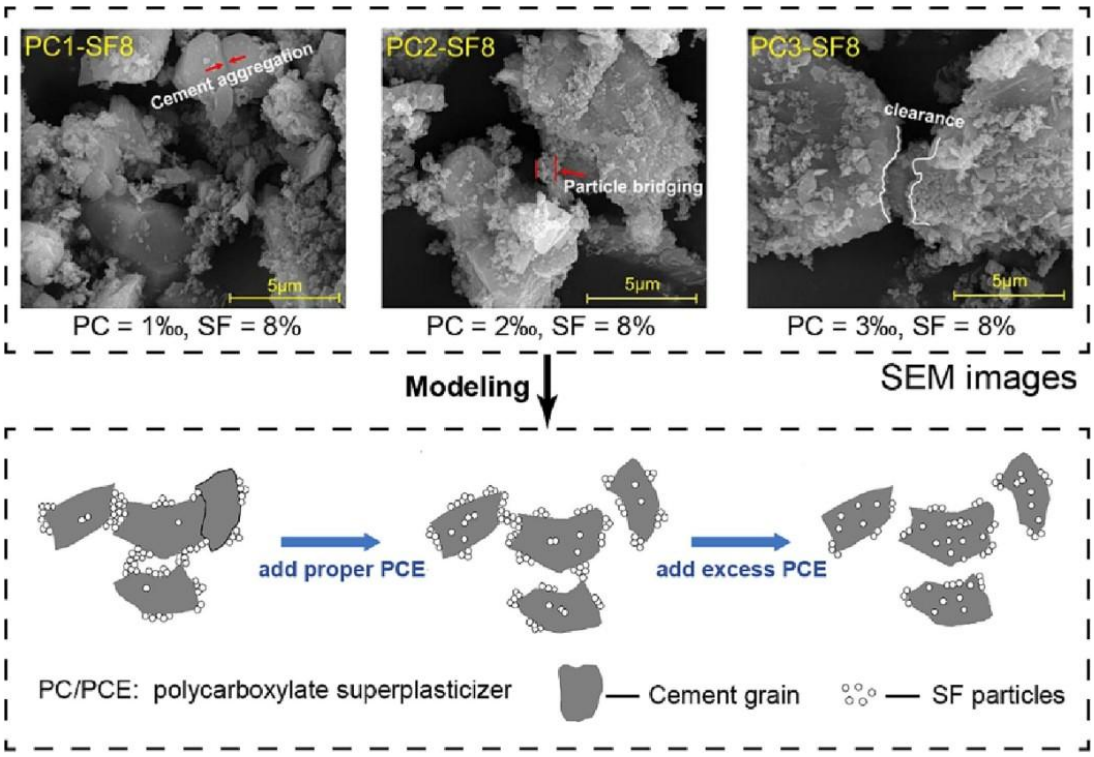

Figure I-2: Effect of SP on particle aggregation of cement slurry [23].

- **Superplasticizer-cement incompatibility**

In some cases, the cement and SP are said to be rheologically incompatible, as observed through short-lived workability followed by rapid slump loss [31]. This incompatibility arises from the competitive adsorption of sulfate ions (SO_4^{2-}) onto Celite's ($3CaO{\cdot}Al_2O_3$ (C_3A)) surface particles. In other words, the low availability of SO_4^{2-} within the aqueous medium leads to excessive SP adsorption onto C_3A. Consequently, less SP remains within the medium solution, reducing its dispersant effect on Alite ($3CaO.SiO_2$ (C_3S)) and Belite ($2CaO.SiO_2$ (C_2S)).

However, an adequate amount of SO_4^{2-} ions promotes ettringite formation ($3CaO.Al_2O_3.3CaSO4.32H_2O$), which absorbs much less of the active molecules, which are thus available to fulfill their dispersing function. The cement and SP incompatibility is also related to the aluminate phase [32]. This is when the stiffening of the concrete slurry is observed in the presence of SP, even though the amount of SO_4^{2-} ions is appropriate for the C_3A content [33]. A highly reactive aluminate phase forms a large amount of ettringite, which can incorporate SP and crystallize into fine needles. The plasticity of the cement suspension is then significantly impaired [34].

Regarding SP compatibility with other admixtures, it is reported that accelerators, retarders, water reducers, and air-entraining admixtures are typically compatible with superplasticizers. In some cases, their combined effects can be synergistic [24]. However, due to their distinguishing chemical interactions, evaluating their combination is essential to anticipate unexpected issues.

b) Set-controlling admixtures: Set-Accelerator

As a second admixture used in the present study, the set-accelerator (SA) can consist of calcium chloride, calcium carbonates, silicates, aluminates, alkali metal hydroxide, and organic chemicals [35,36]. However, the NF EN 934-2+A1 [20] restricts the use of calcium chloride-based SA to avoid corrosion of the rebars in reinforced concrete. The SA expedites the cement's initial and final setting time, mortars, or grouts. Their acting mechanism involves the acceleration of the C_3A–gypsum reaction, leading to the rapid formation of a significant amount of ettringite in the form of needles, which reduces the mobility of the cement grains and contributes to early stiffening [37]. The SA also interferes in the C_3S hydration by promoting its rapid dissolution, leading to faster formation of calcium silicate hydrate (C-S-H) and, thus, increasing the rate of early strength development [38]. They are particularly beneficial in cold weather conditions and precast concrete applications [35].

2.1.2 Mineral additions

In addition to admixture, mineral additions are essential for SCC conception. Even though these materials are also used in CVC, their proportion is undoubtedly higher in SCC [39]. A wide variety of mineral additions, also known as or used as supplementary cementitious materials (SCMs), are being used in concrete formulation, such as granulated blast furnace slag (GBFS), fly ash (FA), silica fume (SF), limestone (LS), and natural pozzolans (NP) [40].

Two groups categorize the SCMs:(i) fillers (non-active SCMs) and (ii) pozzolans (active SCMs) [41]. The pozzolanic reactivity of SCMs is governed by their chemical reaction with cement or cement hydrates. Meanwhile, the effectiveness of their filling effect and their physical ability to act as nucleation cores for cement particle hydration depend on a proper arrangement of particles, particle surface characteristics, and particle size distribution [42]. Although the positive impact of the pozzolanic effect on concrete performance is well acknowledged, in some cases, the filler effect contributes equally, or even more significantly, to performance enhancement [43]. Both pozzolans and fillers influence the rheological properties of SCC [44], and its performance in the hardened state, due to the expected change in the microstructure of the pores' network features and the Interfacial Transition Zone (ITZ) thickness [45]. Collectively, they lead to an enhanced packing density of the hydrated binder, thereby improving the compressive strength of SCC. A finer particle size distribution of SCMs leads to improved reactivity and, consequently, a further increase in the compressive strength of SCC [46,47].

2.2 Fundamental fresh-state properties of Self-Compacting Concrete

The fresh SCC should comprise four main fresh properties. The first three properties include the mobility, filing ability, and passing ability. The two formers enable SCC to flow freely under its own weight and fill all corners within the formwork [48,49]. The latter allows it to flow through confined spaces and ensures that placement remains unobstructed by unacceptable blocking phenomena. The fresh SCC must meet the required levels for these properties. In addition, its composition must remain uniform (good cohesion) throughout the transport and placement process without bleeding, guaranteeing its fourth property: resistance to segregation. The main tests conducted to verify the requirement level of each fresh property are summarized in Table I-1.

Table I-1: Testing methods for evaluating SCC fresh properties [48,50].

Method	Property	Range values
Slump flow - Abrams cone	Filling ability	SF1: 550–650 mm
		SF2: 660–750 mm
		SF3: 760–850 mm
t_{500} slump flow	Filling ability	2-5 s
J-ring	Passing ability	0-10 mm
V-funnel	Filling ability	6-12 s
L-box	Passing ability	h_2/h_1: 0.8-1.0 mm
U-box	Passing ability	h_2/h_1: 0-30 mm
Fill box	Passing ability	90-100%
GTM screen stability test / Sieve segregation	Segregation resistance	SR1 ≤ 20
		SR2 ≤ 15
Orimet	Filling ability	0-5 s

Furthermore, instability in SCC can occur during and after casting and manifest in a static or dynamic form. By definition, the static segregation for an SCC in rest arises when the yield stress of the suspending matrix is insufficient to support the weight of the aggregate minus its buoyancy. Dynamic segregation occurs when the fluid structure breaks down due to motion, reducing the yield stress and leading aggregates to settle [51,52].

In complement to the experimental testing method, visual observation of the flowed SCC can help assess fresh properties by inspecting it for signs of instability, using the so-called Visual Stability Index (VSI) scale (Table I-2) [53].

Table I-2: VSI Scale for SCC [53].

VSI Scale	Observation	SCC stability
0	No evidence of segregation in the slump flow patty, mixer drum, or wheelbarrow	Highly stable mix
1	No mortar halo in the slump flow patty, but some slight bleeding on the surface of concrete in the mixer drum and/or wheelbarrow	Stable mix
2	Slight mortar halo (< 10 mm) in the slump flow patty and a noticeable layer of mortar on the surface of the testing concrete in the mixer drum and wheelbarrow	Unstable mix
3	Clearly segregating by evidence of a large mortar halo (> 10 mm) and a thick layer of mortar and/or bleed water on the surface of testing concrete in the mixer drum or wheelbarrow	Highly unstable mix

2.3 Main Properties of hardened SCC

As mentioned in (§ 2), the SCC is designed to flow and compact without external vibration. Its unique composition, characterized by a higher paste volume and specific additives, distinguishes it from CVC. Hence, the mechanical properties of SCC, particularly its instantaneous deformations, are assumed to differ. All concretes exhibit better compressive than tensile resistance. The compressive strength of concrete, which tends to be governed as much by the type and volume of the paste as by the water-binder (w/b) ratio [54], is one of the most crucial properties for concrete applications. As reported, the SCC exhibits an improved microstructure, characterized by a lower void ratio within the ITZ and a more uniform pore distribution. These improvements, in turn, enhance its compressive strength compared with CVC. It is, however, worth mentioning that the compressive strength of SCC does not significantly surpass that of CVC [55,56]. The influential factors on the compressive strength of SCC include (i) the lower w/b ratio, (ii) the size, nature, and shape of aggregates, (iii) the SP dosage and its compatibility with the binder and other admixtures, (iv) the category of SCMs, and (v) curing condition, with moist curing being the most effective [46].

2.4 Self-compacting concrete incorporating alternative binders and aggregates

As previously discussed, SCC exhibits exceptional rheological behavior and competitive mechanical performance compared to CVC. These intrinsic properties, however, can be influenced by the mix design, particularly its precursors, which include the binder and the nature of the coarse aggregates (natural or recycled). All parameters constitute the influential parameters considered in the present study. Therefore, this section provides a comprehensive overview of SCC, containing: Scallop

shell powder (SSP) versus limestone powder (LS) binders, and recycled coarse aggregates (RCA) versus natural coarse aggregates (NCA).

2.4.1 Fresh properties

a) Effect of limestone and scallop shell powders

In the fresh state, particle size distribution, particle packing effect, particle shape, and particle surface texture dominate the workability and water demand of SCC. According to several studies, SCMs with a spherical shape minimize friction forces occurring at the aggregate-paste interface, creating a ball-bearing effect at the contact point [47,57]. This allows the spherical particles to easily roll over one another, thereby improving the workability of SCC. In contrast, when mixed with water, rough, modular, and angular particles tend to agglomerate, which reduces their ability to fill voids between other particles and prevents proper deflocculation within the paste [57–59]. However, this behavior can be mitigated when adequate SP is adsorbed onto particle surfaces, forming an electrical double layer at their surfaces (§ 2.1.1).

Moreover, SCMs with lower density occupy a larger volume. Therefore, when cement is replaced by or mixed with lower-density SCMs, for an equivalent total mass of solids, the volume of the solid phase increases. As a result, the particles move more easily, interparticle friction decreases, and the plasticity and cohesiveness are improved, thereby increasing the workability of the mix [57,59].

Furthermore, the workability of fresh SCC is also governed by the distribution of water within the mix, which interacts closely with particle characteristics. The total water content consists of two main portions: the water filling the spaces between solid particles, which has only a minor influence on flow, and the surface water surrounding the particles. The latter includes both absorbed water and a thin water film coating the particle surfaces. The thicker the film is, the more fluid the SCC becomes, thereby dominating the SCC's flow [57]. However, excessive addition of fine particles can have an adverse effect due to the increase in specific surface area, which in turn raises water demand, intensifies interparticle friction, and ultimately disrupts the flowability of SCC.

Building on the general influence of particle characteristics on SCC rheology, several studies report that LS predominantly exhibits grains angularly shaped with rather smooth and flat surfaces (Figure I-3a) [60–63], and a highly compacted mineral grain structure with well-defined inter-grain connections (Figure I-3b) [64]. However, other studies [65–67] have observed a spherical morphology of LS (Figure I-3c). It has also been reported that the well-defined edges of LS result in a higher specific surface area than that of spherical particles of the same size, thus requiring more water for surface wetting.

The particle size of LS also critically modifies SCC rheology. Increasing the content and reducing the particle size of LS lead to higher yield stress, plastic viscosity, and thixotropy, consequently

reducing slump flow [68]. For instance, substituting cement with a 15 µm LS increases both the plastic viscosity and the yield stress. In contrast, replacing cement with finer LS particles (0.7 µm and 3 µm) decreases these rheological parameters [60,69–71]. These differences may also result in different rheological behavior of SCC over time

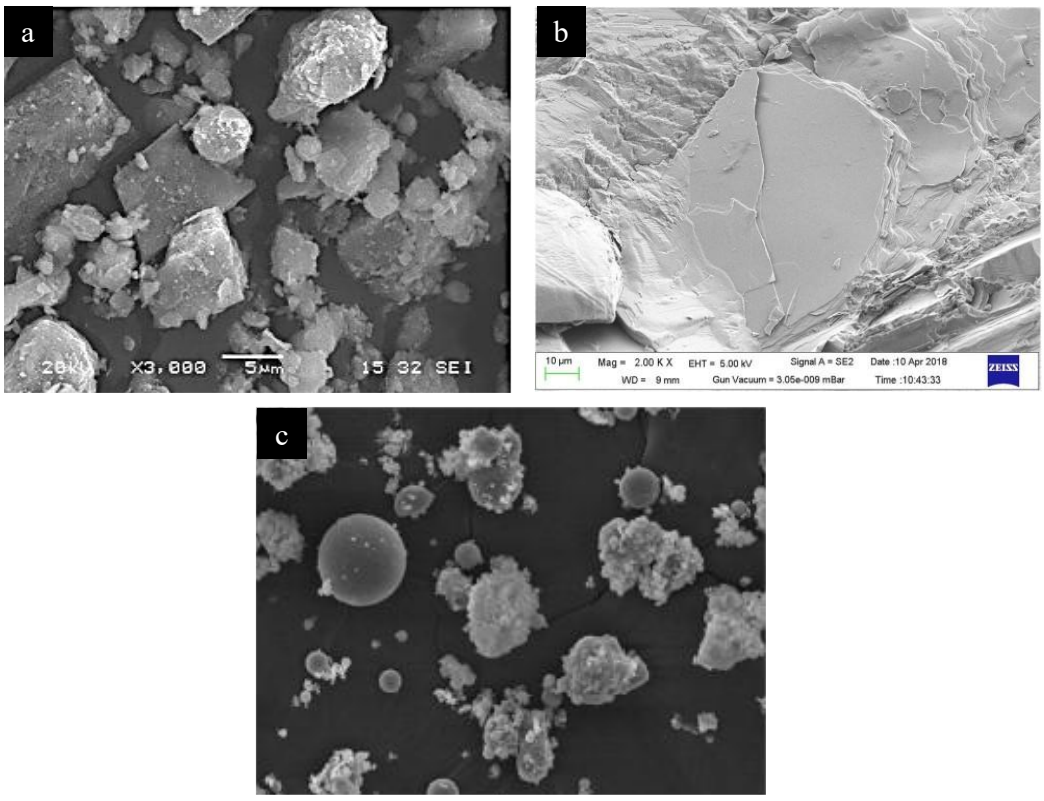

Figure I-3: SEM images of LS particles: (a) [60–63], (b) [64], and (c) [65–67].

Turning our attention to SSP, SSP seashells are made of calcite biocrystals, exhibiting lamellar shapes, intersected in lamella-stacked bundles of vanion orientations (Figure I-4). From the outer to the innermost layers of the shell, three main complex crossed lamellae layers are observed [72]. All these layers are incorporated in our SCC differentially after grinding. Only a few studies have investigated the influence of waste seashell powder on the rheological properties of SCC, particularly SSP. As previously reported, using seashell powder (composed mainly of aragonite) as a partial cement replacement or additional filler modifies the rheological properties: it decreases yield stress with increasing seashell content, reduces thixotropy, and enhances workability [73]. However, this study recommended adjusting the seashell powder dosage to ensure adequate flowability. Additionally, it has been reported that organic matter, particularly chitin, in seashell powder disrupts rheological properties, thereby reducing mini-slump values [74,75].

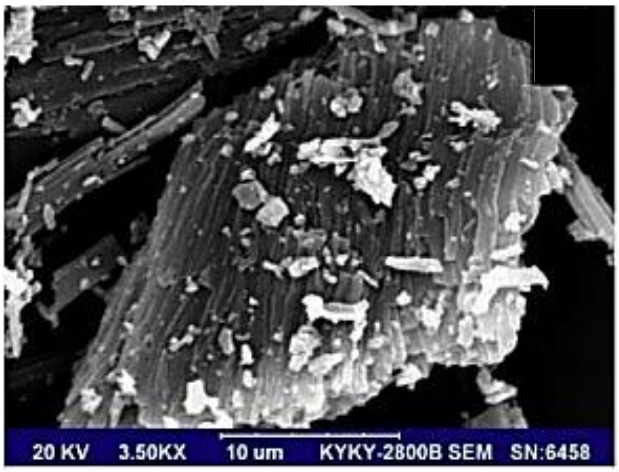

Figure I-4: SEM image of SSP particles [61].

Therefore, considering the distinguished physical properties of LS and SSP, the SCC rheology may be anticipated. It is, however, worth mentioning that further studies under controlled conditions (varying SSP and LS while keeping the other components constant) are needed to increase the reliability of these predictions, considering the chemical composition of both powders, their surface protonation in water, and their compatibility with SP and other admixtures.

b) Effect of Natural Coarse Aggregates (NCA) and Recycled Coarse Aggregates (RCA)

Regarding the effect of the nature of the coarse aggregates, the second influential parameter of the study, on SCC rheology, the ability of SCC to maintain the homogeneity of the aggregates distribution is governed by the aggregates volume fraction, distribution, and physical properties. The particle shape factor is the key physical property for SCC, among others. Unlike angular and semi-rounded aggregates, round aggregates offer better flowability and reduced blocking potential for a given water-to-binder (w/b) ratio. Flaky and elongated particles can also cause blocking problems in confined systems [17].

NCA possesse a smoother surface compared to RCA, which increases the flowability of the SCC. Improper SP dosage or w/b ratio may increase the bleeding likelihood and reduce the segregation resistance of SCC incorporating such aggregates. Moreover, one significant difference between RCA and NCA is water absorption. The tendency of RCA to absorb more water during mixing, due to the residual mortar adhered to their surfaces, leads to SCC with lower flowability. Pre-saturation and water compensation are among the most common approaches to mitigate this issue. Although both approaches led to concrete with the same slump, the slump measurements are more consistent with water compensation. These similarities are only relevant when measuring the slump immediately following the mixing phase [76,77].

As time proceeds, RCA reduce the workability retention of SCC compared to SCC with NCA [77], but its bleeding and segregation resistance are simultaneously improved. Moreover, the moisture state of RCA critically influences the rheological behavior. For instance, saturated surface dry RCA (the aggregates are pre-saturated and then dried until their surfaces are free of moisture, but their internal pores remain filled with water [78]) initially increase the cumulative bleeding of SCC, but tends to stabilize rapidly after 45 minutes [76]. In contrast, air-dry RCA, with a water compensation technique, increase the effective w/b ratio of SCC, thereby enhancing flowability and cumulative bleeding [77,79]. Moreover, the adhered old mortar imparts a rough surface texture to RCA, consequently increasing the yield stress and introducing yet another factor that negatively affects SCC workability [80–82]. Furthermore, it also reduces their bulk density [83], causing the fresh concrete density to follow a decreasing linear trend as the substitution rate increases, with an average loss of about 5% at a 100% substitution rate [84].

2.4.2 Cement hydration

a) Effect of limestone and scallop shell powders

When used in binder compositions for SCC, either as a cement substitute or as an addition, LS has been shown to accelerate and even alter the early stages of cement hydration reactions, as evidenced by isothermal calorimetry results [85]. Several experimental studies [86,87] report that cement-LS mixtures, which can be extended to SCC, exhibit a shortened induction period followed by a sharp increase in hydration heat, which was related to the possible promotion of heterogeneous nucleation of hydration products. In more depth, LS is an effective SCM in providing nucleation sites, compared to others (for instance, quartz) [88]. In addition, LS particles increase the shearing rate during mixing due to a decreased distance between particles, depending on density and particle size. Therefore, the two physical phenomena together further promote the heterogeneous nucleation of C-S-H [87–89].

- **Limestone powder- cement hydration chemical interactions**

Initially, LS was considered chemically inert in cement hydration, as the transformation of ettringite into monosulfate, accompanied by heat release, was observed during cement hydration [90,91]. Later, however, it was recognized as an active part in cement hydration [19]. LS was found to interfere particularly with the hydration of the C_3A phase, with no observed reaction with C_3S. As a result of this chemical interaction, Hemicarboaluminate (Hc) and Monocarboaluminate (Mc) ($C_3A{\cdot}CaCO_3{\cdot}10\text{-}12H_2O$ (AFm phases)) form, thereby inhibiting the conversion of ettringite into monosulfate and accelerating the hydration rate [92,93].

Furthermore, the reaction between LS and C_3A phase progressively intensifies with greater C_3A contents and a larger concentration of LS [94,95]. These factors are also found to dominate the timing of the appearance of Mc [19].

The detailed chemical mechanism involves first the reaction of monosulfate with carbonate ions (CO_3^{2-}) dissolved from the finely ground $CaCO_3$ (LS), forming initial ettringite and intermediate Hc, and further Mc in a more concentrated CO_3^{2-} medium [92]. The formation of Mc results from the anion exchange of sulfate ions SO_4^{2-} with CO_3^{2-} ions, due to the thermodynamic stability of the Mc and sulfate-AFm phase (monosulfate). The former is thermodynamically stable at 25 °C, while the latter is metastable at the same temperature [96]. As a result, the availability of the sulfate increases, which is the sole cause behind the inhibition of the ettringite conversion [97].

- **Scallop shell powder-cement hydration chemical interactions**

Considering the preceding discussion, it is reasonable to expect a similar contribution from SSP in the hydration reaction due to their chemical composition similarities. However, the slight differences between the two powders, including chemical composition, mineralogical structure, impurity content, or particle morphology, may result in distinct hydration kenitics. Although LS and SSP are mainly composed of $CaCO_3$, their mineralogical characteristics differ. The geological LS-$CaCO_3$ typically exhibits a pure calcite crystalline structure, while the biological SSP-$CaCO_3$ consists of a mixture of calcite and minor aragonite phases, with the aragonite content varying among different seashell species [98].

This structural distinction is noteworthy: several studies [99–101] have shown that both polymorphs accelerate cement hydration through the filler effect, but the calcite surface appeared more privileged for hydration product growth. The underlying reason lies in their atomic arrangements, where calcite is characterized by protruding oxygen (O) atoms and calcium (Ca) sub-lattice along its cleavage planes [102], a similar planar configuration of O and Ca atoms in CaO layers in C-S-H [103]. Aragonite's surface is usually stably terminated with only Ca, leading to a comparatively weaker nucleation effect [104].

Another possible explanation for the reduced filler effect of SSP is the presence of organic matter within the shell matrix, which may terminate the surfaces of biogenic calcite and aragonite grains, thereby inhibiting crystal growth [105]. Although SSP particles exhibit angular and stepped surface features, as described in § 2.4.1.1, these morphological advantages appear insufficient to compensate for the latter adverse effects. From a chemical standpoint, aragonite exhibits a slightly higher solubility than calcite at 25 °C, resulting in a comparable CO_3^{2-} release in the medium. However, this trend reverses at higher temperatures and with pH variations. Consequently, aragonite may contribute equally, or even more effectively, than calcite to the formation of carboaluminate phases [73,100]. In this direction, aragonite is also metastable, with +1 $kJ.mol^{-1}$ compared to calcite; the former being then a priori less stable in the mix.

b) Effect of Natural Coarse Aggregates (NCA) and Recycled Coarse Aggregates (RCA)

Macro *et al.* [106] investigated how the moisture state of coarse aggregate affects the hydration reactions of concrete. Their results demonstrated that (i) the moisture condition of NCA, either dry or saturated, does not perturb the hydration kinetics due to the low water absorption of NCA; (ii) in contrast, the moisture condition of RCA had a significant influence, where the authors reported that the mix containing saturated RCA exhibits a lower temperature peak and prolonged hydration. Although the original study did not aim to compare RCA with NCA directly, an additional observation emerged from comparing the hydration behavior of the mixes containing each type of aggregate. The comparison revealed that under dry conditions, the aggregate type does not significantly affect hydration, as both mixes displayed similar temperature evolution profiles. However, under saturated conditions, the mix with saturated NCA exhibits a higher and earlier temperature peak compared to its counterpart with RCA. Similar results are highlighted in another study [107]. The two studies attributed the lowest heat release and the extended reaction period of the saturated RCA mixes to the additional water introduced by the saturation water, which increases the w/c ratio.

2.4.3 Hardened properties

a) Effect of limestone and scallop shell powders

When comparing two powders with similar chemical compositions, the subtle particularities of each powder determine the extent to which they influence the fresh properties and hydration kinetics and, consequently, the final hardened properties of the resulting concrete. Of course, the intrinsic physical properties of the powders can influence the hardened properties of SCC; however, these effects can be generalized to other SCMs of the same category, the case of LS and SSP, depending not on the powder type itself but on their specific physical attributes. For instance, it was found that when LS particles are finer than cement particles, the packing density improves, thereby enhancing the compressive strength and durability of the concrete, which can include SCC [103,108]. In contrast, when the LS particles are coarser than the cement particles, they increase the interparticle-trapped water. As a result, the thickness of ITZ increases, leading to higher overall porosity and subsequently affecting other hardened properties [87,103]. However, it is worth noting that a decrease in long-term compressive strength was observed in concrete containing finer SCM, attributed to the dilution effect caused by the finer particle size distribution. Therefore, if these changes are related to particle size, finer or coarser SSP particles are expected to exhibit the same effects as LS.

Extending beyond the physical aspects, among all SCMs, LS and SSP exhibit the lowest reactivity (if considered pozzolans). The higher the proportion of each powder participating in carbo-aluminate phase formation, the greater the beneficial effect on hardening properties. The lower densities of these phases Mc: 2.17g/cm^3 and Hc: 1.98 g/cm^3, compared to cement hydrates C-S-H: 2.22–2.33

g/cm^3, C-A-S-H:1.5–2.4 g/cm^3, CH: 2.20 g/cm^3, and Ms: 2.02 g/cm^3, led to improvements in macroscopic properties: densification of the microstructure of the cement matrix, further reductions in system porosity, and an increase in compressive strength [95]. Furthermore, when the LS sustains an increase in hydration rate for up to 90 days [96], ensuring the compressive strength development, SSP decreases the long-term compressive strength. The observed decrease was attributed to organic impurities present in the SSP [105,109]. Although this effect may not significantly affect early-age compressive strength, potentially due to the SSP physical characteristics, it may lead to Delayed Ettringite Formation (DEF), resulting in expansion and microcracking at later ages [110–113].

b) Effect of Natural Coarse Aggregates (NCA) and Recycled Coarse Aggregates (RCA)

Compared to NCA, RCA influence the hardened properties of SCC through their reactions with cement hydration kinetics, their effects on fresh-state behavior, and their direct impact on the physical and structural characteristics of the concrete. The alterations in hydration kinetics and fresh-state performance of SCC, outlined in § 2.4.1and § 2.4.2, can be correlated with variations in compressive strength. The RCA's high water absorption capacity, if not considered during mix design, reduces the local effective w/c ratio. As is well known, the modifications in the w/c ratio directly impact the compressive strength development of concrete [107]. However, the water compensation method (adjusting the mixing water), when combined with adequate curing, is widely accepted as the most practical and least intrusive solution to overcome this issue compared to other techniques [114]. The considered property helped reduce the bleeding, thereby enhancing the homogeneity and stability of the mix, which can contribute to improving mechanical performances [115].

Regarding RCA's direct effect on compressive strength, the surface roughness of RCA plays a pronounced role when using them in a dry state, which improves mechanical interlocking and enhances the adhesion between the aggregate and the fresh mortar. The so-called nailing effect can positively influence compressive strength [76,80]. Furthermore, although it is hypothesized that residual mortar on RCA might chemically bond with new mortar, microstructural analyses revealed a morphologically different ITZ, typically characterized by increased porosity, weaker and less dense, due to their higher porosity alongside their high water absorption capacity [81,116]. Additionally, the preponderance of research pointed out the weaknesses of RCA, lower mechanical properties, and its consequences on the internal stress distribution within the paste, potentially affecting the strength [107]. Nevertheless, in SCC, the greater paste volume surrounding the RCA potentially strengthens them and enhances the weak region of ITZ [115]. Figure I-5 shows that SCC mixes incorporating RCA exhibit lower compressive strength compared to those made with NCA, with the extent of strength reduction varying from one study to another.

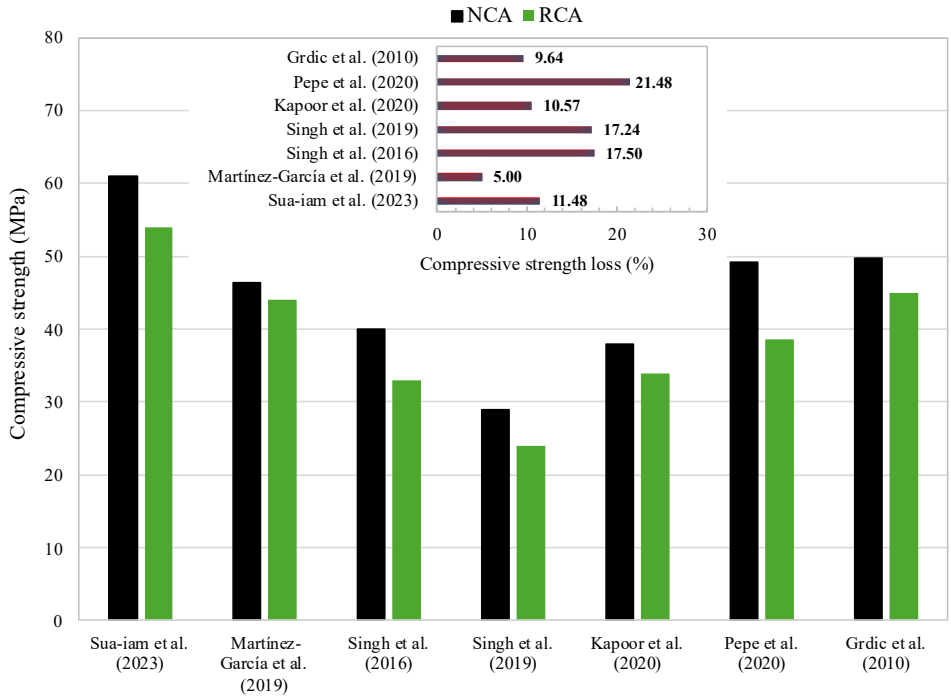

Figure I-5: 28-day compressive strength of SCC mixes with 100% RCA substitution [106,117–122].

Furthermore, the inclusion of RCA in SCC decreases the overall density while increasing the porosity and water absorption. The sole cause of these modifications remains in the above-mentioned characteristics of old mortar surrounding their surface. Additionally, RCA concrete features two distinct ITZs: one between the old mortar and RCA and another between the aged NCA surface and the new mortar. These zones create a heterogeneous area that increases porosity and consequently results in greater water absorption and lower compressive strength [123]. Eventually, the hardened properties of RCA SCC, like in other types of concrete, are strongly influenced by the intrinsic characteristics of the RCA, including the porosity, density, and quality of its former adherent mortar [124,125]. This explains the observed variability in the properties of concrete incorporating these aggregates, which is the key reason why the use of RCA in concrete is still met with hesitation and limited trust, particularly for structural purposes (Figure I-6).

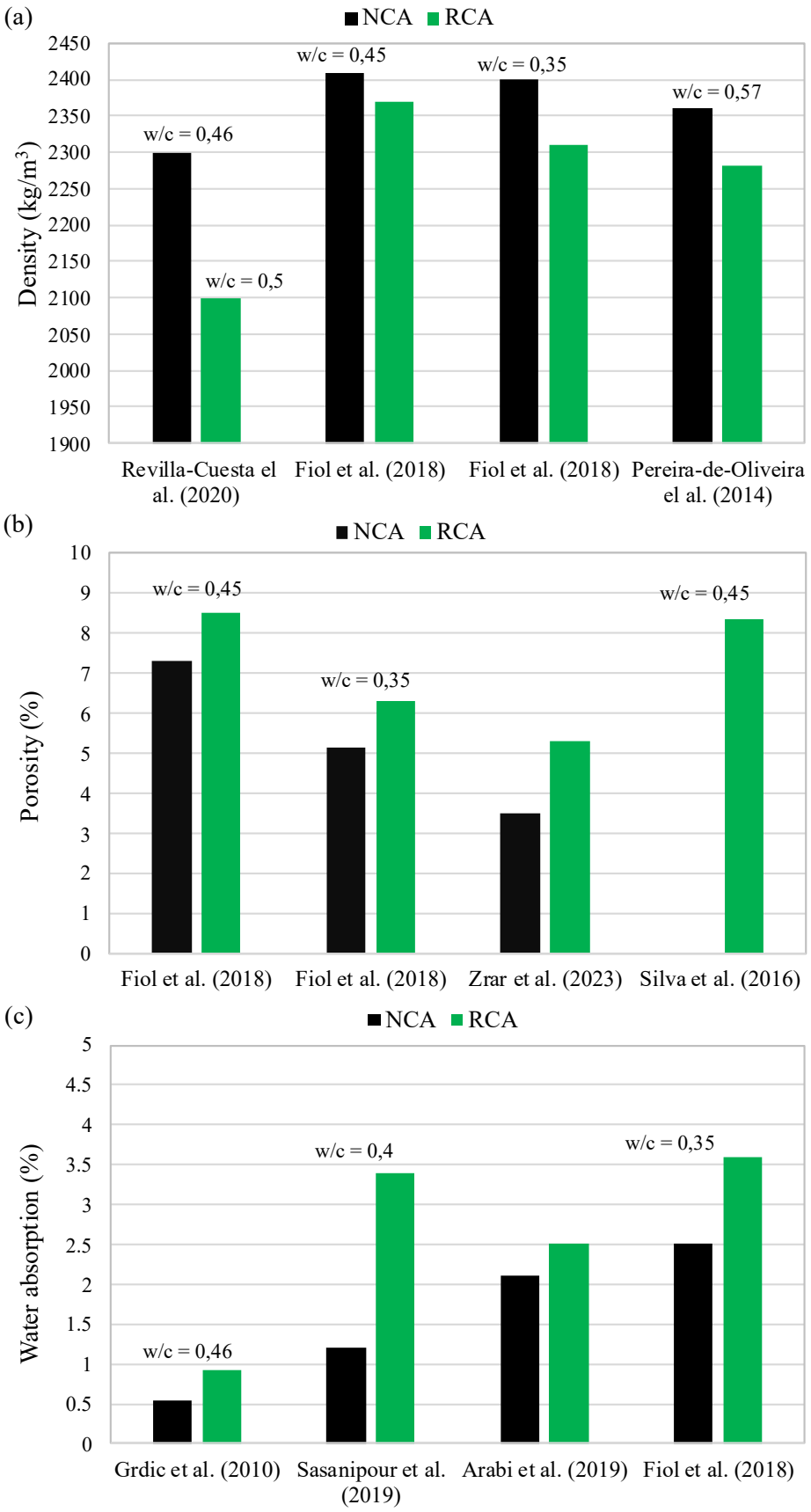

Figure I-6: 28-day a) density [123,126,127], b) porosity [126,128,129], and c) water absorption of SCC mixes with 100% RCA substitution [122,126,130,131].

3 Carbone Capture Storage, and Utilisation (CCSU) technologies: Ex-situ carbonation

3.1 Ex-Situ Carbonation pathways: Suitability for self-compacting concrete

3.1.1 Mineral carbonation

Mineral carbonation involves reacting CO_2 with natural or residual alkaline materials containing calcium (Ca) or magnesium (Mg) within a reactor. The reaction results in the permanent conversion of CO_2 into stable carbonates, either Ca or Mg carbonates ($CaCO_3$/$MgCO_3$), as in natural processes. The process is primarily divided into direct and indirect carbonation, each of which can occur under dry or aqueous conditions. The considered pathways begin with the initial grinding of the feedstock into a fine powder. This powder is mixed with distilled water to form a slurry (aqueous carbonation) or kept in solid form (dry carbonation). The slurry formed or the solid material is introduced into a reactor and combined with CO_2 [132,133]. In indirect routes, an extraction agent, such as chloride hydroxide (HCl), is necessary to accelerate the dissociation of ions from materials [134]. The effectiveness of these pathways depends on the water availability for the dissolution of CO_2, the high divalent cation materials composition [135,136], the ions dissolution rate (strongly depends on acidic conditions (indirect route) [137,138], and the fineness of the feedstock [139,140]. Otherwise, the amount of carbonate formed is minimal, limiting their feasibility for large-scale industrial applications.

Consequently, neither the operating procedures of these pathways are suitable for CO_2 storage in SCC, nor does the SCC constitute an appropriate feedstock, unlike other industrial wastes such as steel slags [141–143] red mud [144], FA [145,146], and fine cement and concrete wastes [147,148] which are commonly used in such pathways.

3.1.2 Accelerated carbonation

This category involves artificially increasing the carbonation reaction rate using CO_2 pressure [149] during the mixing phase of concrete, known as carbonation mixing, or during the fresh and hardened states of concrete, known as carbonation curing. Carbonation mixing involves the incorporation of pressurized high-purity carbon dioxide at a specified flow rate directly into the concrete mix during the mixing step [140,150]. The injected CO_2 then reacts with calcium silicate clinker, forming amorphous or nanocrystalline $CaCO_3$ and C-S-H gel [151]. In contrast, carbonation curing is a method in which freshly cast concrete is exposed at an early age, generally from 2 to 24 h, to a controlled flow of pressurized, high-purity carbon dioxide within a sealed chamber. Nevertheless, the potential of CO_2 uptake during carbonation mixing seems to be lower than during carbonation curing [152].

3.2 Carbonation curing in laboratory settings

Among all the various ex-situ carbonation pathways discussed earlier, carbonation curing is the most suitable for SCC and is particularly interesting to the precast concrete industry [153]. Carbonation curing can be implemented by injecting a CO_2 gas flow or by curing the SCC in carbonated water [154,155]. However, carbonation curing by injecting a CO_2 gas flow is the most frequently used technique, the most suitable for precast concrete, and the most effective in terms of CO_2 uptake capacity [156]. Although carbonation curing was initially proposed in the 1970s, it has only been widely adopted in recent decades [153]. The process typically involves three steps: pre-conditioning, CO_2 exposure, and post-conditioning [157].

3.2.1 Pre-conditioning monitoring

The preconditioning phase starts after casting, proceeds before the CO_2 exposure, and ensures the carbonation reaction's effectiveness. During this phase, a controlled amount of free water should be removed from the specimens before their exposure to CO_2 (Figure I-7). The optimal degree of water removal varies depending on the w/c ratio and concrete type and ranges between 40-45% or 58%-62% [158,159].

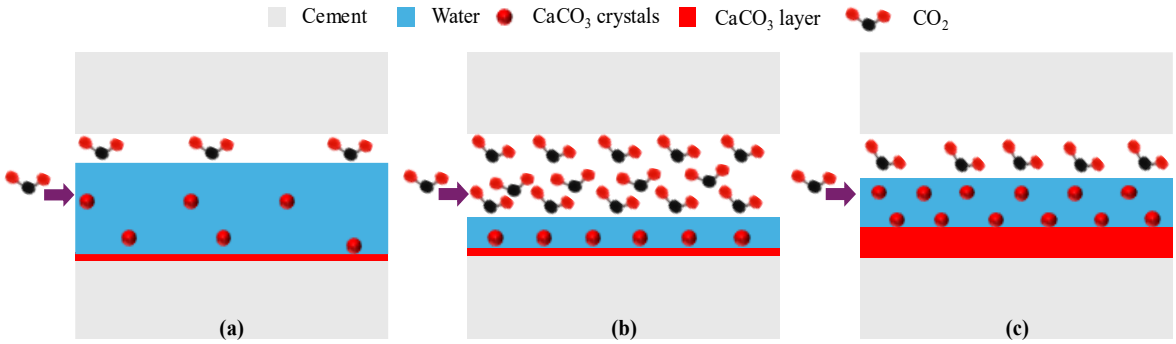

Figure I-7: CO_2 diffusion in the concrete's pore network, adapted from [160].

Insufficient water removal limits CO_2 diffusion within the specimens, while excessive water removal leads to water starvation and interrupts the subsequent hydration and carbonation reactions [153,161]. Several studies [162,163] provide different approaches to managing water removal, such as reducing the w/c ratio to eliminate the need for preconditioning, though this is particularly challenging for SCC. Another consists of demolding the samples right after the initial setting for the high slump concrete, including SCC, after 4 h to 18 h of in-mold curing, or immediately after casting for dry-mix products, to maximize the surface area for moisture aeration [153,164,165].

Following demolding, preconditioning starts under different environmental conditions: at temperatures ranging from 22 °C to 25 °C, at ambient relative humidity (RH) to 30% RH, 40% RH,

50% RH, 60% RH, and 90% RH, for 3 h to 9 days [165–169]. However, other studies report that the temperature reached 50 °C during the in-mold or out-mold curing to optimize the preconditioning duration [170,171].

3.2.2 Carbonation or CO_2 exposure

In laboratory experiments, CO_2 exposure operates in a sealed chamber, where the samples are exposed to a pure CO_2 high-pressure gas under controlled conditions for a specific period [172]. The materials' CO_2 uptake is optimized by carefully monitoring the reaction conditions. CO_2 uptake increases significantly with higher CO_2 concentrations and gas pressure.

The optimal temperature for carbonation remains under discussion. Controversial studies have reached diverging results. Some researchers claim that high temperatures slow down the rate of carbonation due to the evaporation of water required to dissolve CO_2 [149]. Other teams have identified an optimal carbonation temperature of around 100 °C [173] but generally maintained between 20 and 25 °C to avoid excessive energy consumption. Contrary to usual ionic salt behaviors, for which more dissolution in water occurs for higher temperatures, $CaCO_3$ precipitation is favored at temperatures around 40 °C for water containing only Ca^{2+} and CO_3^{2-} ions [174]. It is consequently not surprising that higher temperatures give rise to more $CaCO_3$. However, we could not find any study dealing with such precipitations in cementitious media, particularly in the presence of silicates.

Moreover, to our knowledge, no study has clearly defined the optimal duration of carbonation curing and the specific factors to consider in achieving this target without compromising the concrete's strength [175–177]. Additionally, no conclusive information is available on the ideal timing for initiating carbonation to ensure optimal hydrate formation and maximum interaction of CO_2 with these phases. Excessive precipitation of $CaCO_3$ in the outer layer of the sample could impede CO_2 diffusion. RH also influences the CO_2 uptake of concrete. Yoon *et al.* [178] reported an optimal RH range of 50-70%, giving rise to the highest carbonation depth. Moreover, the use of multi-component gases, such as NO_2 and SO_2, can influence the dissociation of CO_2 due to the considerable competition between these gases, thus reducing the CO_2 uptake efficiency [179].

3.2.3 Post-conditioning

The earlier steps focus on boosting CO_2 uptake at the expense of the water content. Therefore, subsequent hydration (water spraying or placing specimens in a moisture room in most cases [180]) follows to restore water levels, thereby promoting further hydration [158]. This step aims to improve the microstructure and mechanical properties of the carbonated materials [181]. However, this step tends not to be included in all research [182,183].

3.2.4 The influential parameters of CO_2 uptake of carbonation-cured materials

As a continuation of the discussion in previous sections regarding the influence of experimental settings on CO_2 uptake, it is crucial to recognize that the material composition also significantly affects the efficiency of the accelerated process. Among these is the selection of SCMs. As confirmed by Yoon *et al.* and Younsi *et al.* [178,184], the carbonation rate increases when SCMs, particularly high-calcium FA, replace cement. Xuan *et al.* [182] associated the increase in carbonation degree to: (i) the rise in porosity due to OSP incorporation, which enhances the diffusion coefficient of the samples; and (ii) the preferential precipitation of carbonation products on OSP, which boosts its affinity for CO_2 and reduces the interfacial energy required for the precipitation of carbonation products.

Moreover, LS provides preferred nucleation sites for $CaCO_3$ precipitation over portlandite, $Ca(OH)_2$, and C-S-H phases [185,186]. The type of aggregate indicates that RCA promote CO_2 uptake by decreasing pore saturation due to their high water absorption and enhancing CO_2 transport due to their high porosity. The old mortar surrounding their surface can also serve as an additional calcium source for the carbonation of the newly formed SCC [187].

Another critical factor to consider is the w/c ratio. A higher ratio benefits hardened cement-based materials by providing greater porosity and improved CO_2 diffusion, as explained by Greve-Dierfeld *et al.* [188]. These dynamics change in freshly cast cement-based materials. The degree of carbonation remains notably low due to the slow penetration rate of CO_2 gas into water-saturated pores, which is approximately 10,000 times lower than that in unsaturated pores, as reported by Liu *et al.* [160].

Table I-3 summarizes the experimental CO_2 uptake data from various studies, focusing on different experimental settings. These include material conception, pre-curing processes, and carbonation curing parameters.

Table I-3: CO_2 uptake under different experimental conditions.

Samples	w/c	[CO_2]% P (bars)	Temperature (°C)		% RH		Pre-curing time (h)	CO_2 exposure (h)	CO_2 uptake (wt%)	Ref
			Pre-curing	Carbonation	Pre-curing	Carbonation				
Mortar	0.3	1 bar pure	20 ± 3	-	60	-		1	18.2	[189]
		1 bar flue gas						1	10.5	
		7 bars pure						1	21	
		7 bars flue gas						1	11.5	
		1 bar pure						12	22	
		1 bar flue gas						12	24	
		7 bars pure						12	24.9	
		7 bars flue gas						12	26	
Mortar	0.35	20	20	20	60	70	2	2	0.5	[190]
								4	0.8	
								8	1.9	
								16	4.9	
								24	7.4	
							16	2	1.9	
								4	3.1	
								8	5.7	
								16	8.9	
								24	10.3	
Cement paste	0.4	20	20 ± 3	20 ± 3	-	60 ± 5	24	4	9.43	[191]
Cement, 20% LP paste									10.42	
Cement, 20% GGBS paste									11.6	
Cement, 20% FA paste									13.94	
30% HFA Mortar	0.4	20	20 ± 1	20 ± 0.5	60 ± 2	70 ± 2	12	3 days	6.44	[192]
30% CHFA Mortar									5.59	
Concrete	0.4	5 bars	25	-	50 ± 5	-	5 to 6	12	15.81	[158]
	0.3								10.13	
OPC-Concrete	0.4	5 bars	25	-	50 ± 5	-	5.5	12	14.3	[193]
FHOPC-Concrete			26	-	50 ± 5				17.06	

3.3 Carbonation chemistry of cement-based materials: CO_2 uptake mechanism

In cement chemistry, the mechanism of CO_2 uptake by cement-based materials, including SCC, is called carbonation. The carbonation of these materials involves complex and disproportionate interactions between CO_2 (captured from the air and subsequently dissolved in the pore solution) and various phases of the cementitious matrix, including $Ca(OH)_2$, C-S-H, ettringite, monosulfoaluminate ($3CaO.Al_2O_3.CaSO_4.12H_2O$), and anhydrous phases.

Accelerated carbonation differs from its natural counterpart primarily in the CO_2 concentration to which concrete (or other cement-based materials) is exposed and the resulting phase transformations. Castellote *et al.* [194] demonstrated that when concrete is exposed to 0.03 vol% of pure CO_2 flux, simulating natural carbonation, C-S-H decomposes into Ca-modified silica gel and remains in the samples. At the same time, $Ca(OH)_2$ also remains but diminishes with a slight increase in CO_2 (3 vol%). Ettringite and anhydrous phases remain stable under natural exposure conditions. The reactivity of these phases can be limited by environmental conditions, particularly rainfall and moisture availability. For instance, CO_2 is transported by water within concrete. If water cannot reach the anhydrous phases, CO_2 cannot either. As confirmed by Boumaaza *et al.* [195], the carbonation of anhydrous materials was minimal. A minimum of 33% RH is necessary to initiate their carbonation. Similar results were observed for ettringite. However, $Ca(OH)_2$ and C-S-H can carbonate even at lower RH levels. Whether the carbonation process is natural or accelerated, the $CaCO_3$ particles formed from these reactions precipitate rapidly and randomly in the solid matrix, with a particular preference for the smaller pores, where water condenses more effectively [196].

3.3.1 Dissolution of CO_2 in the interstitial solution

During the dissolution phase, the dissolved CO_2 exists in different forms depending on the medium's pH. When the pH exceeds 4, a minority fraction of CO_2 molecules combines with water to form carbonic acid (H_2CO_3) at 25 °C (Eq. I-1) [197].

$$CO_{2(g)} + H_2O_{(l)} \rightarrow H_2CO_{3(aq)} \qquad \text{Eq. I-1}$$

The carbonic acid, in turn, dissociates and releases two protons, forming hydrogen carbonate (HCO_3^-) and carbonate (CO_3^{2-}) ions through the following reactions (Eq. I-2 and Eq. I-3) [197,198].

$$H_2CO_{3(aq)} \rightarrow HCO_{3(aq)}^- + H_{(aq)}^+ \qquad pKa_1 = 6.35 \qquad \text{Eq. I-2}$$

$$HCO_{3(aq)}^- \rightarrow CO_{3(aq)}^{2-} + H_{(aq)}^+ \qquad pKa_2 = 10.33 \qquad \text{Eq. I-3}$$

Consequently, CO_3^{2-} ions are the dominant species in the medium at pH larger than 10.33 (at 25°C), as H_2CO_3 is completely dissociated. At intermediate pHs [6.3-10.3], HCO_3^- ions predominate [199]. The overall process is summarized for large enough pH values (Eq. I-5) [197].

$$CO_{2(g)} + H_2O_{(l)} \rightarrow H_2CO_{3(aq)} \rightarrow CO_{3(aq)}^{2-} + 2H_{(aq)}^{+} \quad \text{Eq. I-4}$$

3.3.2 Portlandite carbonation

The reaction between $Ca(OH)_2$ and CO_2 follows the reaction (Eq. I-5) [190].

$$Ca(OH)_{2(s)} + CO_{2(g)} \rightarrow CaCO_{3(S)} + H_2O_{(l)} \quad \text{Eq. I-5}$$

Eq. 5 presents the overall reaction but doesn't show the intermediate steps of the process, which are important, from our perspective, for understanding the medium in which the carbonation reactions occur. In contact with water, $Ca(OH)_2$ dissolves, undergoing the two dissociations (Eq. I-6 and Eq. I-7) [200].

$$Ca(OH)_{2(s)} \leftrightarrow CaOH_{(aq)}^{+} + OH_{(aq)}^{-} \quad \text{Eq. I-6}$$

$$CaOH_{(aq)}^{+} \leftrightarrow Ca_{(aq)}^{2+} + OH_{(aq)}^{-} \quad \text{Eq. I-7}$$

Due to the low solubility of $Ca(OH)_2$, with a solubility product (K_{sp}) of 5.5×10^{-6} at 25°C [201], it was reported that only a minimal fraction of $Ca(OH)_2$ dissolves in the interstitial solution of concrete or cement. Consequently, the CO_3^{2-} reacts directly with $Ca(OH)_2$ crystals, leading some researchers to suggest that the carbonation occurs via a solid-state reaction [202]. Others, in contrast, suppose that the reaction occurs via a dissolution-precipitation state, which aligns with the claim that carbonation requires water [203,204]. In other words, the $Ca(OH)_2$ dissociates in the pore solution into three ionic species: $CaOH^+$, Ca^{2+}, and OH^-, with no $Ca(OH)_2$ crystals remaining.

Once the equations (Eq. I-6 and Eq. I-7) occur, Ca^{2+} ions react with CO_3^{2-} ions to form $CaCO_3$ (Eq. I-8). This can only happen if OH^- ions are present in the medium to form CO_3^{2-} ions via HCO_3^- ions, also present in the medium, i.e., only at high pH values (Eq. I-9). In cement-based materials, such pH values are provided through the dissolution of $Ca(OH)_2$ (Eq. I-6 and Eq. I-7). After $CaCO_3$ formation, the progressive consumption of OH^- ions results in a pH drop, typically from 13.5 to 8.5 [28]. The reduction in pH is also related to the release of H^+ resulting from HCO_3^- dissociation to restore the CO_3^{2-}/HCO_3^- equilibrium once the CO_3^{2-} is consumed (further discussion can be found in § 3.3.6) [201,205].

$$Ca_{(aq)}^{2+} + CO_{3(aq)}^{2-} \rightarrow CaCO_{3(s)} \qquad K_{sp} = 4.14 \times 10^{-5} \quad \text{Eq. I-8}$$

$$HCO_{3(aq)}^{-} + OH_{(aq)}^{-} \rightarrow CO_{3(aq)}^{2-} + H_2O_{(l)}$$ Eq. I-9

3.3.3 Calcium silicate hydrate carbonation

Calcium silicate hydrates, C-S-H, are generated during the hydration of the two phases of clinker, namely C_3S and C_2S [206]. These hydrates can undergo carbonation in the presence of CO_2 (Eq. I-10) [207].

$$(CaO)_x(SiO_4)_y(H_2O)_{z(s)} + xCO_{2(g)} \rightarrow xCaCO_{3(s)} + ySiO_2 \,.\, tH_2O_{(s)} + (z - yt)H_2O_{(l)}$$ Eq. I-10

Where:

$$0.6 < x/y < 2\,;\ 1 < z < 4 \text{ and } t < z$$

The previous reaction depends on the initial C-S-H 's Ca/Si ratio. However, the initial stoichiometry of C-S-H phases and their carbonation reaction is unclear. In a nearly saturated C_3S paste (water content ≈ 42%), the chemical composition of C-S-H is approximately l.7CaO.SiO_2.4H_2O [208]. In equilibrated conditions, when the sample is not previously dried, crushed, and conserved under 11% RH and 25 °C atmosphere, the C-S-H chemical composition tends to be 1.7CaO.SiO_2.2.1H_2O [208,209]. While subjecting C_3S paste to D-drying (equilibrating the samples with ice at -79° C by continuous evacuation using a rotary pump through a trap cooled in a CO_2–ethanol mixture), with 20.4-22% of water content remaining in the fully hydrated samples, the chemical reaction of C-S-H corresponds to 17CaO.SiO_2.1.3-1.5H_2O [209]. As a result of C-S-H carbonation, the Ca/Si ratio drops continuously with the increase of the C-S-H decalcification [149,159]. Once completely decalcified, the acid-stable gel maintains the original hydrate morphology [210]. The carbonation reaction is as follows (Eq. I-11) [149].

$$(CaO)_3(SiO_4)_2(H_2O)_{2(s)} + 3CO_{2(g)} \rightarrow 3CaCO_{3(s)} + SiO_{2(s)} + 3H_2O_{(l)}$$ Eq. I-11

A recent study on C-S-H carbonation highlights that three periods exist during C-S-H carbonation, including the dissolution period characterized by a rapid release of Ca^{2+} ions from the interlayer of C-S-H, the diffusion period dominated by calcium availability, and the slowly ongoing reaction period due to thickening of carbonation products [211].

Furthermore, numerous studies report conflicting findings regarding the carbonation sequences of $Ca(OH)_2$ and C-S-H. In some research, both reactions occur concurrently [212], while in others, $Ca(OH)_2$ carbonation occurs before C-S-H decomposition [213]. Regardless of the reaction sequences, both reactions depend on the types and quantities of Lewis bases, the redox status, and the pH of the

medium [210]. Although carbonation rates are comparable, the degree of carbonation of $Ca(OH)_2$ reaches a relatively advanced level when C-S-H gel carbonation is still in progress [214].

3.3.4 Carbonation of sulfoaluminate hydrates

To examine the sensitivity of ettringite and monosulfoaluminate phases to carbonation, Nishikawa *et al.* [215] demonstrated that the synthetic ettringite samples decompose through carbonation into gypsum, $CaCO_3$, and alumina gel according to Eq. I-12 and Eq. I-13. These findings are consistent with [216–220]. Moreover, a recent study [221] confirms that carbonation affects these phases and the monosulfoaluminate carbonates as soon as CO_2 is present, producing $CaCO_3$, aluminum hydroxide, gypsum, and water (Eq. I-14) [195].

$$3CaO.Al_2O_3.3CaSO_4.32H_2O_{(s)} + 3CO_{2(g)} \rightarrow 3CaCO_{3(s)} + 3CaSO_4.2H_2O_{(s)} + Al_2O_3.xH_2O_{(s)} + (26-x)H_2O_{(l)} \quad \text{Eq. I-12}$$

$$3CaO.Al_2O_3.3CaSO_4.12H_2O_{(s)} + 3CO_{2(g)} \rightarrow 3CaCO_{3(s)} + 3CaSO_4.2H_2O_{(s)} + Al_2O_3.xH_2O_{(s)} + (10-x)H_2O_{(l)} \quad \text{Eq. I-13}$$

$$3CaO.Al_2O_3.CaSO_4.12H_2O_{(s)} + 3CO_{2(g)} \rightarrow 3CaCO_{3(s)} + Al_2(OH)_{3(s)} + CaSO_4.2H_2O_{(s)} + 10\,H_2O_{(l)} \quad \text{Eq. I-14}$$

3.3.5 Anhydrous phases carbonation

In the case of the anhydrous C_3S, C_2S, and Celite ($3CaO{\cdot}Al_2O_3$ (C_3A)) carbonation, Boumaza *et al.* [195] designed and validated an experimental setup to assess the CO_2 binding capacity of cementitious materials, with particular emphasis on these phases. The outcomes show that no direct carbonation of these phases is possible. They exhibit carbonation reactions only if they happen concurrently with their hydration. The chemical reactions of the three anhydrous phases are given below (Eq. I-15, Eq. I-16, and Eq. I-17).

$$3CaO.SiO_{2(s)} + nH_2O_{(l)} + 3CO_{2(g)} \rightarrow 3CaCO_{3(s)} + SiO_{2(s)} + nH_2O_{(l)} \quad \text{Eq. I-15}$$

$$2CaO.SiO_{2(s)} + nH_2O_{(l)} + 2CO_{2(g)} \rightarrow 2CaCO_{3(s)} + SiO_{2(s)} + nH_2O_{(l)} \quad \text{Eq. I-16}$$

$$3Ca_3.Al_2O_{6(s)} + 6H_2O_{(l)} + 3CO_{2(g)} \rightarrow 3CaCO_{3(s)} + 2Al_2(OH)_{3,s)} + 3H_2O_{(l)} \quad \text{Eq. I-17}$$

3.3.6 pH-dependent stability of cement hydrates

Although only briefly referred to in § 3.3.3, the pH of the medium controls the stability of cementitious hydrates by influencing their dissolution, the precipitation of secondary phases, and the equilibrium of ionic species. The consumption of $Ca(OH)_2$ reduces the amount of OH^- in the medium, necessary to achieve a pH above 10.33 to dissolve H_2CO_3 into CO_3^{2-} before any $CaCO_3$ can form.

Indeed, as soon as CO_3^{2-} forms, $CaCO_3$ precipitates [222]. In other words, pH fluctuations in the pore solution affect the equilibrium between carbonate species, HCO_3^- and CO_3^{2-}, thereby affecting the Ca^{2+}/CO_3^{2-} ratio in the medium [205,223]. The decrease in pH also affects the Ca/Si ratio of C-S-H, which decreases with decreasing pH, lowering the C-S-H carbonation reaction rate (Table I-4).

Table I-4: Phase changes through the carbonation process [224] [225].

Contact concrete → Carbonated concrete				
Stage 1	Stage 2	Stage 3	Stage 4	Stage 5
pH > 12.5	pH < 12.5	pH < 11.6	pH < 10.5	pH <. 10
$Ca(OH)_2$	-	-	-	-
C-S-H, Ca/Si > 1.5	C-S-H, Ca/Si > 1.5	C-S-H, Ca/Si > 0.5		SH, some CaO, Ca/Si > 0.5
-	$CaCO_3$	$CaCO_3$	$CaCO_3$	$CaCO_3$
AFm	AFm	AFt / $Al(OH)_3$	$Al(OH)_3$	$Al(OH)_3$
AFt	AFt	AFt	$Fe(OH)_3$	$Fe(OH)_3$

Furthermore, Shi *et al.* [226] proposed a thermodynamic model (Figure I-8), which was later adopted by Greve-Dierfeld *et al.* [188], predicting the carbonation reaction sequence induced by pH changes as follows:

- Destabilization of (monosulfate / Hc)-AFm phases into Mc-AFm, if available.
- Carbonation of the first major hydrate, $Ca(OH)_2$, with a pH around 12.5.
- Once the accessible $Ca(OH)_2$ is completely consumed, C-S-H decalcification starts at a Ca/Si ratio of around 1.3, with a marginal decrease in pH.
- Decomposition of Mc into strätlingite, accommodating the releases of aluminum and silicon from the C-S-H. Simultaneously, C-S-H is continuously consumed, with the Ca/Si ratio remaining the same.
- After the consumption of Mc, C-S-H decalcification and decomposition continue down to Ca/Si of around 0.75, with a drop in pH to 11.
- Decomposition of strätlingite and ettringite at a pH of around 10, with continuous consumption of C-S-H until the Ca/Si decreases to approximately 0.67.
- Decomposition of C-S-H into calcite and hydrated amorphous silica, with a rapid drop of pH from 10 to 8.5.
- Finally, hydrotalcite decomposes at this pH level.

The mentioned sequence was observed in white Portland cement [188], calcium sulfoaluminate cements [227], Portland cement blended with fly ash [228], and metakaolin and LS [226].

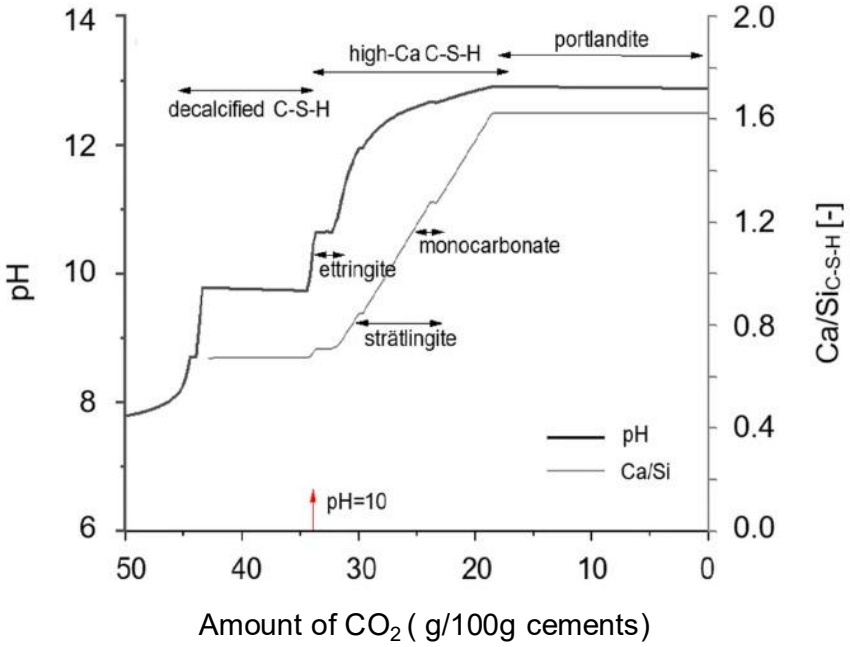

Figure I-8: Changes of the hydrate phases as a result of carbonation for different blends predicted by thermodynamic modeling [188,226].

3.4 Carbonation reaction products

3.4.1 Calcium carbonate polymorphs mineralogy

The six major minerals of interest that contain calcium carbonate in their composition are crystalline calcite, aragonite, vaterite, calcium carbonate monohydrate ($CaCO_3.H_2O$), ikaite ($CaCO_3.6H_2O$), and amorphous $CaCO_3$ [229]. Calcite displays a rhombohedral habit, aragonite typically appears as prisms or needle-like crystals, and vaterite tends to form polycrystalline spherulites. These three polymorphs exhibit a wide range of crystalline habits depending on thermodynamic and chemical conditions [174]. These three polymorphs are the most discussed in the literature and are usually detectable while artificially increasing the rate of CO_2 [230]. As mentioned earlier, calcite, crystallizing in a trigonal space group, is the most thermodynamically stable crystalline phase among the others. Aragonite, with an orthorhombic crystal structure, is more soluble and denser than calcite under standard temperature and pressure conditions (Table I-5). Vaterite is the least stable of the three polymorphs and has long been described in a hexagonal crystal structure before being recently shown as a modulated monoclinic [231]. Due to their metastable nature, both aragonite and vaterite usually revert to calcite under normal conditions, except for biomineral aragonite, found in most mollusk shells, which is also recycled in concretes.

Table I-5: Solubility products [229] and density [232] of the three crystalline calcium carbonate polymorphs.

Polymorph	Structure	-log k_s at 25 °C	Density (g/cm^3)
Calcite	Rhomboedral	8.48	2.71
Aragonite	Orthorhombic	8.34	2.93
Vaterite	Hexagonal	7.91	2.54

Carbonate minerals are typically stable in a hexagonal or rhombohedral crystal structure [233] when the ionic radii of the divalent cation are less than 0.99Å. On the contrary, orthorhombic minerals are stable for ionic radii exceeding 0.99 Å. The Ca^{2+} cation radius in the structure is at 0.99 Å, which means, depending on the ambient conditions, either hexagonal or orthorhombic $CaCO_3$ can form. In other words, Ca^{2+} possesses an ideal size, making it versatile in terms of the crystalline carbonate structures that can form compared to other cations. Calcite and aragonite can also differ in their tendency to accept other divalent cations than Ca^{2+} in a solid solution. Cations such as Mg^{2+}, whose ionic radii do not exceed that of Ca^{2+} (0.66 Å), cannot fit into the aragonite structure, being too small to stabilize the orthorhombic lattice. They therefore commonly crystallize in the hexagonal structure, like in dolomite. Conversely, larger cations are more likely to be accommodated within the orthorhombic aragonite structure (Figure I-9) [234]. Mg^{2+} cations also destabilize calcite in aqueous media [235,236].

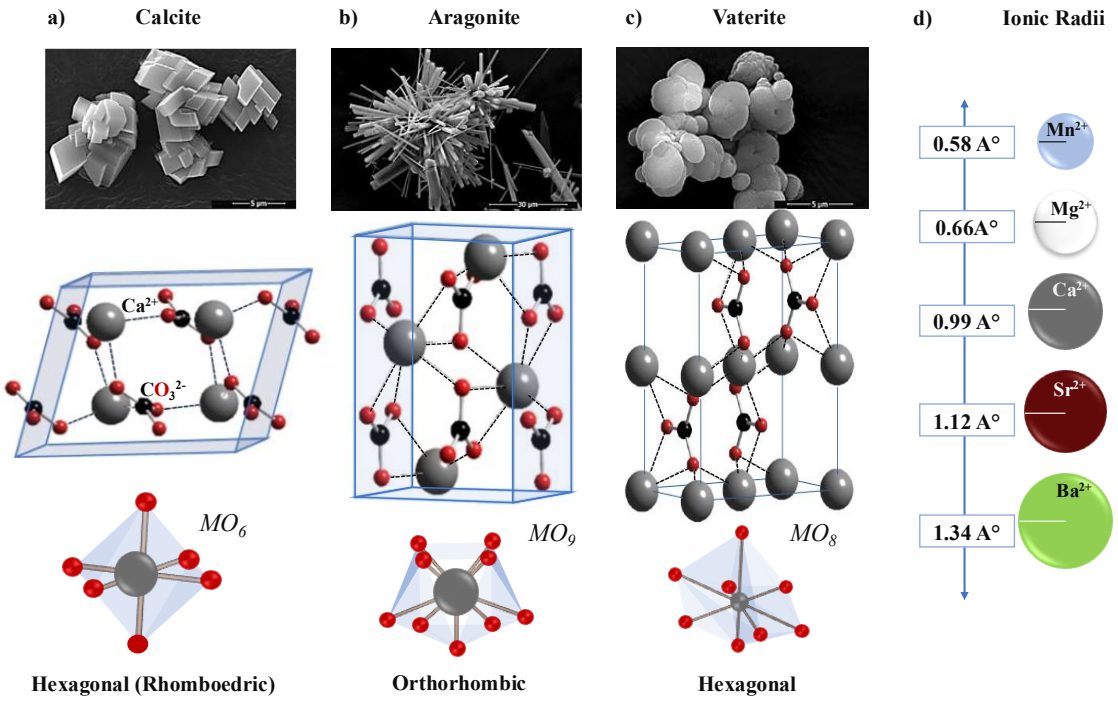

Figure I-9: $CaCO_3$ crystalline polymorphs and structural unit cells [237–239].

3.4.2 Calcite, aragonite, and vaterite precipitation

The precipitation of calcite, aragonite, and vaterite during the carbonation process can be affected by kinetic and/or thermodynamic factors dominating the process. The increase in flow rate or CO_2 content, carbonate ions concentration [CO_3^{2-}], and temperature promotes the formation of vaterite and aragonite. This phenomenon was attributed to the fact that these parameters slow down the transformation of these two polymorphs to calcite [240]. Conversely, an increase in Ca content or calcium cation concentration [Ca^{2+}] promotes only the formation of rhombic calcite. The formation of this polymorph was related to the excess of Ca^{2+} in the medium, which speeds up the transformation of vaterite to calcite [241]. Hu *et al.* [235] also reported that low supersaturation and higher temperatures promote the formation of needle-like aragonite. The latter forms above 60 °C, while the vaterite forms between 30 °C to 40 °C [242], depending on the conditions. Therefore, when the kinetic factors predominate, controlled temperature, pH, saturation levels, and additives concentration, $CaCO_3$ precipitates as aragonite or vaterite. Conversely, when the thermodynamic factors dominate, the precipitation of $CaCO_3$ as calcite is thermodynamically favored [243].

Table I-6 regroups the $CaCO_3$ polymorphs detectable during the carbonation curing of cement-based materials, as reported in the literature.

Table I-6: $CaCO_3$ polymorphs detected after carbonation curing from different studies.

Samples	Reaction medium	$CaCO_3$ polymorphs	Ref
Cement mortar w/c = 0.45 5% $Mg(OH)_2$	70 °C 20% CO_2 60% RH	Dominant aragonite Calcite	[244]
Mortar	24 ± 2 °C 544 ± 49 ppm CO_2 40% ± 6 RH	Aragonite Vaterite (Early age of curing)	[245]
β-C_2S and γ-C_2S compacted powder w/solid (s) = 0.15	99.9 % pure CO_2 0.2 MPa CO_2 2h	Calcite Vaterite	[246]
Calcium silicate pastes	23–55 °C 15-100 % CO_2 94% RH	Calcite, aragonite	[247]
Concrete	4h CO_2 exposure	Calcite, Aragonite Vaterite (1 day)	[180]
High-calcium lime pastes w/s = 0.37	20 °C 100% CO_2 pCO_2 = 1 atm 93 % RH	Only calcite	[248]
Cement paste w/c = 1	Room temperature Rich CO_2	Calcite Aragonite Vaterite	[249]
Mortar Calcium silicate powder w/c (0.202-0.206-0.191)	1–55 atm CO_2	Calcite (lower rate of heat and slower reaction) Vaterite	[250]

3.5 Assessment of carbonation efficiency: Measurement methods and approaches

3.5.1 Experimental carbonation potential of reactants

In most research studies on CO_2 storage via ex-situ carbonation, the experimental carbonation efficiency of cement-based material was evaluated through the CO_2 uptake or the carbonation degree. The most common experimental methods used are summarized below.

3.5.1.1 Mass gain method

This method is commonly used for calculating CO_2 uptake. It involves monitoring the mass gain before and after the carbonation of the samples. Thus, the CO_2 uptake can be calculated using Eq. I-18.

$$CO_2 \text{ uptake } (\%) = \frac{m_f + m_w - m_i}{m_c} \times 100 \quad \text{Eq. I-18}$$

With:

- m_i: Sample mass before carbonation.
- m_f: Sample mass after carbonation.
- m_w: Water mass lost collected in the carbonation chamber.
- m_c: Dry cement mass.

The water is collected using absorbent paper and then weighed. However, the water mass loss remains inaccurate [173,251].

3.5.1.2 Mass loss method

The mass loss method involves placing samples in an oven at 105°C for 24 hours, followed by successive heating in a muffle furnace at 525°C and then at 950°C for 2 hours at each temperature. The CO_2 uptake and carbonation degree (CD) are then determined using (Eq. I-19 and Eq. I-20), respectively, provided by Xuan *et al.* [252].

$$W_{CO2} \text{ (Sample)} = \frac{\Delta m_{CO2} - \Delta m_{525-950}}{m_{950}} \quad \text{Eq. I-19}$$

Where:

- Δm_{CO2}: Carbonated sample mass loss between 525°C and 950°C.
- $\Delta m_{525-950}$: Mass loss of original sample constituents between 525°C and 950°C.
- m_{950}: Carbonated sample mass after 950°C.

$$DC = \frac{W_{CO_2} \text{ (sample)}}{m_C \times Th_{CO2}} \quad \text{Eq. I-20}$$

Here:

- m_C: Cement content (wt%) within the sample.
- Th_{CO2}: Theoretical CO_2 sequestration capacity of the cement (0.511).

In the case of RCAs, Zhan *et al.* [253] calculated the carbonation degree as follows (Eq. I-21):

$$\varepsilon = \frac{\Delta m_e}{\Delta m_t} \times 100 \quad \text{Eq. I-21}$$

Where:

- Δm_e: Experimental mass gain of RCA before and after carbonation.
- Δm_t : Theoretical maximum CO_2 uptake by RCA-adherent cement mortar, which can be calculated as follows (Eq. I-22):

$$\Delta m_t = \frac{m_C \times Th_{CO2}\%_{max}}{(m_C + m_S + m_G + 0.23 \times m_C)(1 + Q)} \quad \text{Eq. I-22}$$

Here:

- m_c, m_s, and m_G: Mass proportions of cement, sand, and gravel in the initial concrete mixture.
- Q: Moisture content of the RCA before carbonation.

3.5.1.3 Thermogravimetric Analysis (TGA)

The mass loss occurring between 550 and 1000 °C is attributed to the decomposition of calcium carbonate, during which the carbon dioxide is released, so the CO_2 uptake is calculated using different equations proposed by several studies:

To estimate the CO_2 uptake of RCA, Djerbi *et al.* [254] supposed that only the carbonation of $Ca(OH)_2$ produces water, and calculates the uptake using (Eq. I-23).

$$CO_2 \text{ uptake } (\%) = \frac{(m_f - m_i) + M_{eg}}{m_i} \quad \text{Eq. I-23}$$

Where m_i and m_f are the sample dry masses before and after carbonation, respectively. M_{eg} is given as follows (Eq. I-24).

$$M_{eg} = m_{Ca(OH)2-ATG} \times \frac{M_{H2O}}{M_{Ca(OH)2}} \quad \text{Eq. I-24}$$

With:

- $m_{Ca(OH)2-ATG}$: Portlandite content determined by ATG between 400 °C and 600°C before carbonation.
- M_{H_2O} and $M_{Ca(OH)_2}$: Molar masses of water and portlandite respectively.

Wang *et al.* [173] calculated the carbonation degree of cement paste using TGA results, assuming that all calcium is transformed to calcium carbonate at 100% of carbonation, so the absorbed carbon dioxide is calculated per unit mass using the equation below (Eq. I-25):

$$\mu_C = \frac{C - C_0}{C_{max} - C_0} \times 100 \qquad \text{Eq. I-25}$$

Here:

- C: CO_2 content of the carbonated sample calculated from the mass loss of C-S-H and $Ca(OH)_2$.
- C_0: CO_2 content of the noncarbonated sample.
- C_{max}: Theoretical amount of CO_2 bound with all cement's calcium ions. The calcium ions bound with other components are deducted from C_{max}.

The method assumes that the total calcium content is primarily from $Ca(OH)_2$ and C-S-H. $Ca(OH)_2$ and $CaCO_3$ are quantified from TGA mass losses, and the contribution of C-S-H to $CaCO_3$ is determined by subtracting the non-carbonated state.

3.6 Concrete carbonation mechanism challenges: Contributing factors and Limitations

The carbonation process in concrete is more complex than just the reaction of dissolved CO_2 with divalent cations to form $CaCO_3$. It is a diffusion-governed process. The CO_2 diffusion into the concrete is ensured by a gradient of [CO_2] between the outer layer of concrete and its zero-concentration inner layer [255]. After diffusing through the connected pore network (gaseous phase), the CO_2 dissolves within the pore solution. It is then transported by advection driven by the liquid pressure gradient of the liquid in which CO_2 is dissolved (aqueous phase) (Figure I-10) [185,256]. Despite the dominance of CO_2 transport, whether diffusive or advective, on the carbonation process, it depends on the carbonation conditions outlined in § 3.2.4 and the coexistent reactions [257]. The coexistence of carbonation and hydration reactions in concrete's medium, besides their share of common reactants, makes the two reactions competitive. However, the carbonation reaction is more effective in relatively high CO_2 surface layers, thereby dominating the early-age reactions. The effectiveness of the carbonation reaction also depends on the hydration rate, since the hydration products constitute the principal precursor for the carbonation reaction [257]. The H_2O formed by the carbonation reaction can either increase the water availability, which promotes the hydration reaction, or increase the pore saturation degree, consequently affecting CO_2 transport and CO_2 uptake [185]. Moreover, the precipitation of $CaCO_3$ on the reacting

surface of cement grains impedes the subsequent hydration reaction [258]. It typically surrounds the Ca-containing minerals in narrow pores, inhibiting the mass transport of Ca^{2+} and CO_3^{2-} ions [258].

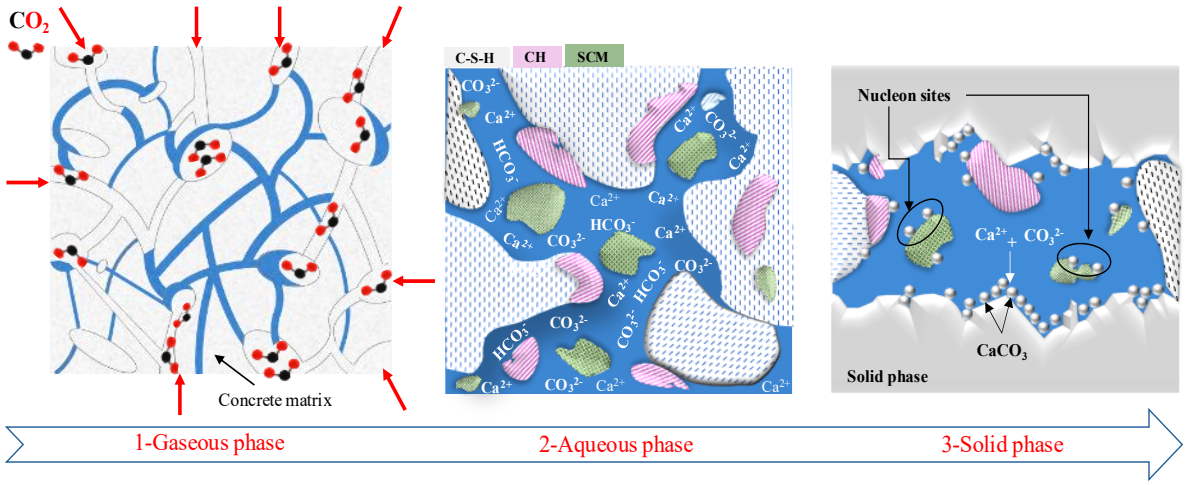

Figure I-10: Concrete carbonation process, adopted from [185].

The major challenge encountered in estimating the CO_2 uptake of cement-based materials, regardless of the method used (see § 3.5.1), is the complexity of the dissolution process of cement phases, where their dissolution depends on the medium's pH values (Table I-5). The competitive dissolution reactions complicate the understanding of each dissolution sequence in real accelerated carbonation [225]. Hence, it complicates the quantification of the $CaCO_3$ formed from each phase and the identification of the reaction coefficients for each carbonation. Moreover, contrasting findings about C-S-H carbonation show that some studies [259,260] claim that the carbonation of C-S-H produces water, while others state that only $Ca(OH)_2$ carbonation produces water [214]. Contrary to the reactional mechanism of $Ca(OH)_2$ carbonation, which is well understood, the reactional carbonation mechanism of C-S-H remains the most complex mechanism and is poorly understood due to its imprecise stoichiometry [149].

3.7 Properties changes in cement-based materials induced by accelerated carbonation

The precipitation of $CaCO_3$ polymorphs, which form depending on the medium's properties (§ 3.4.2), and the cement matrix's microstructural alteration, modify carbonated materials' intrinsic properties. These effects are particularly observable in the properties investigated in this study.

3.7.1 Mechanical properties

Carbonation curing usually improves compressive strength as compared to water-cured samples. Early-age carbonation curing (up to one day) increases the strength by 106%. However, as time progresses, the strength gap between carbonation-cured and water-cured samples narrows. By 28 days,

carbonation curing results in only an 18% increase in strength [159]. Jiang *et al.* [261] reported that carbonation curing improved compressive strength by 18.2% and 54.1% at 1 and 28 days, respectively, compared to water-cured specimens. El-Hassan *et al.*[180] reported that one day of carbonation increased the compressive strength by 13.4 ± 0.9%, with a further improvement of 29.5 ± 2.1% achieved through water compensation, compared to non-sprayed carbonated concrete. By 28 days, the compressive strength increased by 11.7 ± 0.8% with water compensation, while the non-sprayed carbonated concrete exhibited lower strength than the hydrated control. Xuan *et al.* [182] reported that carbonation curing significantly increases compressive strength during the first 7 days, followed by a gradual increase to 28 days.

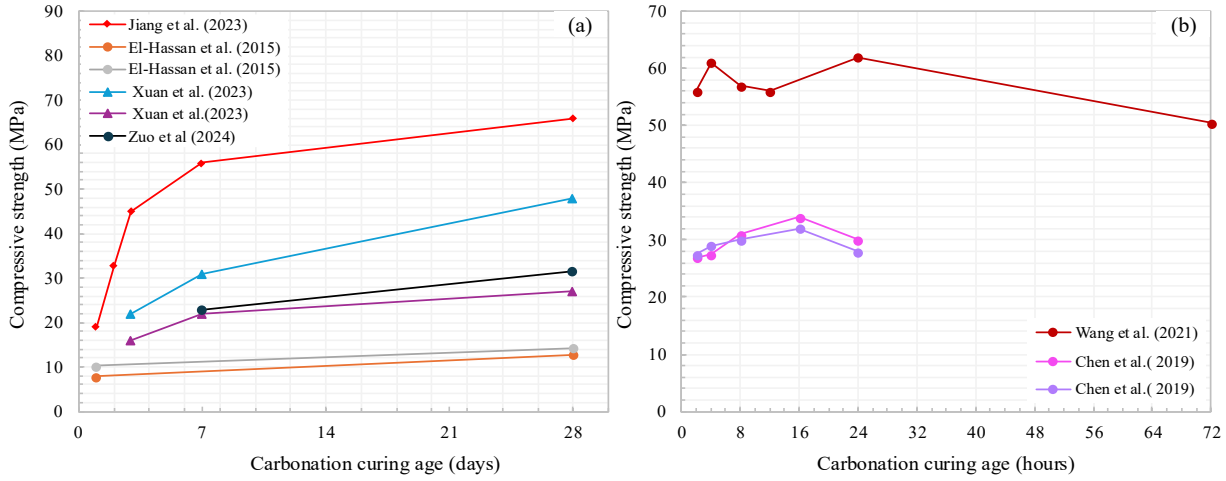

	Jiang et al. (2023)	El-Hassan et al. (2015)	El-Hassan et al. (2015)	Xuan et al. (2023)	Xuan et al. (2023)	Zuo et al (2024)	Wang et al. (2021)	Chen et al. (2019)	Chen et al. (2019)
Specimens	Mortar	Concrete	Concrete	Cement paste	Cement paste	RCA-concrete	Cement paste	Mortar	Mortar
Cement	Portland cement (P-I 42.5)	Portland cement - 15% LS	Portland cement - 15% LS	CEMI-15% OSP	CEMI-30% OSP	Cement-FA		Portland cement	Portland cement
w/c	0.4	0,71	0,71	w/b = 0.50	w/b = 0.50	w/b = 0.50	w/b = 0.22	0.35	0.35
CO_2 (%)	20 ± 2 %	0.7 bars	0.7 bars	10	10	20		20	20
Pre-conditioning	Applied-24h	Applied-18h-air	Applied-18h-air	Applied-24h	Applied-24h	Applied-24h to 120h		Applied-16h	Applied-24h
Post-conditioning	-	subsequent hydration	None	-	-	-		-	-

Figure I-11: Development of compressive strength under carbonation curing.

Moreover, the rate of strength gain decreases with higher proportions of oyster shell powder substitution. A similar trend was observed in concrete containing RCA; however, carbonation was insufficient to reach the strength of hydrated concrete containing NCA, as reported by Zuo *et al.* [187] (Figure I-11a). In contrast to these trends (Figure I-1b), Wang *et al.* [175] and Chen *et al.* [190] reported a decrease in compressive strength with prolonged carbonation. They observed the highest strength with a combination of 16 hours of pre-curing followed by 16 hours of carbonation, and also when carbonation

curing was initiated after 4 hours. These findings indicate that compressive strength is strongly dependent on the carbonation protocol and the efficiency of the carbonation process.

The increase in compressive strength induced by carbonation curing, as discussed above, is associated with calcite precipitation, which densifies the cement or concrete matrix and results in a more cohesive microstructure [156,158,159,262]. Meanwhile, the initial increase followed by a subsequent decrease in compressive strength during prolonged carbonation is attributed to excessive carbonation of the outer surface, which increases the separation between the exterior and interior of the cementitious material. This leads to the degradation of hydration products, ultimately reducing strength [177,190]. Regarding the precursors used in this study, LS and SSP contribute to carbonation-induced strength enhancement mainly through their ability to act as nucleation sites for cement hydrate growth and $CaCO_3$ precipitation. In contrast, RCA's higher porosity facilitates increased CO_2 diffusion, which promotes carbonation and potential strength gain; however, this benefit is offset by the weakening effect of the increased porosity, resulting in an overall decrease in compressive strength.

Furthermore, the precipitation of the metastable polymorph, particularly aragonite, when present in sufficiently large quantities, increases flexural strength rather than compressive strength due to its needle-like shape. As mentioned earlier, the aragonite precipitation increases with the increase in Mg content [263]. However, the increase in Mg content also increases the formation of brucite ($Mg(OH)_2$) and a range of hydrated magnesium carbonates in carbonated materials [264]. A controlled amount of these phases contributes to pore structure refinement, thereby enhancing mechanical strength. However, excessive formation of these phases can lead to expansion, thereby reducing mechanical strength.

3.7.2 Pore structure

The pore system in concrete comprises four types of pores. The first type is the gel pores, which are micropores with a dimension ranging from 0.5 to 10 nm and occupied by C-S-H [265]. The gel pores, 1.5 to 2.0 nm in size, are not detrimental to the concrete strength but are directly responsible for its creep and shrinkage. The second type is the capillary pores. These pores are meso- to macropores with an average radius of 5 to 5000 nm. The third type is the macropores generated by deliberately entrained air, and the fourth type is the macropores resulting from inadequate concrete compaction. Above these, the cracks present in the ITZ are also pores. The presence of mesopores, micropores, and cracks within the solid matrix of concrete leads to modest mechanical properties [266].

Carbonation curing exerts a contracting influence on the solid matrix pore system of carbonated cured cement-based materials. An increase in porosity is reported at an early age of intensive carbonation. This phenomenon is associated with the decalcification of the C-S-H gels [267], which leads to its volume reduction (carbonation shrinkage) [160]. As a result, the pore structure becomes coarser, with greater pore diameter, or the development of large capillary pores, especially for w/c

greater than 0.45 [268]. Any consumption of $Ca(OH)_2$ by the SCMs accentuates carbonation-induced shrinkage, depending on their latent and pozzolanic properties.

In contrast, with further carbonation, the deposition of $CaCO_3$ clogs the pores, reduces their diameter, and unifies their sizes, leading to a denser solid matrix and robust ITZ (Figure I-12) [269]. Furthermore, it is also reported that calcite precipitation generates more nucleation sites, thereby creating additional, smaller pores [160]. Additionally, the origin of the $CaCO_3$ also influences the type of pores affected: precipitates from C-S-H reduce micropores, while those from $Ca(OH)_2$ preferentially fill macropores [270].

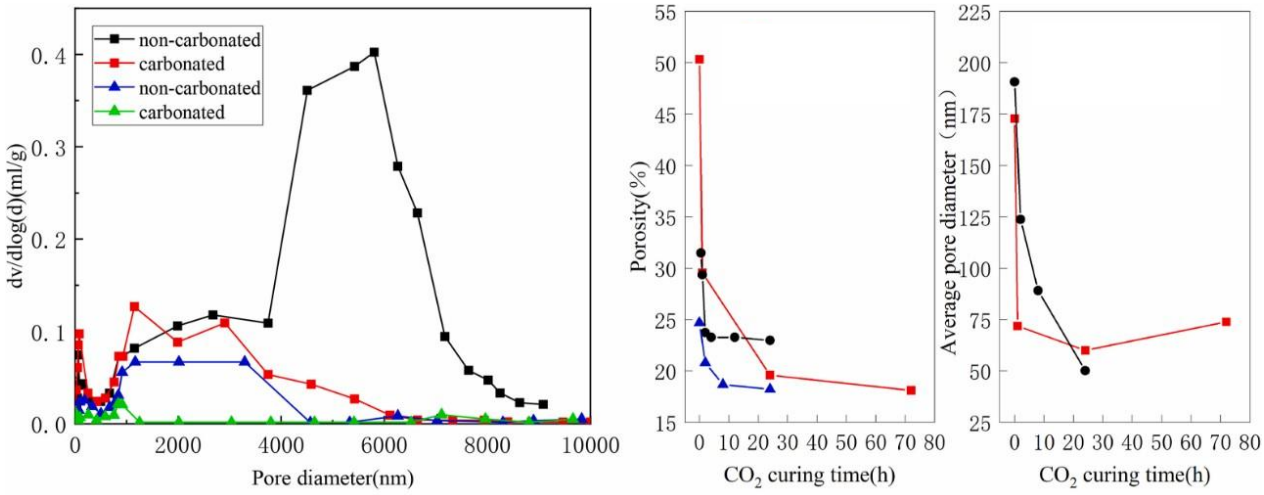

Figure I-12: Pore structure of a carbonation-cured cement paste, measured by mercury intrusion porosimetry (MIP) [159].

Furthermore, improvements in the ITZ (Figure I-12b) and a reduction in capillary porosity due to the pore-filling effect of $CaCO_3$ (Figure I-12d and f) lead to increased compressive strength and concrete density (§ 3.7.1). Carbonation curing also significantly reduces permeability, effectively slowing down chemical degradation, chloride ingress, and water absorption, thereby improving the concrete's durability [267].

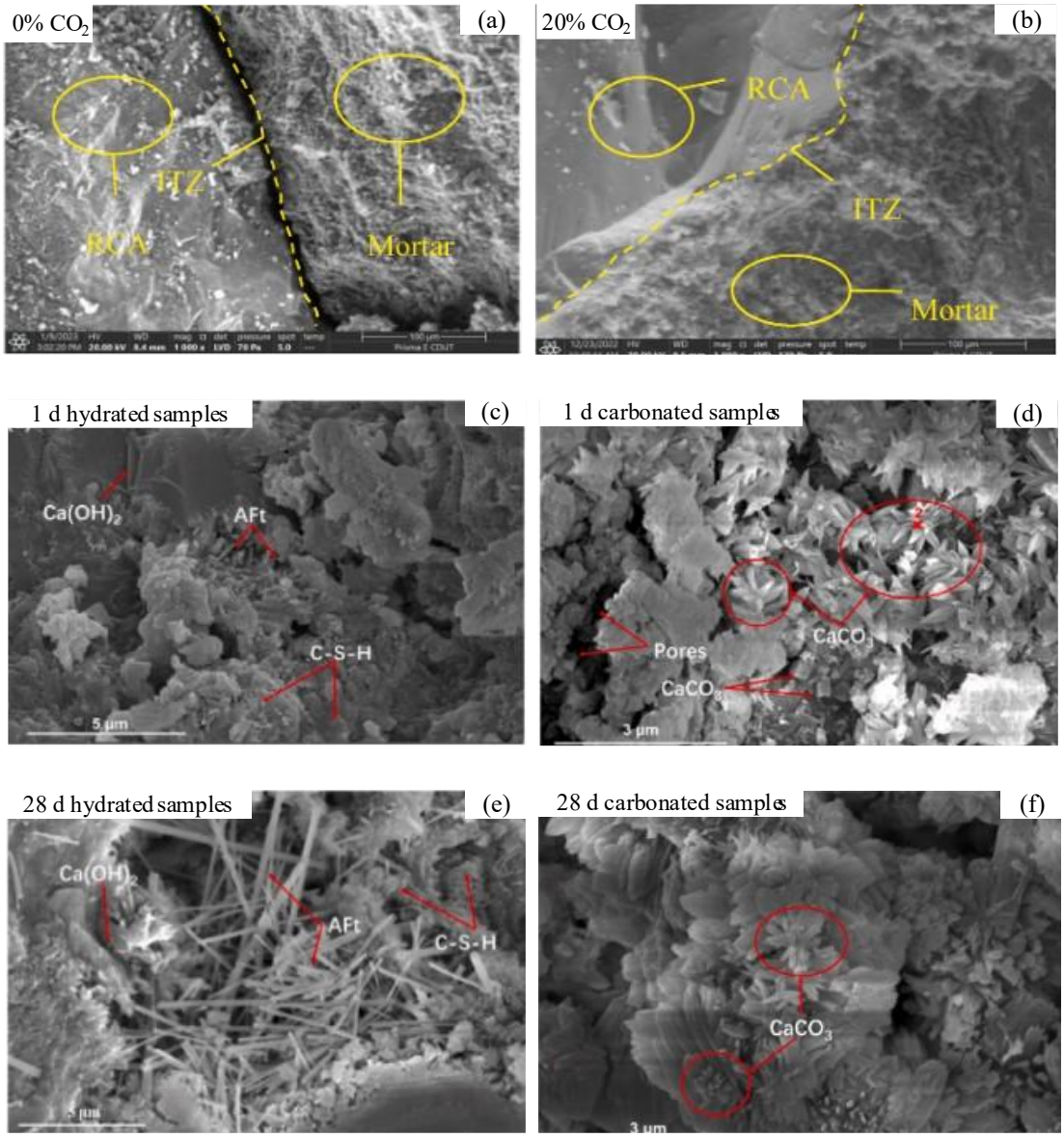

Figure I-13: SEM images of (a, b) carbonated and hydrated RCA concrete [187], and (c–f) hydrated and carbonated samples at 1 and 28 days [261].

3.8 Environmental assets of carbonation technologies

CO_2 sequestration in cement-based materials is considered a direct method, similar to mineral carbonation. However, it has distinct advantages, such as achieving effective CO_2 capture at lower temperatures (below 70 °C) and over shorter periods (less than 24 hours). These conditions demonstrate the superior efficiency of cement-based materials for CO_2 sequestration compared to conventional mineral carbonation processes [267].

Given the diversity of pathways available for CO_2 sequestration, an Life Cycle Assessment (LCA) conducted on seven direct and indirect mineral carbonation pathways, utilizing serpentine, olivine, and steel slag as raw materials, and the resulting carbonated products serving as partial replacements for cement in the final product, revealed that all seven processes effectively mitigated climate impact compared to a traditional route (Portland, CEM, etc.) for concrete fabrication. The outcomes showed reductions ranging from 0.44 to 1.17 tons CO_2-eq per ton of CO_2 stored [271].

Furthermore, a meta-analysis of LCA encompassing 29 different studies on the pathways of carbon CCSU technologies revealed that both direct and indirect mineral carbonation showed a positive environmental impact, indicating a net reduction in CO_2 emissions. Direct aqueous carbonation, carbonation mixing, and carbonation curing (the target pathway of the study) appear to be the most promising (Figure I-14). These three technologies demonstrated a positive impact on global warming and the minerals and metals impact category, regardless of the scenario used in the study, while also positively influencing other impact categories.

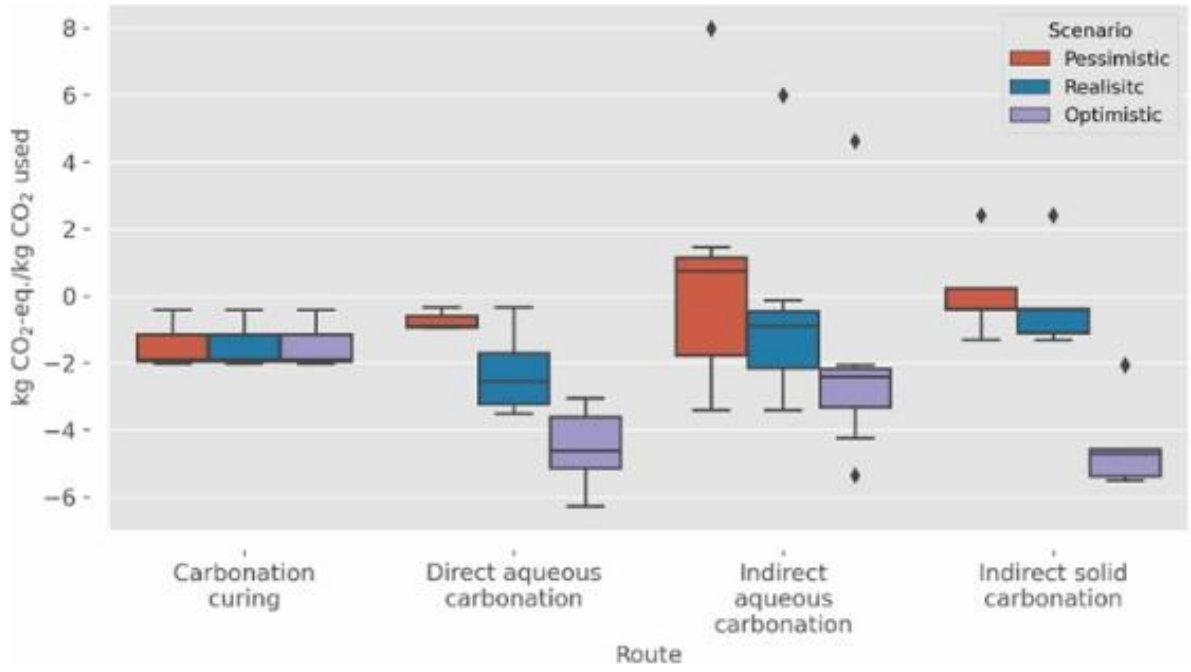

Figure I-14: Global warming impact of ex-situ carbonation technologies [272].

Overall, the LCAs of CCSU technologies have demonstrated promising potential for decarbonizing the concrete industry. However, if ex-situ carbonation technologies aim to neutralize the CO_2 emissions from the construction industry, it would be more environmentally responsible to use the released gas in its original form, without additional purification to avoid creating another source of CO_2.

None of these LCAs accounted for the CO_2 emissions related to the construction and operation of these technologies [272].

4 Synthesis

To assess the CO_2 storage capacity potential of the target SCC mixes, our strategy started by identifying the most effective protocol for CO_2 sequestration in SCC. Consequently, the literature search first focused on exploring different ex-situ carbonation pathways and selecting the most compatible with SCC.

The carbonation curing is the CO_2 storage protocol adopted in this research. Although carbonation curing offers significant potential for CO_2 sequestration, the effectiveness of the adopted protocol depends on several parameters, which need to be optimized for maximum CO_2 uptake.

Although well-documented and extensively studied, the carbonation mechanism in cement-based materials remains a complex and multifaceted process. Thermodynamic modeling can provide insights into the carbonation process; however, it does not perfectly reflect the reaction sequences observed under real carbonation exposure conditions, as the sequencing of each reaction depends on the intrinsic properties of cementitious materials.

Each existing method for estimating CO_2 uptake has advantages and limitations, leading to under- or over-estimating the CO_2 content. Some of these methods, such as TGA and X-ray Diffraction (XRD), might offer high precision but can be sensitive to experimental conditions (sample size (in mg), sample homogeneity, overlapping of mineral phases …). Other methods might be simple but often lack the precision for accurate measurements. None of the mentioned methods correlates the loss of chemically bound water with the amount of carbonate formed at the end of the carbonation process. From our perspective, including this correlation would improve the reliability of CO_2 quantification and provide insights into changes in mechanical strength.

Accounting for CCSU technologies is an optimistic move toward achieving CO_2 neutrality in the construction sector. However, compared to other alternatives, these technologies offer a promising solution. Their potential for CO_2 sequestration is evident, but implementing CCSU at an industrial scale, particularly in cement plants, a major CO_2 source, will require significant innovation, especially in the capturing and purification stages. Continued research and development in these areas will be crucial for reducing the construction industry's carbon footprint and fostering more sustainable building practices in the future.

Based on the aspects discussed in the literature review in this chapter, we laid the groundwork for our experimental research by identifying key concepts and findings that guided our investigations.

The experimental study will expand on this knowledge to further develop and refine the research. The experimental recommendations for optimizing CO_2 uptake have also been considered to enhance the efficiency and effectiveness of the results.

Chapter II

Materials and experimental procedures

1 Introduction

This chapter is organized into two main sections to provide a clear overview of the experimental framework adopted in this study. The first section presents a detailed description of the raw materials used in SCC formulation, including their physical and mineralogical characteristics. The following section outlines the experimental program used to assess the rheological behavior of SCC, its hydration kinetics, and its hardened properties before and after carbonation curing. Additionally, the methods used to quantify the SCC CO_2 uptake are presented.

In summary, the experimental program was designed to examine the properties of four SCC mixes, each incorporating different types of SCMs and aggregates. The SCC specimens were initially cured under standard conditions (water curing) for up to 90 days. This regime is generally considered optimal for the concrete properties. Therefore, the properties of the standard-cured specimens served as a baseline against which to evaluate the impact of the carbonation curing protocol explored in this study on the same properties.

Subsequently, identical SCC specimens were prepared for carbonation curing, following a 24-hour preconditioning step to promote CO_2 diffusion. Afterward, the carbonation-cured specimens underwent a series of experimental characterizations, allowing quantification of CO_2 uptake and evaluating whether the carbonation protocol can serve as a viable alternative to standard curing, particularly in influencing relevant material properties. Under each curing regime, we systematically evaluated the effects of SCM and aggregate type on SCC performance.

2 SCC Components: Key Characteristics

2.1 Binders

The study uses two binder systems: the first system consists of CEM II/A 52.5 N cement combined with LS. The second system combines the same cement with SSP, provided in shell form as separate valves, and then processed in the laboratory. More details on all raw materials are provided in Appendix 1.

2.1.1 SSP preparation

The processing steps (Figure II-1) involved in preparing the SSP, cement substitute precursor, begin with washing the shells with tap water and scrubbing them with a wire brush to remove salt residues and any remaining biomass. The cleaned shells are then ground for 4 hours using a TM500 drum mill from RETSCH©, with a rotation speed of 45 rpm and a ball/material mass ratio of 3:1. The

grounded SSP is then sieved through a 120 µm sieve to collect particles with a maximum size of 120 µm, referred to as LS. Particles retained on the sieve are collected, re-ground in an additional milling cycle, and re-sieved until all can pass through the 120 µm sieve.

Figure II-1: Process for converting SSP from shell form to powder in the laboratory.

2.1.2 Physical characteristics of binder precursors

2.1.2.1 Particle size distribution

Figure II-2 illustrates the particle size distribution of cement, LS, and ground SSP, determined using a laser diffraction particle size analyzer (Beckman Coulter, LS13 320). SSP has a larger fraction of fine particles, with approximately 40% of its particle volume below 1 µm (Figure II-2a), compared to 20% for LS and 10% for cement.

However, both LS and SSP also exhibit coarser particles than cement (Figure II-2.b), with a mean particle size of around 40 and 50 µm, respectively. A comparison of these particle size distributions indicates that, overall, while particle sizes for CEMII are predominantly distributed in an intermediate range from 2 to 40 µm, the size distribution of LS and SSP is bimodal, with a large volume fraction of size either finer than 2 µm or larger than 40 µm for their major contributions.

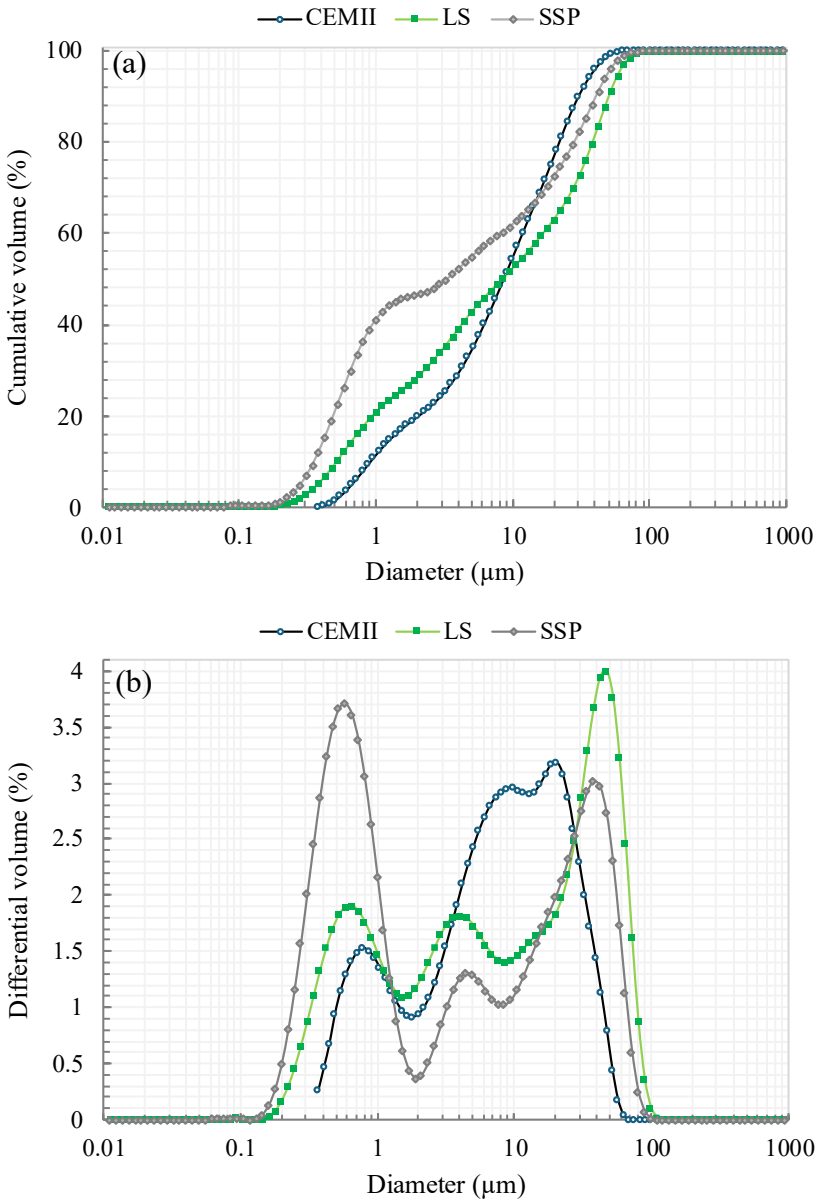

Figure II-2: Particle size distribution of the binder components.

The observed distributions result in mean sizes typically 10 and 4 times larger for cement than for LS and SSP, respectively (Table II-1). The lower density of SSP is accompanied by a larger specific surface of the grains, as seen from Blain and BET values, and correlated with the Rigden voids values. The typical value of organics in mollusk shells is 1-2% in weight. In LS, depending on the calcareous deposits and metamorphism, it is not surprising that a few‰ still remain (LOI).

Table II-1: Mean physical characteristics of binder components.

	CEM II/A 52.5 N	LS	SSP
Density (g/cm^3)	3.11	2.70	2.50
Blaine specific surface area (cm^2/g)	4436	6110	6450
Average grain size (µm)	41.04	10.20	3.90
BET specific surface area (cm^2/g)	-	16566	67565
Loss On Ignition (LOI) at 550 °C (%)	-	0.50	1.60
Rigden voids (%)	-	25	34

2.1.2.2 Particle morphology

SEM images of the LS and SSP particles (Figure II-3) illustrate some of their characteristic features and morphology. The largest LS particles (Figure II-3a) mostly exhibit plate-like shapes, with smooth surfaces and rather well-defined edges. They appear compact with only a few surface steps that signify the existence of subdivisions, either from first- or second-order lamellae, originating from ancient shells (from Brachiopoda or Mollusca) and subsequently lithified through diagenetic processes [273].

The ground LS powder shows fewer signs of fine-particle agglomeration than SSP. In contrast, the SSP particles are more irregular and granular (Figure II-3b). They exhibit rougher surfaces and more porosity, with a noticeable aggregation of finer particles. At larger magnification, the SSP SEM images reveal the original crossed lamellae system from *P. maximus* shells [72].

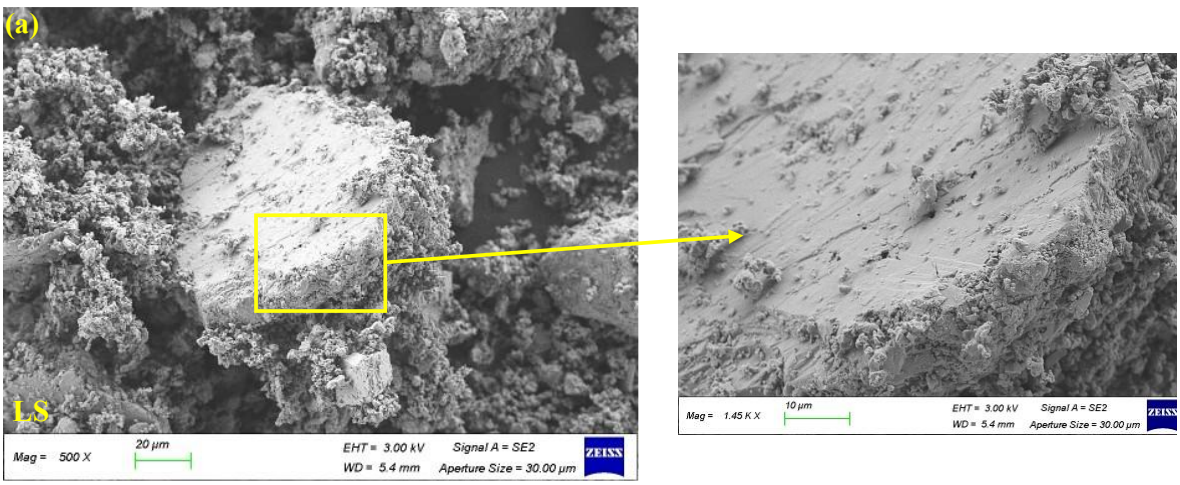

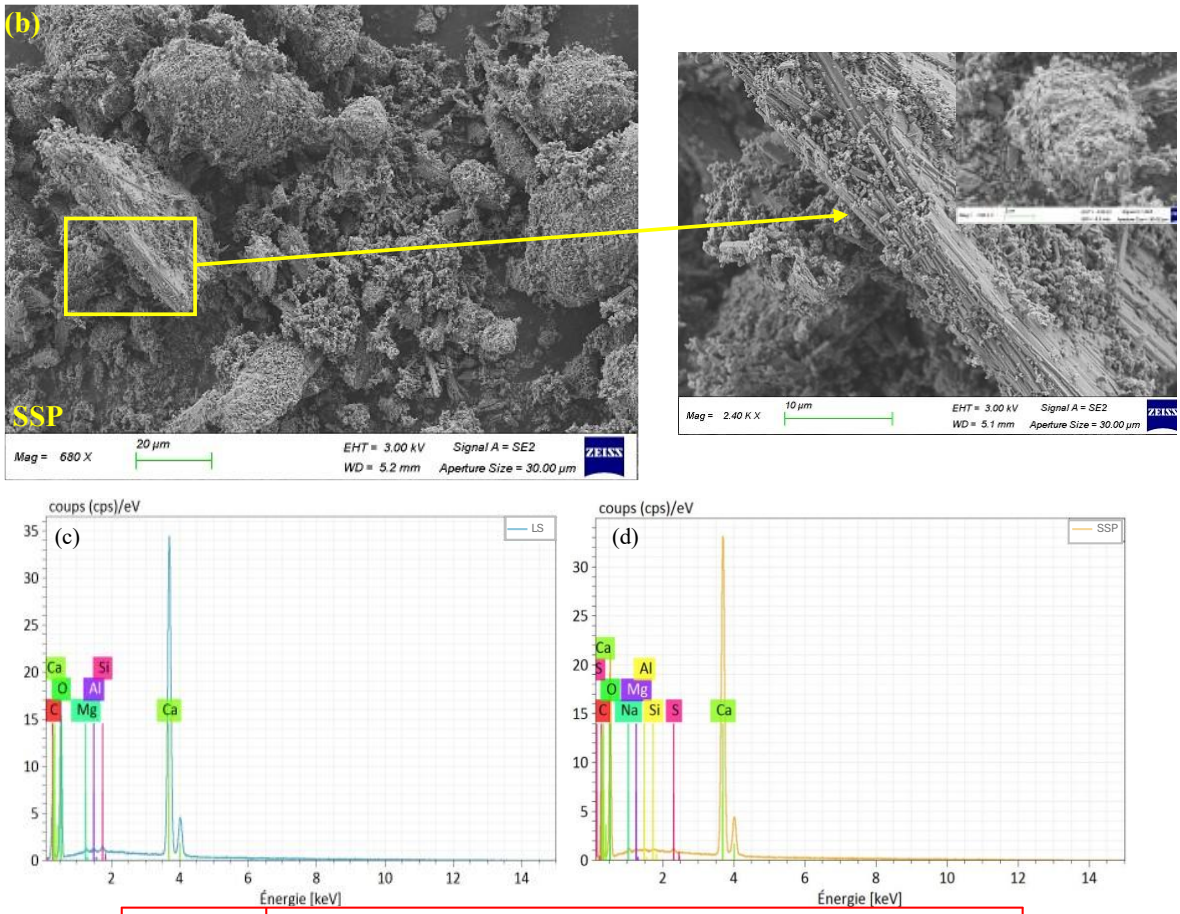

Precursor	Atom. (%)					
	Mg	Al	Si	Ca	Na	S
LS	2.14	0.94	1.24	95.68	0.00	0.00
SSP	1.01	0. 37	0.30	95.40	2.30	0.62

Figure II-3: Backscattering SEM images of the a) LS and b) SSP powders with corresponding EDS spectra shown in (c) and (d), respectively.

The reminiscence of substructural lamellae in the largest grains of LS is coherent with the still significant LOI, though at least two times less than in SSP. Element analysis from EDS spectra (Figure II-3c and d) shows that only Ca appears as a major element in the two precursors, with a trace of Mg, Si, and Al. Although Na and S are detected only in SSP, we do not observe a significant difference in composition between LS and SSP (as far as EDS is concerned), which is consistent with some of the entrapped sodium chloride and biological molecules.

2.1.2.3 Chemical properties

a) Thermogravimetric analysis

TGA weight losses (Figure II-4) for both precursor powders show a significant mass loss occurring in the 726 °C-1000 °C temperature range. This mass loss corresponds to $CaCO_3$ decomposition, which releases CO_2 [274], a classically observed phenomenon for samples mainly composed of $CaCO_3$. However, the decomposition peak in the DTG curve of SSP appears at 905 °C, 20 °C lower than that of LS (925 °C).

The difference in decomposition temperature between the two samples might be a priori associated with various factors, such as grain size, carbonate polymorphs, organic content, and crystallinity. However, both $CaCO_3$ powders exhibit a calcite signature and similar grain size distributions. SSP clearly contains intra- and inter-crystalline organic molecules, as usual in mollusk shells, within a 1-2 wt% range. Such molecules, responsible for the shell growths into oriented patterns and giving rise to unit-cell distortion of the mineral matrix, are much less able to resist high temperatures [109]. Their decomposition occurs in the 200-400 °C range, explaining the quite different evolution of the DTG curve below 500 °C, compared to that of the LS samples (zoom of the corresponding range in Figure II-4). These observations align with the loss on ignition at 550 °C values for both SSP and LS samples (Table II-1). Above 970 °C, the TGA curves show a 56% residual mass, in perfect agreement with the departure of CO_2 from 100% from $CaCO_3$.

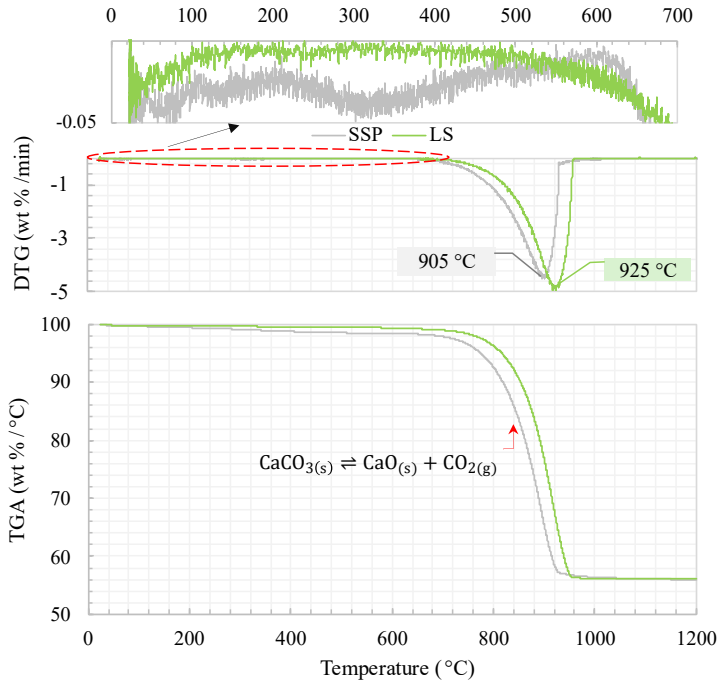

Figure II-4: TGA and DTG curves for LS and SSP powders and zoom of the DTG curves below 700°C (top plots).

b) Crystalline mineralogical phases: X-ray Diffraction

The XRD patterns of LS (Figure II-5a) and SSP (Figure II-5b) indicate that LS is composed exclusively of calcite. In contrast, SSP is primarily composed of calcite, with a minor presence of aragonite of approximately 1.1%. Moreover, we observed an enlargement of the unit cell parameters from pure mineral calcite (Standard, Table II-2) to LS and SSP. Such a unit-cell distortion has already been observed in biogenic aragonites from many shells [109,275,276], due to interactions between organic molecules and the mineral matrix.

In biomineral calcites, Pokroy *et al.* [277] also observed such distortions, though relatively smaller than in biological aragonites. Our values fit within the ranges of these authors. Although a discussion of these in depth is beyond the scope of this work, we observed larger unit-cell distortions for higher organic content (LOI Table II-1and TGA Figure II-4) in our precursors, further confirming its presence in the samples that will be elaborated throughout this work. One can also see that coherent domains (crystallite sizes, Table II-2 and Figure II-5 inserts) appear, on average, smaller in SSP than in LS, which agrees with a loss of organics in more mineralized calcite. This, together with grain shapes (as visible in SEM images), points toward larger porosity in the latter, providing more diffusion paths through the samples.

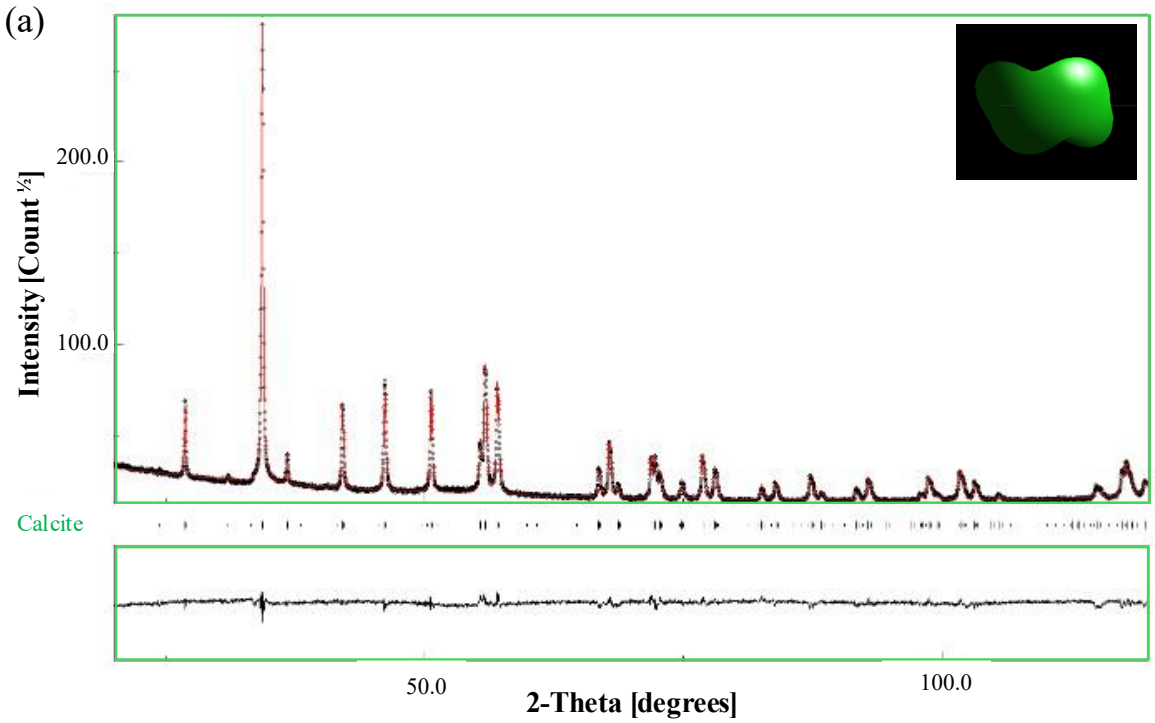

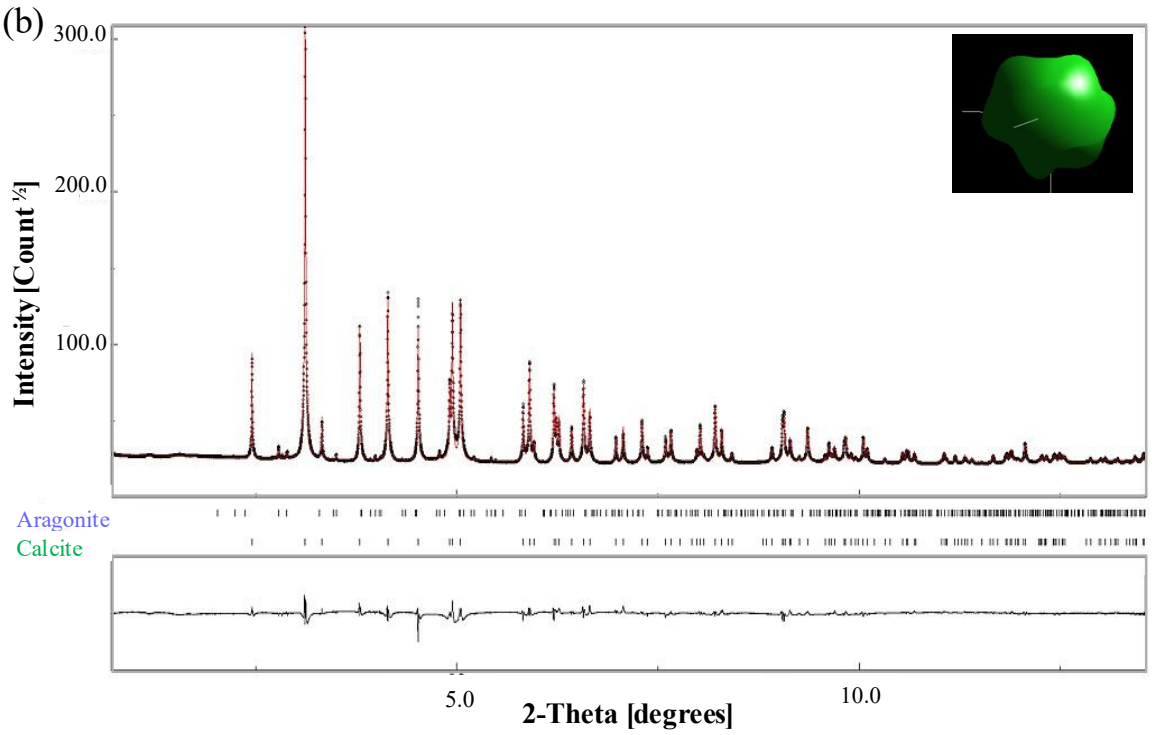

Figure II-5: XRD patterns of a) LS and b) SSP powders.

Table II-2: Crystallographic parameters of calcite and aragonite in standard, LS, and SSP. Numbers in parentheses indicate the standard deviations as 1σ on the last digits from the Rietveld refinement. Absence of standard deviations means that the values were adjusted at best manually and could not be released during the fits without instability of the refinement.

	Standard		LS R_{wp}=7.95% sig =2.02	SSP R_{wp}=7.47%	
cif	Calcite	Aragonite	Calcite	Calcite	Aragonite
COD	1547348	2100187	-	-	-
wt (%)	-		100	99(14)	1.1(2)
Unit-cell parameters (Å and °)	a = 4.98614(1)	a = 4.96183(13)	a = 4. 98680(6)	a = 4. 98849(6)	a = 4.961830(13)
		b = 7.96914(2)			b = 7,9776(25)
	c = 17.0479(3)	c = 5.742852(15)	c = 17.0495(3)	c = 17.0801(1)	c = 5.7471(13)
Mean crystallite size (Å) along main [hkl] directions	-		[300]: 2800(50)	[300]: 1380(5)	
			[012]: 1190(50)	[012]: 1070(20)	
			[006]: 760(50)	[006]: 1050(20)	

2.2 Aggregates

The aggregates used in the SCC mixes include a washed sand with a nominal size range of 0-4 mm as the fine aggregate, and two types of coarse aggregates: semi-crushed natural and coarse aggregate NCA and RCA, both with a size fraction of 4/12.5 mm (see Appendix 1).

2.2.1 Physical characteristics

Figure II-6 reveals that RCA exhibits an absorption capacity approximately twice that of NCA, nearly stable over time. The grain size distribution of the aggregates shows that NCA and RCA have very similar profiles, with particle sizes approximately ten times larger than those of sand (Figure II-7, Table II-3).

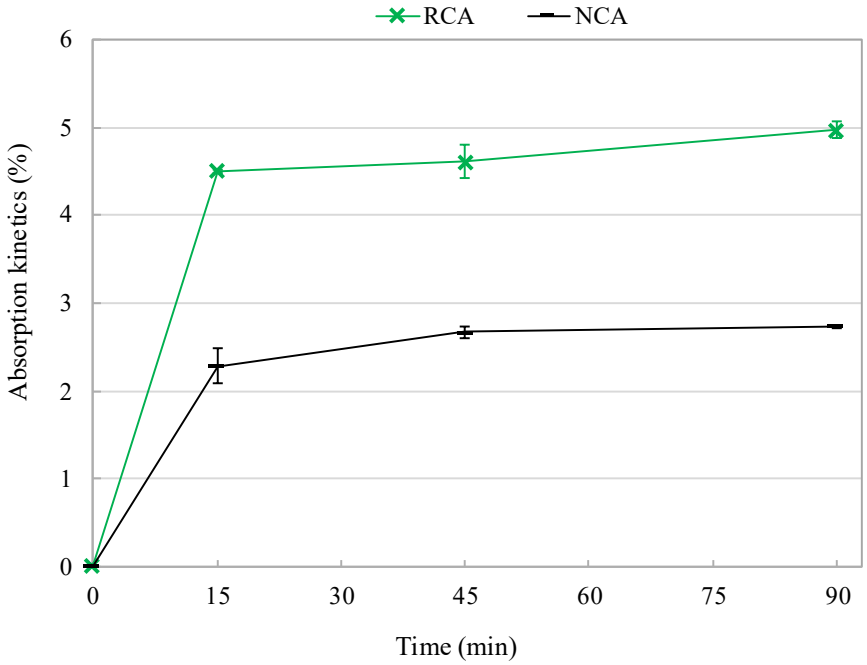

Figure II-6: Water absorption kinetics in NCA and RCA.

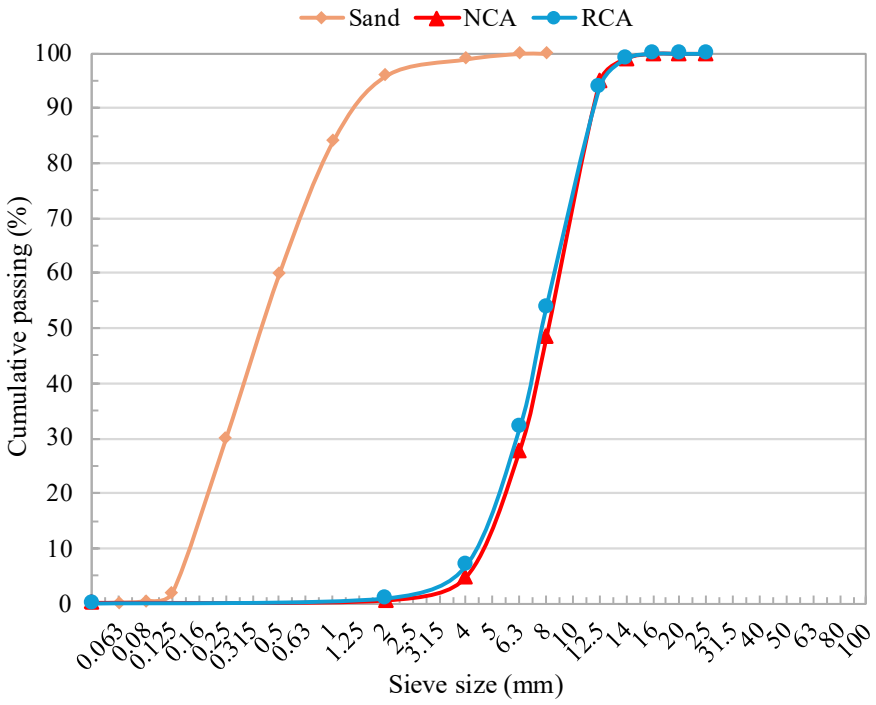

Figure II-7: Grain size distribution curves of aggregates.

Table II-3 presents other physical and mechanical properties of the used aggregates. A significant difference can be observed in the resistance to abrasion and fragmentation between NCA and RCA, the latter exhibiting relatively low mechanical properties in the corresponding tests. They also exhibit a density approximately 10% lower than that of NCA.

Table II-3: Physical and mechanical properties of aggregates.

Aggregate	LA (%)	MDE (%)	ρ (g/cm^3)	w_{24} (%)
Sand	-	-	2.61	0.40 ± 0.09
NCA	16	4	2.46	2.71 ± 0.19
RCA	31.16	46.6	2.21	5.46 ± 0.17

2.2.2 Surface texture of coarse aggregates

The NCA grain surfaces exhibit relatively low porosity (Figure II-8a), a denser texture, and no residual material, compared to the rougher RCA grain surfaces (Figure II-8b) due to the presence of adhered old mortar. The main element atoms in NCA and RCA are Si, Ca, and Al, with RCA displaying the expected aluminosilicate composition. Traces of S and Fe are present in both aggregates, while RCA also contains minor Ti, Mg, K, and Cr (Figure II-8c and d). These trace elements may interact with the matrix in subsequent formulations.

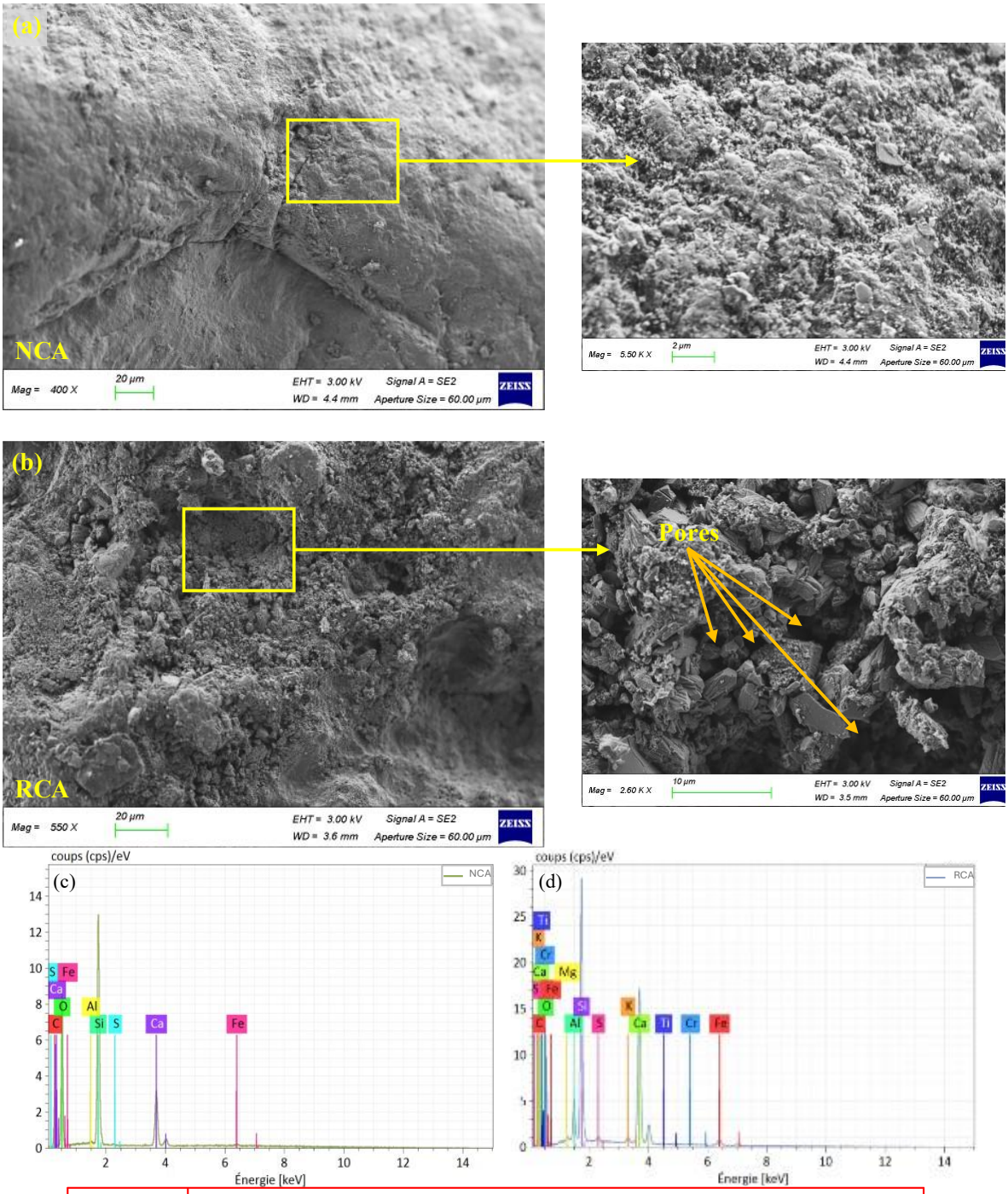

Coarse aggregates	Atom. (%)									
	Al	Si	S	Ca	Fe	S	Mg	K	Ti	Cr
NCA	0.85	74.59	0.47	23.58	0.51	0.00	0.00	0.00	0.00	0.00
RCA	6.40	44.64	0.95	42.82	3.17	0.62	0.45	0.97	0.14	0.46

Figure II-8: SEM backscattered images of the (b) NCA, and (b) RCA surfaces with corresponding EDS spectra shown in (c) and (d), respectively.

2.2.3 Characterization of the residual mortar in recycled aggregates

2.2.3.1 Thermogravimetric analysis

The TGA and DTG analyses indicate the presence of $CaCO_3$ and C-S-H phases within the adherent mortar. At the same time, $Ca(OH)_2$ is notably absent, suggesting its consumption during the natural carbonation of RCA (Figure II-9). However, TGA provides only an indirect indication of phase presence, whereas XRD gives a more direct view.

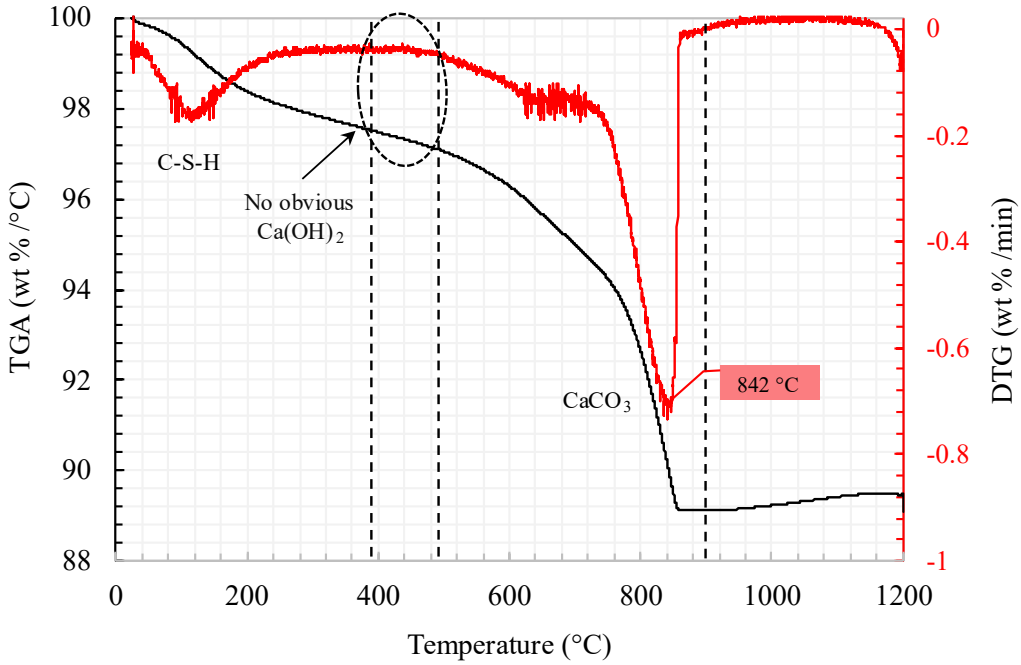

Figure II-9: TGA and DTG curves for the adhered old mortar in RCA.

2.2.3.2 X-ray Diffraction: Crystalline mineralogical phases

The adhered old mortar is composed of major mineral phases: quartz (69 wt%) and calcite (22 wt%), alongside minor constituents such as vaterite, albite low, muscovite, and chlorite, as well as trace amounts of orthoclase and aragonite (wt%, Table II-4). Such compositions are common in recycled aggregates (Figure II-10). Despite care being taken to exclude coarse aggregate (gravel) when preparing the powder for XRD measurements, it is still possible that some grains contributed to the spectrum. This could explain the minor presence of muscovite and albite, which are often found in rocks used for coarse aggregates, along with quartz and calcite (e.g., granites, granitoids…).

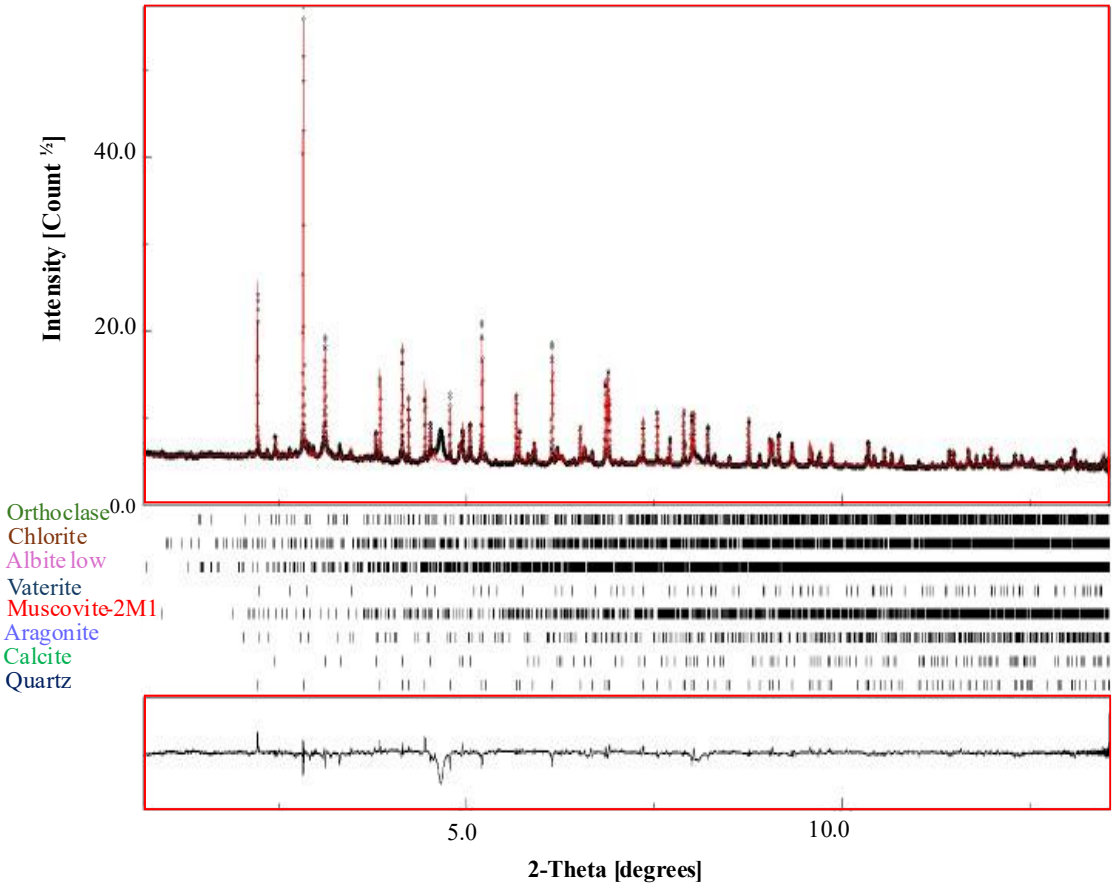

Figure II-10: XRD patterns showing the mineralogical composition of the adhered old mortar in RCA.

Table II-4: Crystallographic parameters of the phases in RCA Adhered Mortar. Numbers in parentheses indicate the standard deviations as 1σ on the last digits from the Rietveld refinement. Absence of standard deviations means that the values were adjusted at best manually and could not be released during the fits without instability of the refinement.

cif	COD	wt (%)	Unit-cell parameters (Å and °)	h k l - Crystallite size
Quartz	1011097	69(18)	a = 4.91345(2)	[1 0 0] = 3525
				[0 0 3] = 527
			c = 5.40527(5)	
Calcite	1547348	22(6)	a = 4.9875(1)	
			c = 17.0634(7)	
Aragonite	2100187	0.5(6)	a = 4.9618	
			b = 7.9691	
			c = 5.7428(7)	
Muscovite-2M1	1011049	1.3(4)	a = 5.224(4)	

			b = 8.980(9)	
			c = 20.02(2)	
			β = 94.25(8)	
Vaterite	9007475	2.4(6)	a = 4.12978(5)	
			c = 8.463(2)	
Orthoclase	9000304	0.8(3)	a = 8.545	
			b = 12.992	
			c = 7.221	
			α = 116.00	
Albite low	2107372	2.3(6)	a = 8.141(2)	
			b = 12.775(4)	
			c = 7.158 (2)	
			α = 94.28(5)	
			β = 116.60(2)	
			γ = 87.80(4)	
Chlorite	9000158	1.0(3)	a = 5.335	
			b = 9.240	
			c = 28.390	

2.3 Admixture

Two types of admixtures were incorporated during the mixing phase of the SCC mixes: PCS MasterGlenium ACE 550 and SA MasterSet AC 555 (see Appendix 1).

3 SCC mix designs and curing regimes

3.1 SCC mix designs

Four SCCs were cast at 15 °C to evaluate the influence of two main variables: binder composition and coarse aggregate type. Their proportions were derived from a previous study in collaboration with the CMEG company. The control mix consists of SCC containing only NCA and LS-cement binder and was designed using the BétonlabPro software, with the following basic parameters: C = 320 kg/m^3 of SCC, consistency class SF2, and strength class C30/37.

The formulation was optimized to ensure the same consistency and paste volume across all mixes by adjusting the w/b ratio and PCS dosage. The following recommendations were considered for SCC formulation:

- A coarse aggregates/sand (G/S) ratio close to 1
- The paste volume is between 330 and 400 l/m^3 of SCC.
- The cement content generally ranges between 300 and 350 kg/m^3 of SCC.
- The fine particle content is between 120 and 200 kg/m^3 of SCC.

All aggregates were dried at 60 °C and cooled before mixing. The water compensation method was applied to account for water loss due to RCA's high water absorption. The additional water was determined empirically through preliminary trial mixes and was adjusted incrementally until the target slump flow and workability of the SCC mix were achieved. Table II-5 presents the four SCC mix designs under investigation.

Table II-5: SCC mix designs.

Constituents (kg/m^3)	SCC			
	LS-NCA	LS-RCA	SSP-NCA	SSP-RCA
Sand	847.77	847.77	842.11	842.11
NCA	719.14	-	714.34	-
RCA 4	-	646.06	-	641.75
CEM II-52.5N	320	320	320	320
LS	137.5	135.7	-	-
SSP	-	-	137.5	137.5
Water $_{tot}$	219.6			
PCS	4.58			
SA	3.66			

3.2 Mixing method and samples preparation

All SCC mixes were blended for 3 minutes in a laboratory mixer at 17 ± 3 °C, including 30 seconds of dry mixing, 30 seconds of mixing with one-quarter of the total mixing water mixed with PCS and SA, and 2 minutes with the remaining water. Triplicate batches were prepared for the evaluation of fresh-state properties and hydration heat. Additional batches were cast into two types of specimens for hardened-state testing. Table II-6 summarizes the quantities and dimensions of the specimens and samples (fragmented or powdered) used for testing.

For tests requiring powdered samples, the matrices of SCC mixes were ground using a mortar and pestle and sieved to <63 µm, taking care to minimize the inclusion of aggregates while avoiding over-grinding, which could increase the sand content in the final powder. Specimens and samples not

tested at the end of the curing period were immersed in acetone to stop cement hydration until the day of analysis.

Table II-6: Specimens and samples: quantities, dimensions, and corresponding tests.

Test	Prepared specimens	Tested specimens/samples
Compressive strength	Cubic 10 cm x 10 cm x 10 cm	6
Bulk density	Cubic 10 cm x 10 cm x 3 cm	9
Porosity accessible to water	Cubic 10 cm x 10 cm x 3 cm	9
Water absorption	Cubic 10 cm x 10 cm x 3 cm	9
Mercury intrusion porosimetry (MIP)	Specimen fragment	1 fragment ≈ 10 mm^3
Carbonation depth	Cubic 10 cm x 10 cm x 10 cm	3
Scanning electron analysis (SEM)	Specimen fragment	1 fragment ≈ 5 mm^3
X-ray diffraction analysis (XRD)	Powder	1 sample ≈ 100 mg
Thermogravimetric analysis (TGA)	Powder	3 samples ≈ 170 mg
pH	Powder	3 samples 1.5 g
Mass loss method	Cylinders 4 cm x 10.4 cm	3
Water content (pre-conditioning phase)	Cubic 10 cm x 10 cm x 3 cm	10

3.3 Curing regimes

In the carbonation curing regime, the specimens undergo an initial in-mold curing phase at 20 °C and 50% RH for 7h. After the initial curing period, the samples are removed from their molds and pre-cured at 60 °C for 17 h to eliminate free water. Following this 24h step, the specimens are transferred into a carbonation chamber for carbonation curing under controlled conditions.

Before finalizing this protocol, preliminary trials were conducted to evaluate the effectiveness of the pre-curing phase. Initially, the pre-conditioning process did not include the 60 °C drying step. Instead, the specimens were air-dried to eliminate free water. However, after 24h of carbonation curing, no detectable carbonation front was observed. Hence, the air drying alone was insufficient to remove adequate moisture from SSC specimens, potentially hindering CO_2 diffusion and subsequent carbonation reactions. Consequently, elevating the temperature to 60 °C was needed to optimize moisture removal and enhance CO_2 uptake. Humidity sensors were used during this step to monitor internal moisture levels at depths of 1.5 cm and 3 cm. After 17h in the drying oven, measurements revealed that the internal RH had stabilized at 65%. Therefore, it was decided to terminate the pre-conditioning at 17h and proceed with carbonation curing to avoid water starvation.

Moreover, during carbonation curing, the CO_2-sealed chamber humidity was maintained at 70%, the maximum recommended level, to ensure sufficient moisture availability for cement hydration. As a result, post-preconditioning was deemed unnecessary and excluded from the final protocol.

3.3.1 Comparative curing regimes

The two other curing regimes are sealed and water curing (called standard curing). In sealed curing, the SCC specimens undergo the same pre-conditioning step as in carbonation curing. After 24h, they are wrapped with aluminum adhesive tape and stored in a climatic chamber at 70% RH. Regarding standard curing, after an in-mold curing of 24h, the specimens were immersed in high-purity water. These curing regimes, with carbonation curing, remain in effect until the day of testing.

The employment of standards and sealed curing regimes primarily aims to prevent CO_2 penetration, thus facilitating the accurate calculation of the quantity of $CaCO_3$ formed during carbonation curing. Additionally, the standard curing regime guarantees complete hydration of the cement, allowing us to assess the impact of carbonation curing on the mechanical properties of SCC mixes. Table II-7 outlines in detail the specifications of the curing regimes.

Table II-7: Curing regimes parameters.

Pre-curing (24 hours)			
In-mold (7 hours)		De-mold (17 hours)	
Temperature (°C)	Relative humidity (%)	Temperature (°C)	Relative humidity (%)
20	60	60	-
Carbonation curing			
Temperature (°C)	Relative humidity (%)	CO_2	Duration (days)
25	70	20	1-7-28-90
Sealed curing			
25	70	0	1-7-28-90
Standard curing			
25	90	-	1-7-28-90

4 Experimental procedures

4.1 Physical and mechanical characterization of raw materials

4.1.1 Particle density

The particle density of LS, SSP, and cement was measured using a Micromeritics AccuPyc 1330 helium pycnometer, according to NF EN 1097-7 [278]. This method allows the determination of the absolute density of a solid with a known mass by measuring the true volume of its solid framework. The volume is determined by the displacement of helium, which can penetrate even the smallest voids between particles, providing an accurate measurement of the material's particle density.

4.1.2 Blaine specific surface area

The Blaine specific surface area was determined using the air permeability method; according to NF EN 196-6 [279]. This technique evaluates the fineness of a powdered sample by measuring the time required for a fixed volume of air to pass through a compacted sample bed. Before measurement, the samples, particularly LS and SSP, were dried and sieved to remove any particle agglomeration.

4.1.3 BET specific surface area

The BET specific surface area was measured using a Micromeritics 3Flex 3500 instrument, according to ISO 9277 [280]. This technique determines the amount of nitrogen adsorbed onto the particle surfaces, capable of penetrating all voids within the sample. By measuring the quantity of nitrogen adsorbed and applying the ideal gas law, the specific surface areas of LS, SSP, and cement were calculated according to the Brunauer–Emmett–Teller (BET) model.

4.1.4 Rigden voids

The Rigden Voids Test was employed to determine the packing capacity and void content of the LS and SSP. The test was conducted in accordance with EN 1097-4 [281], which specifies methods for evaluating the void volume of dry-compacted fine materials. The test aims to assess the maximum bulk density of each precursor, achieved when it is compacted in a dry state within a cylindrical mold using a compaction hammer. The bulk density is defined as the ratio of the dry mass of a compacted sample to its bulk volume, which includes both the solid particle volume and the voids between particles. The void content, expressed as a percentage of the total volume, is then calculated using Eq. II-1.

$$V = \left(\frac{4.10^3 . m^2}{\pi . \alpha^2 . pf . h}\right) \times 100 \qquad \text{Eq. II-1}$$

Where:

- V: voids in percent.
- m: mass of the compacted filler in grams.
- α: inner diameter of the dropping block cylinder in millimeters.
- pf: particle density of the filler in mega grams per cubic meter.
- h: height of the compressed samples in millimeters

4.1.5 Loss On Ignition (LOI)

The loss on ignition, employed to quantify the organic matter content in SSP and LS, was conducted according to NF EN 1535-5 [280]. The precursor samples were placed in crucibles and heated in a muffle furnace at 550 °C ± 25 °C for 3h. The LOI, expressed as a percentage of the dry sample, represents the mass loss that occurs during heating and was calculated using Eq. II-2.

$$\text{LOI}\ (\%) = \frac{m_c - m_d}{m_c - m_a} \times 100 \qquad \text{Eq. II-2}$$

Where:

- m_c: mass of the crucible with the dried sample.
- m_d: mass of the crucible with the ignited sample.
- m_a: mass of the empty crucible.

4.1.6 Laser Diffraction Particle Size Analysis

The particle size distribution of the binder constituents was determined using a Beckman Coulter LS13320 laser diffraction granulometer, operating on the principle of light scattering according to ISO 13320-1 [282]. For the <124 µm SSP and LS particles, the powders were dispersed in water and analyzed while kept in suspension with a stirred bath to avoid settling of coarse particles. For cement, measurements were performed using a dry dispersion unit to prevent any premature hydration.

4.1.7 Water absorption kinetics and density

The water absorption and density of the aggregates (NCA, RCA, and sand) were determined using the pycnometer method according to NF EN 1097-6 [283]. The test sample was first immersed in the pycnometer filled with water at 22 °C, ensuring that all trapped air was removed to avoid measurement errors. Excess water was allowed to overflow, and the pycnometer lid was placed. The exterior of the pycnometer was dried, and its mass was recorded (M_2). The aggregates were then removed and allowed to drain, after which the pycnometer was refilled with water and weighed (M_3). The drained aggregates were surface-dried (M_1) and finally oven-dried at 110 °C to determine their completely dry mass (M_1). The density of water (ρ_w) was taken at 20 °C.

To evaluate the water absorption kinetics of RCA and NCA, three samples of each were prepared and tested at 15, 45, and 90 minutes. The water absorption (WA_{24}) and density (ρ_d) were subsequently calculated using Eq. II-3 and Eq. II-4, respectively.

$$WA_{24} = \frac{M_1 - M_4}{M_4} \times 100 \quad \text{Eq. II-3}$$

$$\rho_d = \frac{M_4}{M_4 - (M_2 - M_3)} \times \rho_w \quad \text{Eq. II-4}$$

4.1.8 Aggregates sieve analysis

Sieve analysis of the aggregate was carried out according to NF EN 933-1 [284].

4.1.9 Deval (MDE) test

The wear resistance of coarse aggregates was determined using the Micro-Deval test, in accordance with NF EN 1097-1 [285]. Three samples of 500 g each, consisting of aggregates passing the 12.5 mm sieve and retained on the 4 mm sieve, were placed in separate cylinders. Five kilograms of steel balls and 2.5 L of water were added to each cylinder, and the lids were placed. The cylinders were rotated at 100 ± 5 min^{-1} for $12{,}000 \pm 10$ revolutions. After the test, the aggregates and steel balls were carefully collected, and the interior of the drums and lids were thoroughly rinsed. The material and all wash water were then poured over a 1.6 mm sieve, protected by an 8 mm guard sieve, and washed under a clean water stream. The Micro-Deval coefficient was calculated as the percentage of the original sample reduced to a particle size smaller than 1.6 mm.

4.1.10 Los Angeles (LA) test

The LA test was conducted according to NF EN 1097-2 [286]. Three samples of 5000 g each, consisting of aggregates passing the 12.5 mm sieve and retained on the 4 mm sieve, were placed in the LA drum along with 12 standard steel balls. The drum was rotated at 31 ± 1 revolutions per minute for 500 revolutions. After completion of the test, the material was removed and sieved through a 1.6 mm sieve. The mass of the material passing the sieve was recorded, and the LA abrasion value was calculated as a percentage of the original sample reduced to particle sizes smaller than 1.6 mm.

4.2 Rheological characterization

4.2.1 Workability retention: Slump flow test

The slump flow test evaluates the flow capacity of SCC. It is a variation of the Abrams cone slump test, which measures the SCC spread after a minute using standard equipment typically employed

for the slump test. The final spread diameter is then determined as the average of two orthogonal diameters. Additionally, the time required to achieve a spread diameter of 500 mm, denoted as t_{500}, is recorded. This value indicates the SCC's viscosity.

Following NF EN 12350-8 [287], the two characteristics are assessed at four time intervals: t = 0, t = 15 min, t = 45 min, and t = 90 min. Nearly 50% of the applications had slump flow values ranging from 650 to 700 mm, while almost 90% fell within the range of 600 to 750 mm [288]. The target flow class at t = 0 was SF2, which corresponds to a slump-flow diameter ranging from 660 to 750 mm. The formed SCC spreads were visually inspected at the end of the flow to determine the VSI.

4.2.2 Segregation resistance: Sieve stability test

As mentioned in the previous chapter, resistance to static segregation is the ability of SCC to keep its particles suspended without the risk of particle settlement due to gravity or bleeding. Therefore, the sieve stability test aims to assess the SCC in terms of the risk of segregation.

Following standard NF EN 12350-11 [289], the test involves pouring 10 liters of concrete immediately after mixing it into a container, covering it to prevent drying, and allowing it to rest for 15 minutes. Then, 4.8 ± 0.2 kg of concrete is poured onto the center of a 5mm sieve from a height of 50 cm, and the SCC passing through the sieve is collected in a receiver. After 2 min of waiting, the weight percentage of laitance is then calculated using Eq. II-5.

$$SR = \frac{(m_{ps} - m_p) \times 100}{m_c} \quad \text{Eq. II-5}$$

Where:

- SR: segregation resistance in percent.
- m_{ps}: total mass of the material that passed through the sieve.
- m_p: mass of the sieve receiver.
- m_c: initial mass of SCC placed onto the sieve.

4.3 Hydration kinetics

The heat of hydration of the SCC mixes is measured according to NF EN 196-9 [45], using a semi-adiabatic method (Langavant type) over 72 h. After 3 minutes of mixing, the SCC was poured into the cylindrical metal container and placed inside the insulated calorimeter. The heat of hydration (Q) is measured using Eq. II-6. The test aims to assess the effect of precursors on the heat released during cement hydration, thereby providing insights into their potential effects on the CO_2 uptake of concrete.

$$Q\ (J/g) = \frac{c}{m_c}\ \theta_t + \frac{1}{m_c} \int_0^t \alpha \times \theta_t \times dt \quad \text{Eq. II-6}$$

Where:

- c: total thermal capacity of the calorimeter, in J K^{-1}
- m_c: mass of cement contained in the test sample, in g.
- t: hydration time, in h.
- α: coefficient of heat loss of the calorimeter in J h^{-1} K^{-1}.
- Θ_t: difference in the temperature of the test calorimeter compared with that of the reference calorimeter at time t, in K.

4.4 Mechanical characterization

The hardening properties of the SCC are determined by performing a compression strength test according to NF EN 12390-3 [290]. The six specimens are trimmed and tested in compression using a 3 R© compression machine with a capacity of 4000 KN and a loading rate of 0.6 MPa/s.

4.5 Bulk density, porosity accessible to water, and water absorption

The water-accessible porosity, water absorption, and bulk density of the hardened SCC are evaluated according to NF P 18-459 [291]. The test involves placing the specimens under vacuum at 25 mbar for the first 4 hours, followed by 44 hours in water, with the pressure remaining constant. The bulk density (ρ_d), expressed in kg/m^3, the porosity accessible to water (ε), expressed as a volumetric percentage, and the water absorption (w) are then calculated using (Eq. II-7, Eq. II-8, and Eq. II-9), respectively.

$$\rho_d = \frac{\mathrm{M_{air}}}{\mathrm{M_{air}} - \mathrm{M_{water}}} \times 100 \qquad \text{Eq. II-7}$$

$$\varepsilon\,(\%) = \frac{\mathrm{M_{air}} - \mathrm{M_{dry}}}{\mathrm{M_{air}} - \mathrm{M_{water}}} \times 100 \qquad \text{Eq. II-8}$$

$$w(\%) = \frac{\mathrm{M_{water}} - \mathrm{M_{dry}}}{\mathrm{M_{dry}}} \times 100 \qquad \text{Eq. II-9}$$

Where:

- $\mathrm{M_{air}}$: mass of the sample in air.
- $\mathrm{M_{water}}$: mass of the specimen submerged in water.
- $\mathrm{M_{dry}}$: mass of the dried specimen at 105 °C, or at 60 °C for SCC containing RCA, until constant weight is reached.

4.6 Pores analysis: Mercury intrusion porosimetry (MIP) test

The total porosity and pore size distribution measurements were conducted using the MIP method, in accordance with ISO 15901-1 [292], using a Micromeritics AutoPore V 9600 porosimeter. The instrument performs low-pressure measurements ranging from 0 to 345 kPa, corresponding to pore sizes between 360 µm and 3.6 µm. It also conducts high-pressure measurements from atmospheric pressure up to 228 MPa, covering pore sizes from 6 µm down to 0.005 µm.

4.7 Microstructural analysis

4.7.1 Thermogravimetric analysis

TGA/DTG analysis involves continuously recording mass variations of the powdered SCC sample as its temperature increases from 25 ºC to 1200 °C, with a heating rate of 10 ºC/min in nitrogen, using a thermo-gravimetric analyzer Jupiter STA 449 F5. The analysis aims to quantify the hydrates, primarily C-S-H and $Ca(OH)_2$, within the temperature range corresponding to their dehydration.

The CO_2 uptake of SCC mixes is not estimated by quantifying $CaCO_3$ within the temperature range of its decomposition in TGA/DTG curves to avoid confusion with the $CaCO_3$ contributed by the SCC precursors. However, the TGA method is not entirely accurate as it is based on several assumptions. The method assumes that only C-S-H and $Ca(OH)_2$ participate in carbonation, excluding the carbonation of other hydrates.

The method assumes: (i) during the C-S-H carbonation, the reaction leads to its complete decalcification and produces water; (ii) the mass loss occurring between 740-920 °C corresponds only to CO_2 release. The small amount of TGA samples and their possible inhomogeneity represent sources of error in estimating the initial amount of $CaCO_3$ before carbonation. The DTG curves may not clearly show the decomposition peaks of the metastable polymorphs, especially if their content is too small.

The TGA/DTG analysis was also conducted to evaluate the thermal behavior of LS, SSP, and the adhered old mortar in RCA.

4.7.2 X-ray diffraction analysis (XRD)

In perfectly crystalline samples, XRD allows the quantitative determination of many sample characteristics:

- The phase fractions corresponding to the various phases (hydrates, $CaCO_3$ polymorphs …), which can be formed or decomposed during the various processes (from the raw precursors to concretes and their carbonation curing, aging …). Indeed, each crystalline phase exhibits diffracted intensities specific to its crystal structure, texture, microstructural state …

- The structure of each phase (atomic arrangement, atomic displacements, unit-cells …)
- The crystallographic texture (preferred orientation of its crystallites) of each phase. This can be important, specifically in clay-containing samples
- The mean crystallite sizes (diffracting coherent domains), their shape, and distribution
- The residual stresses of the crystallites

However, in concretes, samples are mixtures of crystalline and more or less amorphous phases, which makes their quantitative determination a bit more complex. In such materials, simple peak identifications (as mostly practiced in the literature) from positions are strongly subject to mistakes, and cannot be certain for quantifications. Only Rietveld analysis (§ 4.8.3.2) can pretend a proper determination in the majority of cases. Even using Rietveld analysis, some assumptions have to be made concerning the C-S-H gels, for which proper initial models must be chosen for the starting crystal phases (i.e., C_3S, C_2S, C-S-H, C_4AH …). We used the Le Bail approach [293] to represent these gels in the diffraction diagrams.

The measurements were performed using two different instrumental setups. A first setup consisted of a usual laboratory instrument, an X-Pert Pro Panalytical diffractometer operating with a Fe-filtered Co $K\alpha_1/K\alpha_2$ radiation ($\lambda K\alpha_1$ = 1.789010 Å and $\lambda K\alpha_2$= 1.792900 Å) and equipped with an Xcelerator linear detector, in the θ-2θ reflection mode. Using only filtered radiation allows reasonably quantitative estimates for not too complex diagrams. For instance, for a single phase (e.g., Figure II-10a), most of the sample characteristics can be obtained. However, one can be observed from this figure that the remaining Kβ radiation is still present (the filter removes approx. 98% of it) and that the filter creates an absorption edge (near 2θ=30°). Such signatures would prevent any quantitative determination for complex samples, and we decided to operate the measurements on more resolved instruments.

We got the opportunity to benefit from synchrotron radiation at the ESRF facility under the Momentum Transfer program of the 4-year EU project OSCARS [293]. We could measure 15 powder samples, including carbonated samples, at the ID31 beamline in transmission mode, using high-energy X-rays (~75 keV). The detector used on this instrument is composed of 48 detecting elements in a Pilatus CdTe 2M flat panel, placed at 1.5 m from the sample (Figure II-10.b). Such measurements ensure the largest possible resolution and overall conditions for precise determinations.

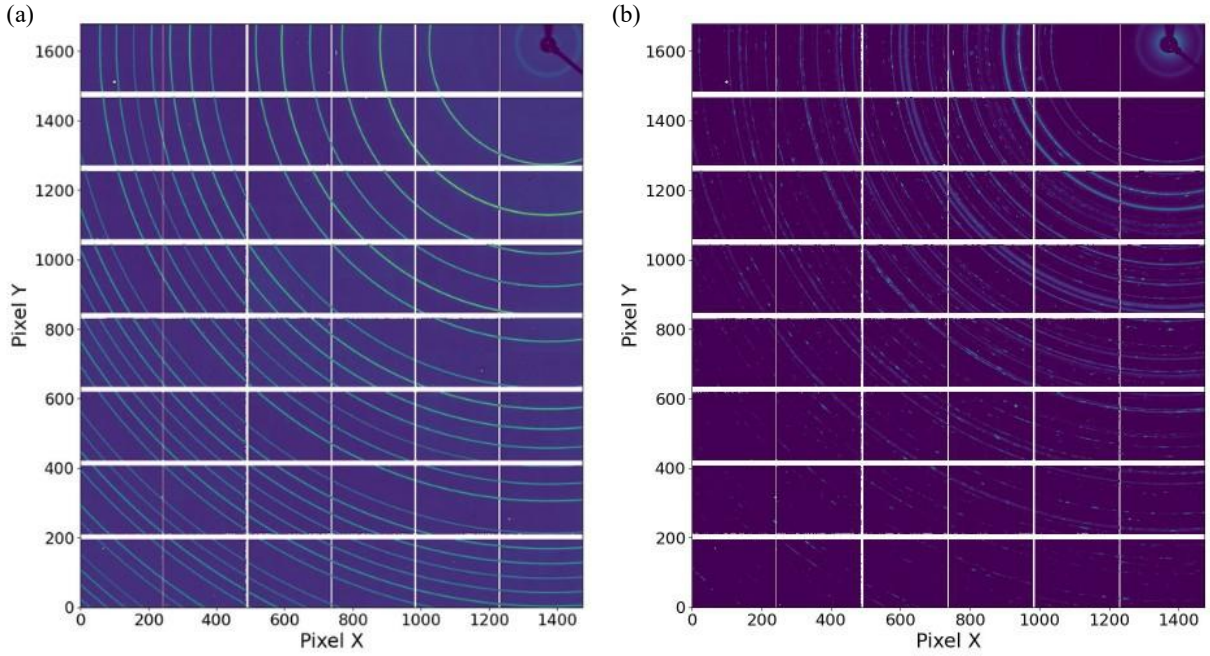

Figure II-11: Example of a Debye-Scherrer experiment at ID31 for a) The LaB6 660b NIST powder used to calibrate the instrument contribution and b) the LS-RCA 1-day carbonated sample.

Once the detector image is acquired, an integration over the rings is operated in order to reconstruct a 2θ diagram for the Rietveld analysis. We will only show such a 1D-integrated diagram and the corresponding fits in the next chapters.

The entire profile refinements were carried out following the Rietveld method as implemented in the MAUD (Materials Analysis Using Diffraction) [294]. MAUD uses an extended Rietveld code able to model and fit all characteristics (structure, texture, phase fractions, stresses …) together [295]. In our samples, when necessary, standard function models were used to account for texture presence for some phases. In all samples, the crystallite sizes and microstrains of the main crystalline phases (i.e., quartz and calcite) had to be modeled. In some samples, we also had to practice this on some minor phases. We used either an isotropic or an anisotropic size and microstrain model to achieve this, using the Popa approach [296].

4.7.3 Scanning Electron Microscopy (SEM)

SEM analysis allows examination of particle morphology of SSP and LS particles, the surface characteristics of NCA and RCA, the ITZ structure and packing density of SCC cured under all curing regimes. For SCC, it provides insights into hydration progression and phase transformations, including $CaCO_3$ formation and hydrate alterations, only if the corresponding phases can be identifiable from their crystal and/or grain shapes, since SEM does not probe crystal planes. The sample's microstructure was

examined through a Carl ZEISS SUPRA 55 microscope in secondary electrons mode, using an applied voltage of 3kV, a 60 µm diaphragm aperture, and a working distance of 3-5 mm to avoid charging as much as possible. The observations were performed on non-coated bulk samples glued with carbon conductive tape on the pad and surrounded with silver lacquer.

4.8 Carbonation characterization

4.8.1 Pre-conditioning step monitoring

The pre-cured specimens are evaluated based on their water content, constituting an input for the carbonation mechanism. The water content (w) of SCCs is determined according to NF EN 1097-5 [297]. Subsequently, the mass loss of the samples is recorded hourly during the drying phase at 60 °C, and the corresponding *w* (%) is calculated using Eq. II-10.

$$w\ (\%) = \frac{M_i - M_f}{M_i} \qquad \text{Eq. II-10}$$

Where:

M_i: mass of the fresh SCC sample.

$M_{f:}$ mass of the sample after drying at 105 °C, or at 60 °C for SCC containing RCA.

4.8.2 Carbonation depth: Phenolphthalein spray test

The phenolphthalein solution is typically used as a pH indicator to assess the alkalinity of the concrete that has undergone carbonation. The phenolphthalein solution is colorless, turns purple when the pH ranges between 9 and 13, and remains colorless when the pH is below 9. The carbonation depth is assessed unidirectionally by exposing one surface to CO_2 or generalized by exposing all the surfaces to CO_2. Generally, 4 to 5 readings are taken on each surface, spaced 1 cm or 2 cm apart, depending on the sample's shape, and collected at different ages of curing [298,299].

The carbonation depth of SCC mixes is assessed according to NF EN 12390-12 [300]. The test considers both unidirectional (one surface exposed) (Figure II-12a) and generalized (all surfaces exposed) carbonation (Figure II-12b). Therefore, the carbonation-cured SCC specimens were broken into two pieces. The cross-sections of fractured specimens were sprayed with a phenolphthalein solution, and carbonation depth was measured using a digital caliper, averaging 20 readings for generalized carbonation and 8 readings for unidirectional exposure, taken at 2 cm intervals (Figure II-12).

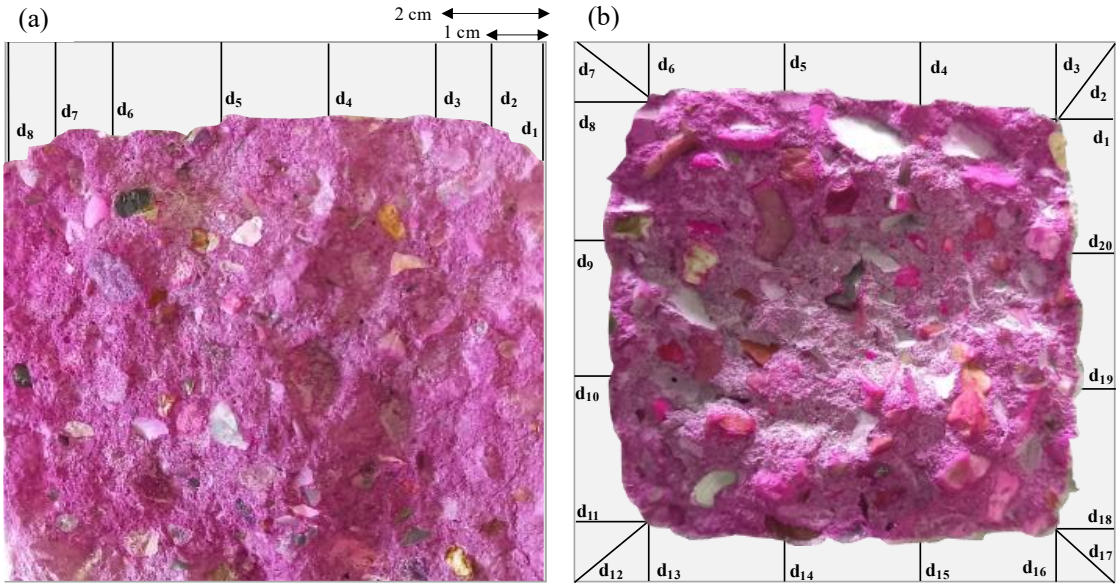

Figure II-12: Schematic illustration of carbonation depth measurement: (a) unidirectional and (b) generalized CO_2 exposure.

4.8.3 CO_2 uptake assessment

4.8.3.1 Thermogravimetric analysis

The CO_2 uptake of SCC mixes prepared for this study is estimated through three steps. (i) calculating the initial mass of the C-S-H gel and $Ca(OH)_2$, the mass of the hydrate participating in the carbonation reaction, by subtracting their amount in sealed cured samples from their carbonated-cured samples (Eq. II-11 to Eq. II-16). (ii) calculating the mass of $CaCO_3$ resulting from their carbonation (Eq. II-17 to Eq. II-22). (iii) calculating the total $CaCO_3$ resulting from each carbonation reaction. The total obtained is used to calculate the CO_2 uptake (Eq. II-24) of the four mixes (Eq. II-23). Table II-8 summarizes the steps to estimate the CO_2 uptake.

Table II-8: CO_2 uptake calculations, with CC referring to $CaCO_3$.

Step 1: Hydrate content participation in carbonations	
$m_{C-S-H\ ini} = m_{C-S-H\ sealed} - m_{C-S-Hcarbonated}$	Eq. II-11
Reaction mechanism of C-S-H	
$1.7CaO.SiO_2.4H_2O \rightarrow 1.7CaO.SiO_2.1.3H_2O + 2.7H_2O$	Eq. II-12
$m_{C-S-H} = \frac{\Delta m_{150\,°C-425\,°C} \times M_{C-S-H}}{M_{H_2O}}$	Eq. II-13
$m_{Ca(OH)_2\ ini} = m_{Ca(OH)_2\ sealed} - m_{Ca(OH)_2\ carbonated}$	Eq. II-14
Reaction mechanism of $Ca(OH)_2$	
$Ca(OH)_2 \rightarrow CaO + H_2O$	Eq. II-15
$m_{Ca(OH)_2} = \frac{\Delta m_{425\,°C-530\,°C} \times M_{Ca(OH)_2}}{M_{H_2O}}$	Eq. II-16
Step 2: $CaCO_3$ content from C-S-H and $Ca(OH)_2$ carbonation	
Reaction mechanism of C-S-H	
$1.7CaO.SiO_2.4H_2O + 1.7CO_2 \rightarrow 1.7CaCO_3 + SiO_2 3H_2O + 0.7H_2O$	Eq. II-17
$m\ CC_{C-S-H} = n_{C-S-H} \times 1.7$	Eq. II-18
$n_{C-S-H} = m_{C-S-H\ ini}/M_{C-S-H}$	Eq. II-19
Reaction mechanism of $Ca(OH)_2$	
$Ca(OH)_2 + CO_2 \rightarrow CaCO_3 + H_2O$	Eq. II-20
$mCC_{Ca(OH)_2} = n_{Ca(OH)_2} \times M_{CaCO_3}$	Eq. II-21
$n_{CH} = m_{Ca(OH)_2 ini}/M_{Ca(OH)_2}$	Eq. II-22
Step 3: Total carbonation (total $CaCO_3$)	
$m_{CaCO_3\ tot} = CaCO_{3_{C-S-H}} + CaCO_{3_{Ca(OH)_2}}$	Eq. II-23
$m_{CO_2} = m_{CaCO_3\ tot} \times M_{CO_2}/M_{CaCO_3}$	Eq. II-24

4.8.3.2 X-ray diffraction: Semi-quantitative analysis of CO_2 uptake

To support a more quantitative interpretation, Rietveld refinement was conducted on the diffractograms, enabling the estimation of the relative weight fractions of the crystalline carbonation phases. This method provides a semi-quantitative perspective on CO_2 uptake, connecting the extent of carbonation to measurable changes in phase composition.

- **Rietveld method**

The Rietveld method is a powerful least-squares fitting technique developed in the late 1960s [301]. Its development was originally motivated by the need to analyze neutron powder diffraction data using monochromatic beams, and it was later adapted for X-ray diffraction. In this method, least-squares refinement (mathematical approach) is performed to find the best fit between the entire observed powder diffraction pattern taken as a whole and the corresponding calculated pattern, by minimizing the squared differences between the observed and calculated intensities. In simpler terms, the Rietveld method involves adjusting the model parameters so that the calculated pattern closely matches the experimental data.

In practice, the calculated intensity y_{ci} at each data point i in the diffraction pattern (at position $2\theta_i$) is obtained by summing the contributions of all reflections κ from all phases ϕ present in the sample x. These calculated values are then compared with the measured intensities y_i, and the refinement proceeds. The quantity minimized in the least-squares refinement is the residuals, S_y (Eq. II-25), and the sum is over all measured points [302].

$$S_y = \sum_i w_i (y_i - y_{ci})^2 \qquad \text{Eq. II-25}$$

Where:

- $w_i = 1/y_i$.
- y_i = observed intensity at the i th step.
- y_{ci} = calculated intensity at the i th step.

With MAUD [302–305], in particular, the residual function is referred to as the Weighted Sum of Squares (*WSS*). The calculated intensity incorporates the calculated contribution from neighboring Bragg reflections plus the continuous background of the diffraction pattern (Eq. II-26).

$$y_{ic} = y_{ib} + S_\emptyset \sum_{\emptyset=1}^{N_\emptyset} \frac{f_\emptyset}{V_\emptyset^2} \sum_{k=K_1}^{K} J_{\emptyset k} Lp_i P_{\emptyset k} \left|F_{\emptyset k}\right|^2 \Omega_{\emptyset k} (2\theta_i - 2\theta_k) A_{\emptyset ki} \qquad \text{Eq. II-26}$$

Where:

- $S_\emptyset$: scale factor, proportional to the volume fraction of each phase in the sample.
- $J_{\emptyset k}$: Lorentz-polarization factor at point i. This parameter is linked to the instrumental geometry and the incident light polarization.
- $P_{\emptyset k}$: component of the pole figure of the phase ∅. This parameter takes account of the preferred orientations of the crystallites, if any.
- $F_{\emptyset k}$: structure factor of phase ∅ for the k^{th} reflection.

- $\Omega_{\emptyset k}$: diffraction peak profile.
- $A_{\emptyset ki}$: sample absorption factor. For non-isotropic sample shapes, both probed volumes and absorption paths through the sample vary and have to be corrected for during the measuring scan

In powder diffraction, the observed diffraction peaks are superimposed on a smooth background signal, which must be accurately modeled to extract reliable peak intensities. Therefore, the continuous background function, y_{ib}, must account for (i) the instrument's contribution, including electronic noise, detector noise, air scattering, parasitic wavelengths, and fluorescence, (ii) the sample environment, including possible scattering or diffraction, and (iii), if significant, cosmic radiation. The sample itself also often constitutes a major part of the background, due to effects such as Compton scattering and fluorescence. A simple way to model y_{ib} is as a polynomial in 2θ of degree N_b, s (Eq. II-27).

$$y_{ib} = \sum_{n=0}^{N_b} a_n (2\theta_i)^n \qquad \text{Eq. II-27}$$

Where a_n are the coefficients of the polynomial used to model the continuous background, this formulation allows effective simulation of the background when it varies smoothly, without abrupt changes such as spurious peaks. In practice, increasing the polynomial degree beyond 5 typically does not result in a significant improvement in background fitting.

The refinement simultaneously accounts for crystal structure, diffraction optics effects, instrumental factors, and specimen characteristics. Parameters refined include overall pattern intensity (scale factors), peak profile (width and shape), peak positions (unit cell parameters and zero-point correction), background contributions (polynomial terms), and atomic thermal factors. A key feature of the refinement is the feedback during the iterative process, where improved knowledge of the structure simultaneously enhances the allocation of observed intensity to partially overlapping Bragg reflections.

A reliable refinement is built not only on correct modeling but also on meticulous experimental practice at every step. The practical aspects of a typical Rietveld refinement include:

Data collection. Before data collection, it is crucial to ensure that the instrument is properly aligned and calibrated, using the most suitable radiation, the wavelength, appropriate sample preparation and thickness, slit sizes, and necessary counting time. The choice of radiation source (laboratory X-rays, synchrotron X-rays, or neutrons) strongly affects data quality, with each having specific advantages and limitations. Smoothing or over-processing of raw data must be avoided. Raw data should not be smoothed or over-processed, as this can introduce errors.

Background contribution. The background can be treated basically by two approaches, either by subtraction or refinement. The former is typically performed by linear interpolation between selected

points between peaks and then subtracted. This approach is straightforward when the peaks are well separated, but it becomes challenging for overlapping peaks and may require repeated adjustments. The latter is based on empirical or semi-empirical functions that allow simultaneous optimization with structural parameters. However, the accuracy of this approach depends on the function's ability to represent the true background. A combined approach often yields the most reliable results.

Peak-shapes function. The peak shapes reflect both sample characteristics (size, strain, defects) and instrumental effects (radiation and geometry). Therefore, accurately describing them is critical for a successful Rietveld refinement. The analytical pseudo-Voigt approximation of the Voigt function is widely used to describe peak shapes in Rietveld refinement. However, regardless of the selected peak-shape function, peak ranges must extend sufficiently beyond the full width at half maximum (typically 10–20 × FWHM) to capture the tails, especially for Lorentzian-dominated peaks, as underestimating this range can lead to significant intensity errors.

Profile parameters. When only a partial structural model is available, a structure-free approach, typically a Le Bail refinement, is recommended for initial profile fitting to align calculated and observed peak intensities; otherwise, the calculated intensities may deviate significantly from the observed ones. Peak positions should first be corrected by refining the unit-cell parameters and 2θ offsets, using internal or external standards as needed. Once aligned, the other profile parameters, Full Width at Half Maximum (FWHM), peak asymmetry, and instrumental broadening can be refined.

Completing the structural model. The refinement of the structural parameter starts once the structural model is complete; if not, difference Fourier maps can be used to locate the missing atoms of the current model. Overlapping reflection intensities can be estimated from the partial model to create a pseudo single-crystal dataset and an approximate electron-density map. By subtracting the model-derived electron density from that obtained from the observed intensities, a difference map reveals regions not yet represented in the model. Maximum-entropy methods can further reduce noise and clarify missing features. Correct scaling of the calculated pattern to the observed data is crucial; high-angle reflections are typically used to determine the scale factor until the model is complete, after which the map can guide the addition of missing atomic positions. In our case, we started using a well-defined tabulated structure from the Crystallography Open Database [306] and did not modify the atomic positions of the structure. Only unit-cell parameters were fitted.

Refining the Structure. After the structural model is complete and other parameters are set, Rietveld refinement begins, with the number of cycles increasing as the structure's complexity increases. The process starts with heavier atoms, followed by lighter ones, and then all atomic positions are refined together. Thermal and occupancy parameters are sensitive and may require constraints or additional data for accuracy. Refinement continues until shifts are minimal, and all structural and profile parameters are refined together for reliable results.

Restraints. Powder diffraction data, being a one-dimensional projection, lose some three-dimensional structural information. To compensate for this loss, geometric data from similar structures, such as typical bond lengths and angles, can be incorporated into Rietveld refinement. These geometric restraints can either increase the number of observations or reduce the number of parameters. Overall, a restraint is a rule applied during refinement to ensure the structure remains chemically and physically reasonable.

Number of observations. In powder diffraction, each point measured in the profile is considered an observation. However, not every point provides unique information about the structure. Only the integrated intensities of individual reflections are truly independent for refining structural parameters. Overlapping peaks reduce the number of unique observations. If a refinement attempts to include more parameters than the data can support, the results become unreliable, which is reflected in very large standard deviations

Estimated standard deviations (e.s.d.'s). These numbers, which appear in parentheses after a value, reflect the precision of refined parameters in Rietveld refinement, but not necessarily their accuracy. Their calculation varies among refinement programs, most of which assume that counting statistics are the sole source of error, thereby neglecting systematic contributions such as background misestimation, peak-shape inadequacies, or deficiencies in the structural model. Consequently, e.s.d.'s often underestimate the true uncertainties associated with the refined parameters. For this reason, it is essential to specify the method used to calculate e.s.d.'s when reporting results, and to ensure that derived quantities (e.g., interatomic distances and bond angles) are evaluated using the full correlation matrix rather than only its diagonal elements.

***R* values.** To distinguish a good refinement from a poor one, several discrepancy indices are employed in Rietveld analysis, including the goodness-of-fit (χ^2) and various R factors (agreement indices). Among these, the most widely used is the weighted-profile R value (R_{wp}), defined as (Eq. II-28).

$$R_{wp} = \left\{ \sum_i w_i \left[y_i(obs) - y_i(calc) \right]^2 \Big/ \sum_i w_i \left[y_i(obs) \right]^2 \right\}^{1/2} \qquad \text{Eq. II-28}$$

Where y_i(obs) represents the observed intensity at step i, y_i(calc) the calculated intensity from the model, and the w_i statistical weight. R_{wp} measures the degree of agreement between the experimental diffraction pattern and that calculated from the refined structural model. However, it can be misleading because it is affected by the background level. Therefore, many programs also report R_{wp} without the background contribution.

In the ideal case of a perfect model, the squared differences between the calculated and observed intensities, $(y_i(obs) - y_i(calc))^2$, are statistically consistent with the measurement uncertainties, $\sigma^2(y_i(\text{obs}))$. When are weighted by $w_i = 1/\sigma^2\,(y_i(obs))$, their average becomes 1, meaning that R_{wp}

reaches its theoretical lower bound for the dataset, which is referred to as the expected R-factor R_{exp} (Eq. II-29).The ratio between these two quantities defines the goodness-of-fit indicator (χ^2) (Eq. II-30).

$$R_{exp} = \left[(N-P)\Big/\sum_{i}^{N} w_i y_i(obs)^2\right]^{1/2} \quad \text{Eq. II-29}$$

Where N and P are the number of observations and the number of parameters

$$\chi^2 = (R_{wp}/R_{exp})^2 \quad \text{Eq. II-30}$$

During the refinement process, χ^2 starts large when the model is poor and decreases as the model produces better agreement with the data (Table II-9).

Table II-9: Interpretation of χ^2 values in Rietveld refinement [302].

χ^2 value	Interpretation
$\chi^2 \ll 1$	Impossible in theory
	In practice, it can happen when proper statistics have been lost during image integration
	Unfortunately, this happened in our case on the diffraction data
$\chi^2 \geq 1$	Refinement is statistically consistent
	Data quality limits discrimination between different models if close to 1. Usually, values below 2 give acceptable results
	Does not guarantee the model is unique or correct. Fitted parameters require inspection of physical reality
$\chi^2 \gg 1$	Underestimated uncertainties
	Systematic errors not included (background, peak-shape issues)
	Incomplete or incorrect structural model
	Very high precision data: minor misfits amplified

Given these R values, Brian [304] stated, " *In my experience, the most important way to determine the quality of a Rietveld fit is by viewing the observed and calculated patterns graphically and to ensure that the model is chemically plausible.*"

4.8.3.3 Mass loss method

The specimens were initially dried in an oven at 105 °C for 24h to remove moisture. Following this drying stage, the specimens were subjected to a controlled thermal treatment in a muffle furnace. The furnace temperature increased from 25 °C to 525 °C at a controlled heating rate, reaching the target temperature within 49 minutes, after which it was held at 525 °C for 2h. Subsequently, the temperature

was further raised from 525 °C to 1000 °C at a controlled heating rate, attaining the set temperature within 49 minutes, and maintained at 1000 °C for an additional 2h (Figure II-13). Afterward, their CO_2 uptake is determined using Eq. II-31 [252].

$$CO_{2\ uptacke}(\%) = \frac{\Delta m_{525\ °C-1000\ °C\ Carb} - \Delta m_{525\ °C-1000\ °C\ NCarb}}{m_{1000\ °C}} \times 100 \qquad \text{Eq. II-31}$$

Where:

- $\Delta m_{525°C\text{-}1000°Ccarb}$: mass loss between 525 °C and 1000 °C of carbonated and noncarbonated samples.
- $m_{1000°C}$: sample mass after 1000 °C.

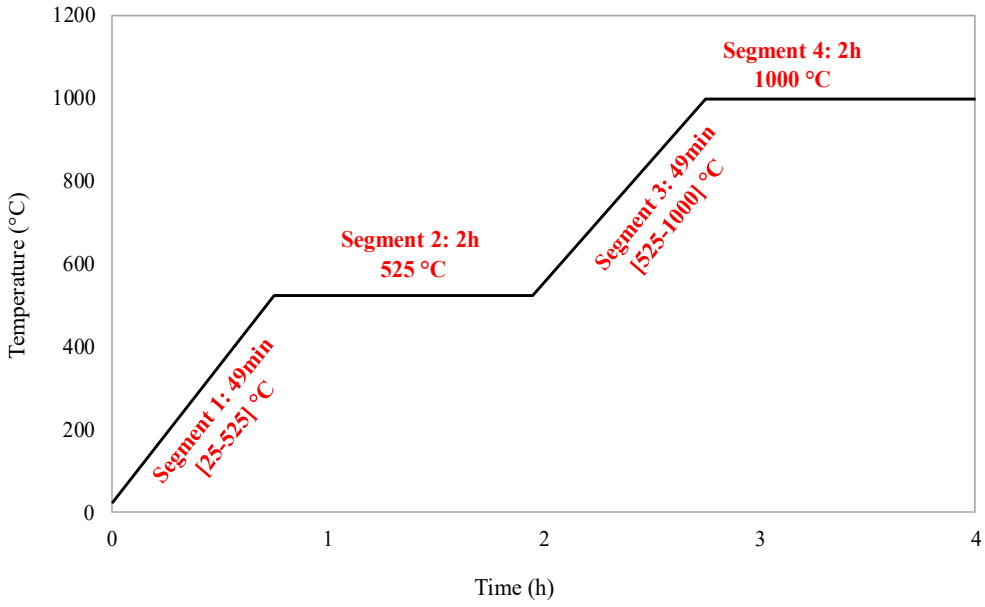

Figure II-13: Temperature segments corresponding to the mass loss process.

4.8.4 pH

As carbonation leads to a drop in pH, pH is measured at each stage of carbonation curing. The pH of each mix is measured at three regions of the specimen's face: (1) colorless region (carbonized surface); (2) pale pink colored region (partially carbonized surface); and pink colored region (uncarbonized surface). The ex-situ leaching method is used to determine pH. This method involves mixing powdered SCC with a solvent. The samples are extracted from the specified regions, manually ground, and sieved through a 60 µm sieve. The passing powder is blended with distilled water with an L/S ratio of 1. The liquid suspension is agitated for 3 minutes. Afterward, the liquid is filtered, and the pH is immediately measured using a digital pH meter.

Chapter III

Analysis of the properties of SCC under standard curing

1 Introduction

This chapter analyzes the properties of the four SCC mixes studied under standard curing conditions. The discussion begins with evaluating the hydration kinetics of each SCC mix, providing insight into their early-age reactivity. The focus then shifts to the examination of key fresh-state properties. The chapter further evaluates the development of the mechanical and physical performance of hardened SCC specimens. Finally, it examines the microstructural characteristics of each mix, providing a deeper understanding of the internal changes that occur during hydration.

To recenter the reader's attention, the experimental program focuses on SCC mixes cured under optimal conditions, i.e., water curing (referred to as standard curing), which serves as a baseline for assessing the influence of carbonation curing on hardened properties. Figure III-1 presents a schematic summary of the analyses performed, illustrating the sequential approach adopted in this study, starting from hydration kinetics and rheological characterization to mechanical, physical, and microstructural investigations using X-ray Diffraction (XRD), Thermogravimetric Analysis (TGA), Scanning Electron Microscopy (SEM), and Mercury Intrusion Porosimetry (MIP).

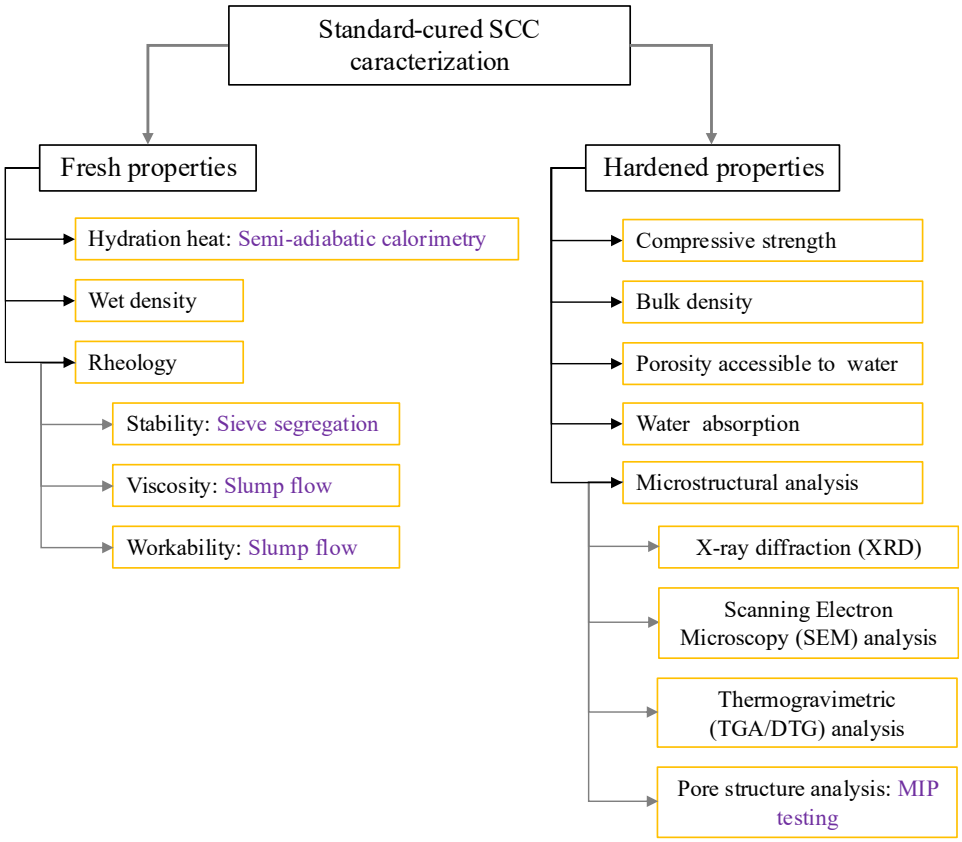

Figure III-1: Overview of the experimental program for the characterization of SCC under standard curing.

2 Hydration heat of fresh self-compacting concrete: Semi-adiabatic calorimetry

Figure III-2 illustrates the heat of hydration of the four SCC mixes under consideration. Across all mixes, the hydration process occurs in five stages: (i) pre-induction (rapid dissolution of C_3S), (ii) induction (dormant period), (iii) acceleration (rapid growth of C-S-H), (iv) deceleration, and (v) slow reaction [101].

During the pre-induction or dissolution period, C_3S rapidly dissolves upon wetting within seconds, but the dissolution rate quickly slows down. Two hypotheses explain the rapid decay of this dissolution rate: (i) the metastable barrier hypothesis, which suggests that a continuous but thin metastable layer forms around the C_3S particles, passivating their surface and thus restricting their access to water or limiting the diffusion of detaching ions away from the surface; or (ii) slow dissolution step hypothesis, where the reaction slowing down is explained by the observed roles of crystallographic defects in the early hydration processes [307,308].

The induction "dormant" period follows the initial dissolution of the C_3S phase and is characterized by low chemical activity [309]. The length of the induction period may indicate how long the cement-based material remains workable. The extent to which the induction period is extended or shortened is linked to several factors [310,311]. The prolonged induction period observed in the LS-NCA mix may be a consequence of its rheological instability. In other words, the bleeding and aggregate settlement observed in this mix may increase the local water availability, which dilutes the ion concentration, and thereby delays the hydration in these areas [312].

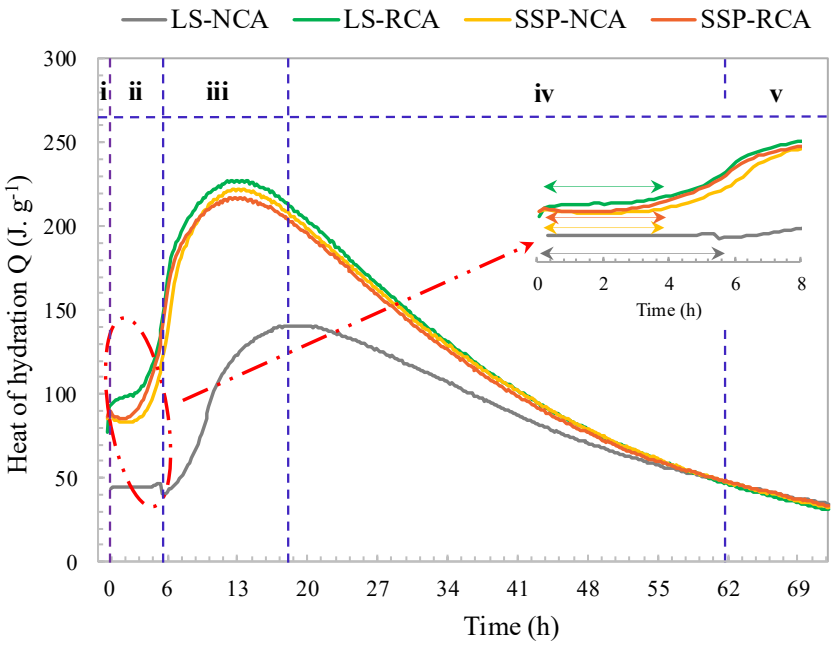

Figure III-2: Heat of hydration of SCC mixes with a zoom on the induction period.

Furthermore, during the acceleration stage, C_3S and a small amount of (β-)dicalcium silicate (β-C_2S) dissolution accelerate, thereby increasing the rate of C-S-H growth. Concurrently, the Ca^{2+} and OH^- ions' concentration steadily rises within the water solution until the $Ca(OH)_2$ precipitation begins [313]. The LS-RCA, SSP-NCA, and SSP-RCA mixes exhibit nearly the same hydration heat. These mixes exhibit the highest exothermic peak, peaking at approximately 49 $J.g^{-1}.h^{-1}$, 51 $J.g^{-1}.h^{-1}$, and 43 $J.g^{-1}.h^{-1}$, respectively (Figure III-3), which aligns with trends previously reported in comparable systems [101,106,107,182,264,314]. The corresponding peaks, which correspond to the exothermic hydration of C_3S and C_2S, are narrow and occur within a similar time range, around 5 hours. In contrast, LS-NCA shows the lowest exothermic peak, approximately 25 $J \cdot g^{-1} \cdot h^{-1}$, and the appearance of this exothermic peak shifts to 10 hours. This suggests that LS-NCA has the lowest C-S-H growth among the mixes, likely due to its rheological properties, as will be discussed further in § 3.

The comparison of heat evolution rates between SSP-NCA and SSP-RCA suggests that the higher water absorption of RCA during hydration reduces the water availability to hydrate C_3S; therefore, the growth of cement hydrates is slightly reduced. Moreover, the difference between LS-RCA and SSP-RCA may rely on the distinct filler effect of LS and SSP. The difference remains in surface area contribution and surface properties of the employed fillers. The additional surface area of SSP compared to LS is expected to offer additional nucleation sites for the heterogeneous formation and growth of early-age hydration products [315].

Nevertheless, the presence of organic matter in SSP may partially block these sites, thereby impeding the cement hydration reactions [105]. The intracrystalline organic matrix of SSP consists of polysaccharides, such as chitin, proteins, and glycoproteins, all of which are rich in amino acids with carboxyl (-COOH) functional groups [316–318]. In the alkaline pore solution, these organics progressively decompose, releasing oxygenated functional groups that create negatively charged sites with a strong affinity for Ca^{2+} (C_3S) and Al^{3+} (C_3A) [319,320]. The chelation of Ca^{2+} and binding of Al^{3+} reduce their availability in the reaction medium, thereby disturbing early hydration reactions, including ettringite formation, and slowing the nucleation rate of C-S-H [110]. Moreover, complexation through these active oxygenated groups can lead to adsorption onto reactive surfaces, blocking active sites for the nucleation and growth of hydration products [321].

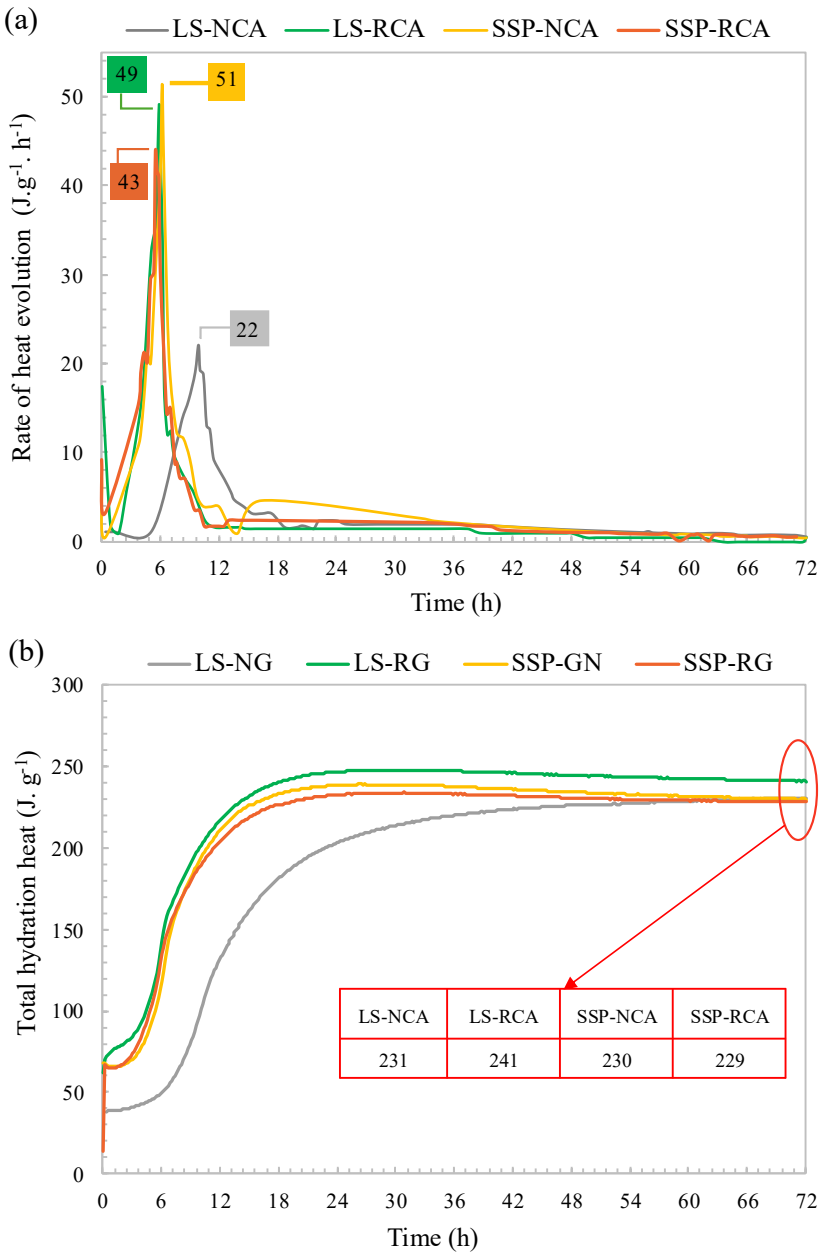

Figure III-3: (a) Rate of hydration evolution and (b) total hydration heat.

During the decelerating stage, none of the mixes exhibited a discernible shoulder peak within the 18-42h. The observed peak typically indicates the conversion of ettringite into monosulfate. The absence of this peak is linked to the stabilizing effect of calcite on ettringite and the subsequent formation of Hc and Mc (AFm phases) (Figure III-3a) [99]. However, the semi-adiabatic test is not sensitive enough to confirm whether these transformations are occurring, particularly when ettringite decomposition is limited.

Regarding the total hydration heat release (Figure III-3b), LS-NCA exhibits a sensibly comparable cumulative heat release to the other mixes by the end of 75h, with values ranging from 229

$J \cdot g^{-1}$ to 241 $J \cdot g^{-1}$. This may indicate that despite its delayed and lower peak heat release rate, it eventually reaches a comparable degree of hydration.

3 Analysis of the Fresh Properties of SCC under Standard Curing

3.1 Workability retention: Slump flow test

Workability retention (indicated by slump flow and t_{500} values) was measured for up to 90 min after the mixing step (Figure III-4), revealing a consistent trend across all mixes. Regarding only the NCA mixes (Figure III-4a and b), both show similar spread values, which tend to decrease over time but remain close to the SF2 range after 90 min of mixing (65 cm for LS-NCA and 62 cm for SSP-NCA). The two mixes exit the SF2 class approximately 80 min and 70 min, respectively, reflecting the longer induction period of LS-NCA (Figure III-4).

The difference in behavior between these mixes is more pronounced when considering t_{500} values. LS-NCA starts at 0.75 s, while SSP-NCA starts higher, at 1.19 s (VS1 class), yet t_{500} increases much more rapidly in the LS-NCA. The initial higher t_{500} value of SSP-NCA relative to LS-NCA, potentially due to the specific physical characteristics of SSP particles and their organic content, which is often porous and hydrophilic ($–COO^-$ groups in the organic matrix forming hydrogen bonds with water) [98], both of which increase water absorption. Over time, the higher content of ultrafine particles in SSP fills most of the voids and redistributes excess water (dilution effect), resulting in lower viscosity [322,323].

For RCA-based mixes, LS-RCA and SSP-RCA exhibit comparable initial spread, 78 cm and 76 cm, respectively, with minimal divergence until 90 minutes, when LS-RCA experiences a more pronounced loss in slump. Both mixes are initially classified within the VS1 category and transition to VS2 after 45 minutes. By 90 minutes, SSP-RCA retains measurable flowability, whereas LS-RCA becomes markedly stiffer. These differences closely mirror those observed in the NCA-based mixes, although to a different extent due to the presence of RCA.

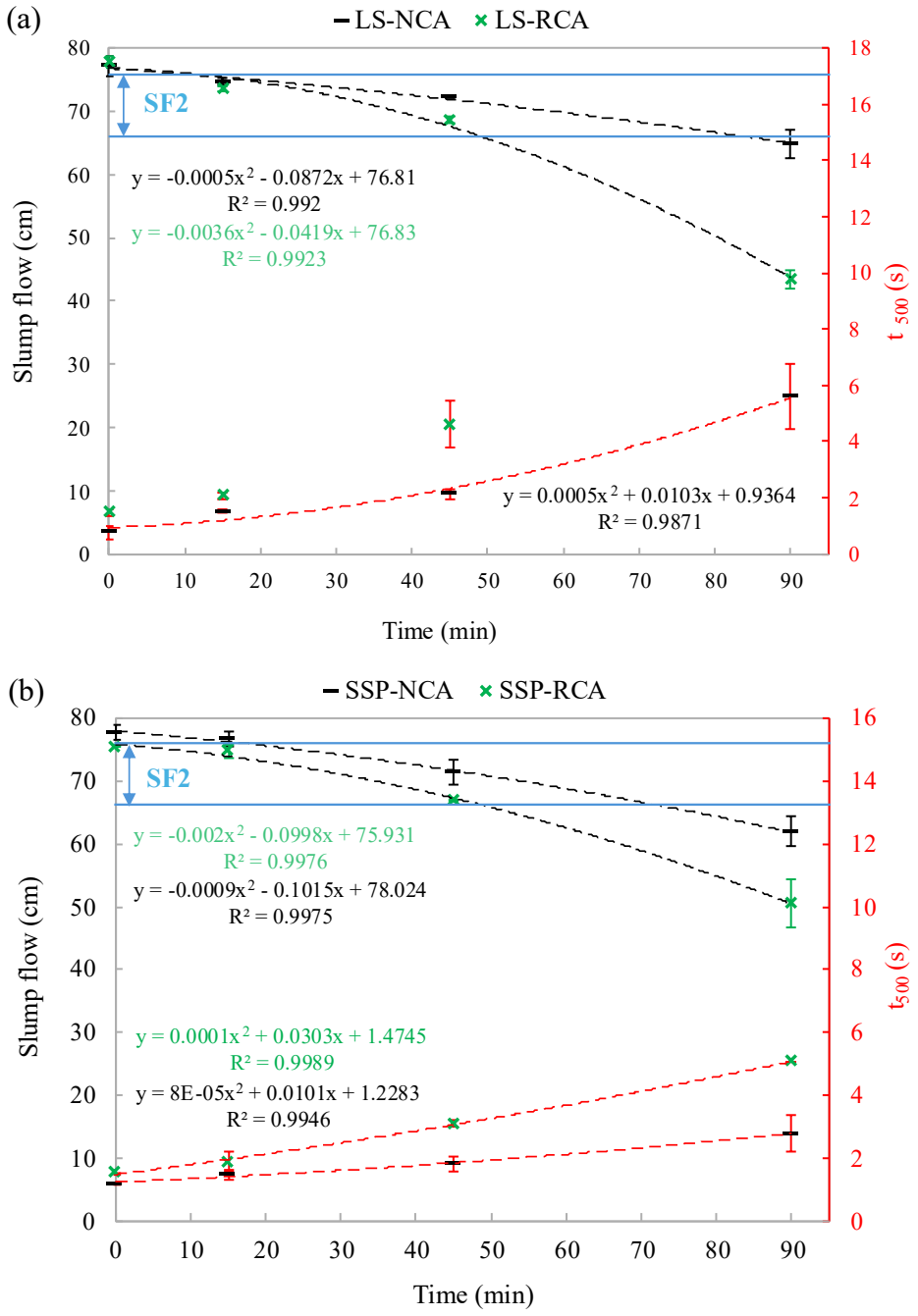

Figure III-4: Slump flow and T_{500} values of (a) LS-based SCC mixes and (b) SSP-based SCC mixes.

Substituting NCA with RCA reduces both flowability and the workability retention period to approximately 45 minutes, due to an increase in viscosity. After 90 minutes, LS-RCA loses around 44% of its initial spread flow, about 11% more than LS-NCA. Similarly, SSP-RCA loses around 35%, approximately 12% more than SSP-NCA.

The reduced workability in RCA-based mixes is further influenced by the porous surface, high water absorption, and dry state of RCA, which modify the rheology of SCC. As can be seen from

(Chapter II, Table II-3), at 24h, RCA exhibit a water absorption coefficient of around 5 %, which is two times larger than that of NCA. Within 15 min of water immersion, around 82% of the 24h absorption value is reached for RCA.

Despite the accentuated loss in the flowability of the LS-RCA, which also did not reach the t_{500} value by 90 min, the roughness of the old cementitious matrix surrounding the RCA might counterbalance some of the increased viscosity and the yield stress by ensuring that the aggregates are well coated with the cementitious paste and less likely to settle [81]. As a result, the homogeneity and the thixotropic behavior of RCA-based mixes are improved. Similar effects were observed with air-dried RCA combined with a water compensation technique, which improved flowability and cumulative bleeding, as will be discussed in the following section [77,79,324].

Based on these results, it can be suggested that by 45 min, the polycarboxylate superplasticizer (PCS) begins to lose effectiveness, as differences between the mixes become more evident [325]. It is reported that SP initially gives a good dispersion effect, typically from 20–30 min, before slump loss persists, due to its adsorption onto cement and filler surfaces [326,327].

3.2 Segregation resistance

3.2.1 Visual Stability Index (VSI)

Visualizing the four fresh mixes, the LS-NCA exhibits the largest VSI (Table III-1). As the mix reaches its final spread, the aggregates settle rapidly, forming a top layer richer in paste and creating a slight mortar halo in the slump flow patty. During standing periods between successive tests, LS-NCA behaves differently from the RCA-based mixes, showing stronger thixotropic behavior and more pronounced bleeding. These visual observations are consistent with the slump flow and t_{500} results.

The low cohesion between aggregates and mortar limits proper flow, which explains why LS-NCA takes longer to reach its final spread (Figure III-4), although this effect is less pronounced in LS-RCA. In contrast, the SSP-based mixes exhibit lower VSI values, falling within the stable to highly stable categories, with SSP-RCA demonstrating the best resistance to segregation. Moreover, the use of RCA in combination with SSP not only enhances the cohesiveness and stability of fresh SCC but also simplifies the preparation of specimens, making handling and casting easier. Overall, these observations highlight that combining RCA with SSP improves both fresh-state performance and practical workability.

Table III-1: VSI of the four SCC fresh mixes.

SCC	VSI operator 1	VSI operator 2	VSI average	SCC stability
LS-NCA	2	2	2	Stable (S) to unstable (US)
LS-RCA	1	1.3	1.15	S
SSP-NCA	1	0.7	0.85	S to highly stable (HS)
SSP-RCA	0.5	0	0.25	HS

3.2.2 Sieve segregation

Building on the VSI observations, the sieve segregation tests (Figure III-5) indicate that both LS and SSP mixes fall between the two reference limits, SR1 (upper limit) and SR2 (lower limit). As expected, the LS-NCA mix, which exhibited noticeable bleeding and higher VSI values, also showed poor segregation resistance (SR). Its SR value is approximately 4% larger than that of SSP-NCA.

The improved performance of SSP mixes can be attributed to the irregular and porous nature of seashell powder particles, which increases internal friction and interlocking within the paste, enhancing aggregate stability and reducing segregation consistent with VSI values. More importantly, these tests further reveal that the presence of RCA in SCC tends to improve resistance to segregation. The observed behavior is consistent with findings previously reported [328,329].

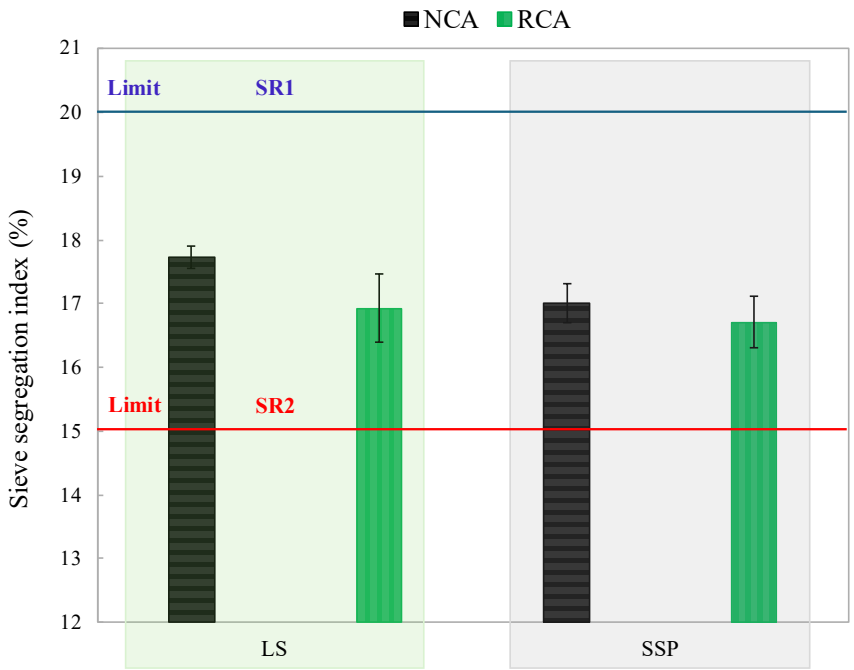

Figure III-5: Sieve segregation index of SCC mixes.

3.3 Wet density

Regarding the SCC mixes' wet densities (Figure III-6a), the LS-NCA mix exhibits the highest density, at 2303 kg/m^3. This latter decreases to 2289 kg/m^3 when substituting NCA with RCA. SSP-NCA demonstrates a further reduction to 2280 kg/m^3, and the lowest value, 2249 kg/m^3, is recorded for SSP-RCA. The decreasing trend in density is mainly due to the lowest density of RCA (2.21 g/cm^3) compared to NCA (4.46 g/cm^3). This trend aligns with previously observed trends showing a linear decrease in density as the substitution rate of RCA increases, with an average loss of approximately 5% at 100% of the substitution rate [79]. Moreover, SSP-based mixes consistently exhibit lower densities than LS-based mixes, which is attributed to SSP's lower density (2.50 g/cm^3) compared to LS (2.70 g/cm^3).

Furthermore, the LS-NCA mix with the highest wet density already exhibited the highest SR, suggesting that SCC segregation is primarily driven by density differences. In other words, in the highest SR mix, the bottom layer of the specimens contains a higher concentration of coarse aggregates, which are denser than the cement paste layer formed at the surface [330,331]. This correlated behavior is shown in Figure III-6.

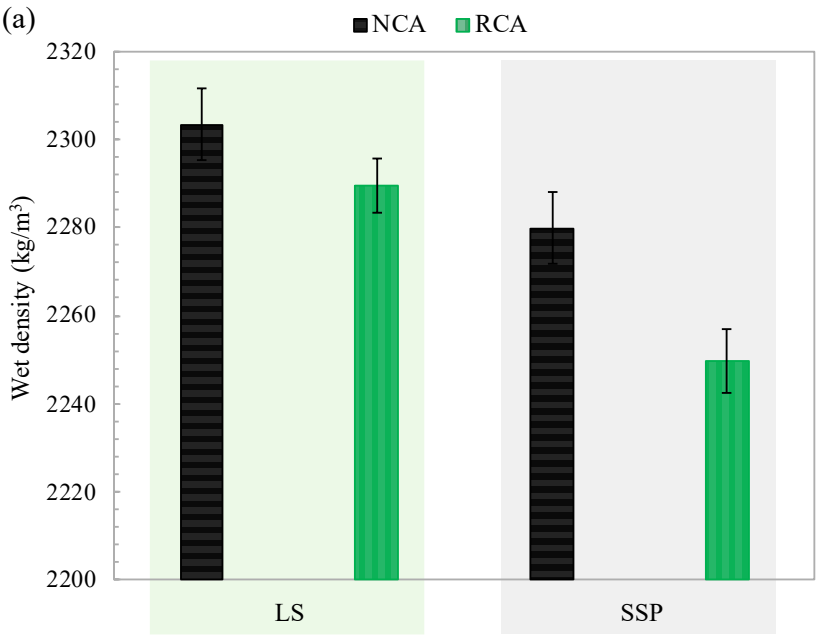

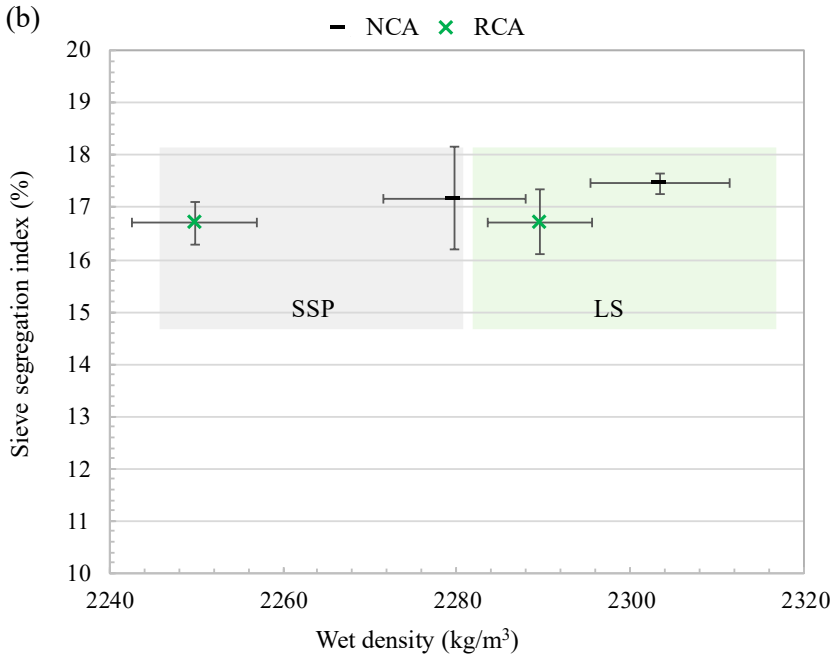

Figure III-6: (a) wet density of SCC mixes and (b) relationship between SR and wet density.

4 Analysis of the hardened properties under standard curing

4.1 Compressive strength

The time evolution of the compressive strength for the cubic specimens of SCC mixes is given in Figure III-7. Despite the delayed hydration rate and high SR of LS-NCA, it exhibits around 8% larger compressive strength than SSP-NCA on the first day of water curing. The higher compressive strength of LS-NCA may be attributed to standard curing conditions, which likely compensate for excessive water evaporation caused by higher bleeding during in-mold curing. The water curing compensates for this moisture loss and supports the mix's strength development. Additionally, the crystalline structure of LS and its surface properties positively influence the early-age compressive strength of concrete with no significant effect at later stages compared to SSP, consistent with the semi-adiabatic calorimetry results (Figure III-3).

After 7 days, the development of compressive strength is more significant in SSP-NCA, with an increase of around 34%, 13% higher than that observed for LS-NCA. This difference in gain can be attributed to the distinct particle characteristics of SSP (Chapter II2.1.2). The particles' rougher surfaces, porous grains, and higher packing density enhance interparticle cohesion and facilitate better mechanical interlocking [332–334]. In addition, the continuous refinement of the pore structure by Hc/Mc phases may further improve the ITZ.

After 28 days, both mixes reach the same compressive strength of 40 MPa. As reported in [335], the 28-day compressive strengths of SCC are mainly dominated by the binder composition rather than the w/b ratio, as in conventional workability concrete. However, after 28 days, the LS mixes continue to gain compressive strength, whereas the SSP mixes exhibit a moderate decline in compressive strength, which is not a typical trend reported in other studies [336,337].

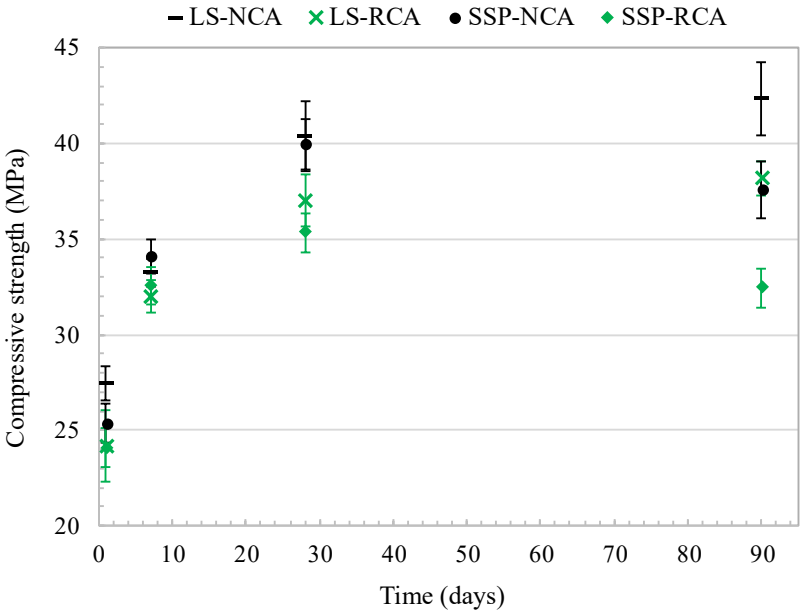

Figure III-7: Compressive strength development of SCC specimens over different curing ages.

Two factors can be the main cause of the observed decrease in compressive strength: (i) the dilution effect of SSP [103,338], and (ii) the organic impurities in the SSP, which cause it to react chemically differently from purely mineral $CaCO_3$, as previously discussed in § 2. While this latter effect may not be particularly detrimental during the first 28 days of curing, it becomes more evident at later ages (90 days). The perturbation of the hydration process by organic matter may lead to delayed ettringite formation (DEF) and even late-stage C-S-H growth within the microstructure, generating internal stresses and promoting the extension of microcracks [339–341], consistent with MIP results, ultimately reducing the long-term compressive strength of the concrete [110,112,113].

Nevertheless, the RCA mixes exhibit lower compressive strength than their NCA counterparts. The compressive strengths of LS-RCA and SSP-RCA converge throughout the curing ages and follow the same increasing trend until the 28th day of curing. At this age, LS-RCA and SSP-RCA showed moderate reductions of approximately 8% and 11%, respectively, relative to their NCA counterparts. These results are consistent with those reported in the literature [342,343] and significantly lower strength loss (i.e., higher strength) compared to values reported in other studies [344,345]. The slight compressive strength loss is mainly due to the RCA's higher water absorption capacity and lower

mechanical properties (Figure II-6, Table II-3). However, the limited compressive strength loss can be attributed to the surface roughness of RCA, the high fine content, the dried state of RCA, and the water compensation method used in the SCC formulation [115,346]. After 90 days of curing (Figure III-7), while the compressive strength gap between LS-RCA and LS-NCA remains approximately the same, it increases to around 14% between SSP-RCA and SSP-NCA.

Furthermore, despite the differences in SR observed across all SCC mixes, compressive strength remains unaffected. This effect is particularly noteworthy in the LS-NCA mix, which exhibits the highest segregation resistance and compressive strength at early ages. Overall, the compressive strength development across all curing ages proceeds without being influenced by variations in SR (Figure III-8) [347]. Even if SR were to exert some influence, the values observed in the studied SCC mixes, particularly LS-NCA, do not reach critical levels that could compromise compressive strength [348].

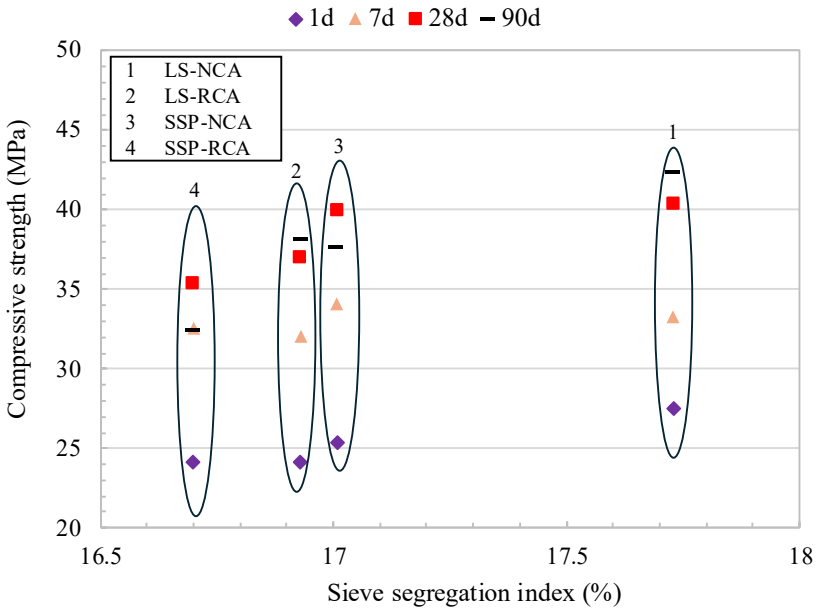

Figure III-8: Relationship between compressive strength and sieve segregation index.

4.2 Bulk density

The overall bulk density evolution of the specimens (Figure III-9) follows the same trend as that observed for compressive strength. As the hydration process proceeds, the formation and accumulation of hydration products enhance the packing density of the SCC, improving the bond between the cementitious matrix and aggregates. In particular, LS-based specimens exhibit a continuous increase in bulk density throughout the 90 days of curing (Figure III-9a), highlighting this trend. As indicated by Wu *et al.* [349], an optimal amount of LS maximizes the packing, leading to tighter spacing and more densely packed C-S-H gel within the ITZ. In contrast, the SSP-based specimens exhibit a comparable

density to their LS-based counterparts and follow a similar increasing trend up to 28 days. Beyond this age, their density decreases up to 90 days of curing (Figure III-9b).

The higher density of LS specimens, whether with NCA or RCA, compared to SSP-based specimens, is probably due to the LS density being slightly higher than that of SSP (Table II-1). The density reduction observed in SSP-based specimens may indicate potential microstructural changes, as will be discussed in § 5.4. One possible explanation may be related to the alteration in the molecular binders between calcite crystals of the shell fragments. Additionally, regardless of the SCM used, RCA-based specimens demonstrate a lower density than their NCA counterparts, partly explaining their lower compressive strengths. The lower density, therefore, is attributed to the lower bulk-specific density of RCA [83]. These findings are consistent with [350–352].

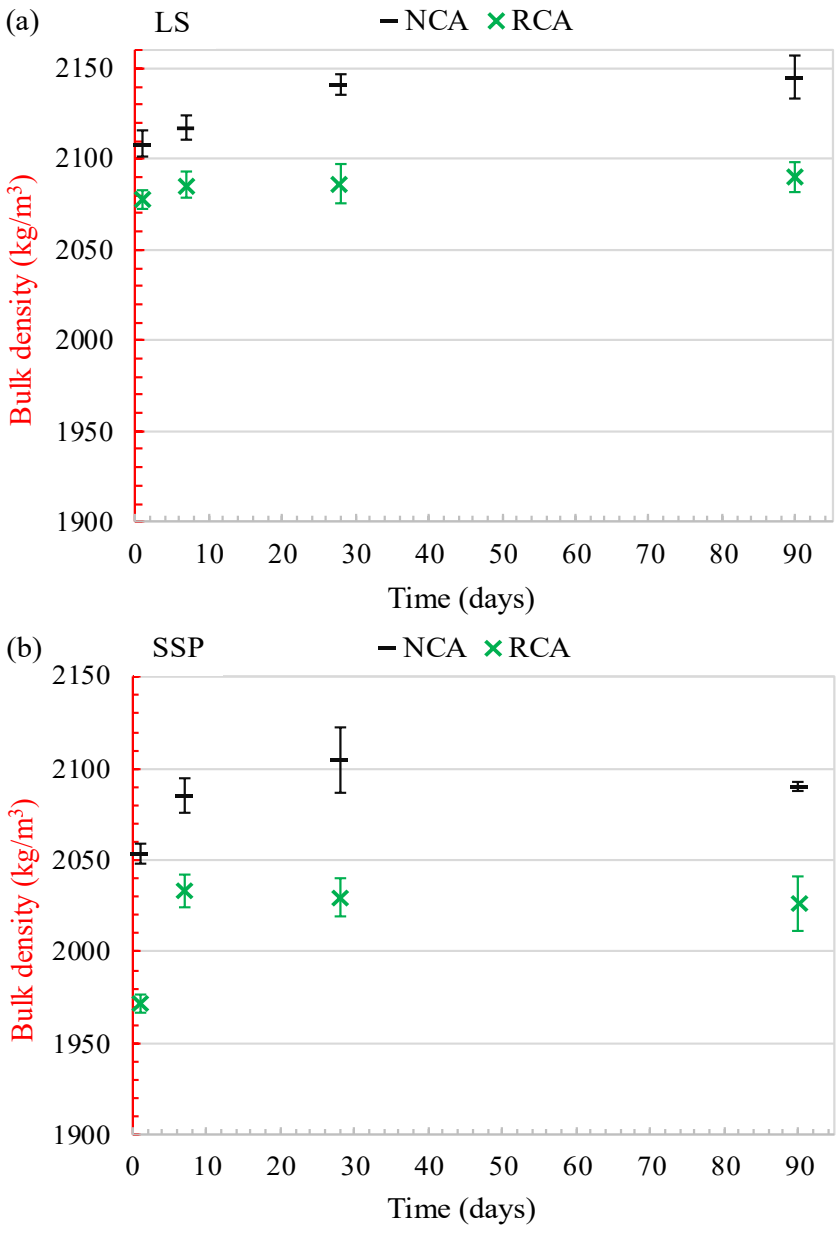

Figure III-9: Density evolution of (a) LS-based SCC and (b) SSP-based SCC specimens over curing ages.

Figure III-10 illustrates this correlated behavior, where regression analysis confirms a strong linear relationship ($R^2 > 0.91$) between the compressive strength development and bulk density across all specimens. Notably, in LS-based specimens, a small increase in bulk density results in a larger gain in compressive strength than in SSP-based specimens.

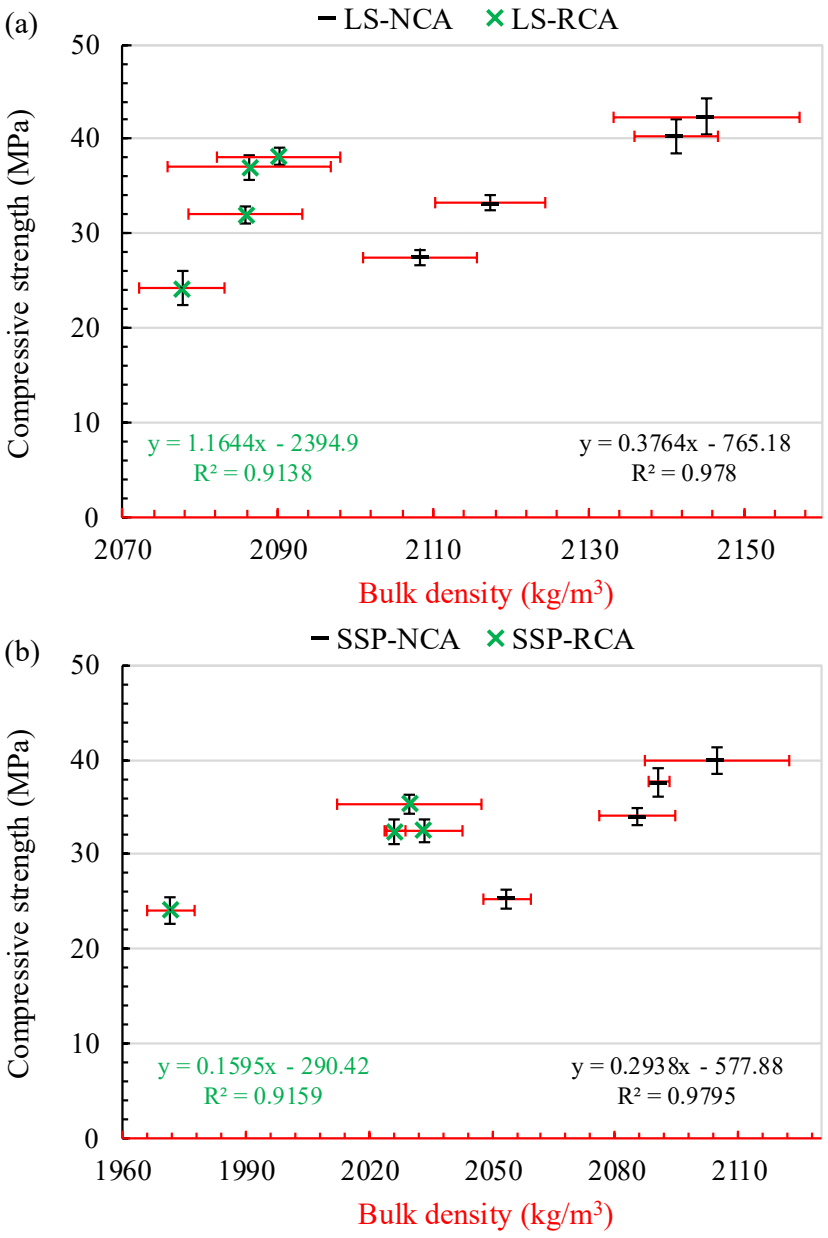

Figure III-10: Relationship between compressive strength and bulk density of (a) LS-based SCC and (b) SSP-based SCC specimens.

4.3 Water-accessible porosity

Among the NCA mixes, the LS-based specimens exhibit a slightly higher porosity than their SSP-based counterparts up to 28 days (Figure III-11). The difference noticed during this period may be attributed to the combined effect of the finer particle size distribution of SSP, the intrinsically lower specific density of SSP compared to LS (Figure II-2, Table II-1), and the rheological properties of the fresh LS-based SSC that may favor the formation of voids that remain as open porosity after hardening (§ 3.2).

Moreover, while the SSP-based specimens (Figure III-11b) show a slight reduction in porosity after 28 days, the LS-based specimens (Figure III-11a) continue to exhibit a gradual decrease until 90 days of curing. This contrast draws attention to the fact that several studies [112,353,354] have reported that SSP leads to a highly porous ITZ and introduces a large volume of macropores, primarily caused by air entrapped by proteins of the organic matrix, which in turn increases porosity and water absorption, as will be discussed in the following section. In addition, in the highly alkaline pore solution of concrete, the organics are prone to dissolution or denaturation, similarly contributing to the alteration of these properties [355]. Considering this, it is reasonable to assume that if the LS-based specimens, particularly LS-NCA specimens, were rheologically more stable, they would likely exhibit significantly lower porosity than their SSP-based counterparts.

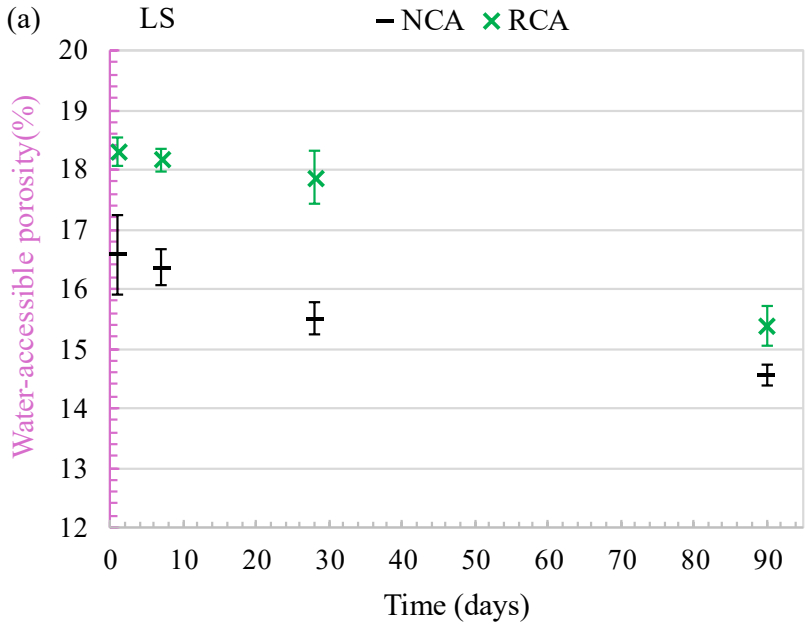

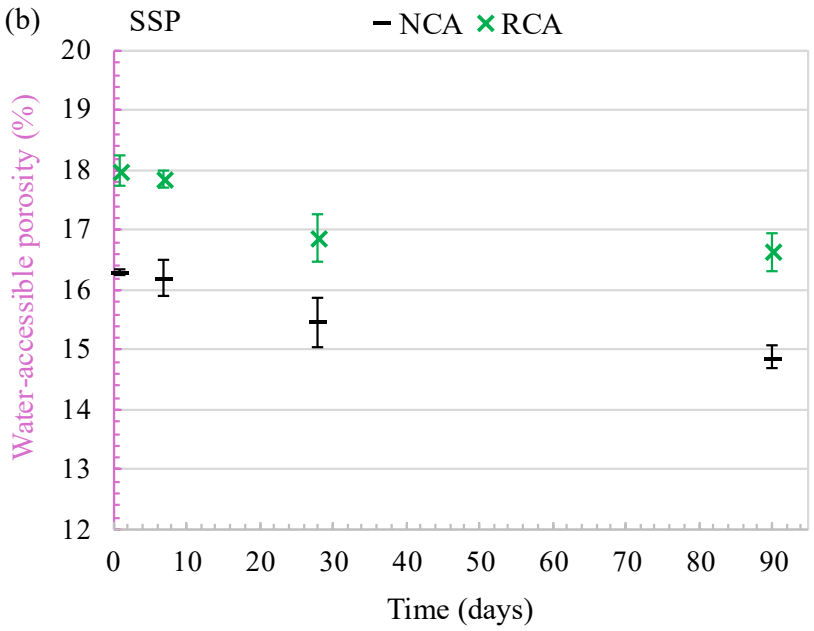

Figure III-11: Evolution of water-accessible porosity within (a) LS-based SCC mixes and (b) SSP-based SCC mixes over curing ages.

4.4 Water absorption

The variation in water-accessible porosity in a specific mix directly affects its water absorption by either providing or restricting pathways for water infiltration into the concrete matrix [356,357]. For all specimens (Figure III-12), changes in water absorption reflect the changes in porosity over time. Up to 28 days, LS-based specimens show similar water absorption to SSP-based specimens. After 28 days, water absorption in LS-based specimens gradually decreases, while SSP-based specimens show only minor change, reflecting the gradual closure of accessible pores during curing.

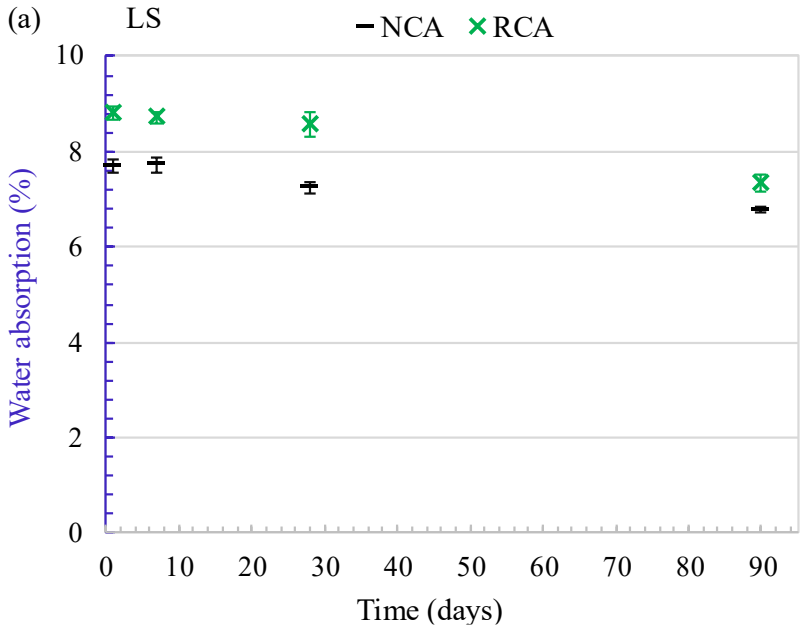

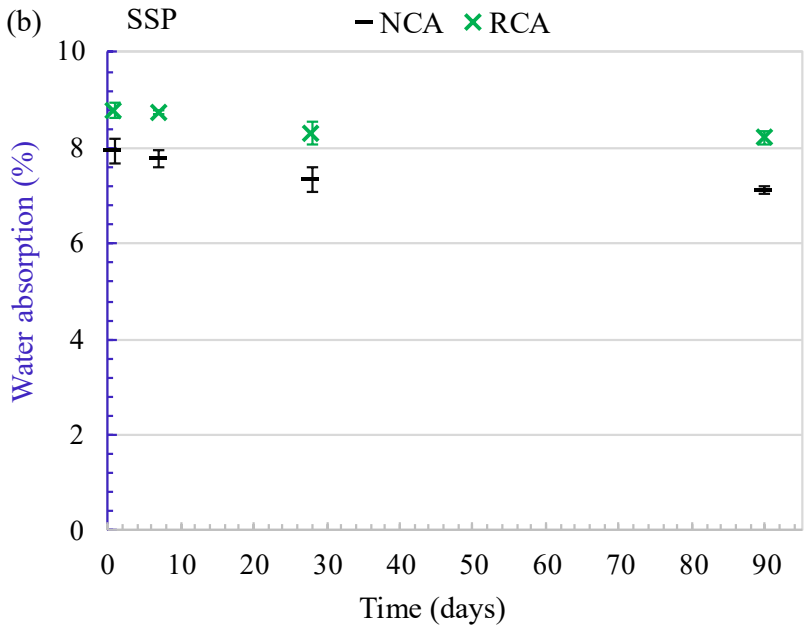

Figure III-12: Variation in water absorption capacity of (a) LS-based SCC mixes and (b) SSP-based SCC mixes over the curing ages.

Regarding RCA-based specimens, the evolution of water absorption in LS-RCA and SSP-RCA follows the same overall trend observed in NCA-based specimens. The observed changes in water absorption can once again be linked to the same factors that influenced accessible porosity, showing that the two properties are closely related. Under the studied conditions, a strong linear correlation is observed between water absorption and accessible porosity (Figure III-13).

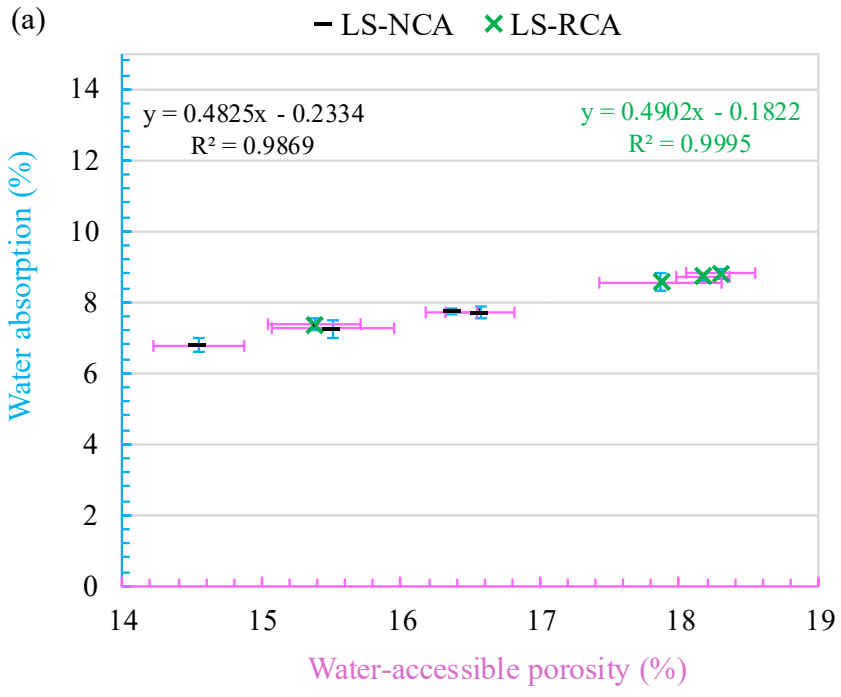

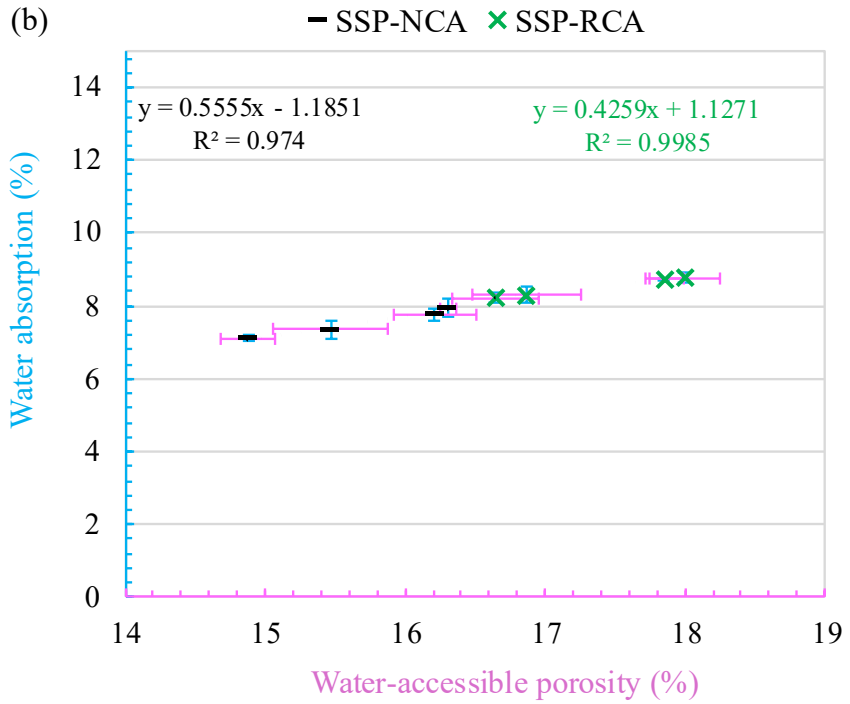

Figure III-13: Relationship between water absorption and porosity accessible to water of (a) LS-based SCC and (b) SSP-based SCC specimens.

5 Microstructural analysis

5.1 X-ray diffraction (XRD) analysis: Phase identification

At this part of the research, XRD provides essential information on the mineralogical composition of the SCC matrix, allowing the identification of phases originating from both the precursors and the hydration process. More importantly, it reveals the reactivity of SSP and LS with the aluminate phases through the formation of Hc/Mc and the extent to which they are present in the specimens at 28 days of curing.

The XRD patterns (Figure III-14) of the SCC specimens indicate a similar mineralogy for all specimens. Quartz and calcite are the dominant crystalline phases across all matrices. Quartz consistently exhibits the most intense diffraction peak, followed by the second most intense peak of calcite (Figure III-14a-d). These phases originate from the sand and the LS and SSP precursors. For the hydration products, secondary peaks corresponding to $Ca(OH)_2$ and Hc are identified, along with low-intensity reflections of ettringite and gypsum. Peaks of C_3S and C_2S are also detected, together with minor reflections of aragonite and vaterite.

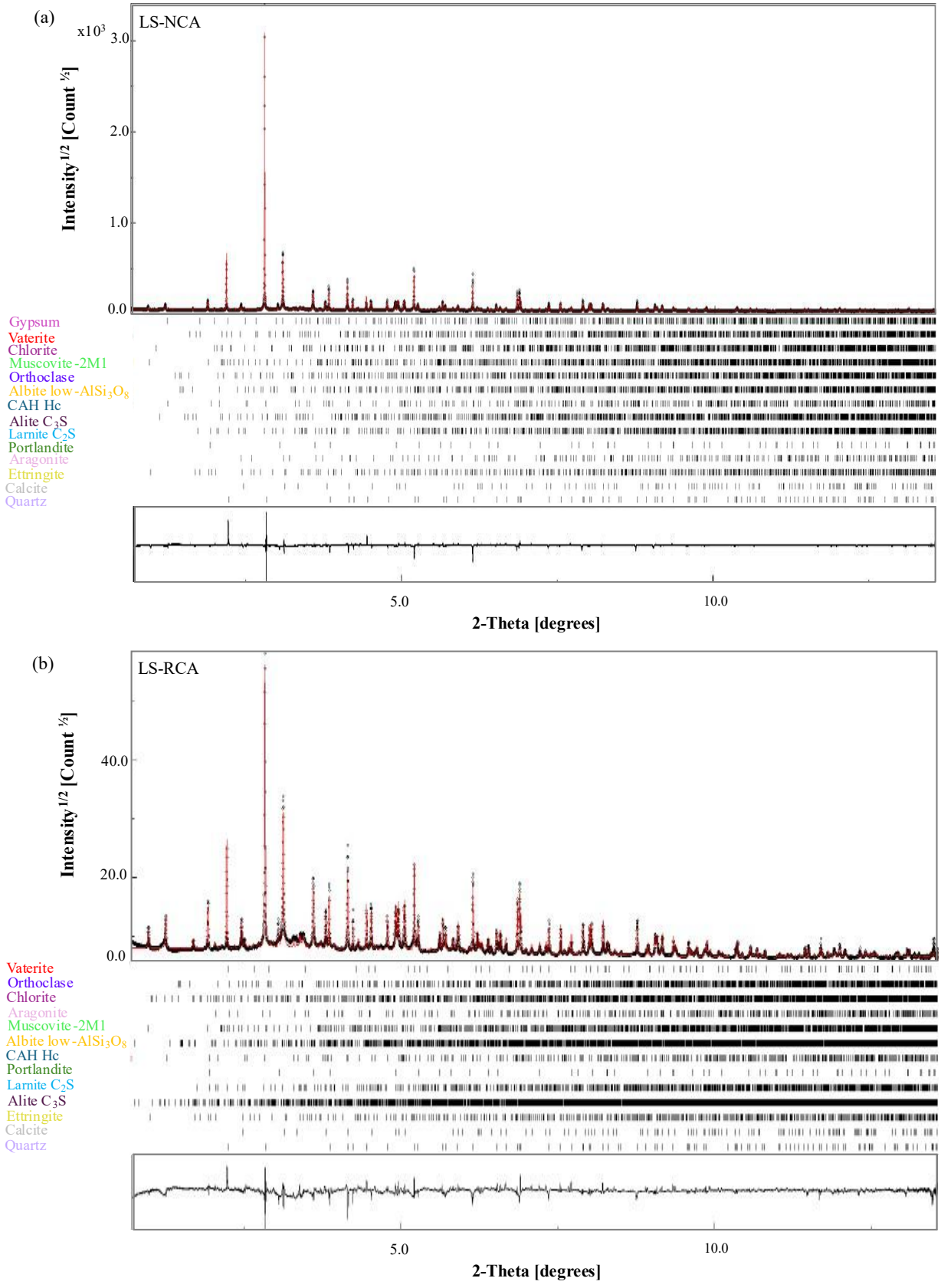
(a)
LS-NCA
x10^3
3.0
2.0
1.0
0.0
Intensity^1/2 [Count ^1/2]
Gypsum
Vaterite
Chlorite
Muscovite-2M1
Orthoclase
Albite low-AlSi3O8
CAH Hc
Alite C3S
Larnite C2S
Portlandite
Aragonite
Ettringite
Calcite
Quartz
5.0
10.0
2-Theta [degrees]
(b)
LS-RCA
40.0
20.0
0.0
Intensity^1/2 [Count ^1/2]
Vaterite
Orthoclase
Chlorite
Aragonite
Muscovite-2M1
Albite low-AlSi3O8
CAH Hc
Portlandite
Larnite C2S
Alite C3S
Ettringite
Calcite
Quartz
5.0
10.0
2-Theta [degrees]

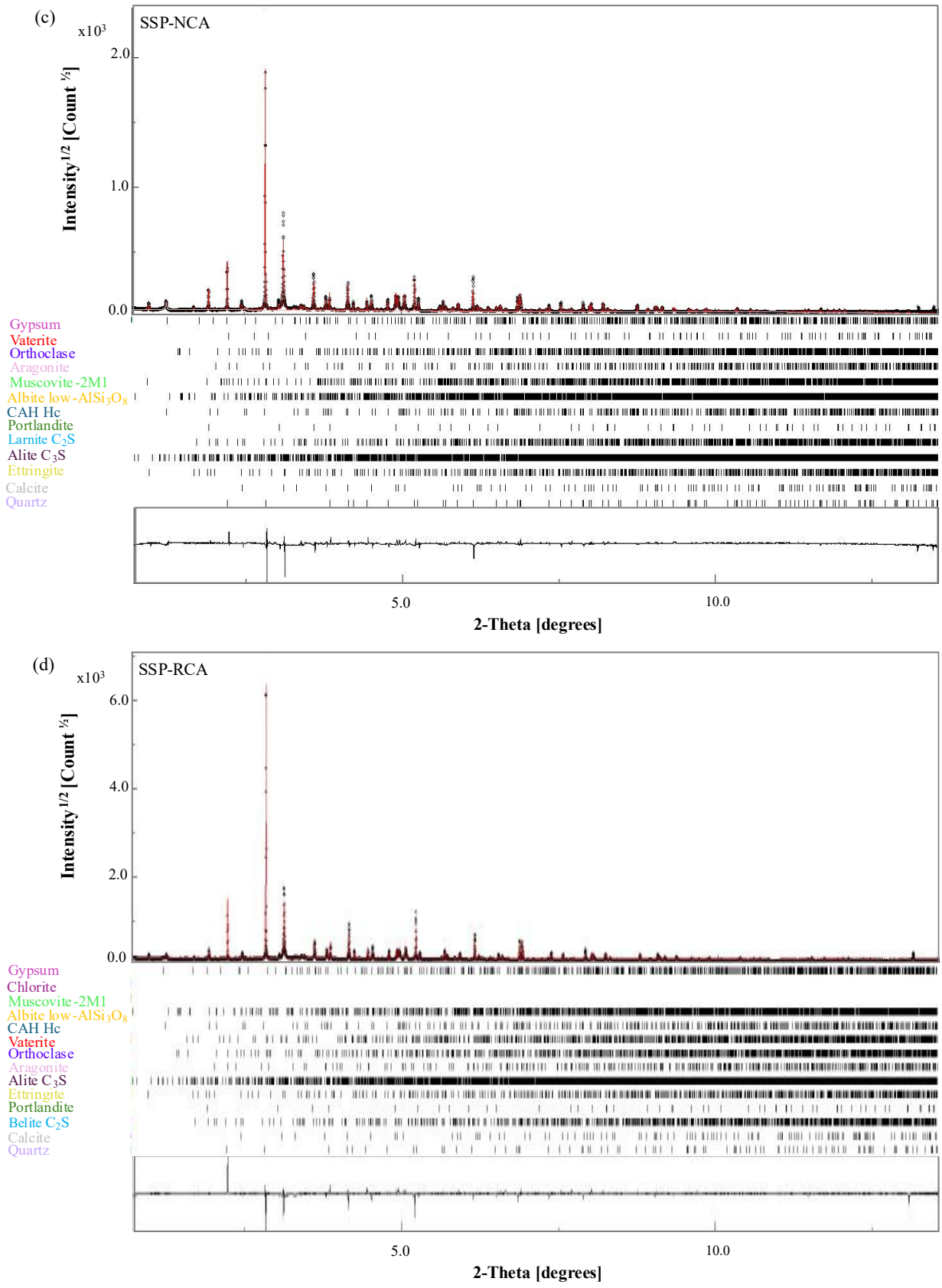

Figure III-14: XRD patterns of (a) LS-NCA, (b) LS-RCA, (c) SSP-NCA, and (d) SSP-RCA after 28 days of curing.

Rietveld quantification revealed that all specimens exhibit advanced hydration, with unreacted C_3S remaining negligible, only about 0.7%. Comparing Hc content, SSP-NCA specimens reach 4%, which is double that found in LS-NCA (Figure III-15). In contrast, for RCA-based specimens, LS-RCA contains more Hc (3.6%) than SSP-RCA (2.1%), reversing the trend seen in NCA-based mixes (Table III-2). This variability makes it difficult to definitively determine which precursor reacts more with aluminates, although all specimens show moderate reactivity. Mc is not measurable in any of the systems, as it typically forms only after the complete consumption of gypsum during ettringite formation.

Ettringite content is lowest in LS-NCA (0.9%), while the other specimens exhibit comparable levels (LS-RCA 3.6%; SSP-NCA 3.3%; SSP-RCA 2.7%). Therefore, the presumed DEF, which could explain the observed effects on compressive strength and pore structure in SSP-based specimens, cannot be confirmed by XRD at a single curing age. This mechanism may result from increased sulfate sorption by C-S-H at elevated temperatures, leading to ettringite destabilization and monosulfoaluminate formation. The latter then subsequently transforms back to ettringite due to the slow desorption of sulphate from C-S-H at ambient temperatures [358]. A more comprehensive assessment of multiple curing ages would be necessary to clarify its evolution.

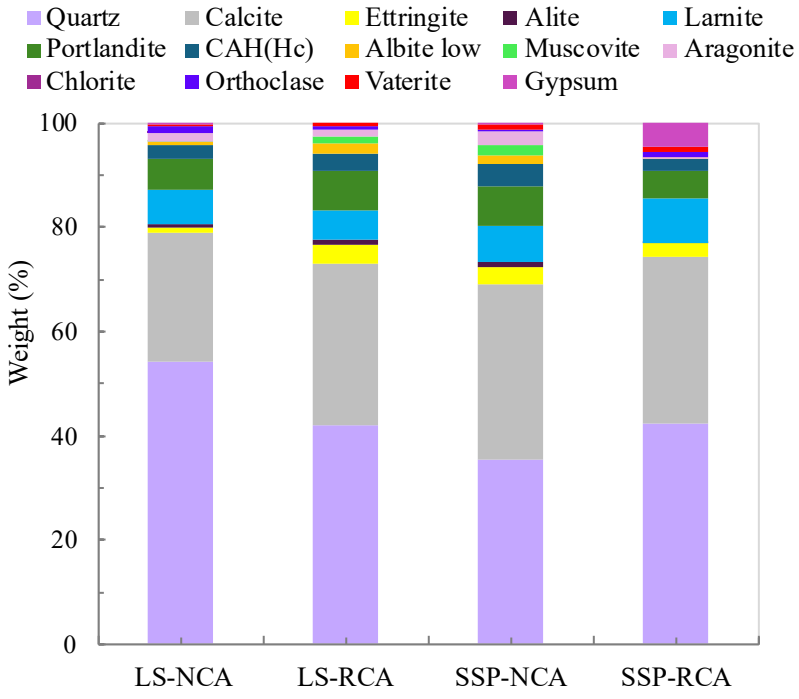

Figure III-15: Quantitative phase analysis based on XRD results of SCC specimens at 28 days of curing.

Table III-2: Numeric phase percentages and reliability assessment of SCC specimens at 28 days. Numbers in parentheses indicate the standard deviations as 1σ on the last digits from the Rietveld refinement.

cif	COD	wt (%) LS-NCA	wt (%) LS-RCA	wt (%) SSP-NCA	wt (%) SSP-RCA
Quartz	1011097	54(0.4)	42(7)	35.5(6)	42.5(0.3)
Calcite	1547348	25(0.3)	31(5)	33.5(5)	32(0.2)
Ettringite	9011576	0.9(0.1)	3.6(1)	3.3(0.1)	2.7(0.2)
Alite-C_3S	9016125	0.7(0.1)	1(0.2)	1.1(0.3)	0.001(0.04)
Larnite-C2S	9017424	6.5(0.2)	5.7(1)	6.8(1.1)	8.3(0.3)
Portlandite	1001768	6(0.1)	7.4(1)	7.8(1.2)	5.5(0.1)
CAH (Hc)	1000459	2.8(0.1)	3.6(1)	4(0.7)	2.1(0.2)
Albite low	2107372	0.4(0.1)	1.4(0.3)	1.8(0.4)	0.4(0.03)
Muscovite	1011049	0.1(0.1)	1.2(0.3)	2.1(0.5)	
Aragonite	2100187	1.6(0.2)		2.4(0.5)	0.04(0.3)
Chlorite	9000158	0.13(0.1)	0.7(0.1)		
Orthoclase	9000304	0.3(0.1)	0.7(0.2)	0.6(0.2)	0.8(0.1)
Vaterite	9007475	0.3(0.2)		0.9	0.9(0.2)
Gypsum	1010981	0.2(0.3)		0.2(0.2)	4.8(0.4)

5.2 Thermogravimetric analysis

Figure III-16 presents the TGA/DTG curves, illustrating the hydration progress of the SCC mixes. Three main mass loss events can be observed across all SCC mixes' TGA curves: C-S-H dehydration, $Ca(OH)_2$ dehydration within the temperature ranges mentioned earlier (Chapter II2.1.2.3), and the decarbonation of $CaCO_3$ occurring between 700 °C and 900 °C. These curves exhibit a characteristic profile consistent with those documented in previous studies [182,359].

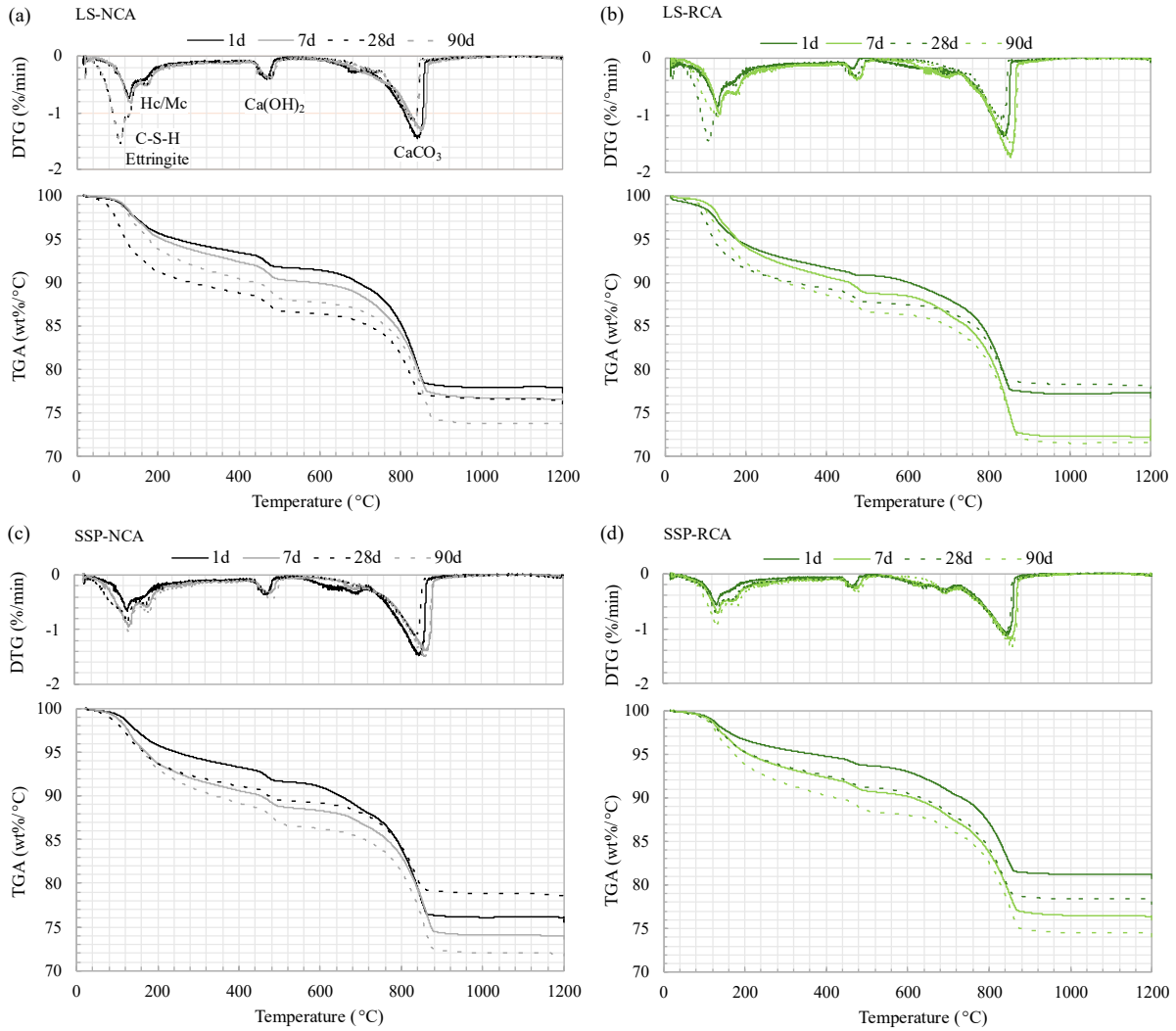

Figure III-16: TGA/DTG curves of (a) and (b) LS-based SCC mixes, and (c) and (d) SSP-based SCC mixes over different curing ages.

The $CaCO_3$ content primarily originates from the LS and SSP in the SCC mixes rather than from natural carbonation. Moreover, examination of the DTG curves reveals a small peak within the C-S-H dehydration domain, occurring between 170 °C and 180 °C in our samples. This peak indicates Hc/Mc decomposition, supporting the claim that including SSP and LS in the SCC mixes promotes the formation of these phases [360]. However, it is difficult to detect this reaction in the TGA curves, as they show only a subtle slope change.

Furthermore, the evolution of hydrate content in SCC mixes across curing ages was evaluated by integrating the DTG curves into the C-S-H and $Ca(OH)_2$ ranges (Figure III-17). It is well known that hydration products fill the pores, densify the cementitious matrix microstructure, and ensure inter-particle binding, with C-S-H being the primary hydrate responsible for the concrete strength.

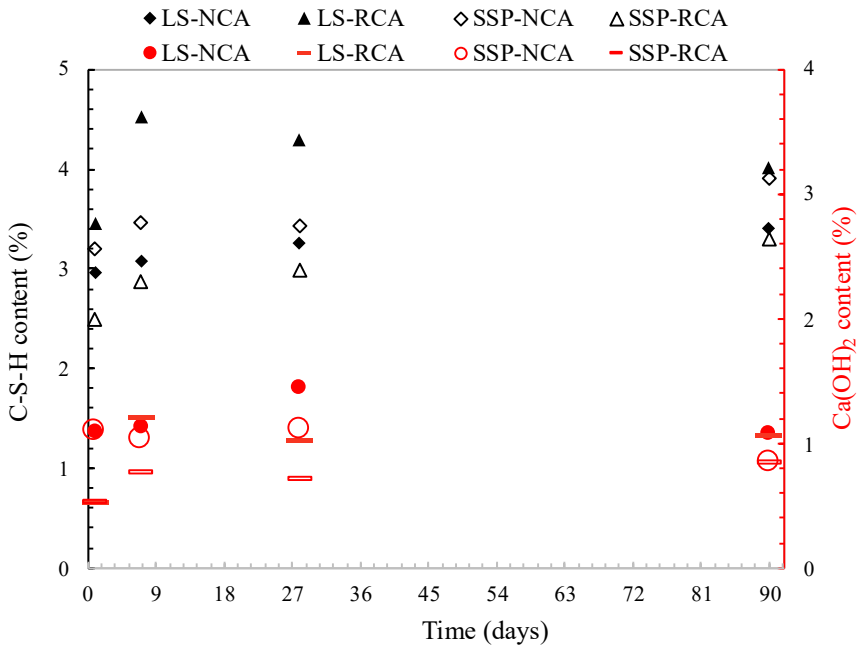

Figure III-17: C-S-H (black symbols) and $Ca(OH)_2$ (red) contents in the mixes as integrated from TGA/DTG curves.

Comparing the C-S-H content in LS-NCA and SSP-NCA, both mixes exhibit similar levels during 28 days of curing, with slightly higher content observed in SSP-NCA, particularly at 7 days. This suggests that the hydration of LS-NCA may be slightly delayed at early ages, possibly due to its rheological properties. Larger porosity in SSP can also contribute to this behavior.

At 90 days, while LS-NCA shows stable C-S-H formation, SSP-NCA continues to develop more C-S-H compared to what was observed at 28 days. Nevertheless, this increase does not translate into improved mechanical performance. As will be discussed later, SEM observations reveal poorly hydrated C-S-H within the SSP-NCA matrix. The poorly formed C-S-H compromises matrix densification and weakens the intrinsic cohesive capacity of the phase [361]. Moreover, it is more susceptible to the initiation of microcracks at its interfaces, further contributing to the observed reduction in compressive strength [362,363].

Comparing the mixes with RCA, LS-RCA exhibits the highest C-S-H content among all mixes, including SSP-RCA specimens. These later exhibit the lowest C-S-H content across all ages of water curing, in agreement with the pore refinement trends observed in MIP testing. It is worth mentioning that it is difficult to attribute the measured C-S-H content in these mixes entirely to ongoing hydration, as the old mortar adhering to the RCA surface already contains pre-existing C-S-H. This may lead to an overestimation of the actual extent of hydration.

In parallel, the evolution of the $Ca(OH)_2$ content follows a distinct trend within SCC specimens. LS-NCA specimens exhibit an increase in $Ca(OH)_2$ content up to 28 days, followed by a slight decrease at 90 days. This trend reflects progressive hydration at early ages, reaching a steady state after 28 days. In contrast, the $Ca(OH)_2$ content in SSP-NCA fluctuates moderately across curing ages, indicating less uniform hydration. For RCA-based specimens, LS-RCA specimens show rapid early growth of $Ca(OH)_2$ that tends to stabilize at later ages, whereas SP-RCA specimens consistently exhibit the lowest $Ca(OH)_2$ content, suggesting overall lower hydration.

Overall, the TGA/DTG analysis indicates that LS-based mixes exhibit more consistent and higher hydrate formation than SSP-based mixes, regardless of aggregate type, suggesting a more efficient hydration process occurring within these mixes.

5.3 Microstructural observations

5.3.1 Interfacial Transition Zone evolution

The SEM images of the ITZ in the four mix specimens allowed observation of its evolution at 1, 28, and 90 days of curing, although the observed details vary depending on the examined region of the ITZ.

The SEM images after 1 day of curing reveal that ITZ in LS-NCA (Figure III-18a) is relatively thin and surrounded by a compact matrix, consistent with its higher early compressive strength. In SSP-NCA (Figure III-18c), the ITZ appears even narrower, although small pores are observed in the adjacent matrix, suggesting slightly less uniformity. For the RCA-based specimens (Figure III-18b), LS-NCA exhibits two distinct ITZs (old and new), reflecting the influence of recycled aggregates and showing a less uniform structure with minor porosity. In contrast, in SSP-RCA (Figure III-18d), the ITZ boundaries and structure are difficult to discern, while the surrounding matrix contains large pores. Overall, the aggregates are already well-embedded in the mortar matrix, though to different extents.

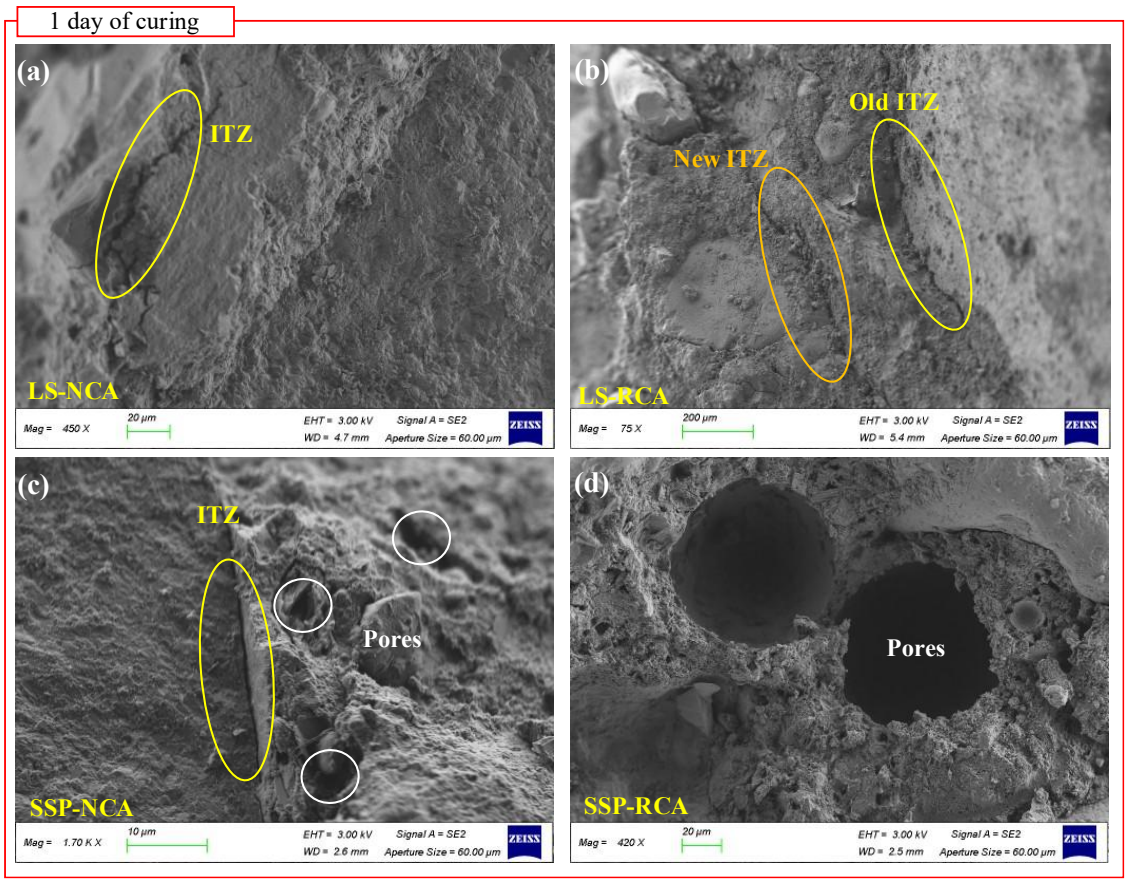

Figure III-18: SEM images on top of ITZ of (a-b) LS-based specimens and (c-d) SSP-based specimens after 1 day of curing.

The SEM images of the different mixes after 28 days of curing (Figure III-19) reveal further changes in the ITZ and the adjacent matrix. In LS-NCA, the ITZ, approximately 5 µm in length, appears rougher, with visible crystal growth in the surrounding matrix (Figure III-19a). In SSP-NCA, the ITZ appears more refined, although microcracks are visible within the matrix, possibly due to stress concentrations from intense crystal growth (Figure III-19c). In LS-RCA, the ITZ is difficult to discern as the matrix appears to envelop the aggregates, with the adjacent matrix exhibiting features similar to those of the NCA counterpart (Figure III-19b). In SSP-RCA, measuring the ITZ also remains difficult, although it appears thicker than in LS-RCA, with a more refined surrounding matrix (Figure III-19d). It should be noted that differences in SEM magnification between the images make it challenging to directly compare ITZ development from 1 to 28 days.

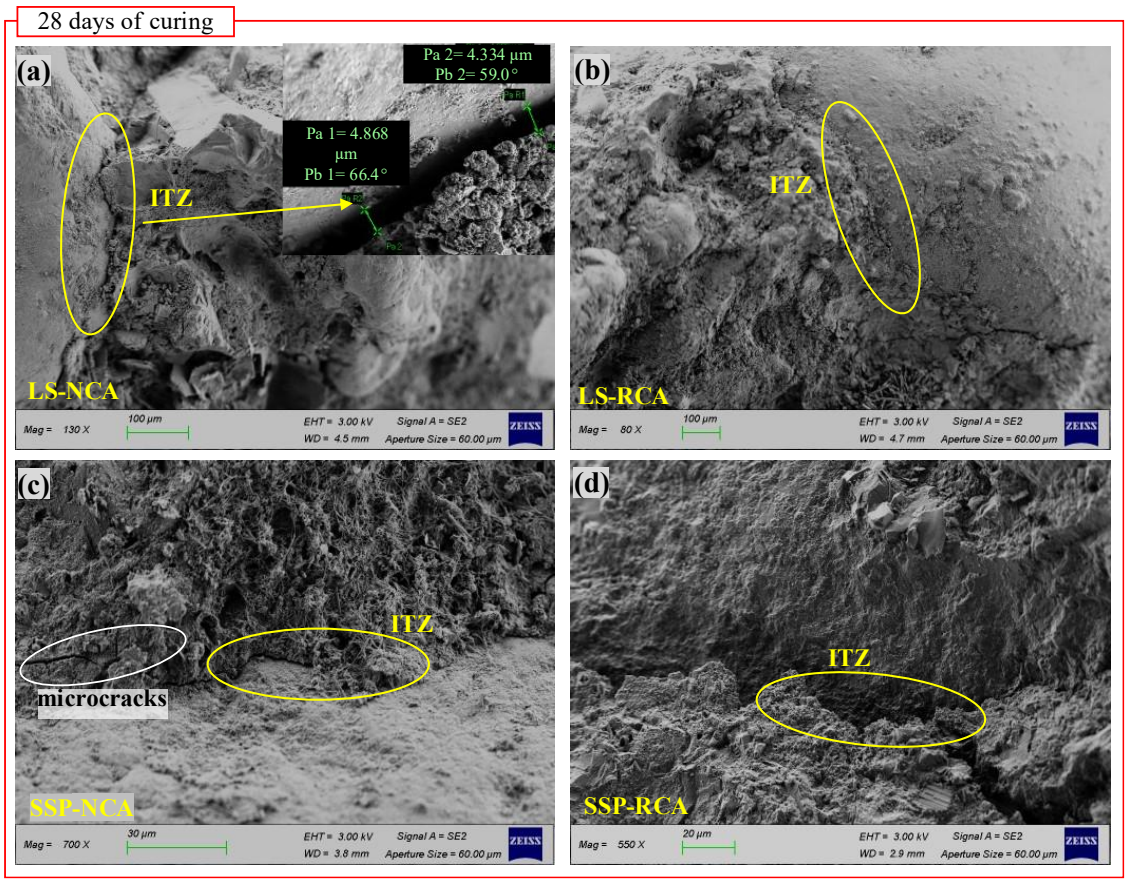

Figure III-19: SEM images on top of ITZ of (a-b) LS-based specimens and (c-d) SSP-based specimens after 28 days of curing.

After 90 days of curing (Figure III-20), the ITZ in LS-NCA appears thicker in the observed area, with further crystal development in the adjacent matrix (Figure III-20a). In SSP-NCA, the ITZ appears thinner, approximately 2 µm in width, with persistent microcracks in the surrounding matrix (Figure III-20c). For RCA-based specimens, although visualizing the ITZ remains challenging, LS-RCA shows a more porous matrix than its NCA counterpart, but with smaller pores than SSP-NCA (Figure III-20b). The matrix microstructure in the latter exhibits larger pores and microcracks (Figure III-20d).

Although some difficulties were encountered while capturing the SEM images, particularly in identifying the ITZ in RCA-based specimens, the observations indicate that NCA-based mixes generally develop a more compact ITZ over time. LS-NCA exhibits a thicker ITZ with uniformly developed crystals, whereas SSP-NCA shows a thinner ITZ with microcracks. RCA-based mixes are more porous and irregular, and the two ITZs are not always clearly distinguishable.

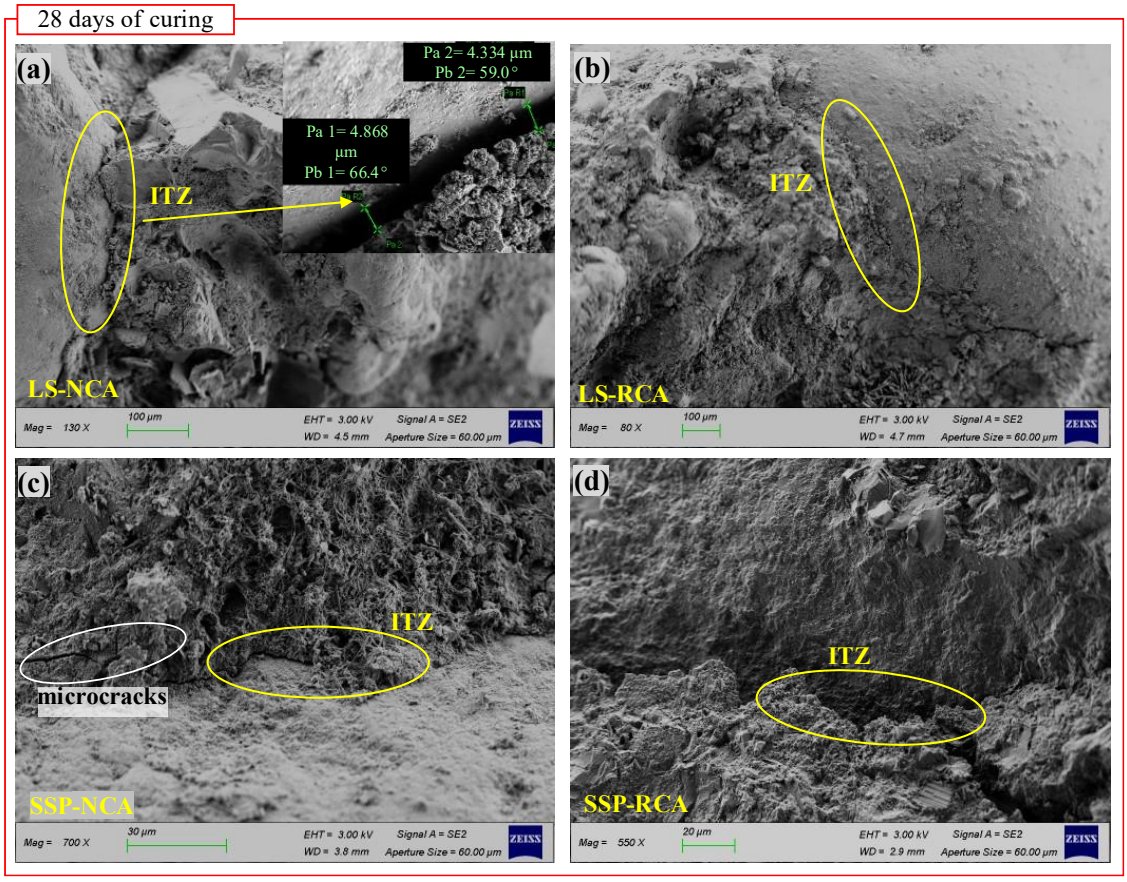

Figure III-20: SEM images on top of ITZ of (a-b) LS-based specimens and (c-d) SSP-based specimens after 28 days of curing.

Beyond the above differences, the measured ITZ thickness (approximately 5 µm in LS-NCA, and around 2 µm in SSP-NCA at 90 days) is significantly lower than that typically observed in normal concrete, where ITZ thickness ranges from 9 µm to 51 µm [364,365]. This reduction may be attributed to the absence of vibration during SCC casting, which limits water accumulation around the aggregates and, consequently, decreases ITZ thickness [366].

5.3.2 Mortar matrix evolution

The tracking of mortar matrix evolution was carried out through the identification of hydration products, which was guided by the morphological characteristics reported in previous studies [367–369].

After 1 day of curing, the mortar matrix in LS-NCA shows early formation of hydration products, with fibrillar C-S-H intercalated with other hydrates, contributing to an already relatively dense matrix (Figure III-21a). In SSP-NCA, fibrillar C-S-H is also observed, along with visible Hc phases, but small pores and microcracks are present (Figure III-21c).

In RCA-based mixes, hydration is less uniform. In LS-RCA, C-S-H exhibits a foil-like morphology, commonly associated with matrices containing high SCM content, along with pores and microcracks (Figure III-21b). In SSP-RCA, the mortar matrix shows poorly developed hydration products, with a noticeable presence of anhydrous cement grains (Figure III-21d).

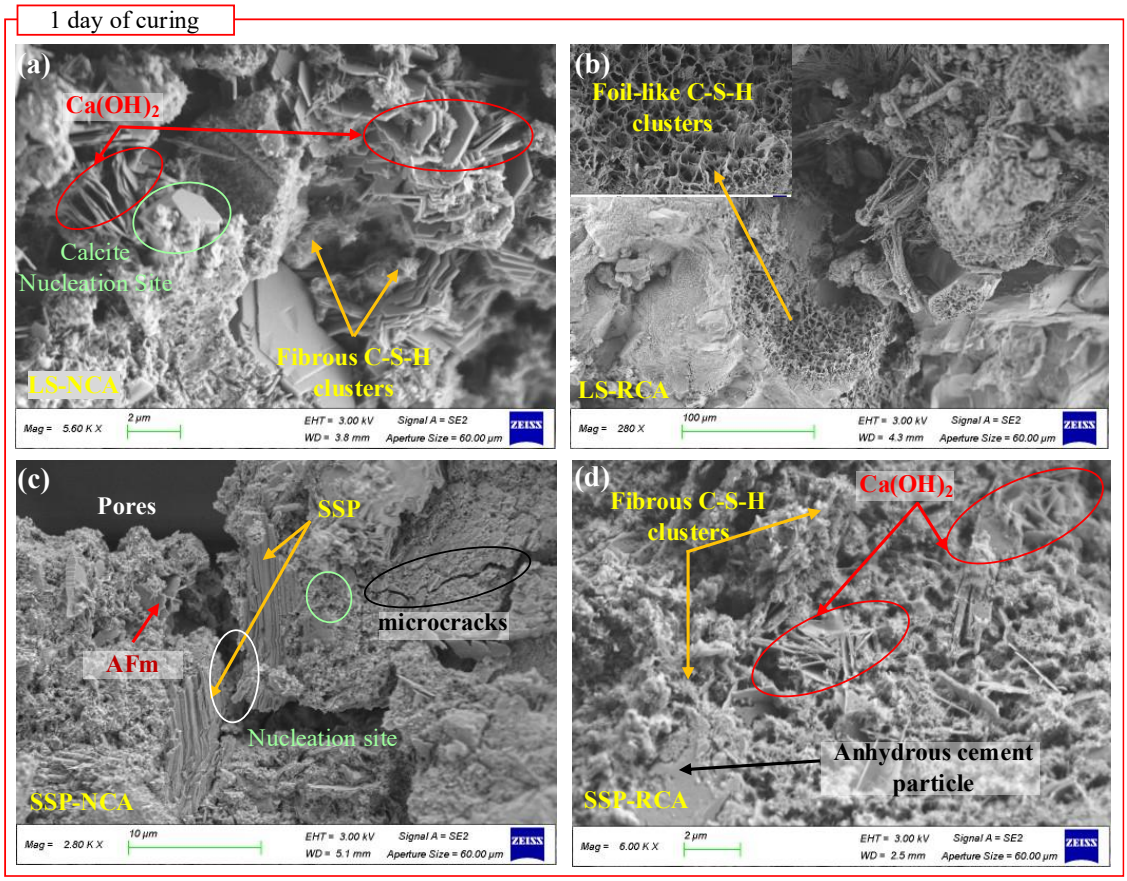

Figure III-21: SEM images of the mortar matrix evolution of (a-b) LS-based specimens and (c-d) SSP-based specimens after 1 day of curing.

After 28 days of curing, the mortar matrix in LS-NCA, LS-RCA, and SSP-RCA does not reveal substantial differences, although a slight difference in densification is observed, with LS-NCA appearing denser (Figure III-22a, b, and d). Notably, in SSP-NCA (Figure III-22c), ettringite growth appears irregular, randomly distributed, and interspersed among other hydration products. Such development may indicate delayed ettringite formation, potentially leading to expansion and, consequently, microcracking within the matrix.

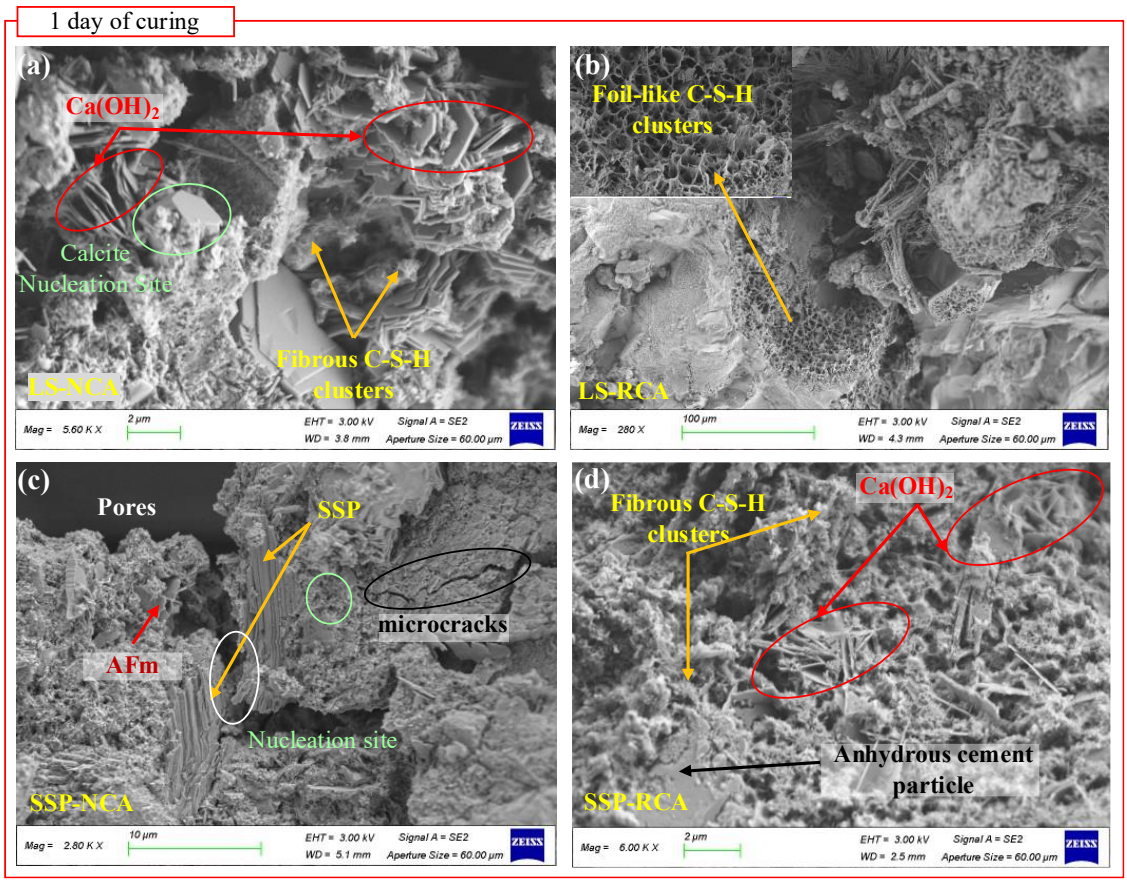

Figure III-22: SEM images of the mortar matrix evolution of (a-b) LS-based specimens and (c-d) SSP-based specimens after 1 day of curing.

Overall, SEM observations of the mortar matrix indicate that NCA-based specimens develop denser, well-structured C-S-H and uniform ettringite. On the other hand, SSP-based specimens show poorly hydrated C-S-H, irregular ettringite, and persistent pores. This further explains their lower compressive strength.

5.4 Pore structure analysis: MIP testing

The results of mercury intrusion porosimetry (MIP) analyses at curing times of 1, 7, and 28 days (Table III-3) reveal a consistent reduction in total porosity across all SCC mixtures with increasing curing time.

After 1 day, the LS-based specimens exhibit a less porous microstructure than the SSP-based specimens, with LS-NCA showing the lowest porosity overall. As curing progresses, total porosity continues to decrease in all specimens. By 28 days, the LS-based specimens display a more pronounced refinement of the pore system, whereas in the SSP-based specimens, the reduction in porosity appears to slow down. It is worth noting that these results are considerably lower than those obtained by water-

accessible porosity § 4.3, with the largest differences observed in the LS-based specimens. We assume that this difference is linked to their lower rheological stability. This might result in more connected capillary pores at the macro-scale, which remain accessible to water but not to mercury during intrusion.

Table III-3: Total porosity of the SCC mix specimens.

SCC mix	1 day	7 days	28 days
LS-NCA	12.04	8.83	5.07
LS-RCA	13.07	11.85	8.90
SSP-NCA	15.21	9.06	7.70
SSP-RCA	16.34	10.41	9.77

A closer examination of the pore network structure in the specimens (Figure III-23) reveals key differences. After 1 day (Figure III-23a), among the NCA-based specimens, LS-NCA's pore network structure is characterized by a sharp, well-defined intrusion peak at 32 nm. In contrast, SSP-NCA specimens exhibit a more varied network with a broader peak at the same diameter, indicating increased heterogeneity. RCA-based specimens show a different pore structure: LS-RCA displays a network dominated by larger pores, approximately 226 nm in size, with a sharp intrusion peak, while SSP-RCA features a dominant peak at 26 nm, accompanied by a secondary one near 180 nm, indicating a more continuous and interconnected system spanning both fine and coarse pores. These findings indicate a clear divergence in early-age pore structure between LS and SSP, particularly when combined with RCA.

After 7 days of curing (Figure III-23b), all specimens exhibit a more refined pore structure due to the progressive formation of hydrates, as their dominant peaks shift toward smaller diameters compared to 1 day. In LS-NCA, the peak shifts from 32 nm to 26 nm, with a decrease in intensity. SSP-NCA also shifts to 26 nm but forms a broader, lower-intensity peak, reflecting increased heterogeneity. In LS-RCA, the dominant peak shifts from 226 nm to 26 nm, overlapping with a secondary feature near 77 nm, reflecting a network composed of both fine and coarser pores. SSP-RCA shows the greatest refinement, shifting further to 21 nm with a narrow, high-intensity peak.

The trend toward refinement continues across all mixes until 28 days (Figure III-23c), with a continuous shift of the dominant intrusion peak. In LS-NCA, the peak shifts from 26 nm to 21 nm with remarkably low intensity. SSP-NCA shifts to 17 nm with slightly lower intensity. LS-RCA shows a sharper, well-defined peak at 21 nm. Finally, SSP-RCA shifts further to 13 nm, where the dominant intrusion peak becomes more intense.

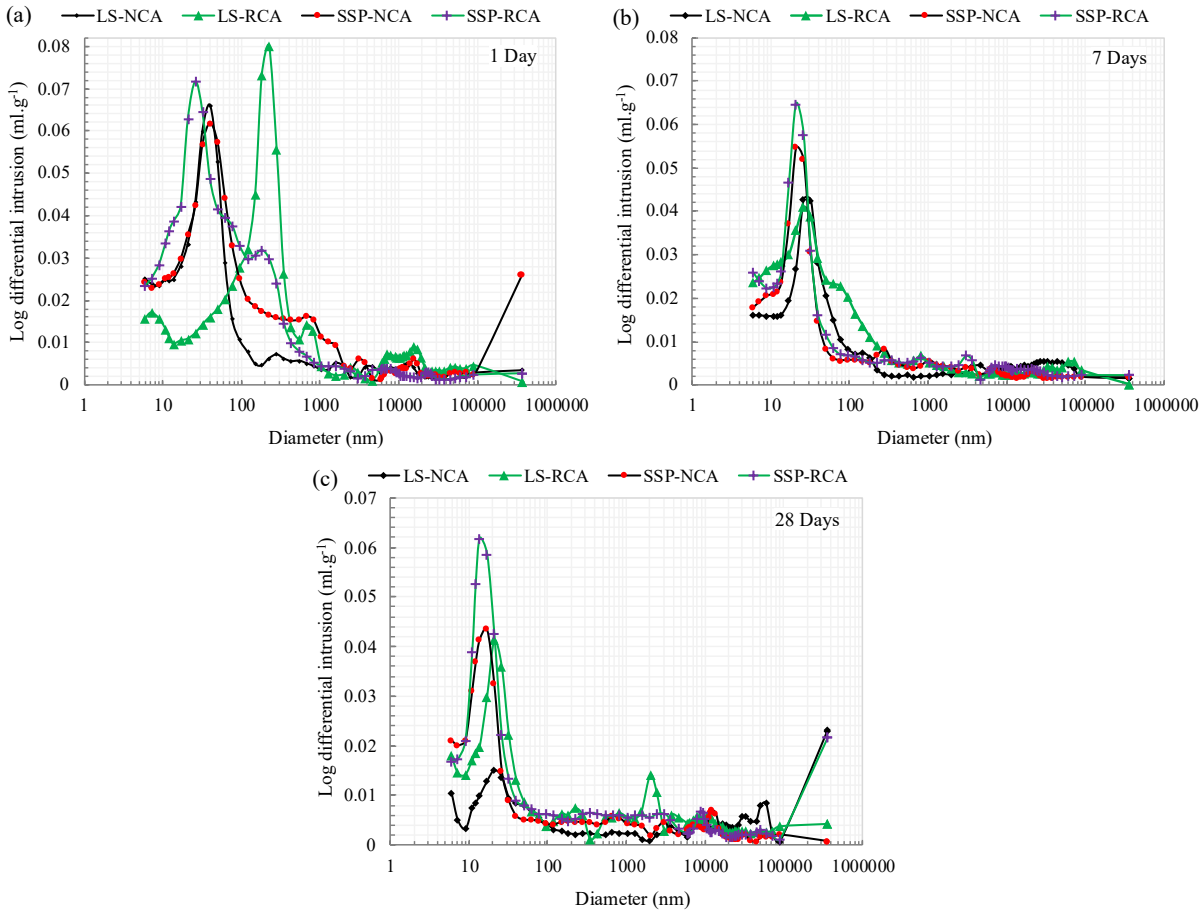

Figure III-23: Pore network structure of SCC specimens after (a) 1 day, (b) 28 days, and (c) 90 days of curing.

Overall, the results indicate a progressive refinement of the pore network across all mixes, with LS-based concretes developing denser structures, while SSP-based mixes retain higher heterogeneity and porosity. This evolution is consistent with the compressive strength observed at 28 days.

MIP testing also provides pore categories proportion dominating the pore network structure of the SCC specimens. As mentioned earlier (Chapter I3.7.2), the concrete pore system comprises four categories according to the pore diameter and their potential impact on performance: harmless (<20 nm), less harmful (20–50 nm), harmful (50–200 nm), and more harmful (>200 nm) [370].

Considering these general considerations, the pore size distribution after a day of curing (Figure III-24a) indicates the pore system of LS-NCA comprises approximately 60% of pores with diameters larger than 200 nm, in contrast to 20% in LS-RCA, 46% in SSP-NCA, and 53% in SSP-RCA. Notably, LS-based specimens exhibit a higher proportion of pore sizes smaller than 20 nm. Within this pore size range, pores of 0.5–10 nm are occupied with C-S-H [265], indicating a better early hydration of these specimens.

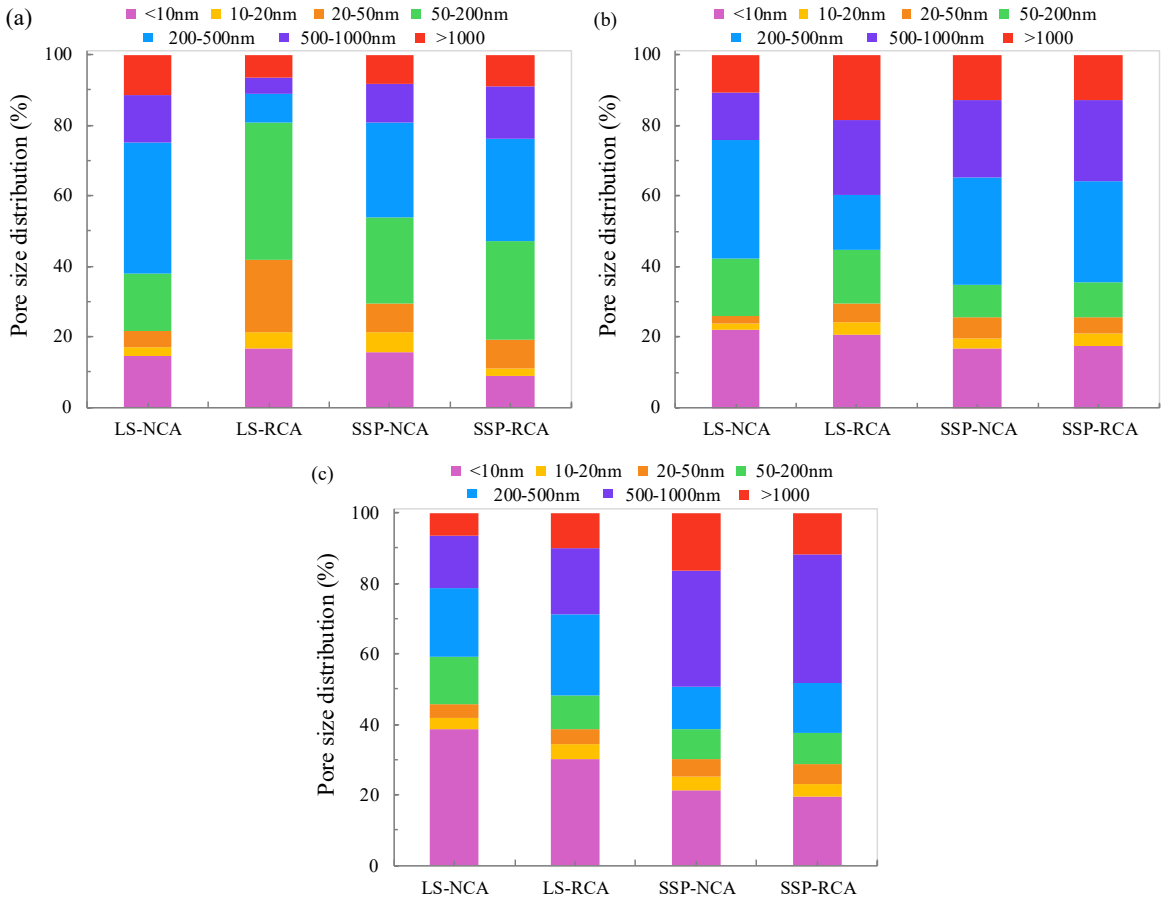

Figure III-24: Pore size distribution of SCC specimens after (a) 1 day, (b) 7 days, and (c) 28 days of curing.

After 7 days of curing (Figure III-24b), the gel pore diameter (<10 nm, shown in pink) increases across all specimens, with a slightly higher proportion in LS-based specimens compared to their SSP-based counterparts. Notably, in LS-NCA, the main change in pore size distribution occurs in pores smaller than 50 nm, whereas in the other specimens, the main changes remain in pores larger than 500 nm, resulting in a coarser structure with an increased proportion of large pores. The limited improvement in pores larger than 200 nm in LS-NCA specimens can explain their slightly lower compressive strength compared to their SSP-NCA counterparts. Particularly when pores with a diameter below 20 nm are directly responsible for creep and shrinkage, rather than being harmful to concrete strength [370].

This trend continues at 28 days (Figure III-24c), where a more pronounced refinement in the pore structure is observed in LS-NCA and LS-RCA mixes, characterized by a significant increase in harmless pores and a corresponding decrease in harmful pores, consistent with previously observed trends [359]. This observation suggests a more refined pore structure in these mixes, attributed to

enhanced hydration kinetics. In contrast, SSP-NCA and SSP-RCA exhibit a notable development of harmful pores (> 500 nm) at 28 days, a phenomenon previously reported in the literature [371],

It was not surprising that the pore system of SSP-based specimens coarsens over time, as previously indicated by their higher water absorption, lower bulk density, and SEM images. This evolution is likely due to the presence of the organic matrix in the SSP precursor, which both traps air through proteins and perturbs the growth of hydration products. The resulting perturbation can increase internal stress and lead to expansion due to the delayed formation of hydrates [110,128,129].

6 Synthesis

This chapter investigated the effects of binder and aggregate type on hydration kinetics, the fresh and hardened properties over 90 days of standard curing. Data analysis has allowed us to draw the following key conclusions:

- **Rheological properties**: Evaluating the fresh properties of the four SCC mixes reveals distinct behaviors between SSP and LS. SSP proves to be more beneficial for the rheological properties of SCC in terms of segregation resistance and plastic viscosity, despite a slight reduction in slump flow. Regarding the use of RCA, its high absorption capacity, although not favorable for long-term workability retention, resulted in slump flow values comparable to those of NCA during the first 15 min, due to the drying and water compensation. Nevertheless, RCA enhanced SCC cohesion, reduced bleeding, and improved resistance to both static and dynamic segregation.
- **Hydration kinetics:** The semi-adiabatic calorimetry results revealed a delayed onset of hydration in the LS-NCA mix during the initial stage, but the other mixes exhibited similar hydration kinetics.
- **Compressive strength:** The incorporation of RCA resulted in moderate reductions in strength of approximately 8% (for LS-RCA) and 11% (for SSP-RCA), respectively, compared to mixtures containing NCA. SSP specimens demonstrated higher compressive strength development at mid ages, but this trend reversed beyond 28 days, with a slight reduction in strength at 90 days. These trends were observed in water accessibility and bulk density and are potentially due to the organic content of natural biominerals of the SSP, which interfered with hydration reactions and consequently affected pore distribution.
- **Microstructure properties:** The MIP results at 28 days revealed that the pore system of SSP mixes developed a higher proportion of harmful pores (> 500nm) than LS mixes, explaining the differences in the measured compressive strength. The pore refinement of each mix correlates with hydrate formation, as evidenced by TGA results, and with microstructural development

observed by SEM. XRD analysis indicates moderate chemical reactivity for both SSP and LS, but the data are insufficient to ascertain which precursor exhibits greater reactivity.

These findings underscore a critical factor that may significantly influence the CO_2 uptake of SCC, either by enhancing or inhibiting the process, primarily through alterations in hydration kinetics or the rheological behavior of the mixes. Furthermore, our results support the use of SSP and RCA as sustainable alternatives to LS and NCA, providing valuable insights into their effects on both the fresh and hardened properties of SCC to ensure consistent and reliable performance. They also emphasize the importance of further research on their long-term performance, particularly the slight decline observed in SSP-based mixes

This concludes the current chapter and sets the stage for the next Chapter IV, which focuses on analyzing the CO_2 uptake capacity of the four SCC mixtures and estimating the CO_2 stored within the matrix of each SCC, advancing more environmentally friendly concrete solutions

Chapter IV

Analysis and quantification of CO_2 uptake

1 Introduction

This chapter provides an analysis of the CO_2 uptake capacity of the four SCC mixes subjected to carbonation curing. The primary goal is to evaluate the potential of the considered mixes to permanently store the absorbed CO_2 by examining both the carbonation depth and the amount of $CaCO_3$ precipitated within their matrix.

The assessment begins with an evaluation of the remaining water content during the pre-conditioning step of the carbonation curing protocol, specifically tailored for this study. Accordingly, the residual water content during the drying step of each SCC is measured to establish baseline internal moisture profiles.

Afterwards, CO_2 diffusion within the mixes is assessed by measuring carbonation depth and the carbonated surface area. These measurements indicate the progression of the carbonation front and help determine whether the observed depth truly reflects the extent of the reaction zone or the actual amount of CO_2 stored. To complement this, the chapter also quantifies the CO_2 absorbed and retained within each SCC mix using TGA, mass loss, and XRD.

2 Pre-conditioning step monitoring

The water content remaining in the SCC specimens at a measurement point reflects their behavior during the drying step, particularly at 60 °C (Figure IV-1). The initial water content values before the pre-conditioning step divide the SCC specimens into two groups. The first group includes the NCA-based specimens with the lowest initial water content values. The second group consists of RCA-based specimens, showing the highest initial water content.

For the NCA-based specimens, LS-NCA (Figure IV-1a) and SSP-NCA (Figure IV-1b) initially (in-mold) exhibit similar water contents of 8.80 ± 0.01% and 8.83 ± 0.01%, respectively. During drying, the water content sharply decreases across all specimens between 7 and 10 h, followed by a gradual slowdown. At 24 h, LS-NCA reaches a water content of 2.2 ± 0.1%, which is not only lower than that of SSP-NCA (3.0 ± 0.2%) but also the lowest residual water content among all four specimens.

The finer particle size distribution of SSP, together with the hydrophilic nature of its organic constituents, increases the retention of both physically and chemically bound water, thereby reducing the fraction of free water available for evaporation. In contrast, the water content in LS-NCA is influenced by the distinct properties of LS compared to SSP, as well as the relatively higher instability (higher bleeding) of the fresh mix, which increases the free water available for evaporation, resulting in the lowest residual water content.

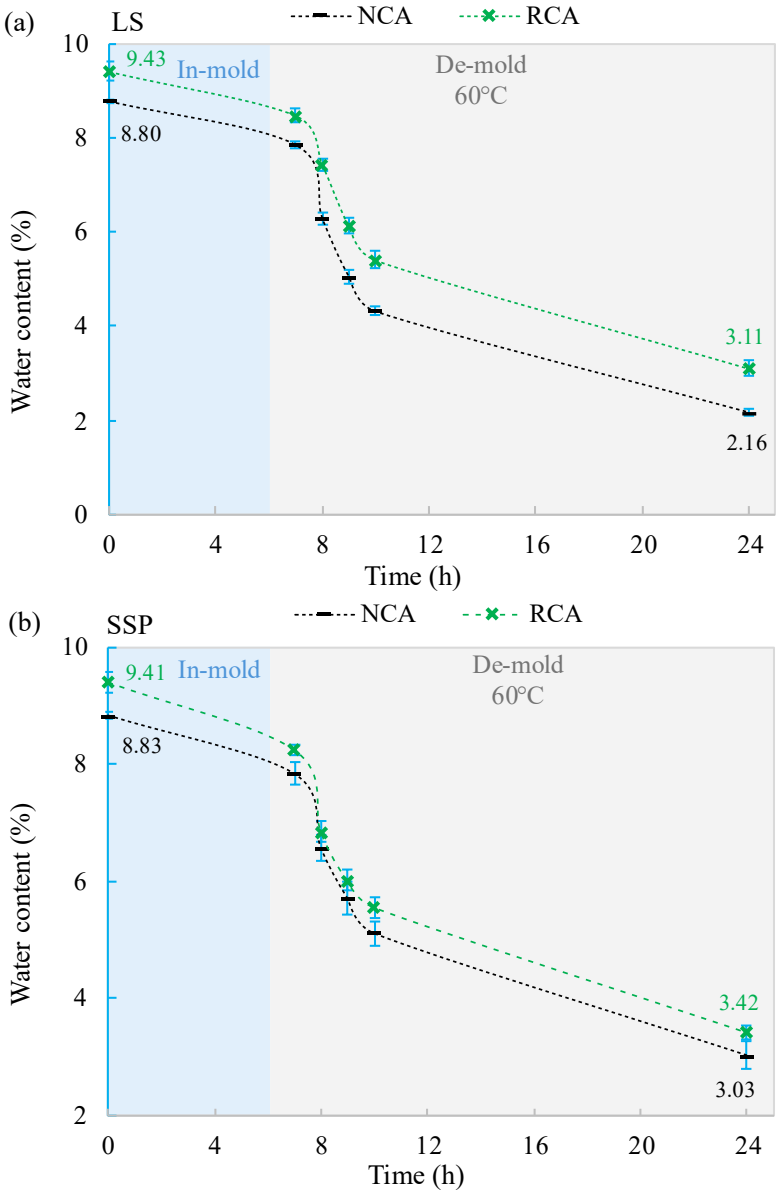

Figure IV-1: Internal water content evolution during the pre-conditioning step: (a) LS-based and (b) SSP-based specimens.

For RCA-based specimens, LS-RCA (Figure IV-1a) and SSP-RCA (Figure IV-1b) both initially (in-mold) exhibit similar water contents of 9.43 ± 0.01% and 9.41 ± 0.02%, respectively. During drying, their water decreases gradually, ultimately reaching comparable final values of 3.11 ± 0.02% and 3.42 ± 0.01% at 24 h, following the same trend observed in NCA-based specimens, albeit with slightly higher residual water content.

The differences observed between RCA- and NCA-based specimens concerning water retention are primarily linked to the characteristics of the coarse aggregates. The porous surface of RCA, as previously noted, enables specimens to retain more water, both as free water within the pores and as

bound water in the old mortar, which is harder to remove during drying. In comparison, NCA are denser and less porous, resulting in lower water retention.

Overall, the drying behavior of SCC specimens is mainly influenced by aggregate porosity and the cement's precursors (LS or SSP). Therefore, the initial water content before carbonation curing of the specimens in increasing order is: 2.2 ± 0.1% (LS-NCA) < 3.0 ± 0.2% (SSP-NCA) < 3.11 ± 0.02% (SSP-RCA) < 3.42 ± 0.02% (LS-RCA).

3 Carbonation depth assessment: phenolphthalein spray test

3.1 Carbonation depth under one-dimensional diffusion (Digital caliper)

- **Early carbonation (1-7 days)**

In Figure IV-2, the progression of carbonation depth in SCC specimens is illustrated as a function of the square root of time, with measurements taken over curing ages. In all specimens, the carbonation depth increases over time following similar non-linear kinetics, deviating from the classical solid-state diffusion $\sqrt{t}$-low (Fickian diffusion) [188].

A comparison between specimens shows that, after 1 day, LS-NCA specimens (Figure IV-2a) exhibit moderately higher carbonation depths (17.36 ± 0.09 mm) than SSP-NCA specimens (14.75 ± 0.60 mm) (Figure IV-2b). Both NCA-based specimens display greater carbonation depths than their RCA-based counterparts. Meanwhile, the LS-RCA and SSP-RCA specimens exhibit similar depths of 14.75 ± 0.52 mm and 13.75 ± 1.24 mm, respectively.

After 7 days, the difference between LS-NCA and SSP-NCA specimens becomes more pronounced, with LS-NCA exhibiting a greater carbonation depth of 33.50 ± 1.48 mm (compared to 25.97 ± 1.65 mm for SSP-NCA). Meanwhile, the carbonation depths of LS-RCA (Figure IV-2a) and SSP-RCA (Figure IV-2b) specimens remain lower than those of their NCA counterparts, 23.24 ± 0.32 mm and 21.29 ± 0.94 mm, respectively.

To understand these observations, it is important to note that it is well established that, at an early age (particularly pronounced at 1 day), carbonation is a diffusion-controlled process, meaning that CO_2 diffusion is primarily governed by how easily it can move through the specimen's pore network [372]. Porosity, in turn, depends on the cement precursor (SSP or LS), the characteristics of the coarse aggregates, and the internal water content.

Regarding the cement precursor, as previously shown (Chapter III5.4), SSP generates more pores in the specimen's matrix compared to LS. However, despite this higher porosity, SSP-based specimens exhibit lower carbonation depths, as one can see from the t = 0 values of the 2nd order

polynomial fits (Figure IV-2a). This suggests that the influence of cement's precursor porosity is less significant than that of the capillary pores available after the pre-conditioning step. The higher water retention of SSP leads to greater pore saturation, which restricts CO_2 diffusion and limits early carbonation. Therefore, the connectivity and saturation state of the pores are more relevant to carbonation than total porosity alone.

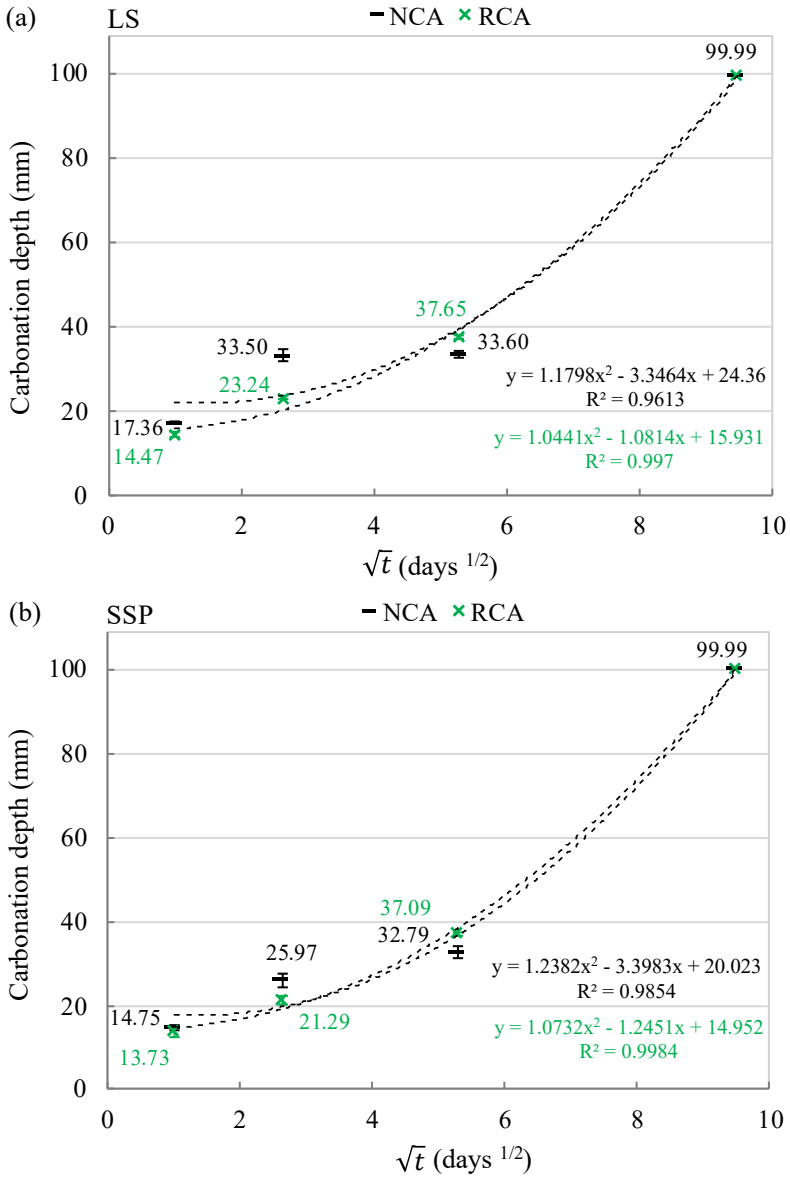

Figure IV-2: One-dimensional carbonation depth of (a) LS-based and (b) SSP-based specimens over time.

The strong correlation between initial water content and the early carbonation (Figure IV-3) supports the above assumption. The highest carbonation depths were observed in specimens with the lowest internal water, with carbonation depth decreasing as water content increased. This trend reflects the drying behavior of the specimens: those with more water retained less accessible pore space for CO_2

diffusion, resulting in lower carbonation depths, while those with lower water content had more available pore space and sufficient moisture to transport the dissolved CO_2, leading to higher carbonation depths.

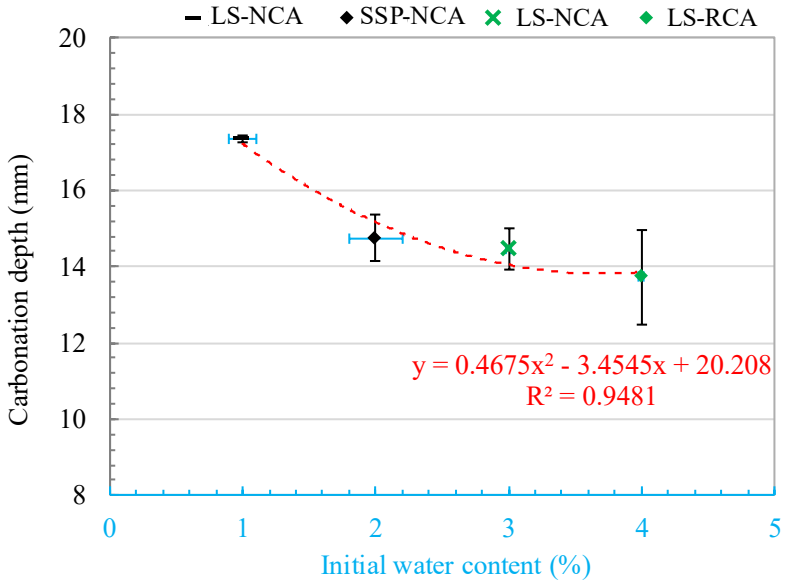

Figure IV-3: Relationship between carbonation depth and the water content of the specimens before carbonation curing.

Furthermore, the intrinsic characteristics of RCA do not appear to promote CO_2 diffusion, at least during the early stages of carbonation curing. According to Mi *et al.* [373], CO_2 diffuses through five kinds of typical diffusion paths within RCA concrete, including natural mortar (NM), old mortar (OM), original aggregate (OA)-NM-ITZ, OA-OM ITZ, and NM-OM ITZ. The complexity and heterogeneity of these diffusion paths may slow down the early progression of carbonation into the deeper layers of the concrete.

In summary, early-age CO_2 diffusion, indicated by the carbonation front, is strongly influenced by specimen water content and, to a lesser extent, by coarse aggregate characteristics. This front is stable for some days, with no major differences between specimens.

- **Later-age carbonation (28-90 days)**

After 28 days, carbonation depth increases across all specimens, with LS-NCA (Figure IV-2a) and SSP-NCA (Figure IV-2b) ultimately reaching comparable values. However, the evolution of carbonation depth between 7 and 28 days reveals distinct behaviors.

In LS-NCA specimens (Figure IV-2a), the carbonation front at 7 days was well-defined at 33.50 ± 1.48 mm as mentioned above, with an intermediate zone of about 1 mm containing uncarbonated spots across the section. This suggests that carbonation advances rapidly during the initial stage but is not

fully complete within this intermediate zone. As a result, carbonation, particularly within these specimens, remains concentrated in this zone rather than progressing deeper (Figure IV-5, 7 days), reflecting saturation or stagnation in overall depth until the 28th day. On the other hand, SSP-NCA specimens (Figure IV-2b) exhibit a continuous increase in depth, indicating progressive carbonation throughout the curing period. The carbonation front eventually reaches the center of both specimens by 90 days.

Regarding RCA-based specimens, the carbonation depth in LS-RCA and SSP-RCA specimens (Figure IV-2a and b) reaches similar values, which are moderately higher than their NCA counterparts at 28 days, which may be attributed to the higher porosity of RCA. By 90 days, these specimens are also fully carbonated.

These observations indicate that, at early ages, CO_2 diffusion is initially dominated by the mix design porosity, through which CO_2 diffuses, and the water content, where the CO_2 dissolves and transports, before becoming diffusion-controlled by the coexisting carbonation and hydration reactions and the microstructural changes they induce [257,258]. These factors will be discussed further in the following section. While these findings describe how carbonation depths evolve within each SCC specimen, it is also important to examine how carbonation spreads across all specimen surfaces.

3.2 Carbonation Depth under Generalized Conditions

3.2.1 Measurements using a digital caliper

Exposing all surfaces of the specimens to carbonation provides an overall view of how carbonation progresses within the material and allows for the evaluation of its influence on the specimens' overall properties, as will be addressed in the next chapter.

When the entire specimens are subjected to generalized carbonation, two additional outcomes emerge. In SSP-based and LS-RCA specimens, carbonation progresses heterogeneously over time across all specimen surfaces (Figure IV-4a and b). LS-NCA specimens (Figure IV-4a) represent a particular case, exhibiting higher carbonation depths at 7 days, consistent with one-dimensional exposure due to the presence of the previously noted intermediate, partially carbonated zone. These observations are based on carbonation depths measured under generalized exposure, calculated as an average of 20 points across all exposed surfaces, which are lower than those measured under one-dimensional carbonation. This difference arises from non-uniform development across different surfaces, caused by variations in surface porosity, local moisture content, aggregate distribution, and microcracks formed during demolding. Consequently, leading to a heterogeneous distribution of CO_2, with the greatest heterogeneity observed in LS-NCA specimens, particularly at early ages, and in LS-RCA at 28 days (Table IV-1).

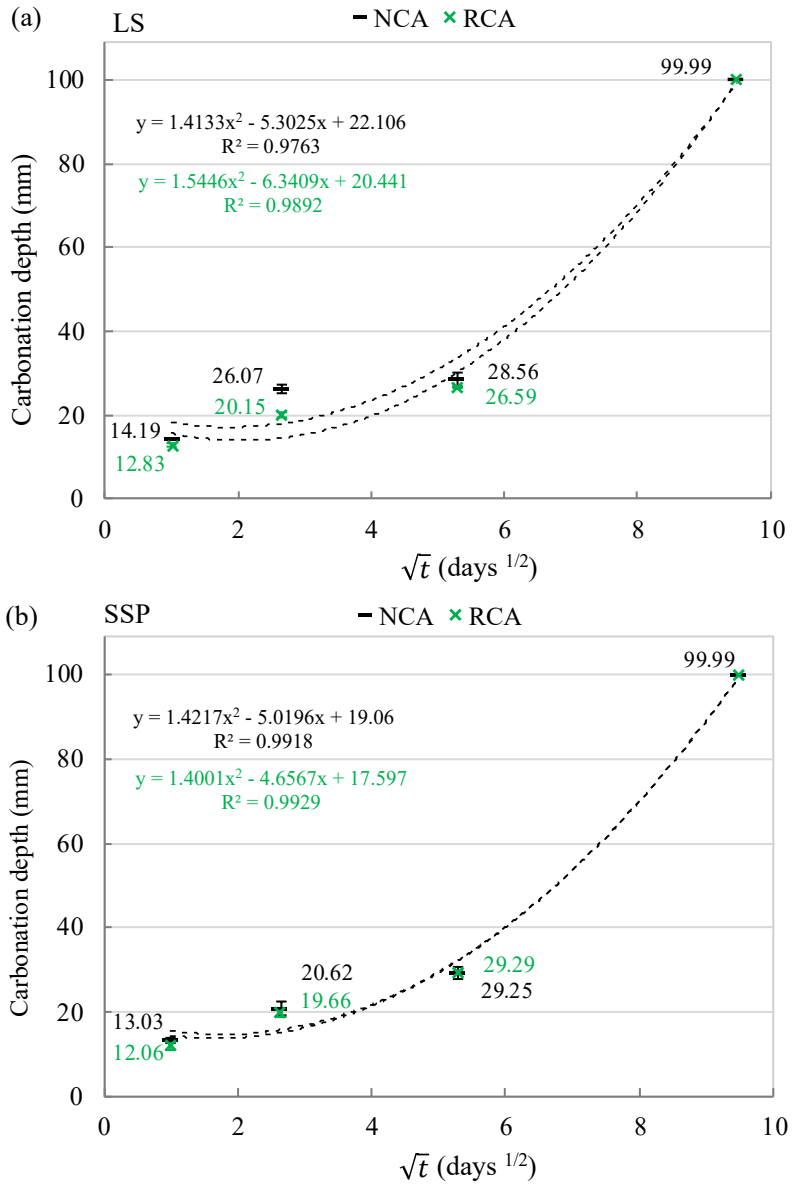

Figure IV-4: Generalized carbonation depth of (a) LS-based and (b) SSP-based specimens over time.

Table IV-1: Relative reduction (%) of carbonation depths under generalized carbonation compared to one-dimensional carbonation at different ages.

Specimen	1 day	7 days	28 days	90 days
LS-NCA	22 %	29 %	18 %	-
LS-RCA	13 %	15 %	41 %	-
SSP-NCA	5 %	3 %	21 %	-
SSP-RCA	12 %	8 %	21 %	-

3.2.2 Carbonated area using MATLAB-based image analysis

The total carbonated area was calculated using MATLAB-based image analysis, enabling automated segmentation and area computation. Carbonation fronts imaging over time (Figure IV-5) shows that carbonation initially spreads uniformly, roughly following the initial shape of the specimens. Such progression begins with CO_2 diffusion through the tortuous pore networks of the exposed surfaces.

Over time, the carbonation front becomes increasingly heterogeneous, with faster progression at corners and edges. It evolves radially, as the effective diameter of the uncarbonated core gradually decreases until it vanishes, at which point the specimens are fully carbonated.

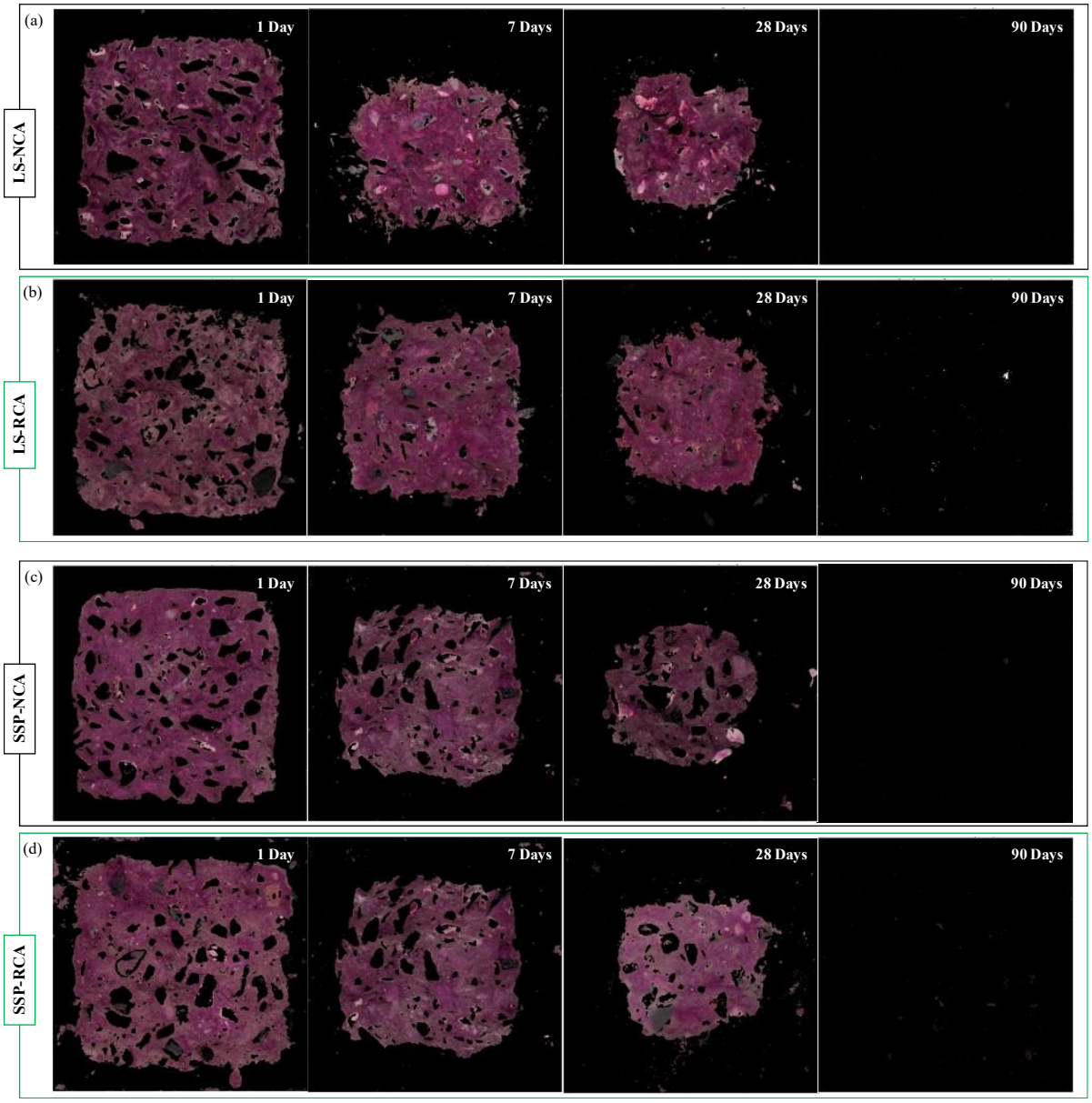

Figure IV-5: Carbonated area development over time as observed through MATLAB image analysis of: (a-b) LS-based and (c-d) SSP-based specimens.

Quantitative analysis using surface integration of Figure IV-5 reveals that the SSP-based specimens exhibit slightly lower carbonated areas than their LS-based counterparts after 1 day of carbonation curing (Figure IV-6a). No notable variation in carbonated area is observed between NCA and RCA-based specimens at this age. These differences become more pronounced after 7 days of curing (Figure IV-6b). Moreover, the LS-NCA specimens exhibit a notably higher carbonated area compared to the others. By 28 days of carbonation curing (Figure IV-6c), all specimens show comparable carbonated areas, with slightly higher values observed in NCA-based specimens. At 90 days (Figure IV-6d), all specimens reached approximately 99% carbonation, broadly supporting the one-dimensional measurements obtained using a digital caliper, despite slight differences.

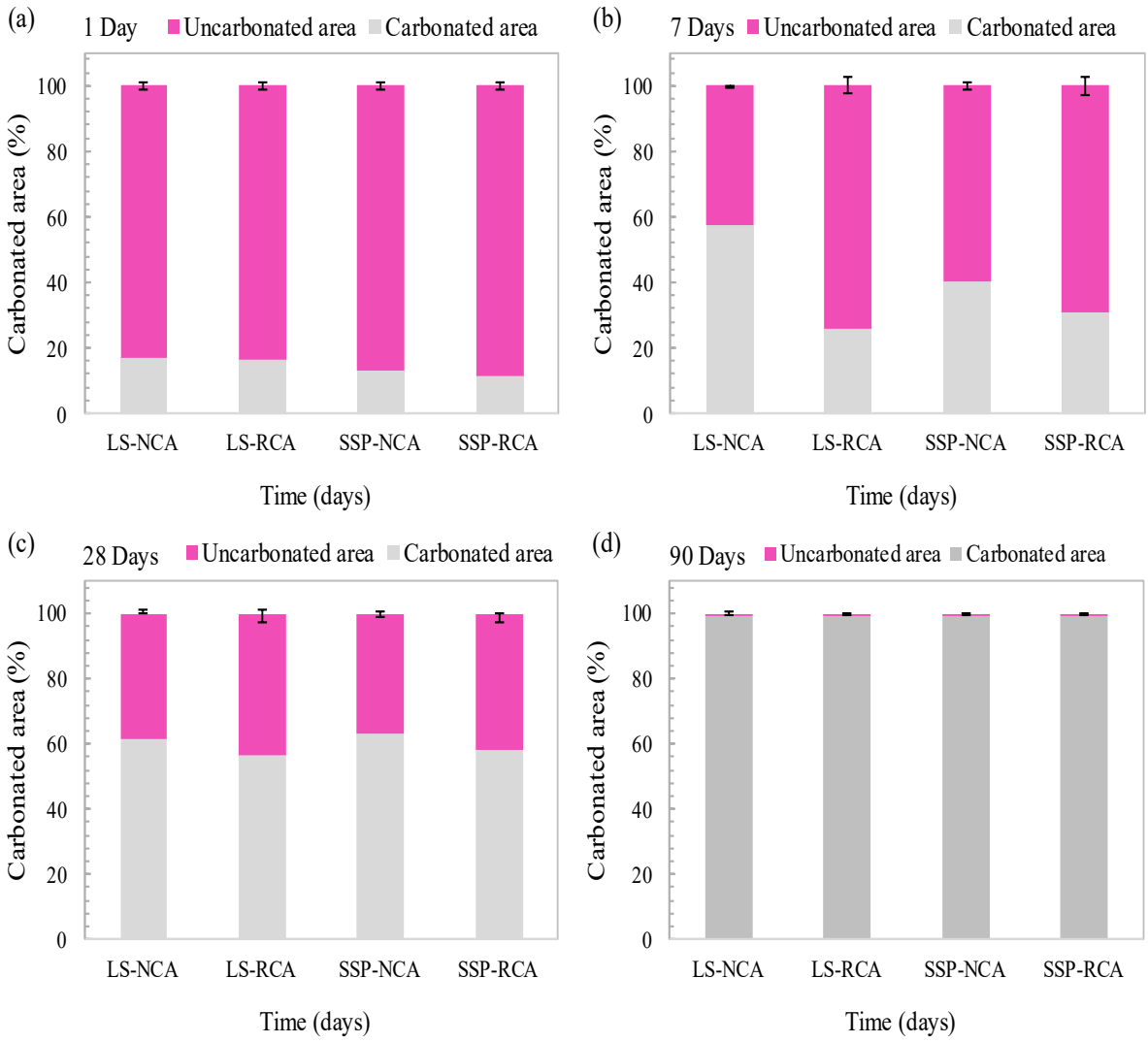

Figure IV-6:Carbonated area results of specimens after (a) 1 day, (b) 7 days, (c) 28 days, and (d) 90 days of carbonation curing, based on MATLAB image analysis.

It should be noted that some inconsistencies were encountered during the measurements. For the digital caliper, readings were straightforward when the carbonation front was a shape-like specimen, but became more difficult when the carbonation front became circular. Similarly, in the MATLAB analysis, some coarse aggregates disturbed the calculations, potentially affecting the accuracy of the carbonated area measurements.

Overall, despite these measurement uncertainties, the combined results from caliper and MATLAB analyses consistently demonstrate a nonlinear CO_2 diffusion across all specimens, with LS-NCA exhibiting faster early diffusion (up to 28 days) and greater heterogeneity. It then appears an intermediate regime, i.e., typically 4-30 days, during which carbonation front development is modulated by the various constituting materials in the specimens, these being smoothed out for longer reaction times, up to complete carbonation. Whether reaction dynamics at intermediate times can influence the material resistance must be characterized.

4 Estimation of CO_2 uptake

4.1 Thermogravimetric analysis

4.1.1 Analysis of TGA/DTG Curves

The TGA/DTG measurements of the carbonated- and sealed-cured specimens were carried out on powdered samples collected from the depths reached by carbonation at each curing age, as determined by the phenolphthalein spray test (§ 3). For consistency, samples from the sealed-cured specimens were extracted at the corresponding depths (Figure IV-7).

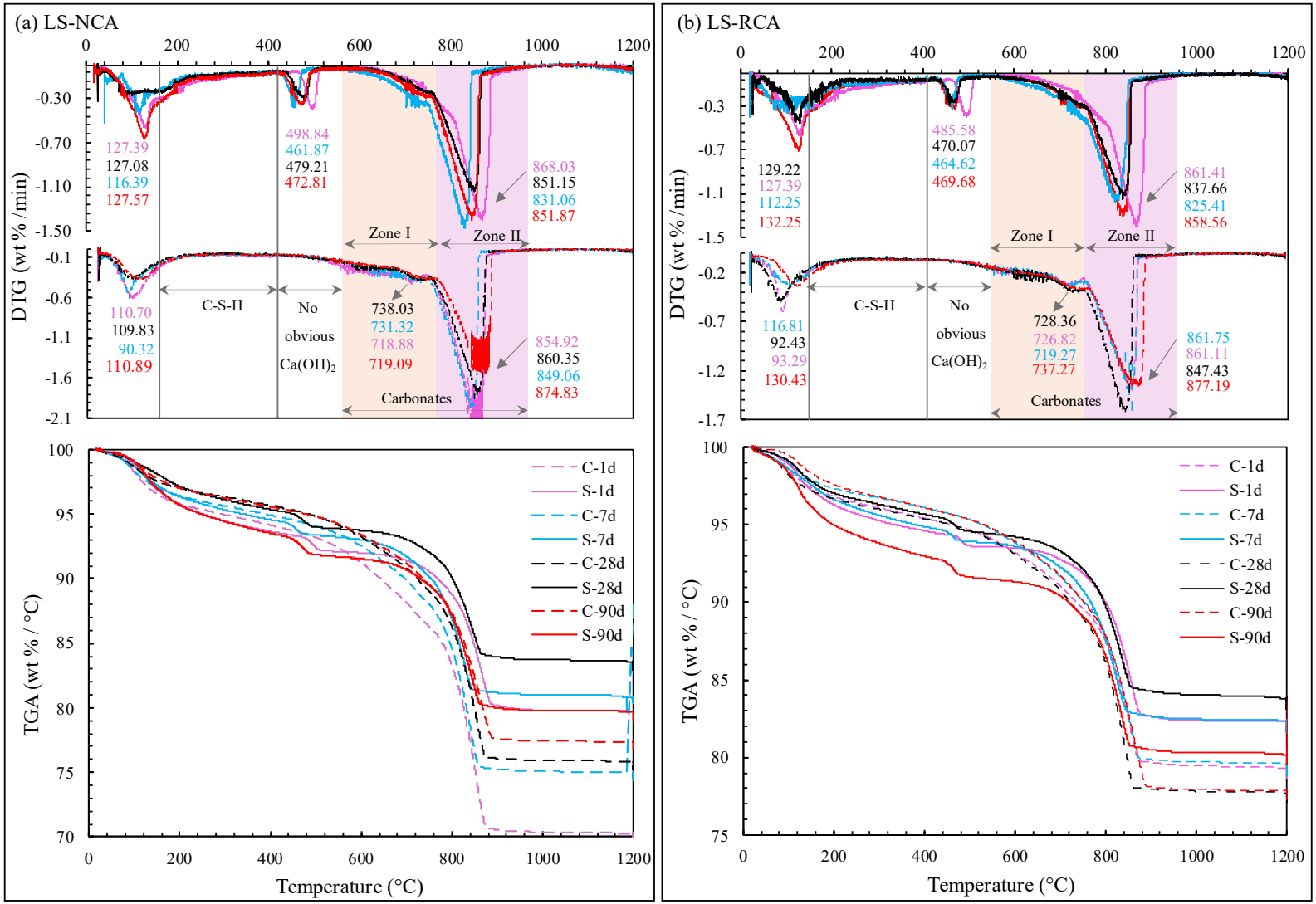
(a) LS-NCA
(b) LS-RCA
DTG (wt %/min)
TGA (wt % / °C)
Temperature (°C)
Zone I
Zone II
C-S-H
No obvious Ca(OH)2
Carbonates
127.39
127.08
116.39
127.57
498.84
461.87
479.21
472.81
868.03
851.15
831.06
851.87
110.70
109.83
90.32
110.89
738.03
731.32
718.88
719.09
854.92
860.35
849.06
874.83
129.22
127.39
112.25
132.25
485.58
470.07
464.62
469.68
861.41
837.66
825.41
858.56
116.81
92.43
93.29
130.43
728.36
726.82
719.27
737.27
861.75
861.11
847.43
877.19
C-1d
S-1d
C-7d
S-7d
C-28d
S-28d
C-90d
S-90d

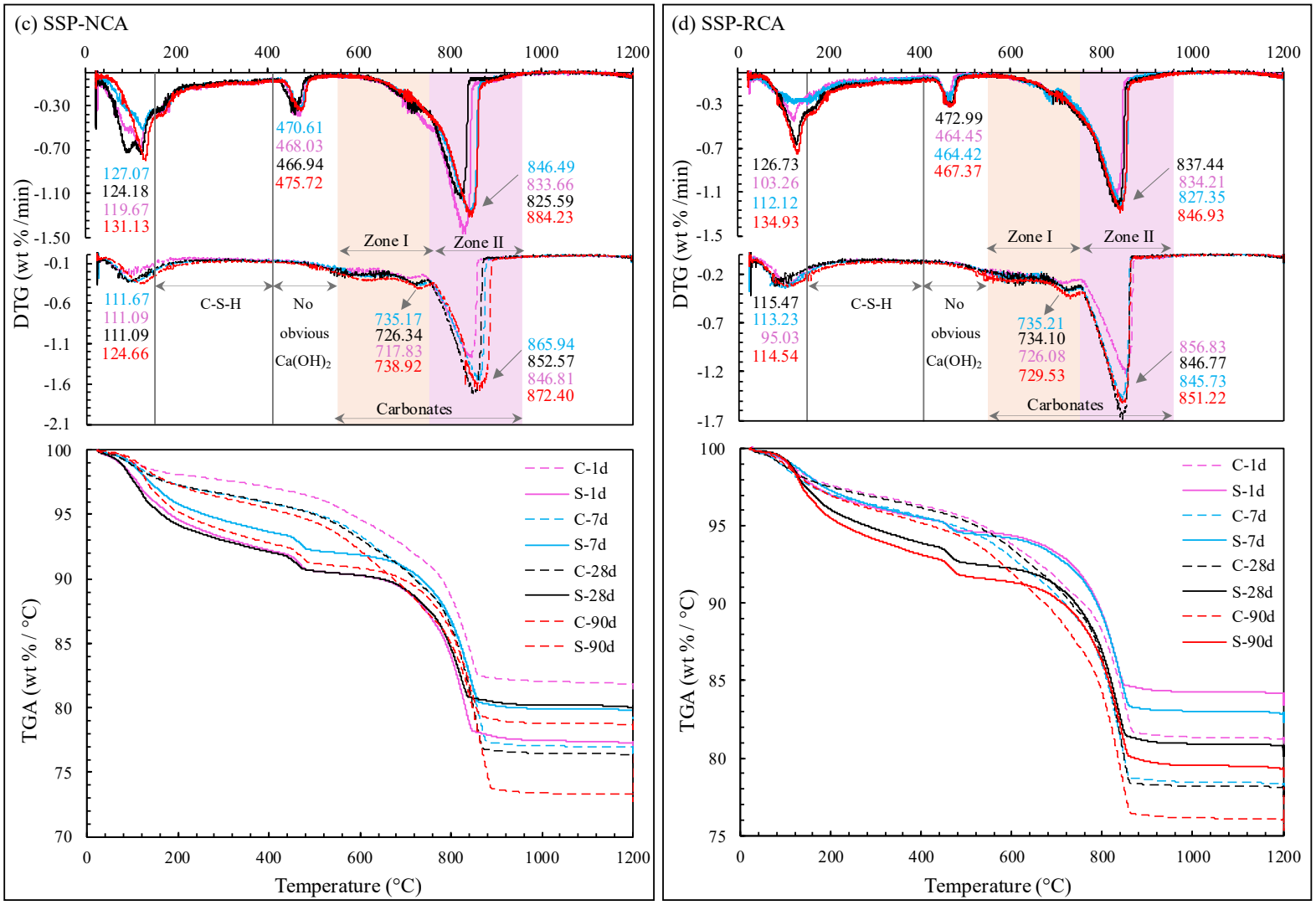

Figure IV-7: TGA/DTG curves of sealed- and carbonation-cured specimens over time: (a, b) LS-based mixes; (c, d) SSP-based mixes.

The analysis of the DTG curves indicates that the peaks around 100 °C for the sealed-cured specimens have the lowest intensity in the LS-based samples, particularly after one day of curing (Figure IV-7a and b), compared to SSP-based samples (Figure IV-7c and d), indicating that the hydration reactions were somewhat inhibited within these specimens. The different hydration rates can be related to the water content remaining within the SCC matrix after the pre-conditioning step, where the SCC specimens exhibited different water content before carbonation [374], as previously described in (§ 2).

Moreover, the DTG peaks around 170 °C, corresponding mainly to the thermal decomposition of the Hc/Mc phase, are slightly more intense in SSP-based samples, particularly from 7 days onward (Figure IV-7c and d), compared to LS-based samples (Figure IV-7a and b). This may indicate a slightly higher reactivity of SSP, although confirmation of this trend would require complementary XRD analysis. In addition, the increase in mass loss observed up to 180 °C in carbonation-cured specimens compared to their sealed-cured counterparts indicates that the carbonation reaction releases physically bound water, thereby promoting hydration. However, it remains challenging to determine whether the additional physical water originates from $Ca(OH)_2$ or C-S-H carbonation using TGA.

The TGA curves further indicate that the mass loss from 150 °C up to 425 °C, attributed to C-S-H dehydration, varies among the carbonation-cured specimens, suggesting that C-S-H carbonation occurs differently within each specimen (Figure IV-7, TGA curves). Liu *et al.* [211] identified three distinct stages in the carbonation of C-S-H: a dissolution period characterized by a rapid release of calcium ions from the interlayer of C-S-H; a diffusion period dominated by the availability of calcium; and a slowly ongoing reaction period due to the thickening of carbonation products. The progression through these stages may be influenced by the internal moisture content of the carbonation-cured specimens [375]. Moreover, according to Liu *et al.* [376], and in agreement with Borges *et al.* [374], carbonation curing can simultaneously promote hydrate formation alongside carbonation, decreasing the gap in C-S-H dehydration mass loss between sealed and carbonation-cured specimens.

However, no mass loss was observed between 425 °C and 530 °C within any carbonation-cured specimens, regardless of curing age. The absence of thermal decomposition within this temperature range indicates a rapid conversion of $Ca(OH)_2$ into $CaCO_3$ [260] (Figure IV-7, DTG curves). Lu *et al.* [377] interpreted this behavior as evidence of a fast carbonation reaction that favored the $CaCO_3$ formation before any accumulation of $Ca(OH)_2$. Therefore, the absence of $Ca(OH)_2$ crystals before $CaCO_3$ precipitation, along with the pH decrease to be discussed later, confirms that the carbonation of $Ca(OH)_2$ proceeds via a dissolution–precipitation mechanism rather than solid-state transformation. This provides evidence that contributes to resolving the ongoing debate regarding the mechanism of $Ca(OH)_2$ carbonation.

Furthermore, the thermal decomposition of $CaCO_3$ between 550 °C and 1000 °C in carbonation-cured specimens involves two distinct zones, as indicated by a series of characteristic peaks [378]. The

peaks observed between 550 °C and 680 °C, which are slightly more intense in SSP-based samples (Figure IV-7c and d), are attributed to the newly formed amorphous $CaCO_3$ in all specimens. Hay *et al.* [264] reported that the nucleation effect of SSP and LS promotes the formation of amorphous $CaCO_3$ phases. However, this may be contradicted by the fact that the aragonite present in SSP has a lower tendency to act as a nucleation site for amorphous $CaCO_3$ growth, unless destabilized by the local drop in pH. In contrast, the peaks around 719 °C and 738 °C, more pronounced in the SSP-based samples and absent in the sealed-cured specimens, particularly at later ages, suggest the presence of vaterite or aragonite. However, a portion of the aragonite originates from the SSP rather than being formed during carbonation, although this is unlikely to significantly affect the DTG results due to its low content (a few percent). The thermal decomposition of calcite typically occurs within the temperature range of 740 °C to 990 °C [259]. During the carbonation curing, calcite's decomposition temperature shifts towards higher or lower values. This phenomenon suggests that the crystallinity of $CaCO_3$ is closely related to the local CO_2 concentration in specimens rather than the carbonation duration [190].

In summary, the TGA/DTG curves indicate rapid carbonation of $Ca(OH)_2$, specimen-dependent differences in C-S-H carbonation, formation of multiple $CaCO_3$ polymorphs influenced by CO_2 concentration, and release of physically bound water that promotes further hydration.

4.1.2 $Ca(OH)_2$ and C-S-H carbonation

The extent of carbonation was evaluated primarily by the contents of $Ca(OH)_2$ and C-S-H, the main phases involved in the reaction over time (Figure IV-8).

After 1 day of carbonation curing, the LS-RCA and SSP-RCA samples (Figure IV-8b and d) exhibited the lowest $Ca(OH)_2$ and C-S-H undergoing carbonation contents, compared to their counterparts with NCA (Figure IV-8a and c). This may be attributed to slower CO_2 diffusion within these specimens, potentially due to the factors previously discussed in § 3.1. Among the NCA-based specimens, the SSP-NCA exhibited the highest carbonated $Ca(OH)_2$ content, resulting in a greater C-S-H carbonation extent. According to Borges *et al.* [374], in agreement with Lu *et al.* [379], when $Ca(OH)_2$ carbonation increases, the buffering ability of the pore solution is impaired (a pH drop), consequently causing a rapid decalcification of C-S-H. At this stage, carbonation is likely governed by the availability of early-formed hydrates in the outer layer. This availability is potentially higher in SSP-NCA than in LS-NCA, as indicated by calorimetry results (Chapter III2) showing delayed early hydration and lower heat evolution in LS-NCA.

As carbonation progresses, the $Ca(OH)_2$ and C-S-H contents undergoing carbonation exhibit a non-monotonic trend across all specimens (Figure IV-8). These non-monotonic trends may be attributed not only to variations in CO_2 diffusion rate, which are strongly influenced by changes in open porosity within the specimens, but also to the alternating dominance between hydration-driven phase formation

and carbonation-induced passivation at different depths within each specimen. At certain ages, continued hydration can produce additional $Ca(OH)_2$ and C-S-H, which subsequently become available for carbonation, explaining the observed increases in hydrate contents undergoing carbonation. Meanwhile, the reduction in carbonation may be linked to the formation of a layer of $CaCO_3$ microcrystals on the surfaces of $Ca(OH)_2$ and C-S-H, which inhibits their further carbonation [183,374].

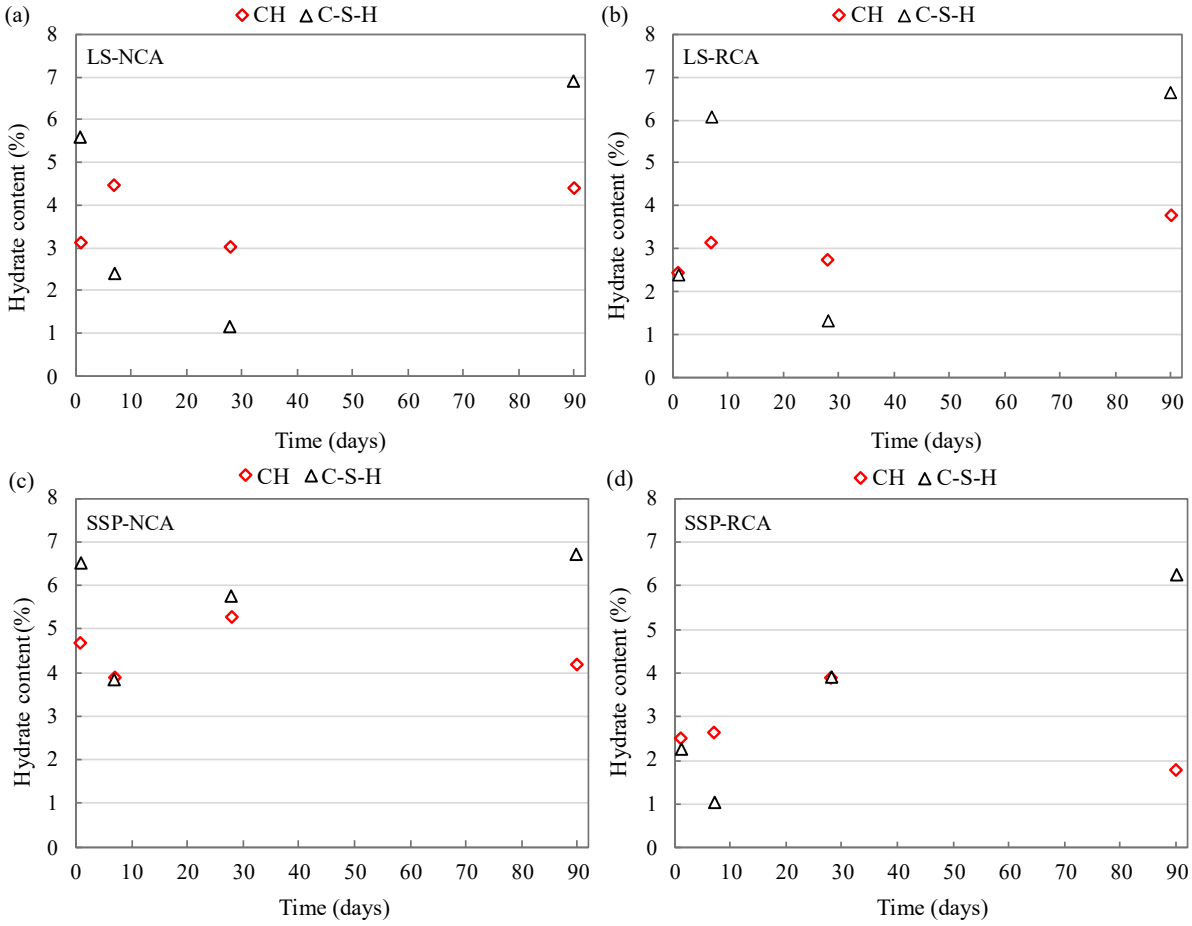

Figure IV-8: $Ca(OH)_2$ (CH) and C-S-H content undergoing carbonation over time: (a-b) LS-based mixtures; (c-d) SSP-based mixtures.

However, the parameters underlying these tendencies cannot be fully elucidated by TGA alone, particularly given that the C-S-H carbonation does not always directly correlate with the simultaneous consumption of $Ca(OH)_2$. For example, at 90 days, all specimens exhibit a greater content of C-S-H undergoing carbonation than $Ca(OH)_2$, due to the cumulative effects of hydration, passivation, and diffusion-related factors mentioned earlier. A more comprehensive interpretation will be achieved by integrating the complementary evidence provided in the XRD results section.

4.1.3 Estimation of the CO_2 uptake

The non-monotonic trends observed in the $Ca(OH)_2$ and C-S-H results indicate uneven total $CaCO_3$ precipitation, independent of sampling depth (Figure IV-9).

After 1 day of carbonation curing, SSP-NCA samples exhibit higher $CaCO_3$ precipitation and, consequently, greater CO_2 uptake than their LS-NCA counterparts, reflecting the higher early carbonation (Figure IV-9a and c). Meanwhile, the RCA-based samples exhibit lower $CaCO_3$ precipitation and lower CO_2 uptake than their NCA counterparts (Figure IV-9b and d), consistent with the slower carbonation trends identified earlier.

After 7 days, $CaCO_3$ precipitation increases in the LS-based samples but decreases in the SSP-based samples. By day 28, $CaCO_3$ precipitation decreases in the LS-based samples, while it recovers in the SSP-based specimens. By 90 days, all samples exhibit comparable $CaCO_3$ precipitation levels, except for the SSP-RCA samples (Figure IV-9d). These results suggest that SSP particles may facilitate faster initial CO_2 uptake in NCA-based specimens, followed by a reduction over time. In contrast, LS particles promote slower but more sustained CO_2 uptake. Once again, however, the mechanisms governing these behaviors remain unclear at this stage.

The inclusion of RCA generally leads to slower and more limited CO_2 uptake throughout the curing period. Saikia *et al.* [380] also reported that carbonation curing of concrete results in uneven CO_2 uptake across the depth of the specimens. They attributed this behavior to the fact that initially, CO_2 uptake is controlled by heterogeneous surface reaction kinetics, which later shifts to a liquid-state diffusion-controlled process. The same tendency is also observed in our carbonation depth assessment (§ 2).

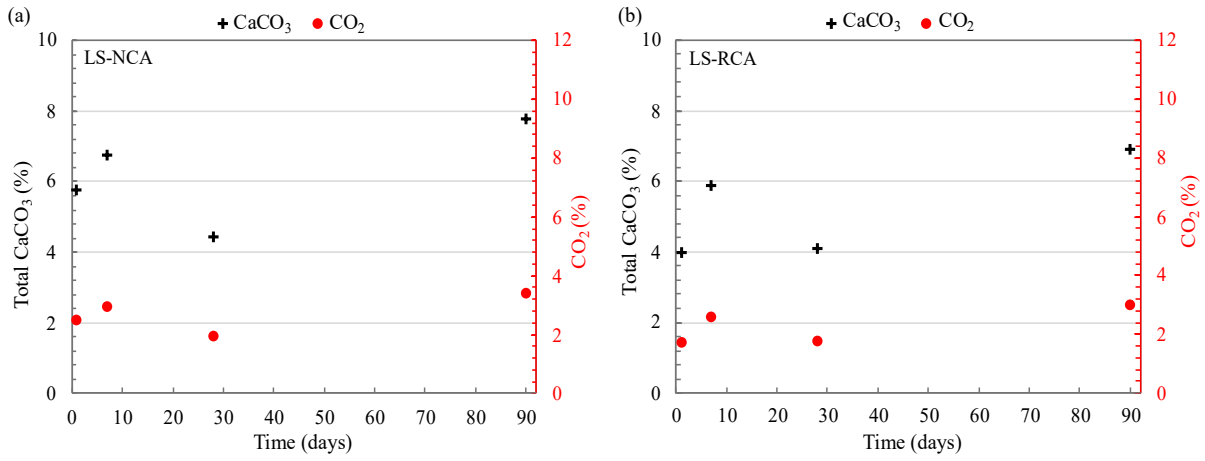

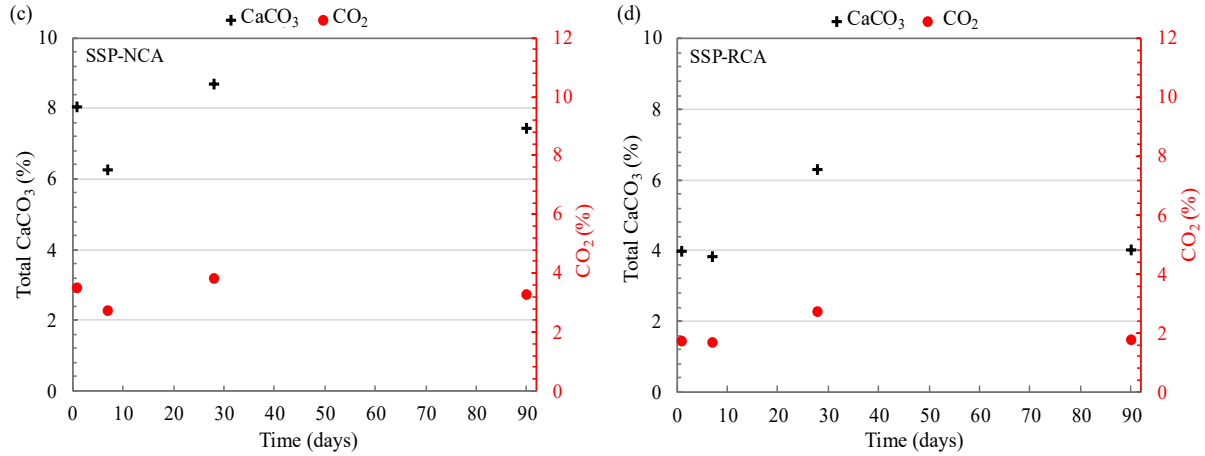

Figure IV-9: Total amount of $CaCO_3$ formed by $Ca(OH)_2$ and C-S-H over time: (a-b) LS-based mixtures; (c-d) SSP-based mixtures.

Overall, the TGA/DTG results suggest that SSP-based specimens may exhibit higher CO_2 uptake compared to their corresponding LS-based specimens. It is worth noting that the higher porosity of SSP also contributes to the rapid initial CO_2 uptake, while the uptake after 90 days is relatively identical. In contrast, the porosity of RCA does not appear to significantly accelerate CO_2 uptake, as RCA-based specimens exhibit lower uptake values than NCA-based specimens, according to TGA analysis. The observed fluctuations in the data highlight the inherent variability of the carbonation process, which may be influenced by sampling depth.

4.2 Mass loss method

4.2.1 Mass evolution during carbonation curing

In this method, cylindrical specimens (Ø 4 cm × H 10.4 cm) were used instead of powdered samples, allowing a more accurate estimation of CO_2 uptake. Before heating the specimens for the mass loss method, the mass of each specimen was recorded after each carbonation curing age and plotted accordingly (Figure IV-10).

In several studies [157,381,382], the CO_2 uptake of cement-based materials is expressed in terms of the carbonation-induced mass gain. However, in our case, the measured masses do not account for the amount of water loss resulting from the exothermic reaction occurring during carbonation curing. Nonetheless, evaluating the mass gain of the specimens provides a meaningful indicator for the comparative assessments of carbonation performance across different curing durations.

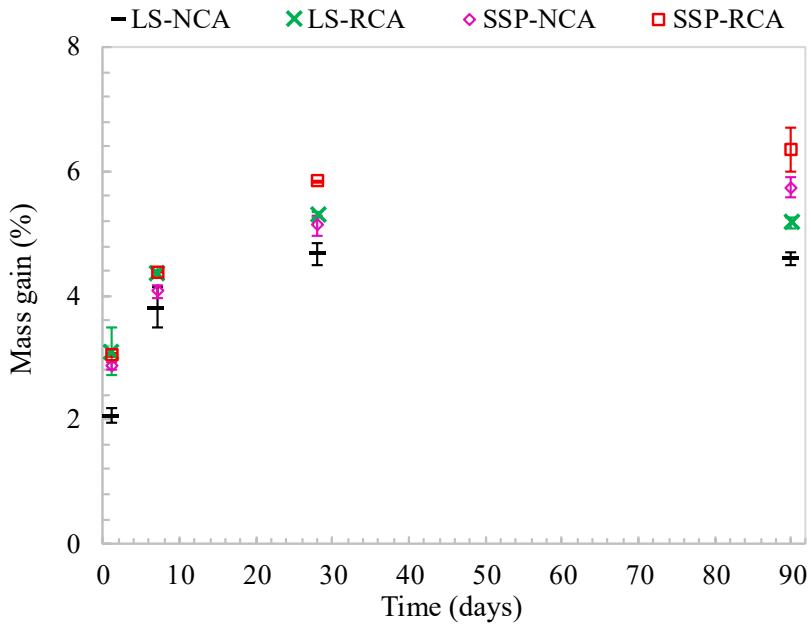

Figure IV-10: Mass gain of the specimens over carbonation curing ages.

All specimens exhibit a steep increase in mass gain during the early ages of carbonation curing, within the first 7 days, followed by a steady state at later ages (Figure IV-10). After one day, the carbonation-cured LS-NCA specimens exhibit the lowest mass gain, whereas the other specimens exhibit comparably higher values. The observed differences remained consistent up to 7 days, after which slight differences in mass gain began to emerge among the specimens from the 28th day of carbonation curing. By 90 days, these differences are more pronounced, with mass gain following the order: SSP-RCA > SSP-NCA > LS-RCA > LS-NCA. At this age, all specimens are considered largely carbonated, and the final mass gains primarily reflect CO_2 uptake. However, they may also include contributions from continued hydration, as total CO_2 consumption in the carbonation chamber was not controlled.

4.2.2 Estimation of the CO_2 uptake

The estimation of CO_2 uptake was primarily based on subtracting the mass loss occurring between 525 °C and 1000 °C of both carbonation-cured and sealed-cured specimens at each curing age.

Analyzing the CO_2 uptake trend (Figure IV-11), the estimated CO_2 uptake across all specimens increases and stabilizes over time. This trend aligns with those reported in previous studies [158,182,381]. However, the magnitude and pattern of change vary among the specimens: LS-NCA specimens, which exhibited the highest carbonation depth (§ 3), remarkably demonstrate the lowest CO_2 uptake compared to SSP-NCA and their RCA-based counterpart, particularly from the 7th day of carbonation curing onwards. Yuan *et al.* [383] predicted that higher porosity facilitates deeper

carbonation but may reduce the overall CO_2 uptake, a behavior that aligns with the characteristics of the LS-NCA specimens. Moreover, although LS is poorly porous, it can allow for significant inter-granular porosity in the SCC, which would require intra-granular porosity from SSP or even RCA; thus, the penetration depth can be greater, but the total uptake can be lower.

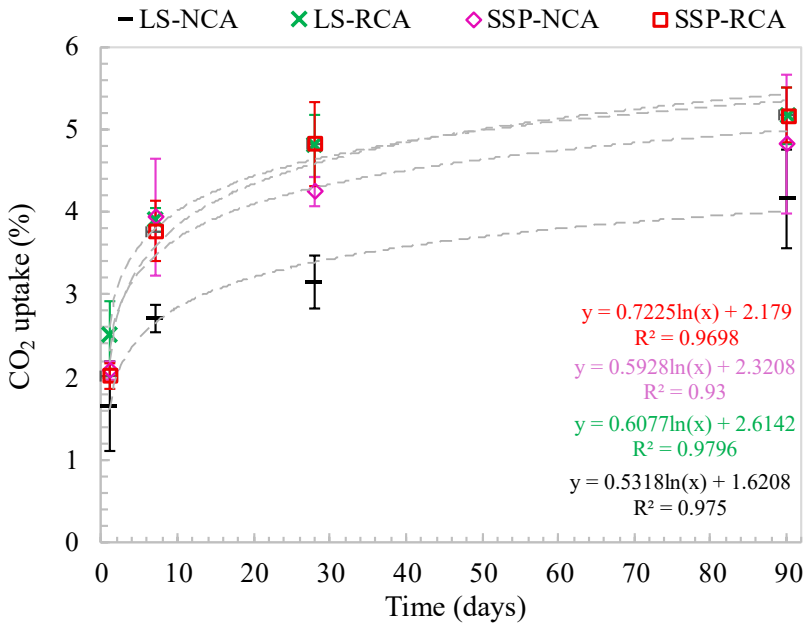

Figure IV-11: CO_2 uptake of carbonation-cured specimens at different ages.

Consequently, the carbonation depths qualitatively reflect the amount of $Ca(OH)_2$ involved in carbonation (Figure IV-8,7 days), rather than the total CO_2 uptake of the specimens. This divergence between carbonation depth and CO_2 uptake is further evidenced in Figure IV-12, which shows that specimens with similar carbonation depths can exhibit remarkably different CO_2 uptake. We attribute this behavior to inter-grains and intra-grains porosities. The former favors the total CO_2 uptake, while the latter facilitates a deeper penetration of CO_2 species.

In contrast, RCA-based specimens, despite slower CO_2 diffusion, exhibit the highest CO_2 uptake, likely due to the additional C-S-H present in the adherent old mortar [384]. Therefore, the mass loss method suggests that CO_2 uptake is most effective in RCA-based specimens, followed by SSP-NCA, and least effective in LS-NCA, independent of their corresponding carbonation depths.

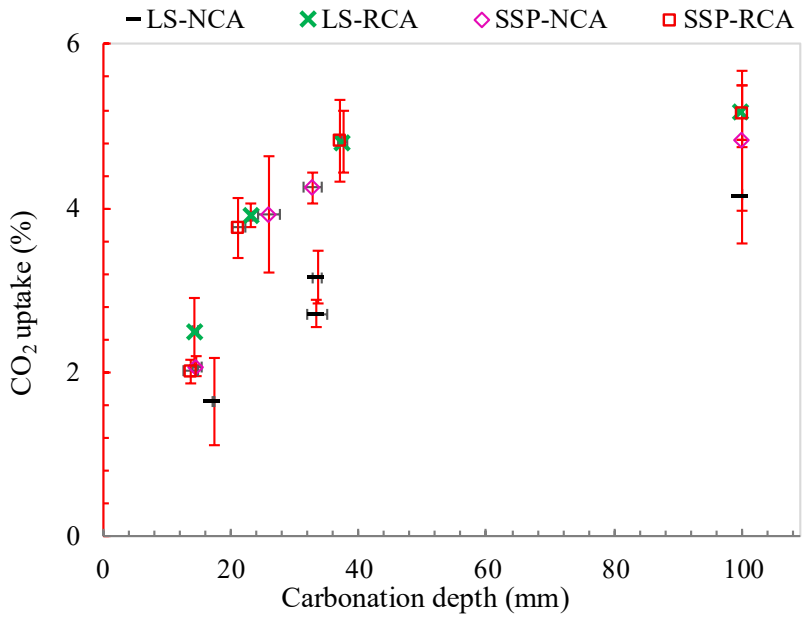

Figure IV-12: Relationship between CO_2 uptake and carbonation depth.

So far, the results indicate that SSP-NCA specimens store more CO_2 than LS-NCA specimens, as observed by both TGA and the mass loss method. LS-RCA and SSP-RCA specimens store comparable amounts of CO_2. However, the extent of CO_2 uptake in RCA-based versus NCA-based specimens appears inconsistent between TGA and mass loss measurements. Additionally, carbonation depth does not necessarily reflect the total CO_2 uptake. Further insights into these observations are provided by the XRD results presented in the following section.

4.3 X-ray diffraction: Semi-quantitative analysis

Similar to the other quantification methods, the calculation relies on the relative increase in $CaCO_3$ content compared to the reference specimens cured under sealed conditions. The exception here is that only the 1-day sealed-cured specimens were used for this comparison, as they represent the initial hydration stage unaffected by carbonation. Therefore, the additional $CaCO_3$ corresponds to the amount exceeding this initial content.

4.3.1 Mineralogical phases analysis

4.3.1.1 Sealed cured specimens

Before proceeding with the quantification, it is essential to briefly underscore which phases are visible in the XRD patterns (Figure IV-13). $Ca(OH)_2$ is the dominant crystalline product in all samples, exhibiting among the most intense diffraction peaks in LS-NCA and SSP-NCA (Figure IV-13a and c)

compared to their RCA counterparts (Figure IV-13b and d). Ettringite is identified by low-intensity peaks across all samples. The Hc phase is detected only through a few weak reflections in LS-NCA (Figure IV-13a), and through a single weak peak in LS-RCA, SSP-NCA, and SSP-RCA (Figure IV-13b to d). No peaks corresponding to Mc are observed in any of the samples. The primary clinker phases, C_2S and C_3S, are present in all samples, with C_3S exhibiting higher peak intensity than C_2S. Quartz shows strong reflections as the major crystalline phase, with calcite displaying the second most intense peaks, except in SSP-NCA, where the intensities of both phases are similar (Figure IV-13c). The differences observed in the relative intensities of these two phases across the samples may be related to sampling heterogeneity. Other phases, albite, muscovite, chlorite, orthoclase, gypsum, aragonite, and vaterite, do not produce distinct individual peaks, but their contributions are accounted for in the Rietveld refinement.

However, it is important to note that these qualitative observations, based solely on phase identification from peak position, are insufficient for a detailed discussion and can severely bias the interpretation. Indeed, peak intensities must be considered to accurately assign phases, deconvolve superposed peaks, and finally calculate the phase amount in the samples. This is what is done using Rietveld refinement, the results of which are detailed in the following.

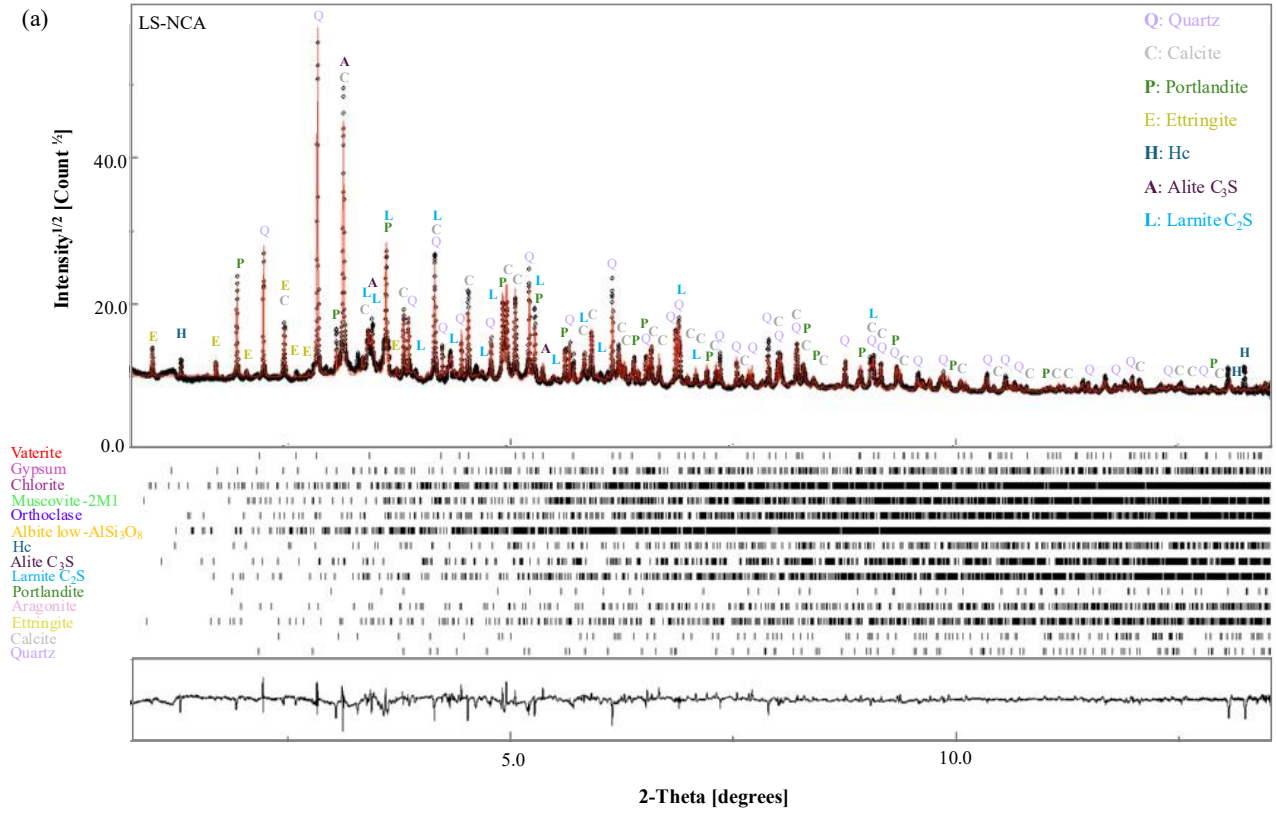

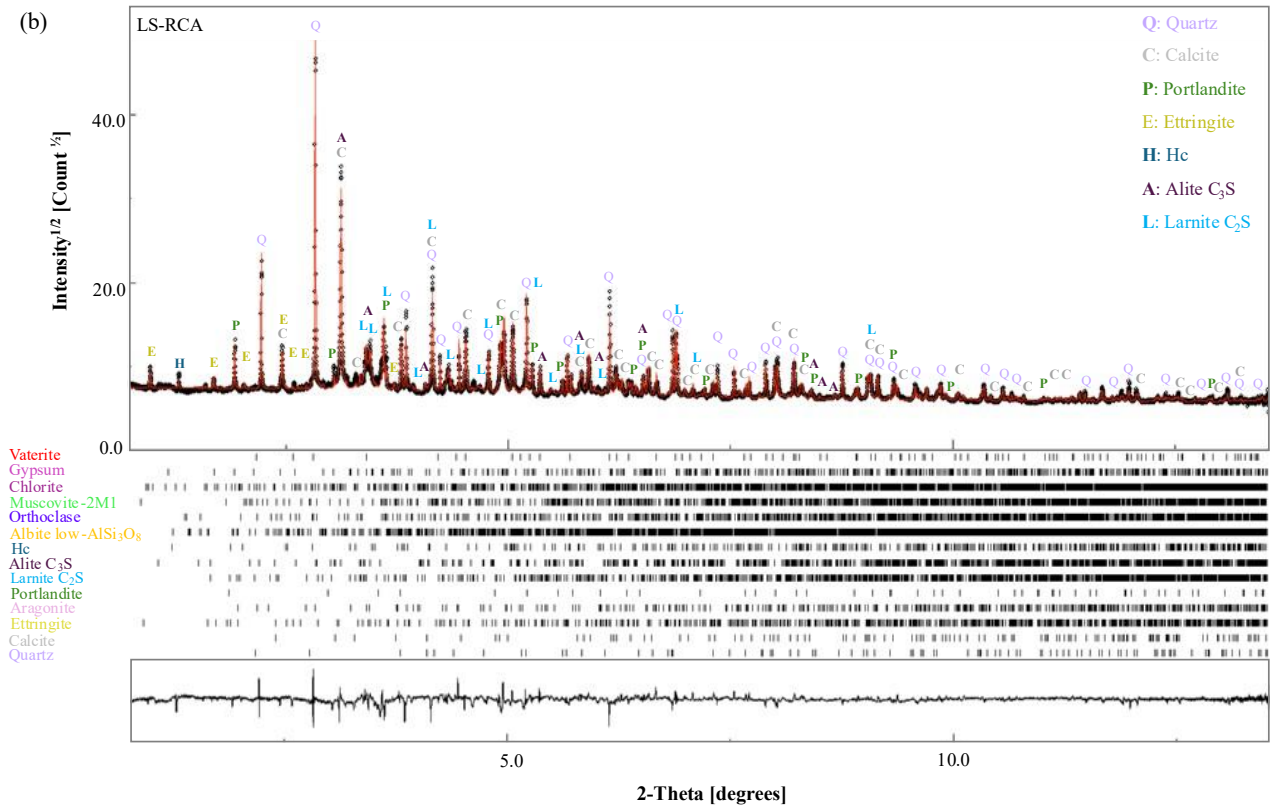
(b)
LS-RCA
Q: Quartz
C: Calcite
P: Portlandite
E: Ettringite
H: Hc
A: Alite C3S
L: Larnite C2S
Intensity1/2 [Count 1/2]
40.0
20.0
0.0
Vaterite
Gypsum
Chlorite
Muscovite-2M1
Orthoclase
Albite low-AlSi3O8
Hc
Alite C3S
Larnite C2S
Portlandite
Aragonite
Ettringite
Calcite
Quartz
5.0
10.0
2-Theta [degrees]

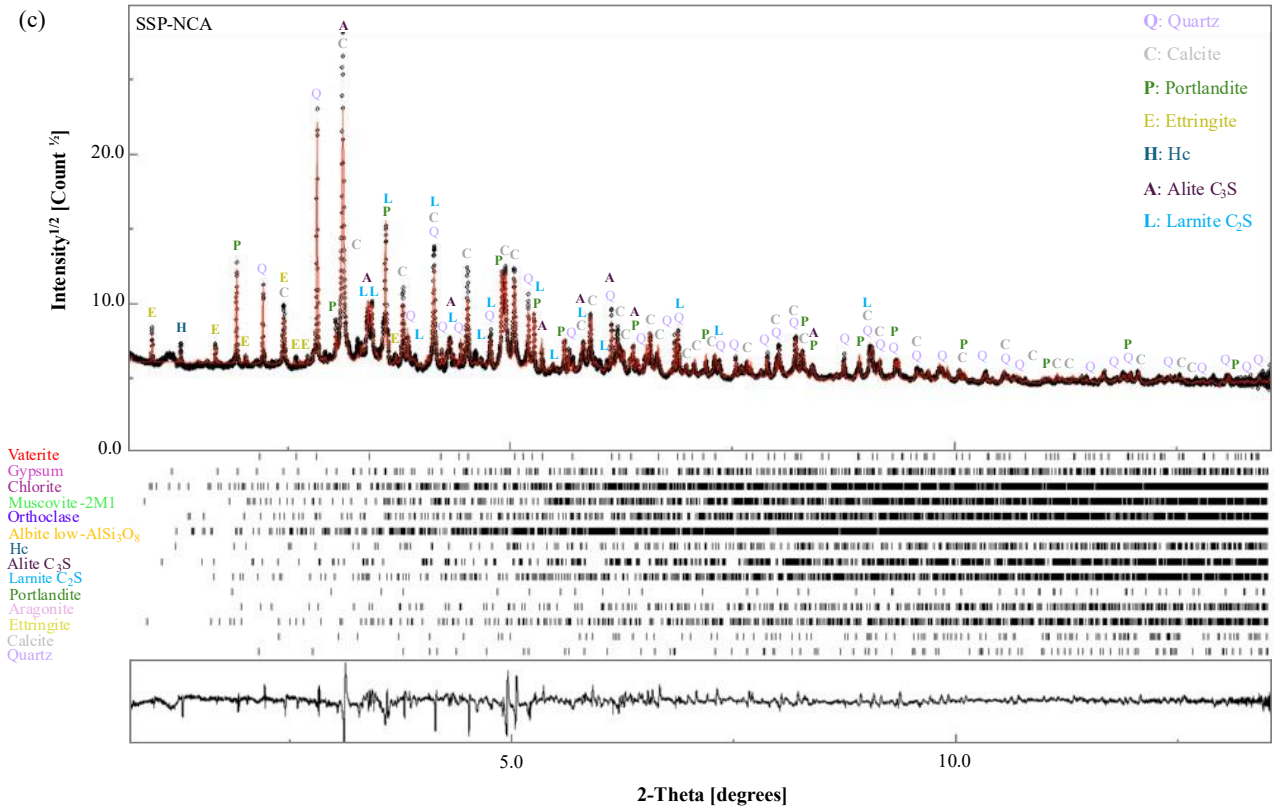
(c)
SSP-NCA
Q: Quartz
C: Calcite
P: Portlandite
E: Ettringite
H: Hc
A: Alite C3S
L: Larnite C2S
Intensity1/2 [Count 1/2]
20.0
10.0
0.0
Vaterite
Gypsum
Chlorite
Muscovite-2M1
Orthoclase
Albite low-AlSi3O8
Hc
Alite C3S
Larnite C2S
Portlandite
Aragonite
Ettringite
Calcite
Quartz
5.0
10.0
2-Theta [degrees]

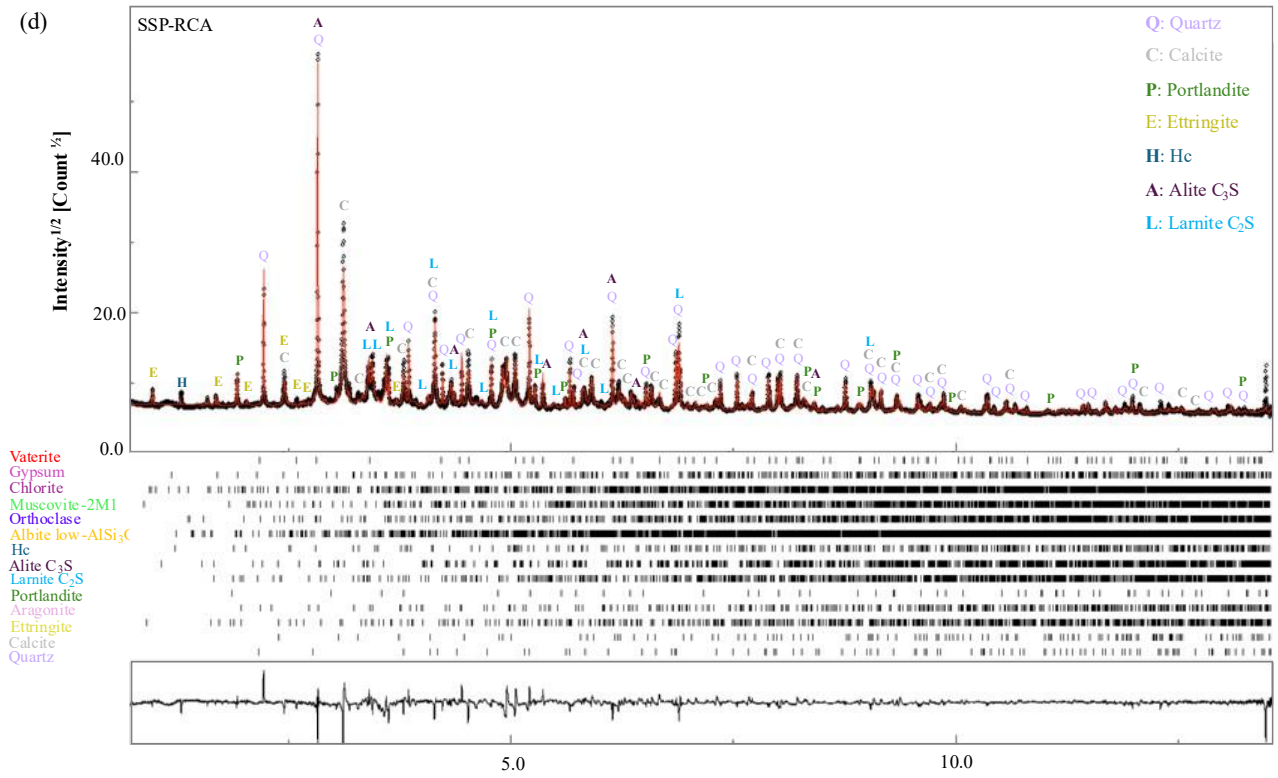

Figure IV-13: XRD patterns of one-day sealed-cured SCC specimens.

Building on the qualitative observations from the diffraction patterns, the phase assembly varies among the samples (Table IV-2). Calcite and quartz contents range from approximately 34.80 to 51.50 wt% and 14.26 to 38.16 wt%, respectively. These differences primarily reflect sampling heterogeneity rather than chemical reactions, as their unit-cell parameters remain essentially unchanged compared to the pure minerals. However, in LS-NCA, the calcite a-parameter (a = 4.856 Å) is contracted relative to pure calcite (a = 4.986 Å), likely due to composition variations toward magnesio-calcite.

$Ca(OH)_2$ is higher in NCA-based samples (≈ 7.80 wt% in LS-NCA and ≈ 6.85 wt% in SSP-NCA) than in RCA-based ones (≈ 3.40 wt% in LS-RCA and ≈ 2.60 wt% in SSP-RCA), reflecting higher early hydration in NCA-based samples. The relative differences in ettringite content (≈ 3.32 wt% in LS-NCA and SSP-NCA; ≈ 2.02 wt% and ≈ 1.41 wt% in LS-RCA and SSP-RCA, respectively) match those of Hc. This suggests that higher Hc levels are associated with greater stabilization of ettringite. Additionally, the comparable Hc content in all samples indicates that SSP and LS contribute similarly to hydration under 1 day of sealed curing.

Among the clinker phases, LS-NCA exhibits the lowest C_3S content (≈ 2.85 wt%) and the highest C_2S content (≈ 19.10 wt%) compared to the other samples, consistent with rapid early hydration and potential for further hydration development. The unit-cell parameters (cell length c) of the two

phases show an enlargement across all samples. Other detected minor phases are present only in trace amounts.

Table IV-2: Quantitative phase composition and corresponding unit-cell parameters of samples after 1 day of sealed curing. Numbers in parentheses indicate the standard deviations as 1σ on the last digits from the Rietveld refinement. Absence of standard deviations means that the values were adjusted at best manually and could not be released during the fits without instability of the refinement.

cif	COD	Standard Unit-cell parameters (Å and °)	LS-NCA	LS-RCA	SSP-NCA	SSP-RCA
			wt (%)	wt (%)	wt (%)	wt (%)
			Unit-cell parameters (Å and °)	Unit-cell parameters (Å and °)	Unit-cell parameters (Å and °)	Unit-cell parameters (Å and °)
Quartz	1011097	-	27.08(1.2)	34.2(0.2)	14.26(0.1)	38.16(0.3)
		a = 4.913	a = 4.91380(5)	a = 4.91380(5)	a = 4.91380(5)	a = 4.91380(5)
		c = 5.404	c = 5.4055(1)	c = 5.4055(1)	c = 5.4055(1)	c = 5.40(1)
Calcite	1547348		39(2)	36.9(0.2)	51.5(3)	34.84(0.3)
		a= 4.98614(1)	a = 4.85660(8)	a = 4.9856(7)	a = 4.98566(8)	a = 4.98566(8)
		c = 17.0479(3)	c = 17.0477(3)	c = 17.0477(3)	c = 17.0477(3)	c = 17.0477(3)
Portlandite	1001768		7.8(0.3)	3.4(0.05)	6.8(0.1)	2.60(0.06)
		a = 3.589(8)	a = 3.59265(9)	a = 3.59265(9)	a = 3.59265(9)	a = 3.59265(9)
		c = 4.911(14)	c = 4.9134(2)	c = 4.9134(2)	c = 4.91345(2)	c = 4.9134(2)
Ettringite	9011576		2.3(0.1)	2.02(0.1)	2.31(0.2)	1.41(0.1)
		a = 11.23	a = 11.215(3)	a = 11.219(3)	a = 11.215(3)	a = 11.215(3)
		c = 10.72	c = 10.601(8)	c = 10.605(8)	c = 10.601(8)	c = 10.601(8)
Alite (C_3S)	9016125		2.8(0.2)	4.9(0.1)	4(0.1)	6.30(0.1)
		a = 11.6389	a = 12.223(2)	a = 12.234(1)	a = 12.248(1)	a = 12.2334(10)
		b = 14.1716	b = 7.069(1)	b = 7.0701(7)	b = 7.0620(8)	b = 7.0706(5)
		c = 13.6434	c = 9.295(1)	c = 9.2919(8)	c = 9.300(1)	c = 9.2919(7)
		α = 104.982				
		β = 94.622	β = 116.13°(3)	β = 116.19°(9)	β = 116.2°(1)	β = 116.17°(1)
		γ = 90.107				
Larnite- (C_2S)	9017424		1.9(1)	16.11(0.3)	15.5(0.4)	14.06(0.4)
		a = 5.5051	a = 5.514(4)	a = 5.515(1)	a = 5.514(2)	a = 5.511(2)
		b = 6.7551	b = 6.767(2)	b = 6.7632(2)	b = 6.766(2)	b = 6.770(2)
		c = 9.3108	c = 9.336(2)	c = 9.373(2)	c = 9.370(3)	c = 9.369(3)
		α = 90°				
		β = 90.59°	β = 93.60°(2)	β = 93.6°(2)	β = 93.7°(3)	β = 93.6°(3)
		γ = 90°				
Hc	2105251		0.28(0.04)	0.26(0.4)	0.24(0.06)	0.2(0.05)

		a = 5.75340(10)	a = 5.76	a = 5.76	a = 5.76	a = 5.76
		c = 46.3890(10)	c = 44	c = 44	c = 44	c = 44
Albite low	2107372		0.20(0.05)	0.2(0.04)	0.21(0.06)	0.14(0.04)
		a = 8.138	a = 8.14	a = 8.14	a = 8.14	a = 8.14
		b = 12.789	b = 12.77	b = 12.77	b = 12.77	b = 12.77
		c = 7.156	c = 7.15	c = 7.15	c = 7.15	c = 7.15
		α = 94.22°	α = 94.3°	α = 94.3°	α = 94.3°	α = 94.3°
		β = 116.67°	β = 116.65°	β = 116.65°	β = 116.65°	β = 116.65°
		γ = 87.65°	γ = 87.8°	γ = 87.8°	γ = 87.8°	γ = 87.8°
Muscovite	1011049		0.013(0.03)	0.02(0.1)	0.05(0.03)	0.08(0.08)
		a = 5.18	a = 5.22	a = 5.22	a = 5.22	a = 5.22
		b = 9.02	b = 8.98	b = 8.98	b = 9.98	b = 9.98
		c = 20.03999	c = 20.03999	c = 20.03999	c = 20.03999	c = 20.03999
		α = 90°				
		β = 95.5°	β = 94.25°	β = 94.25°	β = 94.25°	β = 94.25°
		γ = 90°				
Aragonite	2100187		0.7(0.1)	0.7(0.1)	1.31(0.1)	1.09(0.014)
		a = 4.961830 (13)	a = 4.96	a = 4.96	a = 4.961830 (13)	a = 4.961830 (13)
		b = 7.96914(2)	b = 7.97	b = 7.97)	b = 7.96914(2)	b = 7.96914(2)
		c = 5.742852(15)	c = 5.74	c = 5.74	c = 5.742852(15)	c = 5.742852(15)
Chlorite	9000158		0.1(0.2)	0.02(0.05)	0.23(0.2)	0.26(0.2)
		a = 5.335	a = 5.33	a = 5.33	a = 5.33	a = 5.33
		b = 9.240	b = 9.24	a = 9.24	a = 5.24	a = 5.24
		c = 28.735	c = 28.4	c = 28.4	c = 28.4	c = 28.4
		α, β, γ = 90°	α, β, γ = 90°	α, β, γ = 90°	α, β, γ = 90°	α, β, γ = 90°
Orthoclase	9000304		0.4(0.1)	0.5(0.1)	0.21(0.2)	0.52(0.2)
		a = 8.545	a = 8.545	a = 8.54	a = 8.54	a = 8.54
		b = 12.967	b = 12.99	b = 12.99	b = 12.99	b = 12.99
		c = 7.201	c = 7.22	c = 7.22	c = 7.22	c = 7.22
		α = 90°				
		β = 116°	β = 116°	β = 116°	β = 116°	β = 116°
		γ = 90°				
Vaterite	9007475		0.13(0.9)	0.25(0.1)	0.02(0.2)	0.27(0.1)
		a = 4.13	a = 4.130513	a = 4.130513	a = 4.130513	a = 4.130513
		c = 8.49	c = 8.490557	c = 8.460557	c = 8.460557	c = 8.460557
Gypsum	1010981		0.1(0.1)	0.1(0.1)	0.22(0.12)	0.03(0.09)
		a = 10.47	a = 10.52	a = 10.52	a = 10.52	a = 10.52
		b = 15.15	b = 15.1	b = 15.1	b = 15.1	b = 15.1

		c = 6.51	c = 6.52996	c = 6.52996	c = 6.52996	c = 6.52996
		α = 90°				
		β = 151.52°	β = 151.52°	β = 151.52°	β = 151.52°	β = 151.52°
		γ = 90°				

The tendency of these phases to undergo carbonation or further hydration will be investigated through XRD of the carbonated samples. The three $CaCO_3$ polymorphs (calcite, aragonite, and vaterite) will be cumulatively considered for subsequent quantification. Minor trace phases will be excluded from further analysis, as discussed in the following section.

4.3.1.2 Carbonation-cured specimens

- **One day of carbonation curing**

After 1 day of carbonation curing, XRD patterns show that calcite exhibits stronger reflections in all carbonation-cured samples compared to their 1-day sealed-cured counterparts. The contributions of vaterite and aragonite to the peak intensities also increase slightly (Figure IV-14, Table IV-3). Peaks corresponding to C_2S and C_3S decrease in intensity, with C_2S no longer detectable in the LS-NCA samples. No individual Bragg peaks corresponding to $Ca(OH)_2$ are observed in the NCA-based samples (Figure IV-14a and b).

Rietveld quantification confirms an overall increase in $CaCO_3$ content, with calcite as the primary polymorph (Table IV-3). The relative content of the metastable polymorphs, aragonite and vaterite, also slightly increases [385]. These polymorphs typically form at early ages of carbonation, before or along with calcite precipitation, before eventually reverting into calcite at later ages (Chapter I) [248,386–388]. Notably, the carbonated LS-based samples exhibit higher contents of vaterite and, more prominently, aragonite compared to their SSP-based counterparts (Table IV-3). As reported [389], the polymorphism of $CaCO_3$ may vary in similar mineral systems, which are dominated by physico-chemical conditions such as temperature, pH, and water content, as well as the chemistry of the pore solution. The observed variation in these samples may result from the pre-conditioning step, which left the LS-based specimens, particularly the LS-NCA samples, with a lower water content, thereby limiting the availability of water for polymorph transformation [242].

All hydrated phases undergo carbonation simultaneously upon CO_2 exposure [219,390], with only trace amounts of ettringite and Hc remaining in all specimens. The minor residual $Ca(OH)_2$, present only in RCA-based samples, is not sufficient to maintain the pore solution alkalinity, indicating a general pH drop across all samples and thereby triggering the decalcification of C-S-H. The depletion of C_2S and C_3S, along with Ca^{2+} leaching from the above-mentioned calcium-bearing phases and its combination with CO_3^{2-} ions, leading to increased $CaCO_3$ formation, confirms the concurrent progression of hydration and carbonation mechanisms.

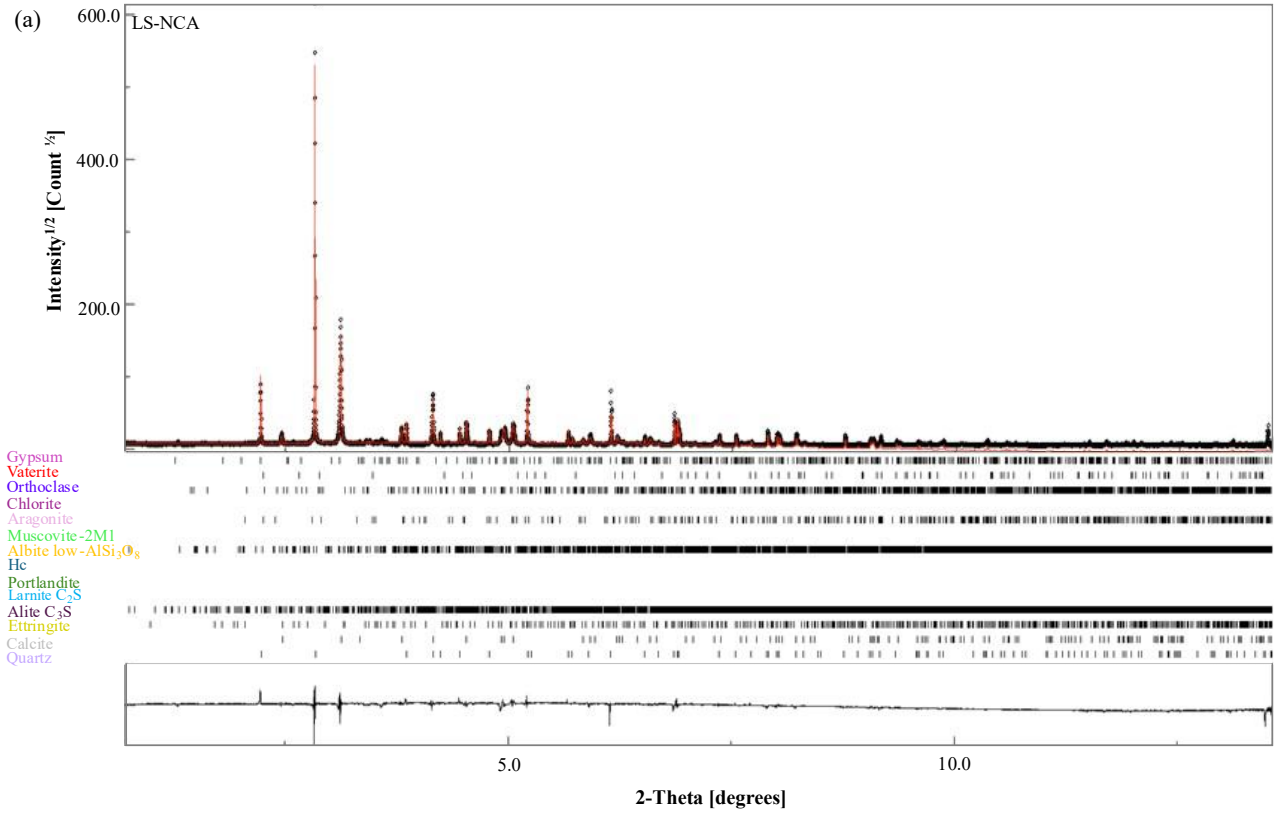
(a)
LS-NCA
600.0
400.0
200.0
Intensity^1/2 [Count ^1/2]
Gypsum
Vaterite
Orthoclase
Chlorite
Aragonite
Muscovite-2M1
Albite low-AlSi3O8
Hc
Portlandite
Larnite C2S
Alite C3S
Ettringite
Calcite
Quartz
5.0
10.0
2-Theta [degrees]

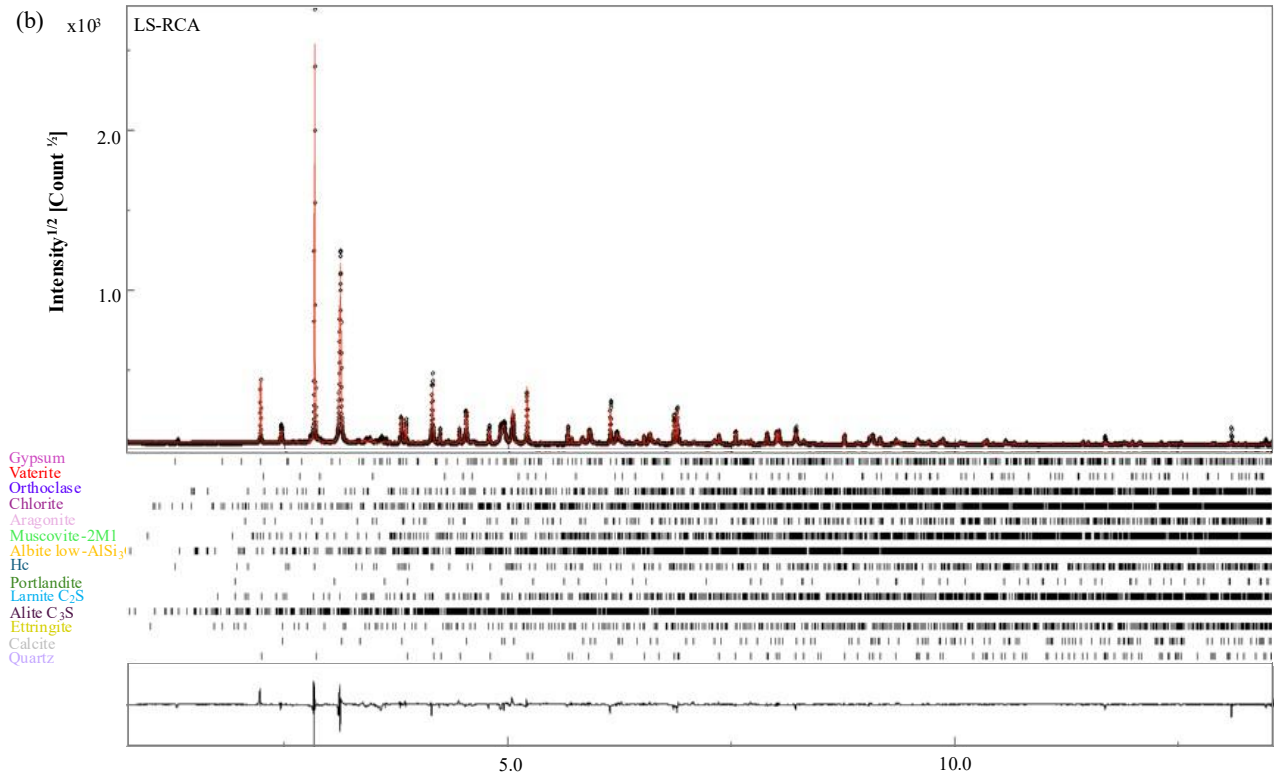
(b)
x10³
LS-RCA
2.0
1.0
Intensity^1/2 [Count ^1/2]
Gypsum
Vaterite
Orthoclase
Chlorite
Aragonite
Muscovite-2M1
Albite low-AlSi3O8
Hc
Portlandite
Larnite C2S
Alite C3S
Ettringite
Calcite
Quartz
5.0
10.0

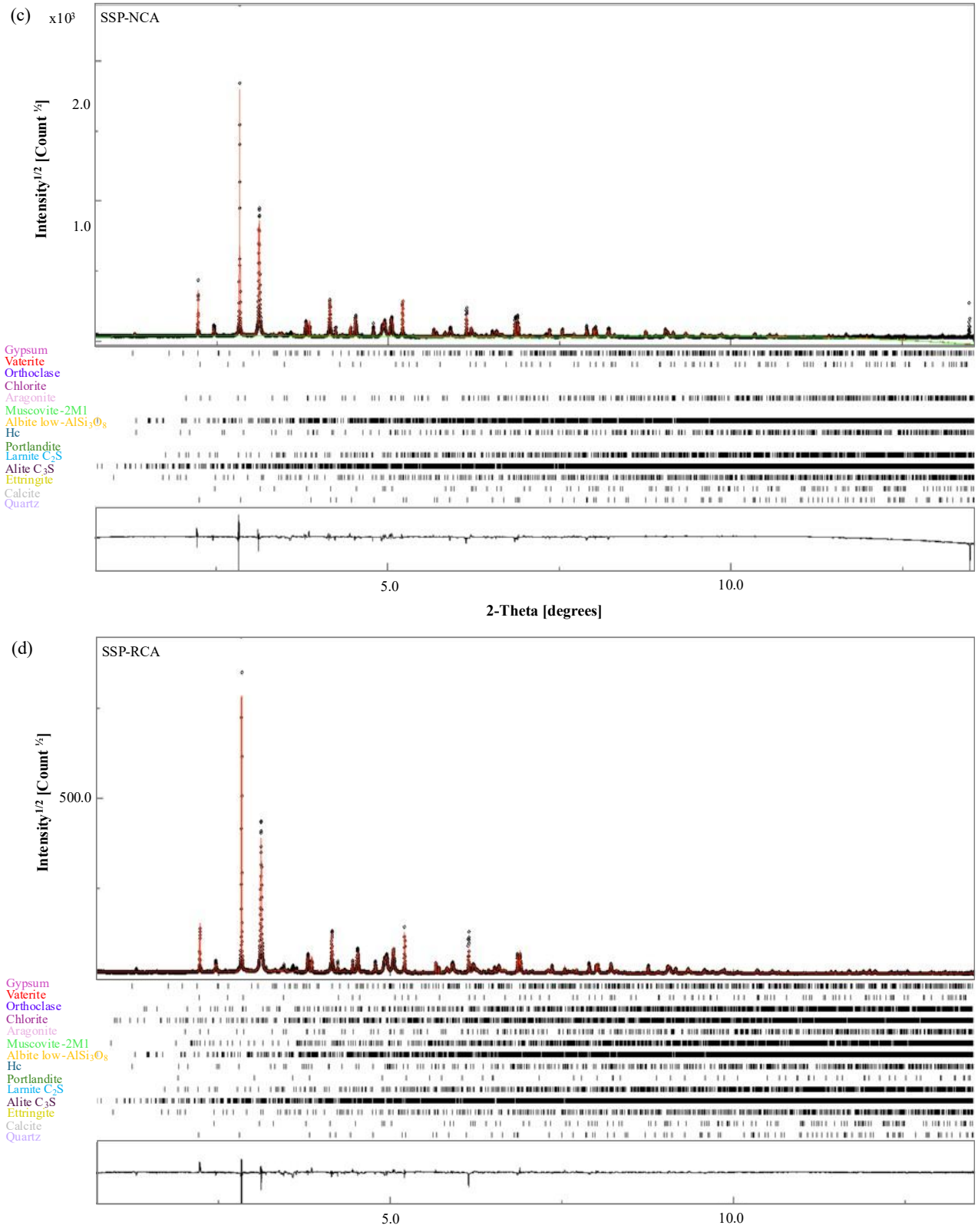

Figure IV-14: XRD patterns of 1-day carbonation-cured SCC specimens.

Moreover, after this carbonation period, the phases exhibit changes in their unit-cell parameters (Table IV-3). Calcite, in particular, shows a slight enlargement in the c-parameter (knowing that calcite is elastically anisotropic and more flexible along the c-axis than the a-axis [391]). During carbonation, early calcite nucleation occurs in a supersaturated solution dominated by Ca^{2+} and OH^- released from $Ca(OH)_2$. Under these conditions, OH^- ions resulting from dihydroxylation of $Ca(OH)_2$ favor their incorporation into the growing calcite crystals, which have not yet fully relaxed into their most stable structure, explaining the observed distortion in the calcite structure [392,393]. The presence of impurities originating from minor phases in the reaction medium may also contribute to the distortion of the calcite lattice.

Table IV-3: Quantitative phase composition and corresponding unit-cell parameters of samples after 1 day of carbonation curing. Numbers in parentheses indicate the standard deviations as 1σ on the last digits from the Rietveld refinement. Absence of standard deviations means that the values were adjusted at best manually and could not be released during the fits without instability of the refinement.

cif	Standard Unit-cell parameters (Å and °)	LS-NCA	LS-RCA	SSP-NCA	SSP-RCA
		wt (%)	wt (%)	wt (%)	wt (%)
		Unit-cell parameters (Å and °)	Unit-cell parameters (Å and °)	Unit-cell parameters (Å and °)	Unit-cell parameters (Å and °)
Calcite		41(1)	52(0.4)	55(1)	54(1)
	a = 4.98614 (1)	a = 4.9843(3)	a = 4.98376(9)	a = 4.9850(2)	a = 4.9847(1)
	c = 17.0479(3)	c = 17.083(2)	c = 17.0822(6)	c = 17.105(1)	c = 17.10352(5)
Aragonite		2.06	2.8(0.1)	1.33(0.2)	1.75(0.1)
	a = 4.961830 (13)	a = 4.9618	a = 4.9618	a = 4.9618	a = 4.9618
	b = 7.96914(2)	b = 7.9691	b = 7.9691	b = 7.9691	b = 7.9691
	c = 5.742852 (15)	c = 5.7428	c = 5.7428	c = 5.7428	c = 5.7428
Vaterite		0.96	1.3(0.1)	0.6(0.2)	0.78(0.07)
	a = 4.13	a = 4.1305	a = 4.1305	a = 4.1305	a = 4.1305
	c = 8.49	c = 8.460557	c = 8.460557	c = 8.460557	c = 8.460557
Portlandite		-	0.2(0.03)	-	0.15(0.03)
	a = 3.589 (8)	a = 3.5929735	a = 3.5929735	a = 3.5929735	a = 3.5929735
	c = 4.911 (14)	c = 4.9130287	c = 4.9130287	c = 4.9130287	c = 4.9130287
Ettringite		0.2(0.6)	0.2(0.1)	0.2(0.9)	0.2(0.1)
	a = 11.23	a = 11.1943245	a = 11.1943245	a = 11.1943245	a = 11.1943245
	c = 10.72	c = 10.622973	c = 10.622973	c = 10.622973	c = 10.622973
Alite-C_3S		1.9(0.3)	1.5(0.1)	2.4(0.2)	2.5(0.1)
	a = 11.6389	a = 33.079163	a = 33.079163	a = 33.079163	a = 33.079163
	b = 14.1716	b = 7.069867	b = 7.0198674	b = 7.069867	b = 7.0198674

	c = 13.6434	c = 13.6434	c = 18.5111	c = 18.5411	c = 18.5211
	α = 104.982°				
	β = 94.622°	β = 94.137°	β = 94.137°	β = 94.137°	β = 94.137°
	γ = 90.107°				
Larnite-C_2S		-	2.7(0.1)	1.8(0.3)	2.58(0.1)
	a = 5.5051		a = 5.514809	a = 5.514809	a = 5.514809
	b = 6.7551		b = 6.7655945	b = 6.7655945	b = 6.7655945
	c = 9.3108		c = 9.347539	c = 9.347539	c = 9.347539
	α = 90°				
	β = 90.59°	β = 94.59°	β = 94.59°	β = 94.59°	β = 94.59°
	γ = 90°				
Orthoclase		0.94	0.4(0.1)	-	0.53(0.1)
	a = 8.545	a = 8.545	a = 8.545		a = 8.545
	b = 12.967	b = 12.992	b = 12.992		b = 12.992
	c = 7.201	c = 7.221	c = 7.221		c = 7.221
	α = 90°				
	β = 116°	β = 116°	β = 116°	β = 116°	β = 116°
	γ = 90°				
Gypsum		0.81	0.5(0.1)	0.1(0.2)	0.36(0.7)
	a = 10.47	a = 10.518893	a = 10.518893	a = 10.518893	a = 10.518893
	b = 15.15	b = 15.103821	b = 15.103821	b = 15.103821	b = 15.103821
	c = 6.51	c = 6.474143	c = 6.474143	c = 6.474143	c = 6.474143
	α = 90°				
	β = 151.52°	β = 115.55°	β = 115.55°	β = 115.55°	β = 115.55°
	γ = 90°				
Quartz		50(1)	37(0.3)	38(0.5)	34.7(0.2)
	a = 4.913	a = 4.1368(1)	a = 4.91371(4)	a = 4.91375(9)	a = 4.91368(4)
	c = 5.404	c = 5.4053(2)	c = 5.40520(7)	c = 5.4056(1)	c = 5.40557(7)
Albite low		2.2(0.8)	1.3(0.1)	1.44(0.4)	1.6 (0.1)
	a = 8.138	a = 8.138	a = 8.138	a = 8.138	a = 8.138
	b = 12.789	b = 12.789	b = 12.789	b = 12.789	b = 12.789
	c = 7.156	c = 7.156	c = 7.156	c = 7.156	c = 7.156
	α = 90°	α = 94.33°	α = 94.33°	α = 94.33°	α = 94.33°
	β = 151.52°	β = 116.57°	β = 116.57°	β = 116.57°	β = 116.57°
	γ = 90°	γ = 87.65°	γ = 87.65°	γ = 87.65°	γ = 87.65°
Hc		-	0.002(0.035)	0.7(0.1)	0.007(0.04)
	a = 5.75340 (10)		a = 5.7687006	a = 5.7687006	a = 5.7687006
	c = 46.3890 (10)		c = 45.44003	c = 43.73003	c = 43.73003

Muscovite		-	0.0005(0.1)	-	0.02 (0.1)
	a = 5.18		a = 5.18		a = 5.18
	b = 9.02		b = 8.96		b = 8.96
	c = 20.03999		c = 20.1		c = 20.1
		β = 95.66°	β = 95.66°	β = 95.66°	β = 95.66°
Chlorite		-	0.3(0.2)	-	0.4 (0.1)
	a = 5.335		a = 5.335		a = 5.335
	b = 9.240		b = 9.240		b = 9.240
	c = 28.735		c = 28.390179		c = 28.390179
	α, β, γ = 90°	α, β, γ = 90°	α, β, γ = 90°	α, β, γ = 90°	α, β, γ = 90°

- **Seven days of carbonation curing**

As the 7-day curing period progresses, the XRD patterns of the second carbonated layer (core) samples undergo notable changes, with particular emphasis on the most significant differences (Figure IV-15). Calcite peaks intensify in LS-RCA, SSP-NCA, and SSP-RCA (Figure IV-15b, c, and d), whereas in LS-NCA, the diffraction peaks of $Ca(OH)_2$ and ettringite show more pronounced intensification (Figure IV-15a). Vaterite and aragonite phases remain detectable in LS-NCA, LS-RCA, and SSP-RCA, but their corresponding peak intensities are negligible in SSP-NCA.

Rietveld quantification confirms ongoing calcite formation in LS-RCA, SSP-NCA, and SSP-RCA, reflected by higher calcite contents (Table IV-4). In contrast, LS-NCA samples exhibit a significant decrease in calcite content (from ≈ 49.93 wt% to ≈ 29.22 wt%). Notably, it is even lower than in the sealed-cured counterpart (36.8%). This decrease reflects the partial dissolution of pre-existing limestone calcite, which is highly pH-dependent and sensitive to pore solution chemistry during the carbonation process. Normally, such dissolution would eventually revert to a re-growth process once the pH rises and sufficient Ca^{2+} and CO_3^{2-} ions are present [394]. However, in LS-NCA, reprecipitation is limited, as the dissolved Ca^{2+} is quickly consumed by hydration reactions, evidenced by the increased $Ca(OH)_2$ and ettringite contents, and eventually C-S-H formation [382]. On the other hand, vaterite and aragonite contents are approximately 1.25 wt% and 0.42 wt% in LS-NCA, 3.09 wt% and 2.47 wt% in LS-RCA, and 1.91 wt% and 1.14 wt% in SSP-RCA, while being negligible in SSP-NCA, indicating their nearly complete conversion to calcite in this sample (Table IV-4).

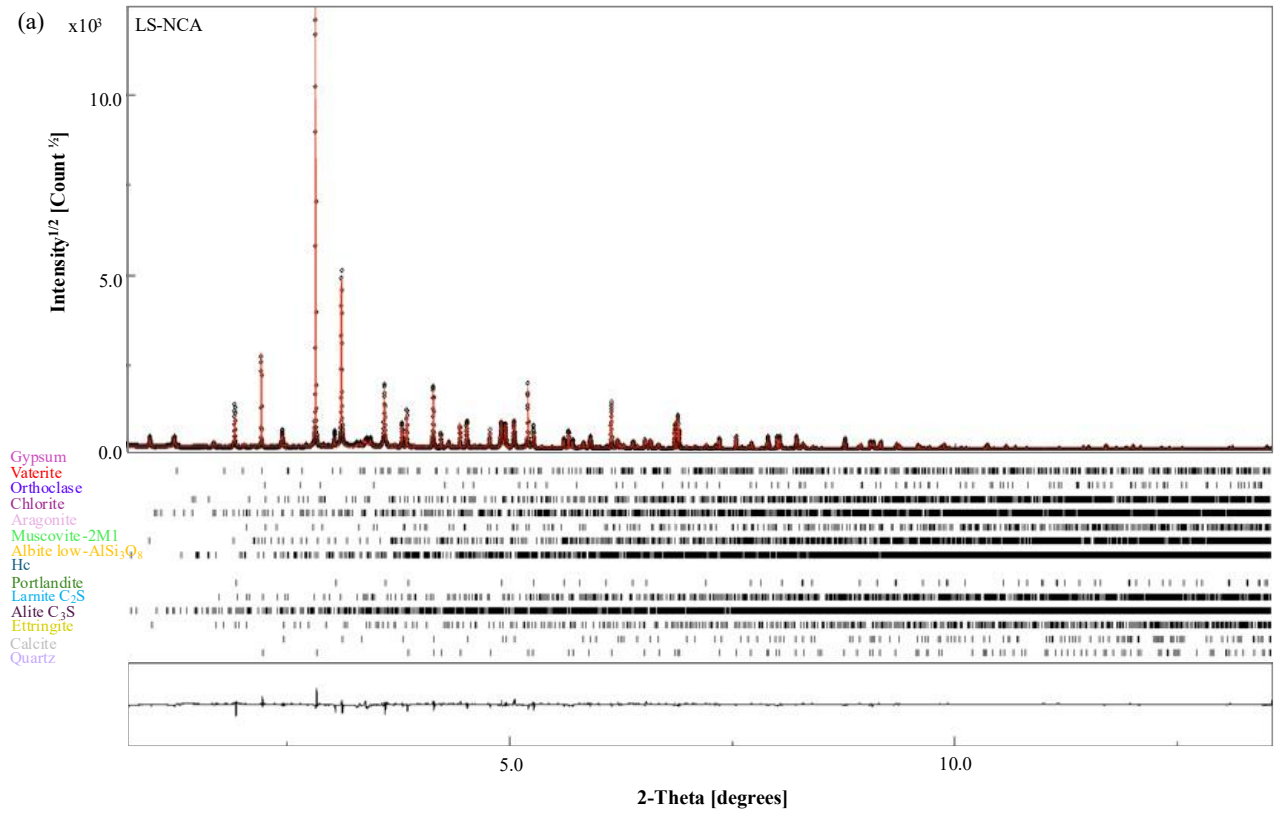
(a)
x10³
LS-NCA
10.0
5.0
0.0
Intensity^1/2 [Count ^1/2]
Gypsum
Vaterite
Orthoclase
Chlorite
Aragonite
Muscovite-2M1
Albite low-AlSi3O8
Hc
Portlandite
Larnite C2S
Alite C3S
Ettringite
Calcite
Quartz
5.0
10.0
2-Theta [degrees]

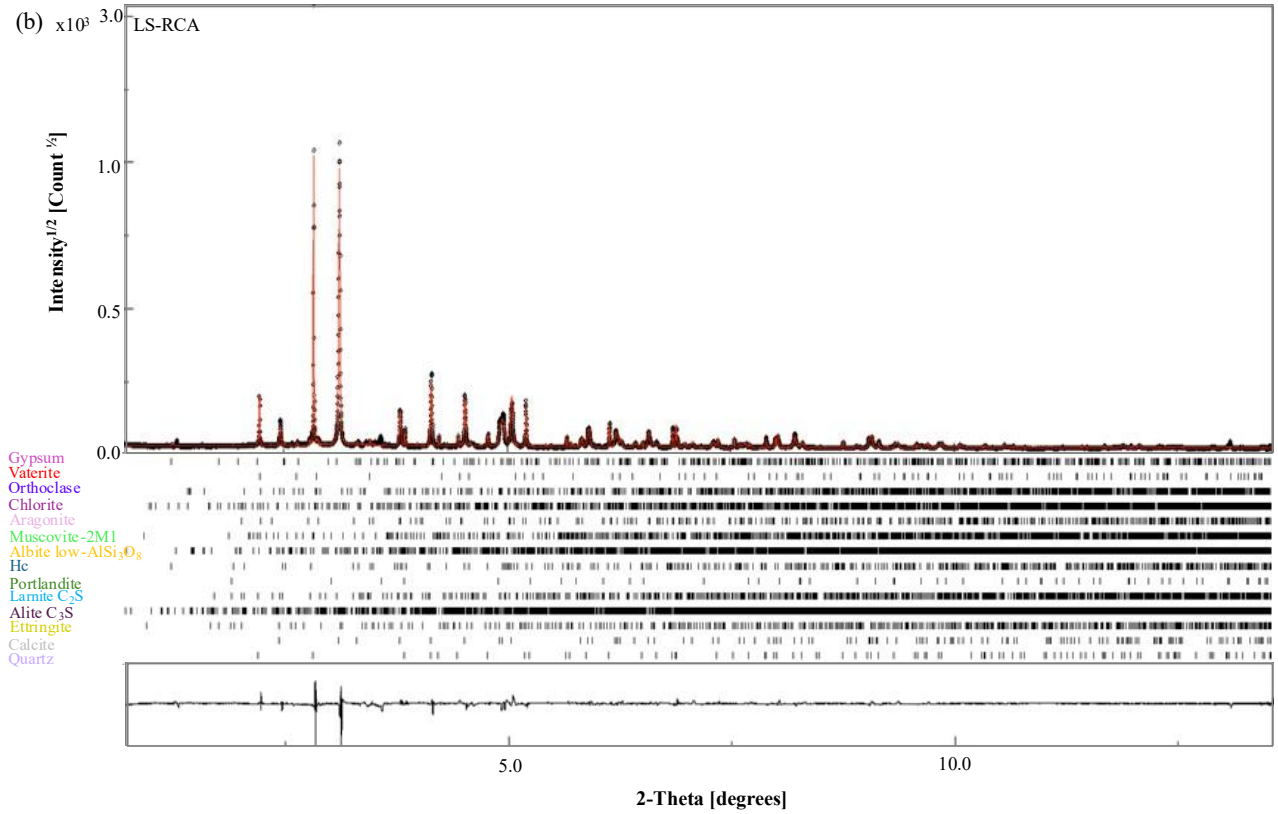
(b)
x10³
LS-RCA
3.0
1.0
0.5
0.0
Intensity^1/2 [Count ^1/2]
Gypsum
Vaterite
Orthoclase
Chlorite
Aragonite
Muscovite-2M1
Albite low-AlSi3O8
Hc
Portlandite
Larnite C2S
Alite C3S
Ettringite
Calcite
Quartz
5.0
10.0
2-Theta [degrees]

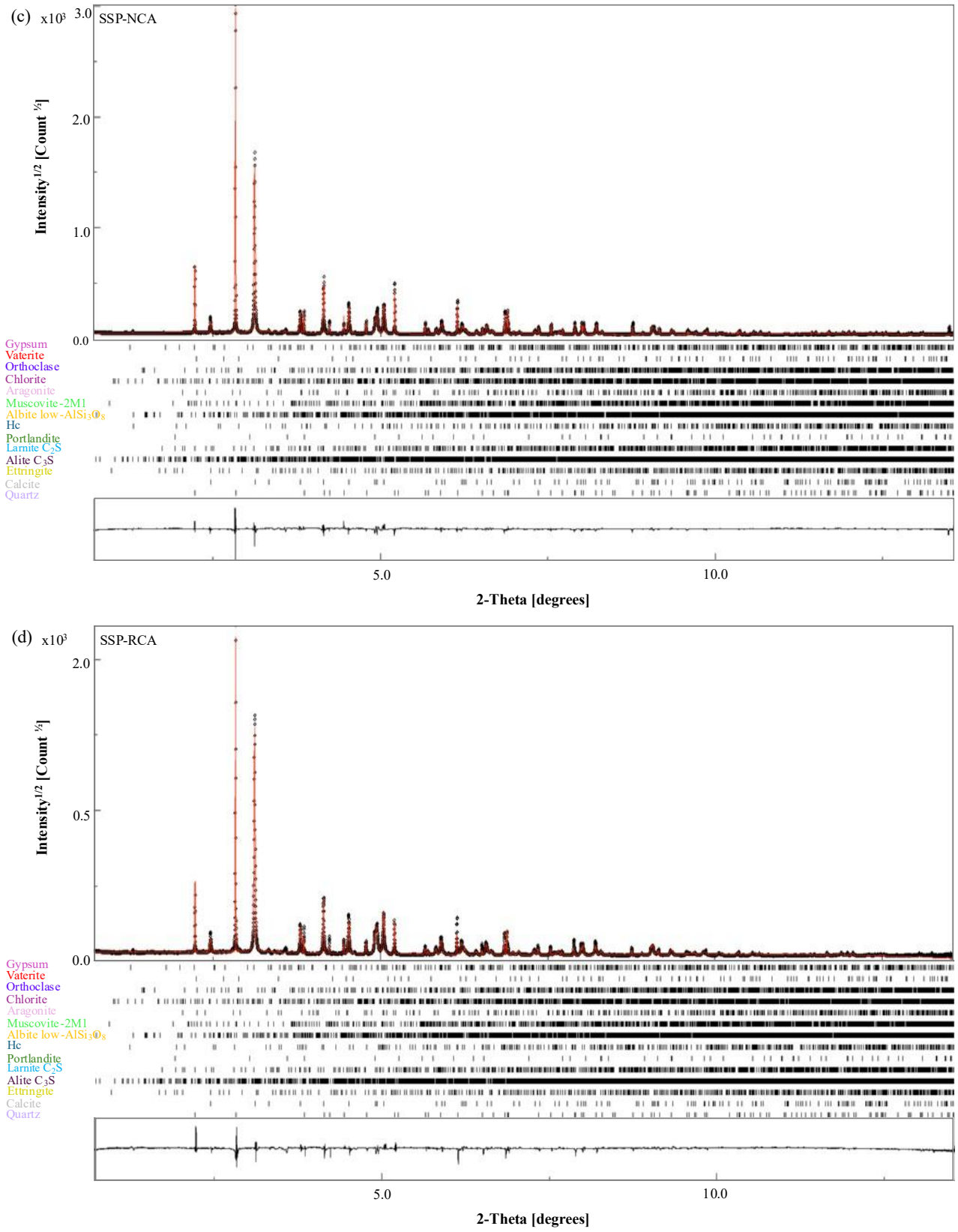

Figure IV-15: XRD patterns of 7-day carbonation-cured SCC specimens.

Table IV-4: Quantitative phase composition and corresponding unit-cell parameters of samples after 7 days of carbonation curing. Numbers in parentheses indicate the standard deviations as 1σ on the last digits from the Rietveld refinement. Absence of standard deviations means that the values were adjusted at best manually and could not be released during the fits without instability of the refinement.

cif	Standard Unit-cell parameters (Å and °)	LS-NCA	LS-RCA	SSP-NCA	SSP-RCA
		wt (%)	wt (%)	wt (%)	wt (%)
		Unit-cell parameters (Å and °)	Unit-cell parameters (Å and °)	Unit-cell parameters (Å and °)	Unit-cell parameters (Å and °)
Calcite		29.2(0.1)	65(0.4)	57.5(0.3)	65.6(0.2)
	a = 4.98614(1)	a = 4.98517(6)	a = 4.98296(8)	a = 4.98494(8)	= 4.9852(1)
	c = 17.0479(3)	c = 17.0438(3)	c = 17.0811(5)	c = 17.1003(5)	c = 17.1034(8)
Aragonite		1.25(0.1)	3.1(0.1)	0.1(0.1)	1.9(0.2)
	a = 4.961830(13)	a = 4.9618	a = 4.9618	a = 4.9618	a = 4.9618
	b = 7.96914(2)	b = 7.9691	b = 7.9691	b = 7.9691	b = 7.9691
	c = 5.742852(15)	c = 5.7428	c = 5.7428	c = 5.7428	c = 5.7428
Vaterite		0.4(0.1)	2.5(0.1)	0.01(0.06)	1.1(0.1)
	a = 4.13	a = 4.130513	a = 4.130513	a = 4.130513	a = 4.130513
	c = 8.49	c = 8.460557	c = 8.460557	c = 8.460557	c = 8.460557
Portlandite		9.6(0.1)	0.17(0.03)	0.004 (0.03)	0.01(0.07)
	a = 3.589(8)	a = 3.5929735	a = 3.5929735	a = 3.5929735	a = 3.5929735
	c = 4.911 (14)	c = 4.9130287	c = 4.9130287	c = 4.9130287	c = 4.9130287
Ettringite		4.1(0.1)	0.04(0.08)	0.003(0.064)	0.001(0.041)
	a = 11.23	a =11.1943245	a = 11.1943245	a = 11.1943245	a = 11.1943245
	c = 10.72	c = 10.622973	c = 10.622973	c = 10.622973	c = 10.622973
Alite-C_3S		1.6(0.1)	0.6(0.1)	0.02(0.08)	0.01(0.08)
	a = 11.6389	a = 33.079163	a = 33.079163	a = 33.079163	a = 33.079163
	b = 14.1716	b = 7.069867	b = 7.0198674	b = 7.0198674	b = 7.0198674
	c = 13.6434	c = 18.5411	c = 18.5211	c = 18.5211	c = 18.5211
	α = 104.982°				
	β = 94.622°	β = 94.137°	β = 94.137°	β = 94.137°	β = 94.137°
	γ = 90.107°				
Larnite-C_2S		7.2(0.1)	1.4(0.1)	0.01(0.3)	0.6(0.2)
	a = 5.5051	a = 5.514809	a = 5.514809	a = 5.514809	a = 5.514809
	b = 6.7551	b = 6.7655945	b = 6.7655945	b = 6.7655945	b = 6.7655945
	c = 9.3108	c = 9.347539	c = 9.347539	c = 9.347539	c = 9.342024
	α = 90°				
	β = 90.59°	β = 94.59°	β = 94.59°	β = 94.59°	β = 94.59°
	γ = 90°				

Orthoclase		0.5(0.1)	0.6(0.1)	0.03(0.08)	0.1(0.2)
	a = 8.545	a = 8.545	a = 8.545	a = 8.545	a = 8.545
	b = 12.967	b = 12.992	b = 12.992	b = 12.992	b = 12.992
	c = 7.201	c = 7.221	c = 7.221	c = 7.221	c = 7.221
	α = 90°				
	β = 116°	β = 116°	β = 116°	β = 116°	β = 116°
	γ = 90°				
Gypsum		4.5(0.5)	0.1(0.1)	5.1(0.6)	0.9(0.2)
	a = 10.47	a = 10.518893	a = 10.518893	a = 10.518893	a = 10.518893
	b = 15.15	b = 15.143821	b = 15.143821	b = 15.143821	b = 15.143821
	c = 6.51	c = 6.474143	c = 6.474143	c = 6.474143	c = 6.474143
	α = 90°				
	β = 151.52°	β = 151.55°	β = 151.55°	β = 151.55°	β = 151.55°
	γ = 90°				
Quartz		39(0.2)	23.9(0.1)	35.7(0.2)	26.5(0.3)
	a = 4.913	a = 4.91348(3)	a = 4.91346(6)	a = 4.91352(3)	a = 4.91403(9)
	c = 5.404	c = 5.40504(5)	c = 5.4056(1)	c = 5.40509(7)	c = 5.4062(1)
Albite low		1.9(0.2)	1.6(0.1)	1.1(0.1)	1.1(0.2)
	a = 8.138	a = 8.138	a = 8.138	a = 8.138	a = 8.138
	b = 12.789	b = 12.789	b = 12.789	b = 12.789	b = 12.789
	c = 7.156	c = 7.156	c = 7.156	c = 7.156	c = 7.156
	α = 94.22°	α = 94.33°	α = 94.33°	α = 94.33°	α = 94.33°
	β = 116.67°	β = 116.57°	β = 116.57°	β = 116.57°	β = 116.57°
	γ = 87.65°	γ = 87.65°	γ = 87.65°	γ = 87.65°	γ = 87.65°
Hc		-	0.001(0.055)	0.4(0.1)	0.002(0.019)
	a = 5.75340 (10)		a = 5.7687006	a = 5.7687006	a = 5.7687006
	c = 46.3890 (10)		c = 45.44003	c = 45.44003	c = 45.44003
Muscovite		0.41	0.0009(0.1)	0.01(0.13)	0.7(0.3)
	a = 5.18	a = 5.18	a = 5.18	a = 5.18	a = 5.18
	b = 9.02	b = 8.96	b = 8.96	b = 8.96	b = 8.96
	c = 20.03999	c = 20.1	c = 20.1	c = 20.1	c = 20.1
	α = 90°				
	β = 95.5°	β = 95.66°	β = 95.66°	β = 95.66°	β = 95.66°
	γ = 90°				
Chlorite		2.49(0.02)	0.01(0.0)	0.01(0.10)	0.3(0.3)
	a = 5.335	a = 5.335	a = 5.335	a = 5.335	a = 5.335
	b = 9.240	b = 9.240	b = 9.240	b = 9.240	b = 9.240
	c = 28.735	c = 28.390179	c = 28.390179	c = 28.390179	c = 28.735
	α, β, γ = 90°	α, β, γ = 90°	α, β, γ = 90°	α, β, γ = 90°	α, β, γ = 90°

- **Twenty-eight days of carbonation curing**

After 28 days of carbonation curing, the SCC specimens continue to carbonate, as reflected in the XRD patterns (Figure IV-16). Notably, aragonite and vaterite peaks are no longer observed in the LS-NCA (Figure IV-16a) and SSP-NCA (Figure IV-16c). This indicates that these metastable $CaCO_3$ polymorphs transformed into the more stable calcite (Ostwald's step rule). Peaks corresponding to the clinker phases C_2S and C_3S have completely disappeared. However, it is difficult to distinguish whether these phases were primarily hydrated, producing hydrates that subsequently carbonated, or whether they directly destabilized under the carbonation environment. According to Ibáñez *et al.* [395], the carbonation penetrates deeper into C_2S than into C_3S, consistent with the fact that C_3S hydrates much faster than C_2S. The rapid hydration of C_3S generates $Ca(OH)_2$ near the surface, which quickly carbonates and forms a dense $CaCO_3$ layer that may slow further CO_2 ingress. In contrast, the slower hydration of C_2S allows carbonation to progress deeper, resulting in more extensive destabilization of this phase during prolonged carbonation curing. A minor contribution of Hc remains in the LS-NCA samples (Figure IV-16a). During carbonation, Hc phases first destabilize into Mc, which further destabilizes into strätlingite. However, none of these secondary phases were detected in the XRD patterns throughout the entire carbonation curing period. This is likely due to the rapid destabilization of Hc, which prevented its conversion into these phases, and/or the low initial content of Hc in the system [396].

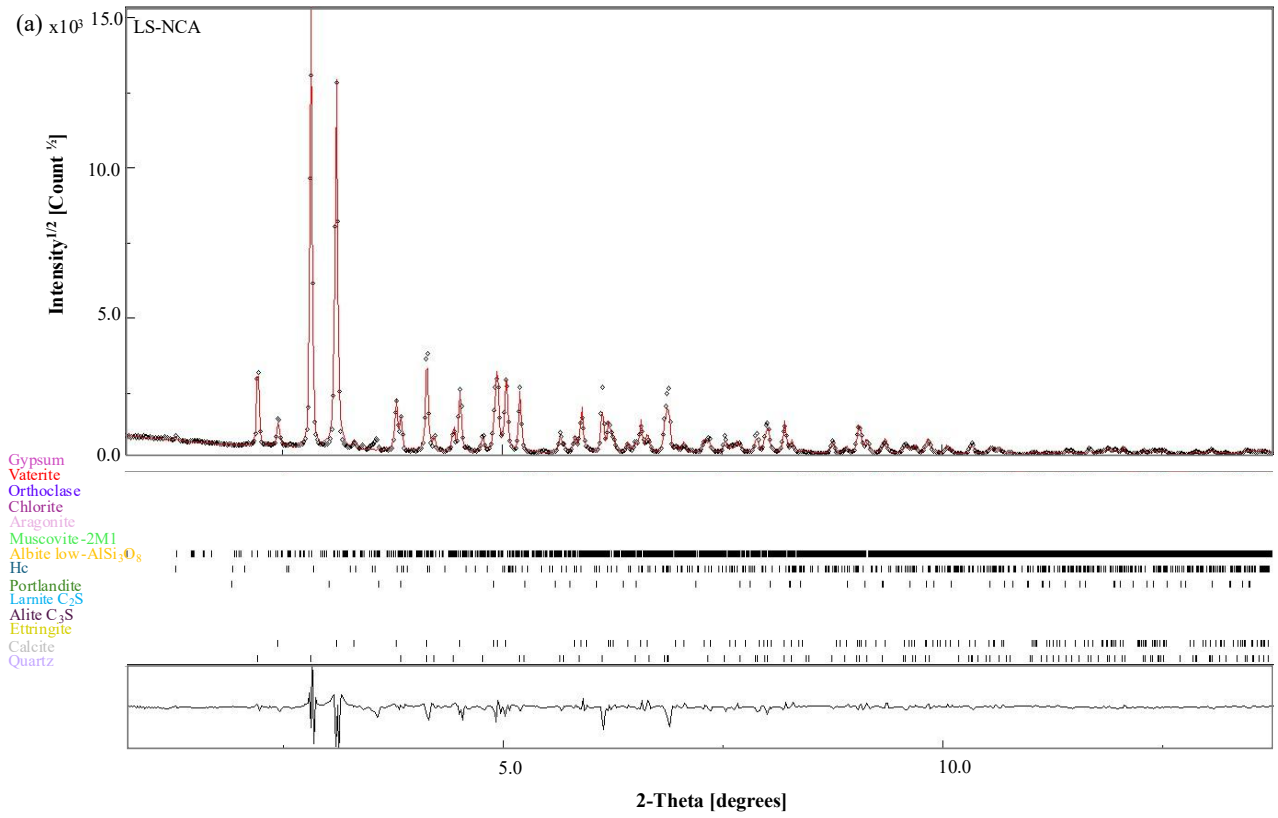

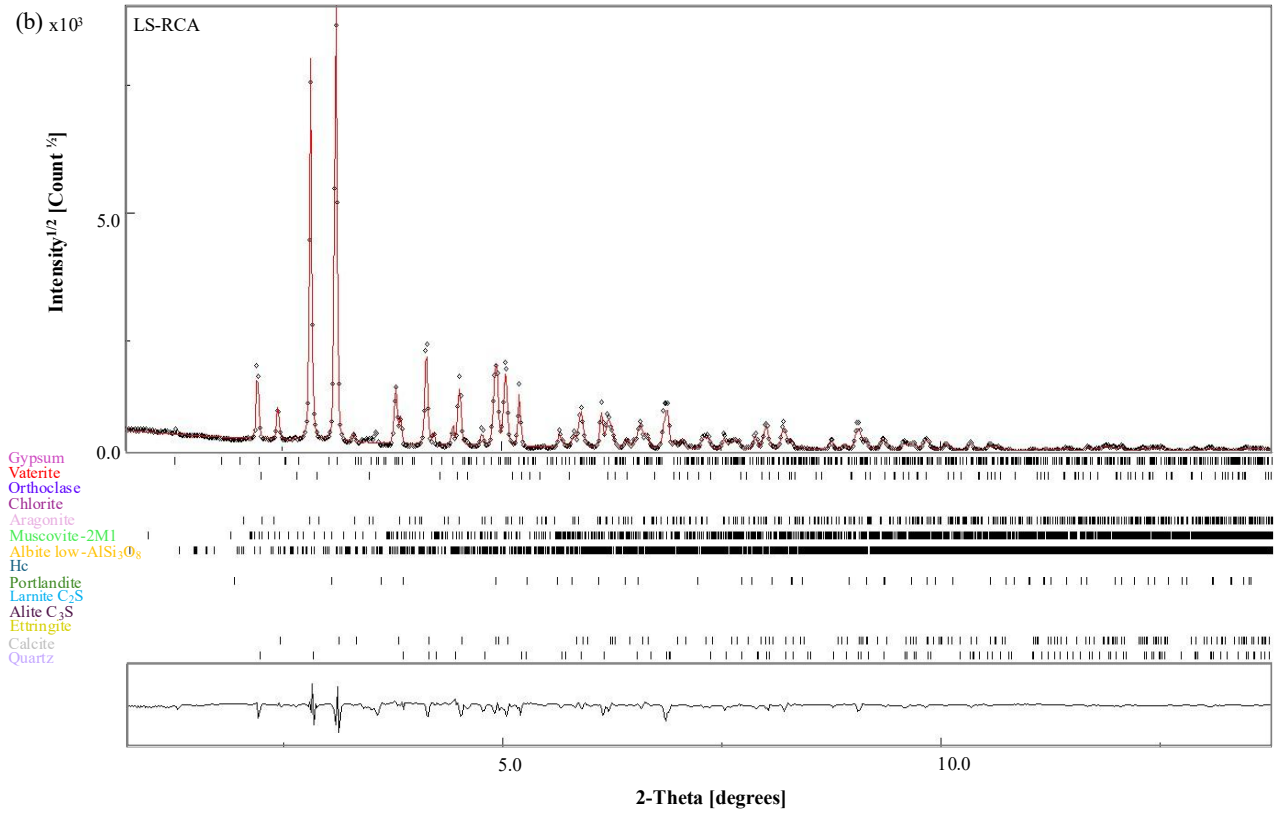
(b) x10³
LS-RCA
Intensity^1/2 [Count ^1/2]
5.0
0.0
Gypsum
Vaterite
Orthoclase
Chlorite
Aragonite
Muscovite-2M1
Albite low-AlSi3O8
Hc
Portlandite
Larnite C2S
Alite C3S
Ettringite
Calcite
Quartz
5.0
10.0
2-Theta [degrees]

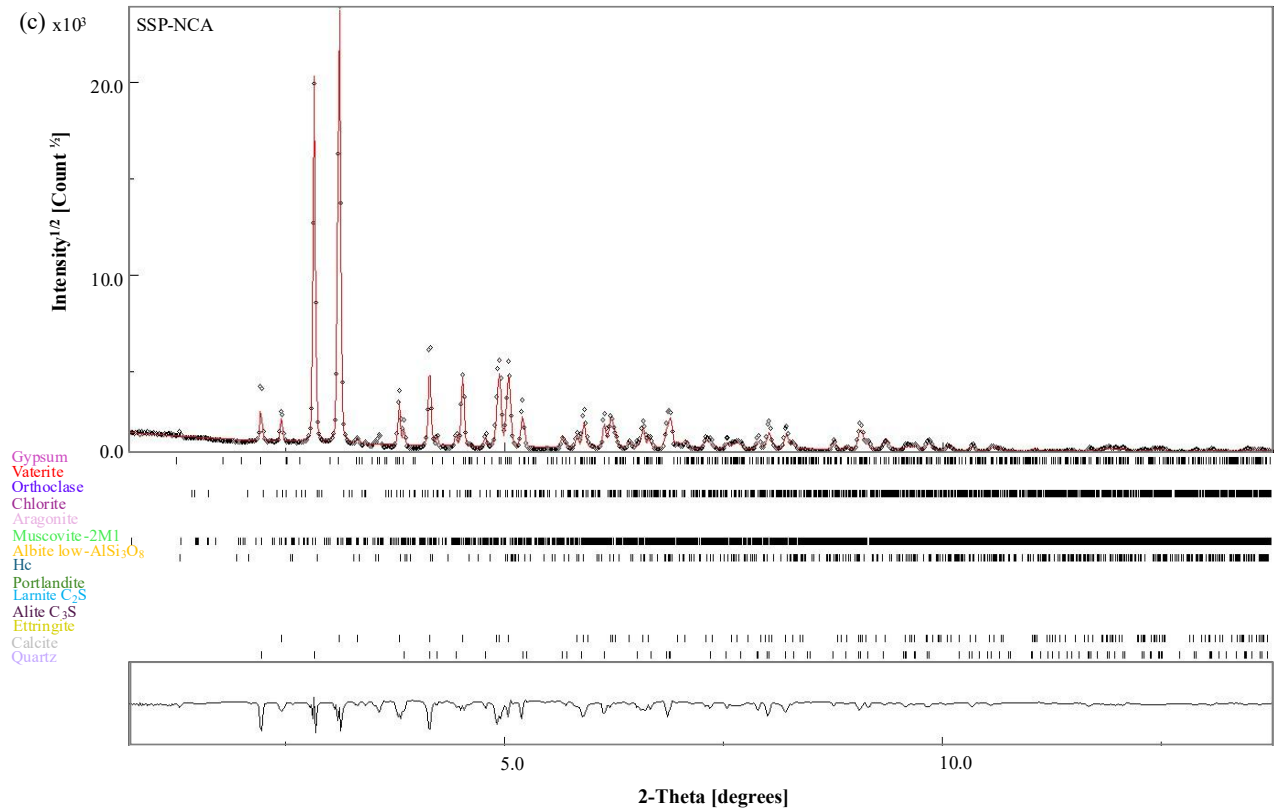
(c) x10³
SSP-NCA
Intensity^1/2 [Count ^1/2]
20.0
10.0
0.0
Gypsum
Vaterite
Orthoclase
Chlorite
Aragonite
Muscovite-2M1
Albite low-AlSi3O8
Hc
Portlandite
Larnite C2S
Alite C3S
Ettringite
Calcite
Quartz
5.0
10.0
2-Theta [degrees]

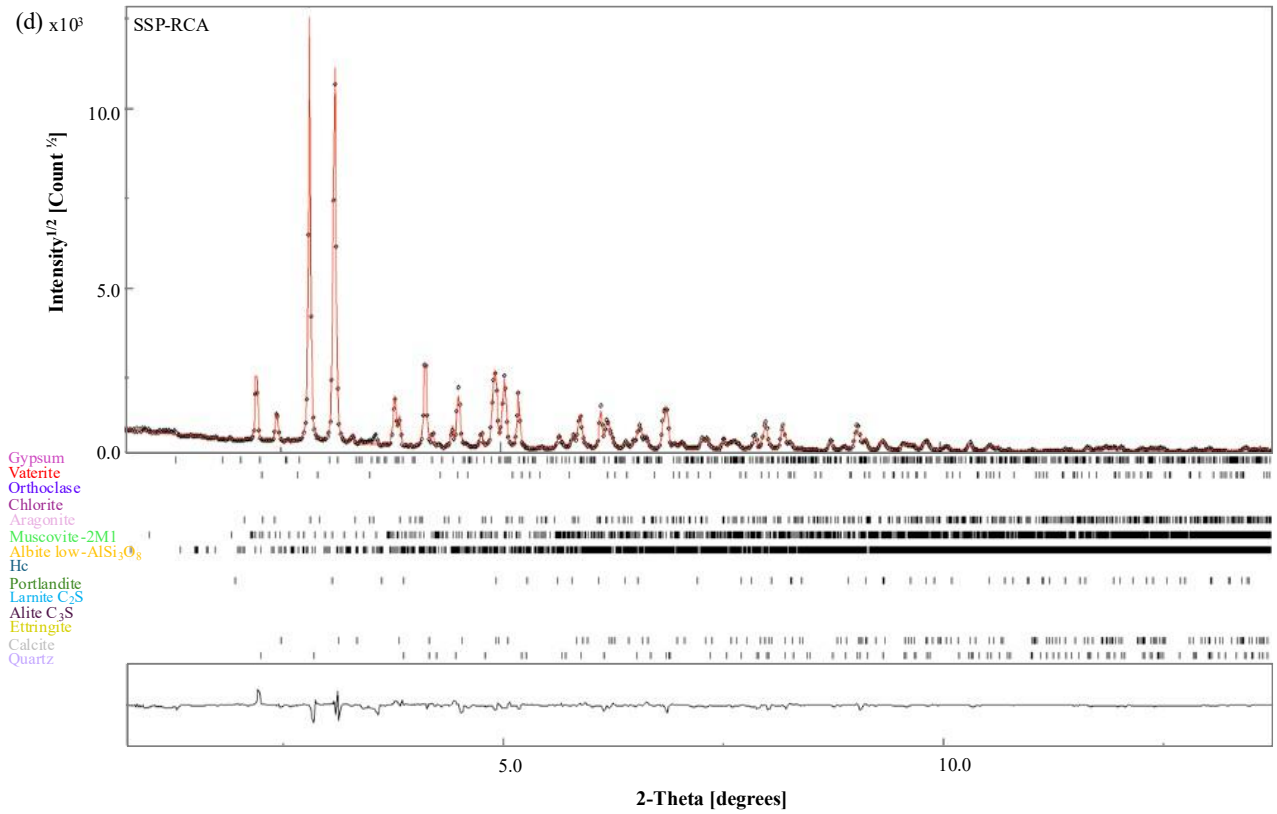

Figure IV-16: XRD patterns of 28-day carbonation-cured SCC specimens.

Regarding the phases' contents (Table IV-5), calcite shows a notable increase in the SSP-NCA samples compared to the other specimens. Trace amounts of aragonite and vaterite remain in the RCA-based samples. Ettringite appears to be completely destabilized by carbonation, while minor amounts of $Ca(OH)_2$ persist in the LS-NCA, LS-RCA, and SSP-RCA samples. The absence of any content of C_2S and C_3S indicates the extra reaction of the anhydrous cement during the carbonation process, as well as an almost complete carbonation of the specimens' inner layers [191,219].

Table IV-5: Quantitative phase composition and corresponding unit-cell parameters of samples after 28 days of carbonation curing. Numbers in parentheses indicate the standard deviations as 1σ on the last digits from the Rietveld refinement. Absence of standard deviations means that the values were adjusted at best manually and could not be released during the fits without instability of the refinement.

cif	Standard Unit-cell parameters (Å and °)	LS-NCA	LS-RCA	SSP-NCA	SSP-RCA
		wt (%)	wt (%)	wt (%)	wt (%)
		Unit-cell parameters (Å and °)	Unit-cell parameters (Å and °)	Unit-cell parameters (Å and °)	Unit-cell parameters (Å and °)
Calcite		57(1)	62.7(0.6)	69 (1.6)	59.3(0.4)
	a = 4.98614(1)	a = 4.9848(4)	a = 4.9841(4)	a = 4.9840(7)	a = 4.985(4)
	c = 17.0479(3)	c = 17.079(2)	c = 17.0857(2)	c = 17.099(3)	c = 17.096(2)
Aragonite		-	0.005(0.194)	-	0.6(0.2)
	a = 4.961830(13)		a = 4.9618		a = 4.9618
	b = 7.96914(2)		b = 7.9691		b = 7.9691
	c = 5.742852(15)		c = 5.7428		c = 5.7428
Vaterite		-	0.3(0.2)	-	0.3(0.2)
	a = 4.13		a = 4.130513		a = 4.130513
	c = 8.49		c = 8.460557		c = 8.460557
Portlandite		0.1(0.1)	0.002(0.06)	-	0.27(0.06)
	a = 3.589 (8)	a = 3.5927832	a = 3.5929735		a = 3.5929735
	c = 4.911 (14)	c = 4.9120345	c = 4.9130287		c = 4.9130287
Orthoclase		-	-	0.004(0.522)	-
	a = 8.545			a = 8.545	
	b = 12.967			b = 12.967	
	c = 7.201			c = 7.201	
	α = 90°				
	β = 116°			β = 116°	
	γ = 90°				
Gypsum		-	0.007(0.220)	0.005(0.542)	0.2(0.2)
	a = 10.47		a = 10.518893	a = 10.518893	a = 10.518893
	b = 15.15		b = 15.103821	b = 15.103821	b = 15.103821
	c = 6.51		c = 6.474143	c = 6.474143	c = 6.474143
	α = 90°				
	β = 151.52°		β = 151.55°	β = 151.55°	β = 151.55°
	γ = 90°				
Quartz		42(1)	37(1)	31(2)	39(0.5)
	a = 4.913	a = 4.9140(6)	a = 4.9145(5)	a = 4.916(3)	a = 4.9141(4)
	c = 5.404	c = 5.408(1)	c = 5.406(1)	c = 5.400(2)	c = 5.4044(8)

Albite low		0.87(22)	5.7 10^{-5}(0.02)	4.1 10^{-7}	0.2(0.1)
	a = 8.138	a = 8.138	a = 8.138	a = 8.138	a = 8.138
	b = 12.789	b = 12.789	b = 12.789	b = 12.789	b = 12.789
	c = 7.156	c = 7.156	c = 7.156	c = 7.156	c = 7.156
	α = 94.22°	α = 94.33°	α = 94.33°	α = 94.33°	α = 94.33°
	β = 116.67°	β = 116.67°	β = 116.67°	β = 116.67°	β = 116.67°
	γ = 87.65°	γ = 87.65°	γ = 87.65°	γ = 87.65°	γ = 87.65°
Hc		0.7(22)	-	-	-
	a = 5.75340(10)	a = 5.7687006			
	c = 46.3890(10)	c = 44.04003			
Muscovite		-	2.8 10^{-6}(0.4)	-	4.5 10^{-7}
	a = 5.18		a = 5.18		a = 5.18
	b = 9.02		b = 8.96		b = 8.96
	c = 20.03999		c = 20.1		c = 20.1
	α = 90°				
	β = 95.5°		β = 95.66°		β = 95.66°
	γ = 90°				

Before concluding this section, it is worth noting that the calcite crystals decrease in size with carbonation curing time. Takasaki *et al.* [397] reported on the evolution of calcite nanocrystals via carbonation under decreasing pH; a crystalline phase initially forms from amorphous $CaCO_3$ via ion-by-ion assembly. Bundles approximately ~50 nm in diameter are initially formed, subsequently fragmenting spontaneously into monodispersed calcite nanograins. Therefore, the reduction in crystallite size observed in the Rietveld refinement results can be attributed to this fragmentation process, which reflects a shift from crystal growth to nucleation-dominated formation, leading to finer calcite domains. Moreover, the total amount of amorphous phases also decreases in carbonation-cured samples, indicating the carbonation of Ca-bearing phases [219].

4.3.2 Estimation of the CO_2 uptake

CO_2 uptake is expressed as $CaCO_3$ content in carbonation-cured specimens up to 28 days. Rietveld refinement results (Figure IV-17) reveal that the CO_2 uptake of RCA-based specimens is relatively higher than that of their NCA-based counterparts. Both LS-RCA and SSP-RCA follow a consistent trend of rapid early carbonation within the first 7 days, reaching approximately 32-33 wt% $CaCO_3$, followed by a slight decline to 25-26 wt% at 28 days.

The NCA-based specimens exhibit similar CO_2 uptake during the initial carbonation stage. They also maintain comparable levels at the final curing age. The main difference between these specimens appears at the intermediate carbonation age, when SSP-NCA specimens retain more CO_2. In contrast,

the LS-NCA specimens appear to undergo continued hydration rather than further carbonation, as previously discussed.

Overall, based on Rietveld quantification, RCA-based specimens exhibit greater potential for CO_2 storage across all stages of carbonation curing. The results align with the mass loss method (§ 4.2). NCA-based specimens achieve comparable CO_2 storage only at the final age, with early-age hydration dominating in LS-NCA specimens.

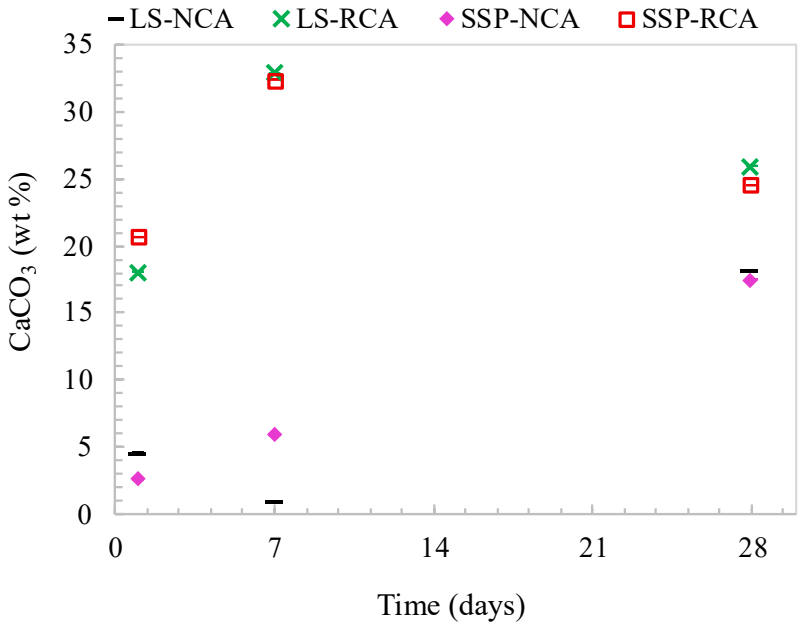

Figure IV-17: Estimation of CO_2 uptake in carbonated samples via Rietveld-based $CaCO_3$ content up to 28 days.

5 Synthesis

The evolution of the CO_2 uptake of the four self-compacting concretes (SCC) mix designs, incorporating either natural coarse aggregates (NCA) or recycled coarse aggregates (RCA), combined with limestone (LS) or scallop shell powder (SSP), was conducted using four complementary methods: carbonation front depth (phenolphthalein test), thermogravimetric analysis (TGA), mass loss profile, and Rietveld refinement of X-ray diffraction data. Each evaluation method provided meaningful insights into the response of each mix design specimen to carbonation. However, when comparing the results obtained from these methods, some inconsistencies were observed. Certain specimens appeared to exhibit higher carbonation levels in one method while showing less pronounced changes in another. These discrepancies suggest that the outcomes from one technique do not always align perfectly with

one another, which may be due to the techniques probing the same material differently or reflecting different pathways in the carbonation mechanism.

The main findings of TGA are that the carbonation process in all specimens resulted in a relatively heterogeneous $CaCO_3$ precipitation within their matrices. This can be relevant, given that carbonation is a diffusion-controlled process in which CO_2 transport and its interaction with the inner concrete matrix may collectively contribute to the observed heterogeneity. The TGA results also indicated that NCA-based specimens, whether incorporating LS or SSP, stored equal or, in most cases, greater amounts of CO_2 than their RCA-based counterparts. Interestingly, this trend aligns with the phenolphthalein results, which showed that these specimens exhibited higher carbonation depths across carbonation curing ages. However, when comparing these results with data from mass loss analysis and Rietveld refinement, notable discrepancies emerged, highlighting inconsistencies in CO_2 uptake trends.

When considering the results of Rietveld refinement and mass loss analysis, both methods indicated that RCA-based specimens stored more CO_2 than their NCA-based counterparts, although the quantified uptake differed between the two methods. These consistent trends, despite the differences in the quantitative data, suggest that these mixes have a greater capacity for carbonation under the studied conditions. This behavior is commonly attributed to the increased porosity introduced by RCA incorporation in concrete, which enhances CO_2 diffusion and facilitates its permanent conversion to $CaCO_3$. However, this assumption appears contradictory when considering the observed carbonation depth results. As discussed earlier, the RCA-based specimens exhibited the lowest carbonation depth, which would typically suggest limited CO_2 uptake. At the same time, LS-NCA specimens showed higher carbonation depth, yet exhibited lower total uptake than SSP-NCA. This indicates a lower reactivity toward carbonation despite greater CO_2 penetration.

Furthermore, SSP and LS showed a limited reactivity toward the aluminate phases, as the Hc content was very low. Therefore, their chemical contribution to carbonation, by providing more hydrates for carbonation, is minimal. Nevertheless, Rietveld refinement results indicated that hydration dominated the reaction mechanism within LS-NCA specimens, particularly at the early ages. This was evident from the higher content of hydration products and the lower total $CaCO_3$ content compared to SSP-NCA. The results analysis also raises a critical question: if both LS-NCA and LS-RCA specimens contain LS, why did LS-RCA exhibit stronger carbonation reactivity, rather than following the same reaction pathway as its LS-NCA counterpart? It can be hypothesized that the lower initial water content in LS-NCA specimens before carbonation may have favored continued hydration over carbonation, especially at early ages. The limited availability of early hydration products may have delayed carbonate formation, with carbonation becoming more effective only after further hydration.

To conclude, while the type of precursors and coarse aggregates used in the mix design does influence CO_2 uptake to some extent, their effect is relatively minor compared to other factors. The

initial water content and the dynamic competition between hydration and carbonation processes play a more critical role in determining carbonation progression and CO_2 storage. Thus, a multi-method approach is not only useful but essential to capture the complex reality of carbonation in modern cementitious materials, particularly those incorporating recycled or alternative constituents

Chapter V

Analysis and quantification of CO_2 uptake

1 Introduction

Carbonation curing is increasingly investigated as a potential alternative to conventional curing methods in the construction industry, with the intended benefits of improving concrete performance while mitigating CO_2 emissions by optimizing the CO_2 uptake. However, the effects of carbonation curing on the properties of SCC remain inconclusive, leaving uncertainty about whether this approach can reliably and effectively replace conventional curing regimes. This chapter also aims to provide an in-depth analysis of carbonation-cured specimens to hopefully address the knowledge gap surrounding the underlying mechanisms and property evolution.

Therefore, this chapter initially investigates the effect of carbonation curing by comparing carbonation-cured and sealed-cured specimens to isolate its influence on the same set of properties previously examined in Chapter 3. These include compressive strength, water-accessible porosity, bulk density, water absorption, microstructural characteristics, pore size distribution, and, additionally, pH evolution. The analysis is then extended to establish correlations and comparisons between the properties of carbonation-cured specimens and those cured under standard curing, to evaluate the extent to which carbonation curing can replicate the performance achieved through standard curing. The chapter concludes with a synthesis of the key findings.

2 Analysis of carbonation curing-induced modification within SCC

2.1 Physical and mechanical properties

2.1.1 Compressive strength

The mechanical properties of the SCC specimens were evaluated through the evolution of compressive strength (Figure V-1). The comparison between carbonation-cured (Figure V-1a) and sealed-cured specimens (Figure V-1b) highlights the influence of curing conditions on strength development at different ages. To complement this analysis, the relative strength gain is also reported (Figure V-1bc and d).

Overall, the compressive strength of all carbonation-cured specimens exhibits an increasing trend over time (Figure V-1a), with no negative long-term impact [176]. After 1 day of carbonation curing, LS-NCA specimens exhibit the highest early strength gain (≈ 8%) compared to their sealed-cured counterparts (Figure V-1c). In contrast, SSP-NCA specimens exhibit lower gain, with an increase of only around 5% (Figure V-1d). Meanwhile, LS-RCA and SSP-RCA specimens demonstrate a similar improvement of about 4%.

As carbonation progresses, the compressive strength increases gradually at different rates depending on the SCC mix design. Ultimately, by the 28th day of carbonation curing, the compressive strength of the specimens follows the decreasing order: LS-NCA (≈ 41 MPa) > LS-RCA (≈ 39 MPa) > SSP-NCA (≈ 36 MPa) > SSP-RCA (≈ 35 MPa). The order remains the same after 90 days, with relative gains of approximately 9%, 1%, 15%, and 3.1% for LS-NCA, LS-RCA, SSP-NCA, and SSP-RCA, respectively (Figure V-1d). The differences in compressive strength observed among the SCC specimens are not only attributable to $CaCO_3$ precipitation during carbonation curing. As demonstrated in Chapter IV, they also reflect the dominant reaction mechanisms within the interstitial solution of the SCC. These differences may further arise from densification of the cementitious matrix induced by variations in the pathways of $CaCO_3$ precipitation [160,398,399].

Furthermore (Figure V-1b), the compressive strength of sealed-cured LS-NCA specimens develops more slowly and reaches a steady state earlier than other specimens. The predictable trend reflects the limited remaining water content in LS-NCA specimens after the pre-conditioning step, as compared to RCA and SSP specimens, which retain more moisture due to their higher porosity and, in the case of SSP, the presence of organic matter (Chapter II2.1.2.3). The remaining specimens exhibit similar strength development patterns, with closely overlapping tendencies. However, across all specimens, the pre-conditioning step leads to a significant reduction in compressive strength of nearly 50%.

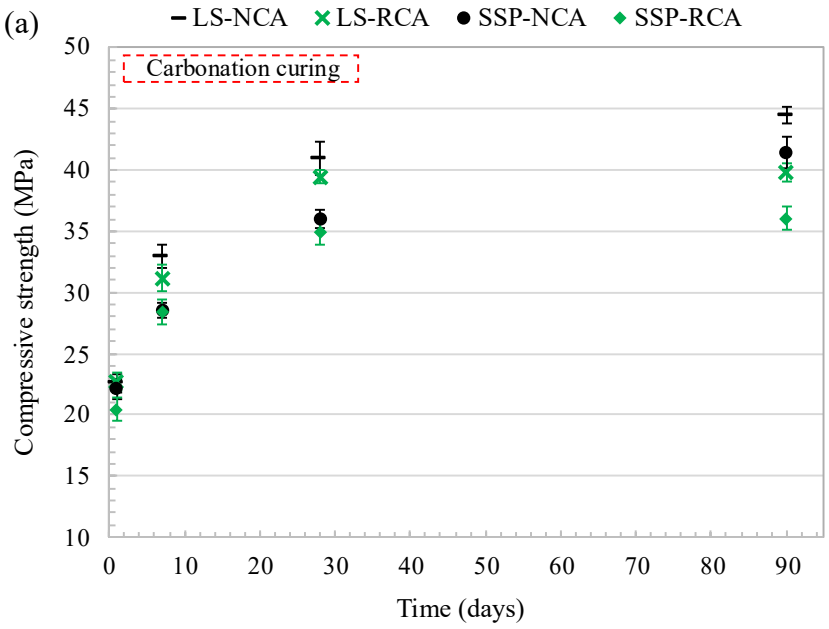

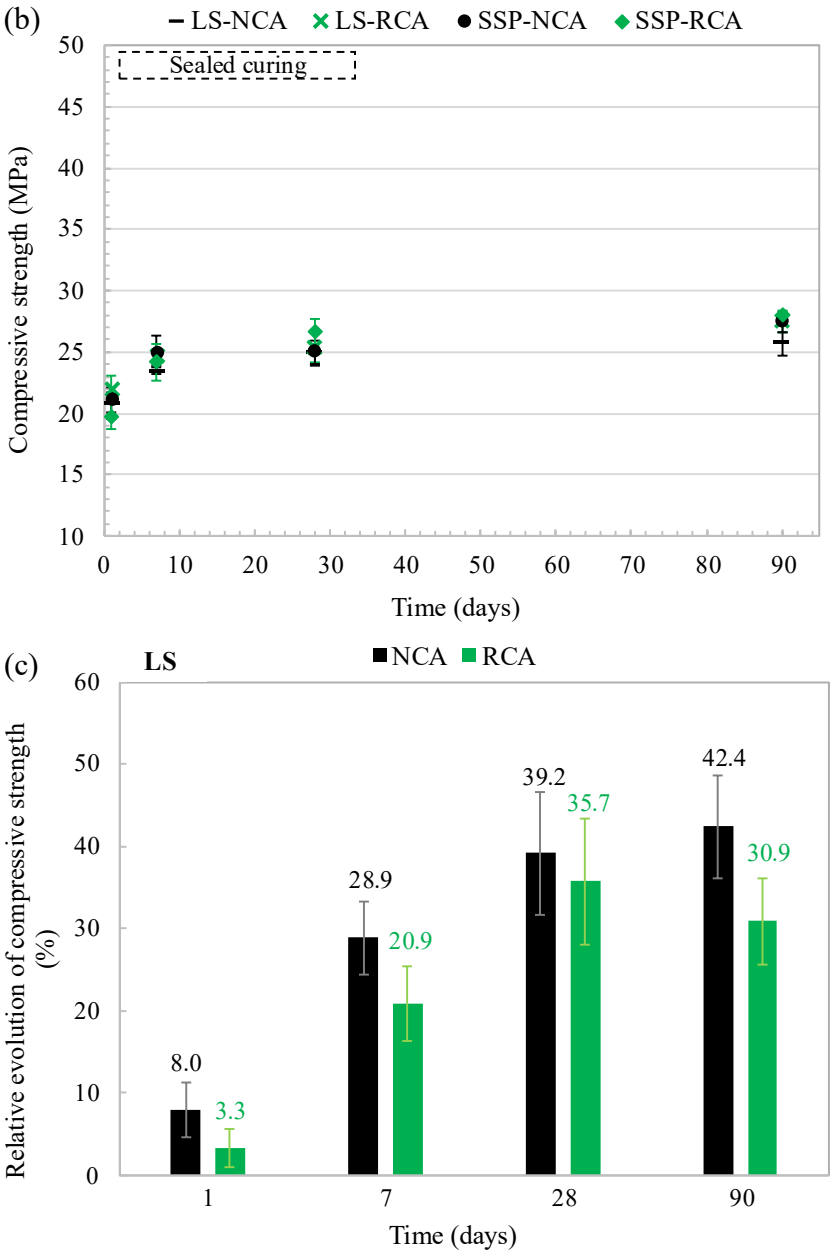
(b)
LS-NCA
LS-RCA
SSP-NCA
SSP-RCA
Sealed curing
Compressive strength (MPa)
Time (days)
(c)
LS
NCA
RCA
Relative evolution of compressive strength (%)
8.0
3.3
28.9
20.9
39.2
35.7
42.4
30.9
Time (days)

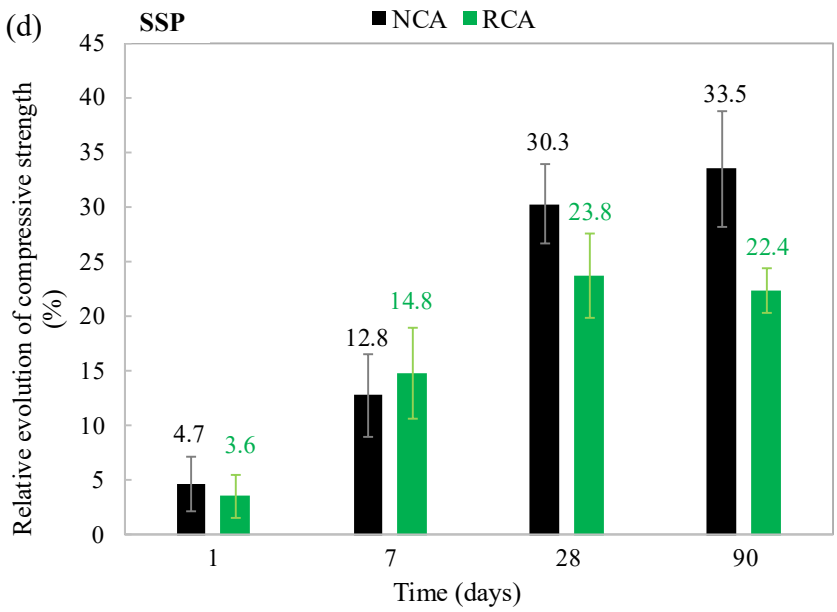

Figure V-1: Compressive strength of SCC specimens: (a) Carbonation curing and (b) Sealed curing; (c-d) Relative strength evolution under carbonation curing for LS- and SSP-based specimens.

Without reiterating the background previously established in the bibliographic chapter on the parameters influencing compressive strength, the focus here is on how the present data support or challenge those earlier insights. Accordingly, the analysis emphasizes CO_2 uptake, carbonation-reactive hydrates as indicated by TGA and XRD, and measurements of the carbonated area, to identify the mechanisms governing fluctuations in the compressive strength of SCC specimens.

2.1.1.1 CO_2 uptake (mass loss method) and the compressive strength relationship

To further understand the underlying factors responsible for the strength development and variation observed among the SCC specimens, the relationship between CO_2 uptake and compressive strength was first examined (Figure V-2). Overall, all specimens demonstrate a positive correlation, with the compressive strength increasing as the overall CO_2 uptake increases, a trend well-supported in the literature [158]. However, a closer comparison reveals that higher CO_2 uptake does not consistently translate into superior strength performance, particularly evident in the LS-NCA specimens. These specimens exhibit relatively higher compressive strength despite moderate CO_2 uptake compared to the other specimens. For instance, at 7 days, LS-NCA specimens with approximately 3% CO_2 uptake exhibit a compressive strength of around 33 MPa, whereas SSP-NCA specimens with approximately 4% CO_2 uptake reach only about 29 MPa. Moreover, the strength development of SSP-NCA follows a nonlinear relationship with CO_2 uptake. Notably, RCA-based specimens exhibit lower compressive strength than their NCA counterparts despite higher CO_2 uptake.

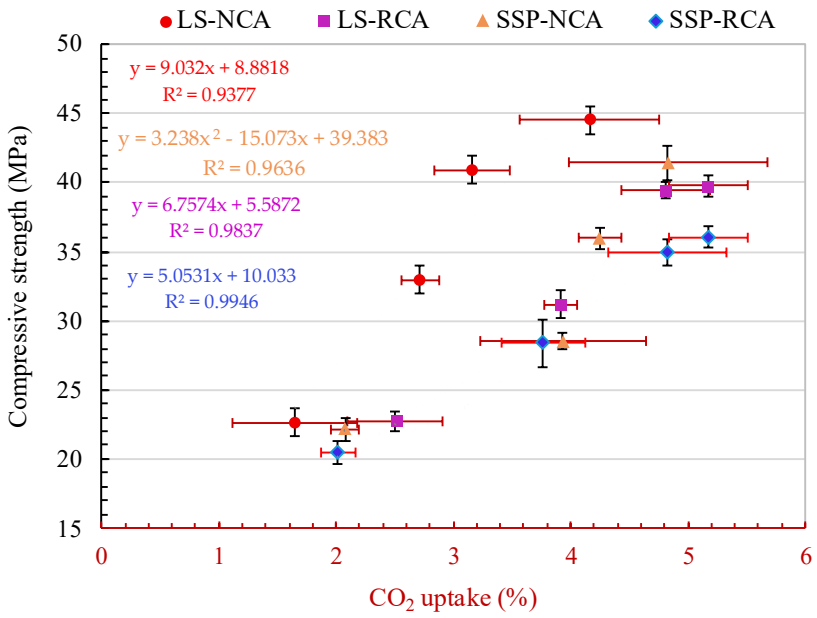

Figure V-2: Relationship between CO_2 uptake by mass loss method and compressive strength of carbonation-cured SCC specimens over different curing ages.

Therefore, it is unlikely that CO_2 uptake is the sole contributor to the observed differences in compressive strength. This emphasizes the significant influence of SCC mix design, aggregate type, and carbonation kinetics on strength development.

2.1.1.2 Impact of carbonation-reactive hydrates on strength development

Expanding on the earlier discussion, it becomes evident that the CO_2 uptake does not necessarily correlate proportionally with the compressive strength of different SCC mix design specimens. A particularly notable case is the LS-NCA specimens, which exhibit higher compressive strength than their SSP-NCA counterparts despite lower CO_2 uptake. The decalcification of C-S-H, a well-recognized mechanism influencing compressive strength [190,194,219,260,400], appears to be less pronounced in LS-NCA. TGA results show that the $CaCO_3$ content formed through carbonation of C-S-H in LS-NCA specimens decreases progressively over 28 days and remains consistently lower than in SSP-NCA specimens (Figure V-3a). This trend is consistent with the lower $CaCO_3$ content derived from $Ca(OH)_2$ (Figure V-3b), which maintains the alkalinity of the pore solution and thus supports C-S-H stability [401].

However, this interpretation may appear contradictory at early ages, particularly at 7 days, when $Ca(OH)_2$ consumption in LS-NCA specimens is higher (Figure V-3b). To clarify this, XRD analysis provides complementary insights into the phase composition at this stage. The XRD results (Chapter IV4.3.1.2) reveal a notable increase in hydration products in LS-NCA specimens, particularly $Ca(OH)_2$.

This indicates that hydration generates more $Ca(OH)_2$ than is consumed by carbonation, offering a plausible explanation for the superior compressive strength observed in LS-NCA specimens.

These findings suggest that superior strength development arises from the synergistic interaction of hydration and carbonation, where ongoing hydration combined with moderate carbonation (without excessive C-S-H destabilization) fosters higher compressive strength. This balance is clearly achieved in LS-NCA specimens, which exhibit the largest gains in compressive strength at later ages.

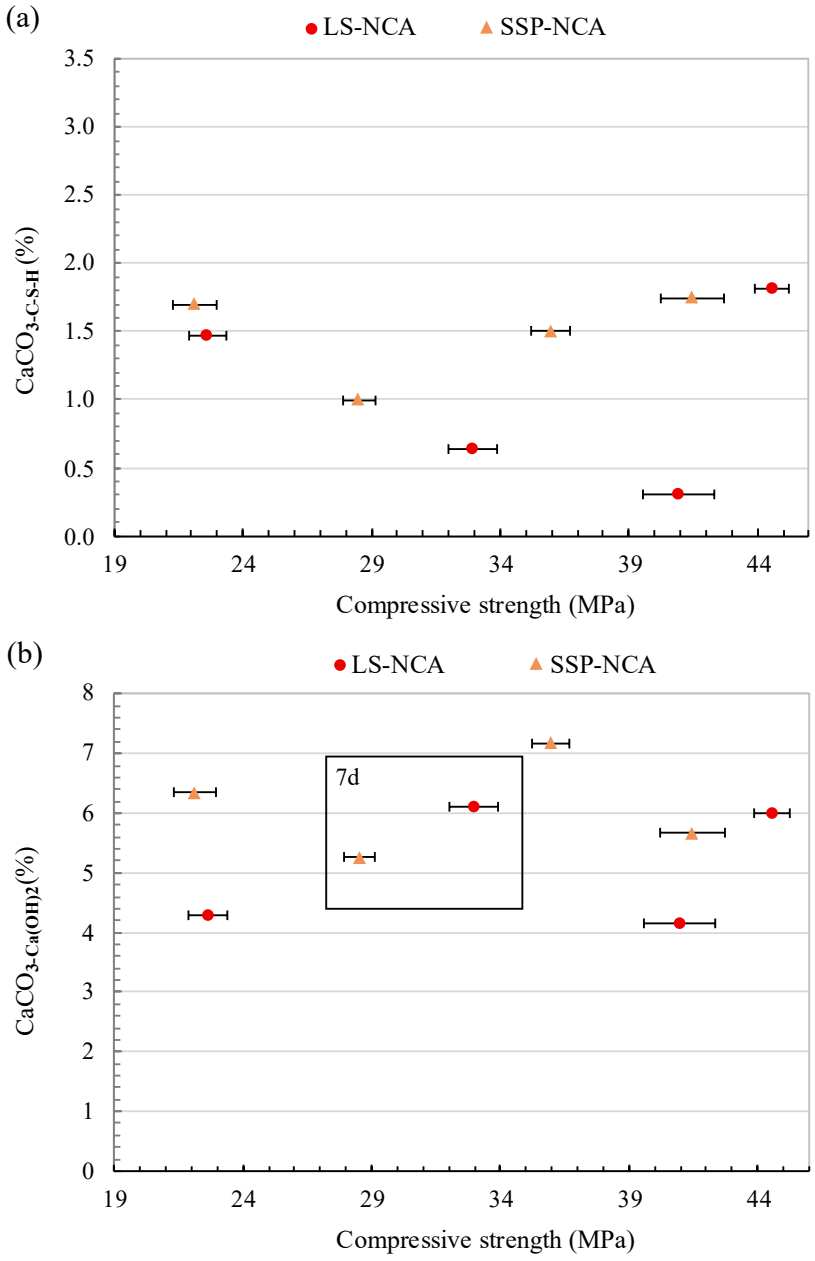

Figure V-3: Relationship between carbonated hydrate phases and the compressive strength exhibited by SCC specimens (TGA results).

Regarding RCA-based specimens, identifying the primary factors responsible for the differences in compressive strength is complicated by the similar mineralogical profiles of LS-RCA and SSP-RCA specimens, as well as the considerable variability in hydrate contents that undergo carbonation. Nevertheless, their lower compressive strength compared to their corresponding NCA counterparts remains apparent. Carbonation curing does not fully compensate for the strength reductions associated with the incorporation of RCA and, to a lesser extent, SSP, which can once again be attributed to the inherent defects of RCA (lower mechanical properties, etc.).

2.1.1.3 Relationship between carbonation depth and compressive strength

Several studies have correlated compressive strength evolution with carbonation depth, reporting that compressive strength decreases as carbonation depth increases. This inverse relationship is attributed to the fact that both carbonation depth and compressive strength are primarily governed by the pore system of the concrete [402,403]. However, this approach may oversimplify the complex interplay between carbonation chemistry and the microstructural changes.

In carbonation curing, compressive strength increases with curing time (Figure V-4). This is not simply a matter of depth but relates closely to the extent of carbonation within the specimen volume. For instance, LS-NCA specimens, which exhibit the lowest initial water content, enable deeper CO_2 diffusion (Figure IV-3), resulting in carbonation occurring across a larger volume despite a relatively low total CO_2 uptake. These observations (Figure V-4a, b, and c), particularly for LS-NCA specimens, suggest that the distribution of precipitated $CaCO_3$ over a larger volume of the specimen, an aspect that will be further discussed in the following section, may be more beneficial for enhancing compressive strength than when the carbonation products are concentrated in more localized zones, potentially explaining the superior compressive strength of these specimens across all carbonation curing ages. Once full carbonation is achieved, the final compressive strength is strongly influenced by the microstructural transformations induced by carbonation and the inherent composition of the SCC mix design (Figure V-4d).

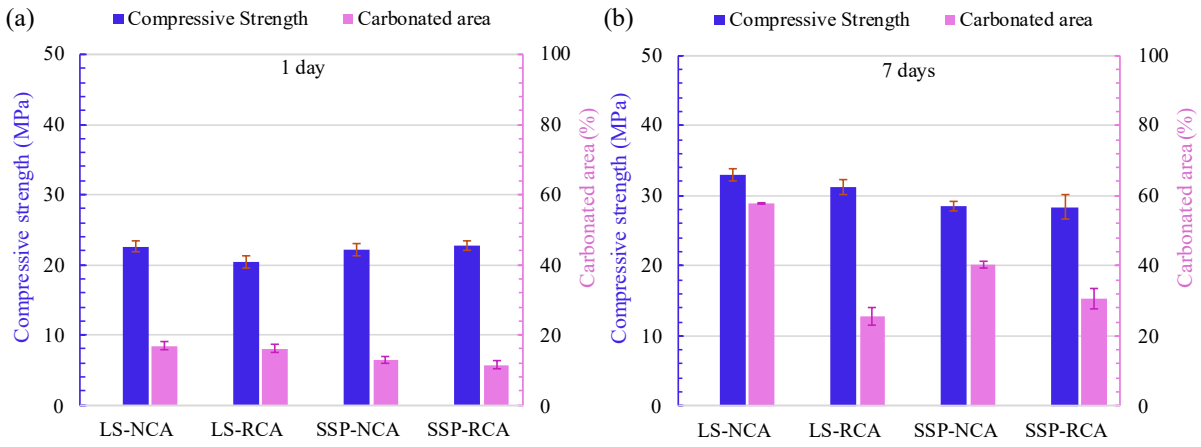

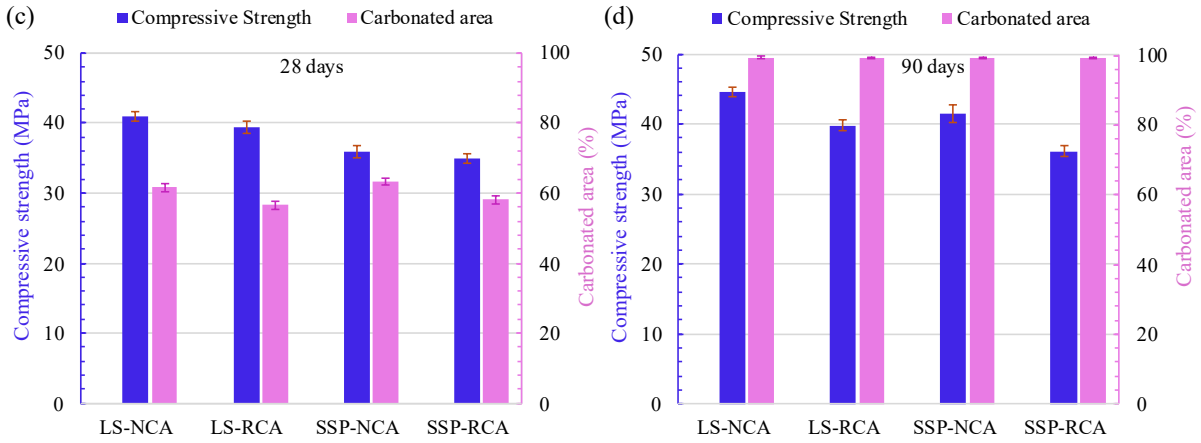

Figure V-4: Relationship between carbonated area and the compressive strength exhibited by SCC specimens.

From the above analysis, the observed variation in compressive strength among SCC specimens can be attributed to the balance between hydration products and carbonation products, as revealed by the TGA and XRD results. A further critical parameter that emerges from this analysis is the distribution of $CaCO_3$ within the matrix, which is strongly influenced by the pore structure and its relationship with CO_2 diffusion. This aspect will be further examined in the microstructural analysis.

2.1.2 Bulk density

The bulk density of the SCC specimens was measured to evaluate the influence of curing on matrix compaction (Figure V-5). A comparison between carbonation-cured (Figure V-5a) and sealed-cured specimens (Figure V-5b) demonstrates how curing conditions affect density evolution over time. To further complement this assessment, the relative density gain is also presented (Figure V-5c and d).

Overall, an increase in density is observed across all SCC specimens subjected to carbonation curing (Figure V-5a). This enhancement is attributed to the formation of $CaCO_3$, which occupies a larger molar volume than some hydration products, such as $Ca(OH)_2$, thereby promoting matrix compaction and contributing to the observed densification [404–406].

After 1 day of carbonation curing, the carbonation mechanism does not appear sufficiently advanced to induce a significant increase in the specimens' density. The carbonation-cured specimens (Figure V-5a) exhibit comparable densities to their sealed-cured counterparts (Figure V-5b). Nevertheless, the early evolution of bulk density appears slightly more pronounced in SSP-based specimens (Figure V-5d) than in LS-based specimens, with LS-NCA and LS-RCA displaying an approximate 1.1% lag in reaching the density of the sealed-cured specimens (Figure V-5c).

By 7 days and beyond, the improvements in density become evident, with the extent of the increase depending on the mix design (Figure V-5c and d). LS-NCA, followed by LS-RCA specimens, exhibit higher densities, with a consistent trend over time (Figure V-5a). SSP-based specimens (Figure V-5b), on the other hand, have lower densities, with SSP-RCA being the least dense.

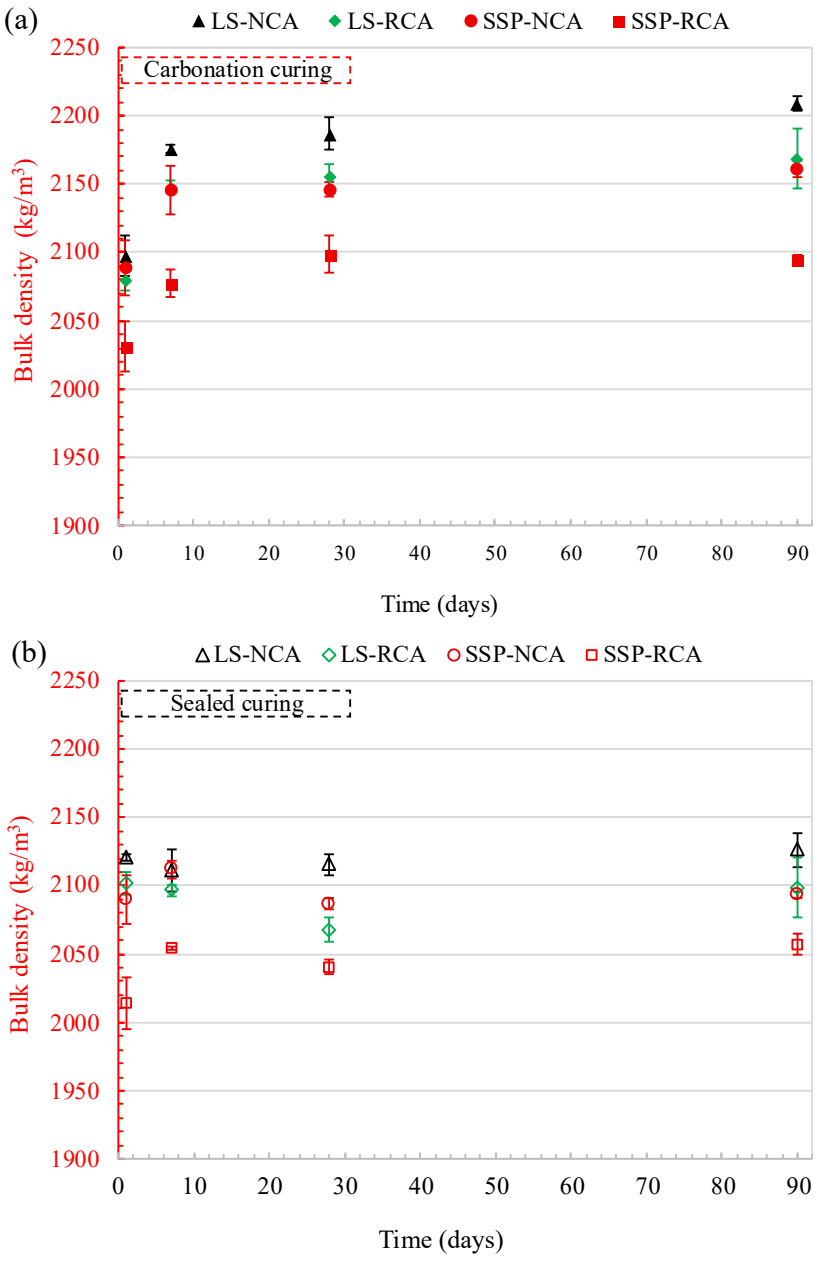

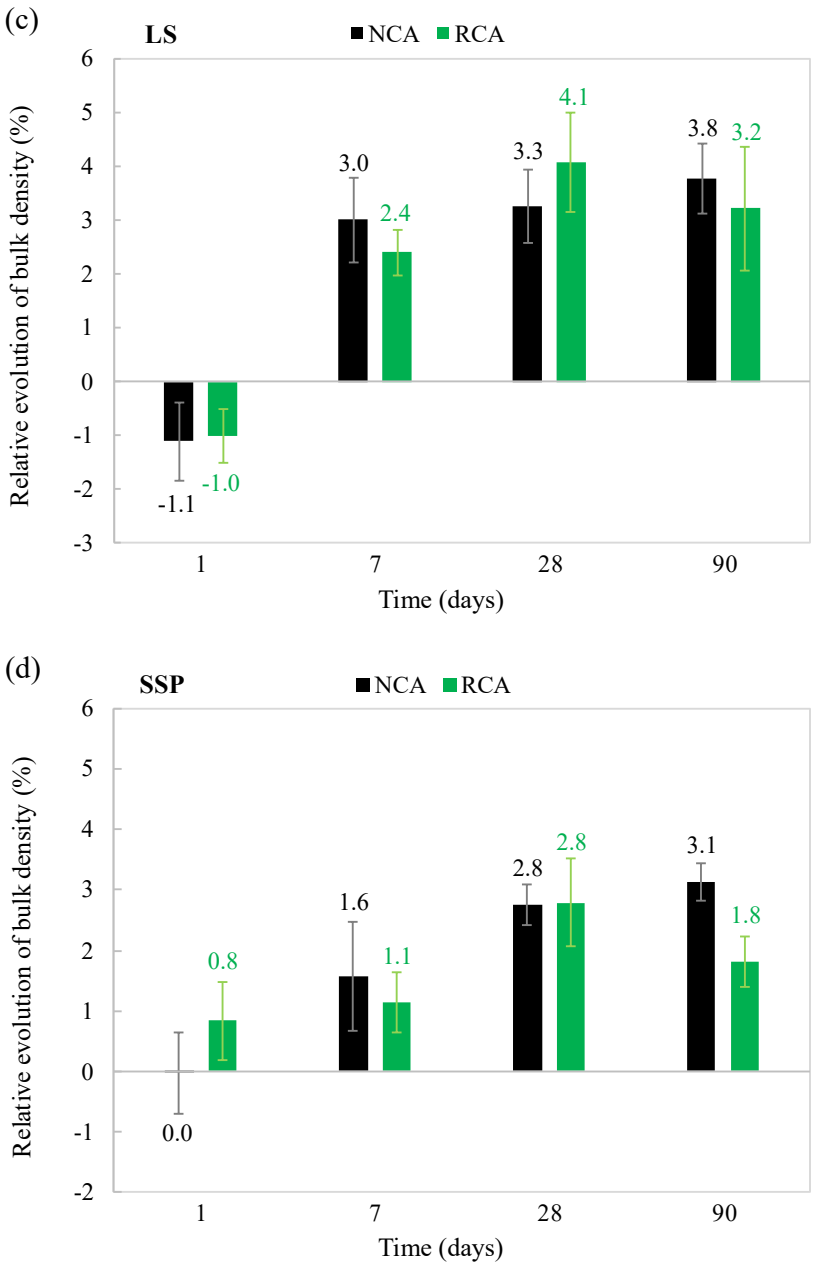

Figure V-5: Bulk density of SCC specimens: (a) Carbonation curing and (b) Sealed curing; (c-d) Relative density evolution under carbonation curing for LS-based and SSP-based specimens.

By 90 days, the LS-NCA, LS-RCA, SSP-NCA, and SSP-RCA specimens reach a final density of 2209 kg/m^3, 2168 kg/m^3, 2161 kg/m^3, and 2095 kg/m^3, respectively. These findings align with the compressive strength results, in which LS-based specimens outperform their SSP-based counterparts in both density and strength. Interestingly, the difference in compressive strength between the LS-NCA and SSP-RCA specimens is 25%, while the difference in their bulk density is around 5%. This disproportionate increase in strength suggests that the microstructural changes from carbonation can cause a much larger increase in compressive strength [158,407].

Overall, all specimens demonstrate a positive correlation, with compressive strength increasing as overall density increases, although the R^2 values differ due to system dependence (Figure V-6). The sustained increase in density observed in LS-NCA specimens over time supports the earlier hypothesis that the distribution of precipitated $CaCO_3$, together with hydration products, enhances microstructural densification and contributes effectively to the development of compressive strength. The lower densities of SSP-based specimens compared to their LS-based counterparts can, once again, be partly attributed, to a lesser extent, to the intra-granular porosity of SSP particles and the presence of organic matter, which prevent optimal particle packing and create micropores that persist even after carbonation, as previously observed during water curing (Chapter III). Furthermore, $CaCO_3$ precipitation may also lead to the formation of additional pores, potentially reducing bulk density, as will be examined in the following section.

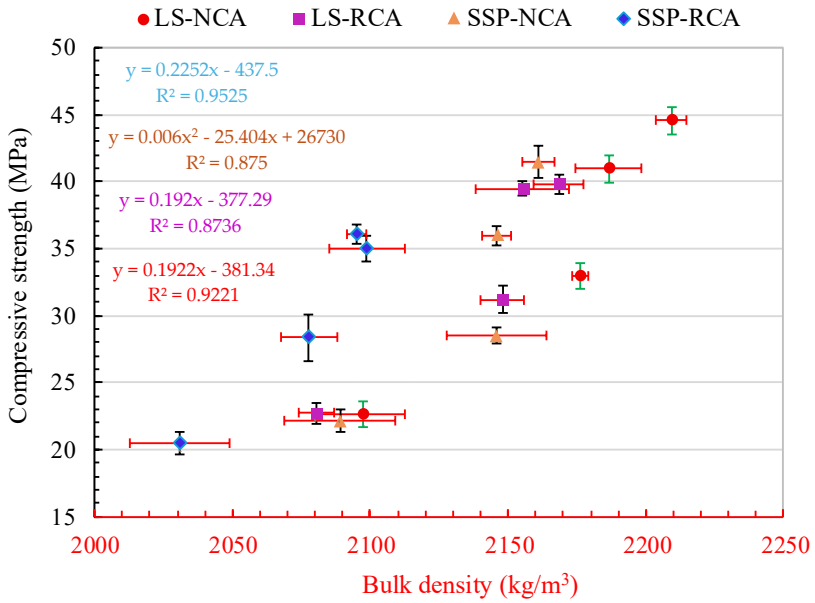

Figure V-6: Correlation between compressive strength and density of carbonation-cured SCC specimens over different curing ages.

2.1.3 Water-accessible porosity

As with other properties of the SCC specimens, the effect of carbonation curing on the water-accessible porosity was evaluated for all four mix design specimens over 90 days (Figure V-7). After 1 day of carbonation curing (Figure V-7a), an overall reduction in porosity is observed for LS-NCA, SSP-NCA, and SSP-RCA specimens compared to their sealed-cured counterparts (Figure V-7b). An exception is noted in LS-RCA specimens, which exhibit a slight increase of approximately 4% (Figure V-7c).

The early decrease in porosity results from the precipitation of $CaCO_3$ from $Ca(OH)_2$, the first phase that undergoes carbonation. Since the molar volume of $CaCO_3$ is about 11–12% greater than that of $Ca(OH)_2$, this transformation induces solid volume expansion and reduces porosity [374,403,408]. In contrast, Junior *et al.* [168] attributed the initial increase in porosity observed during the first 24 hours of curing to extensive surface carbonation, which reduces the water content of the C-S-H gel. C-S-H decalcification, microcracking induced by shrinkage, and transient pore redistribution at the carbonation front may also contribute to this early porosity increase [214,408]. As demonstrated in Chapter IV, RCA-based specimens exhibited higher carbonation than their NCA-based counterparts. This explains the corresponding increase in water-accessible porosity of LS-RCA specimens. The same reaction dynamics may also explain the increased porosity observed in SSP-RCA after 7 days of carbonation curing.

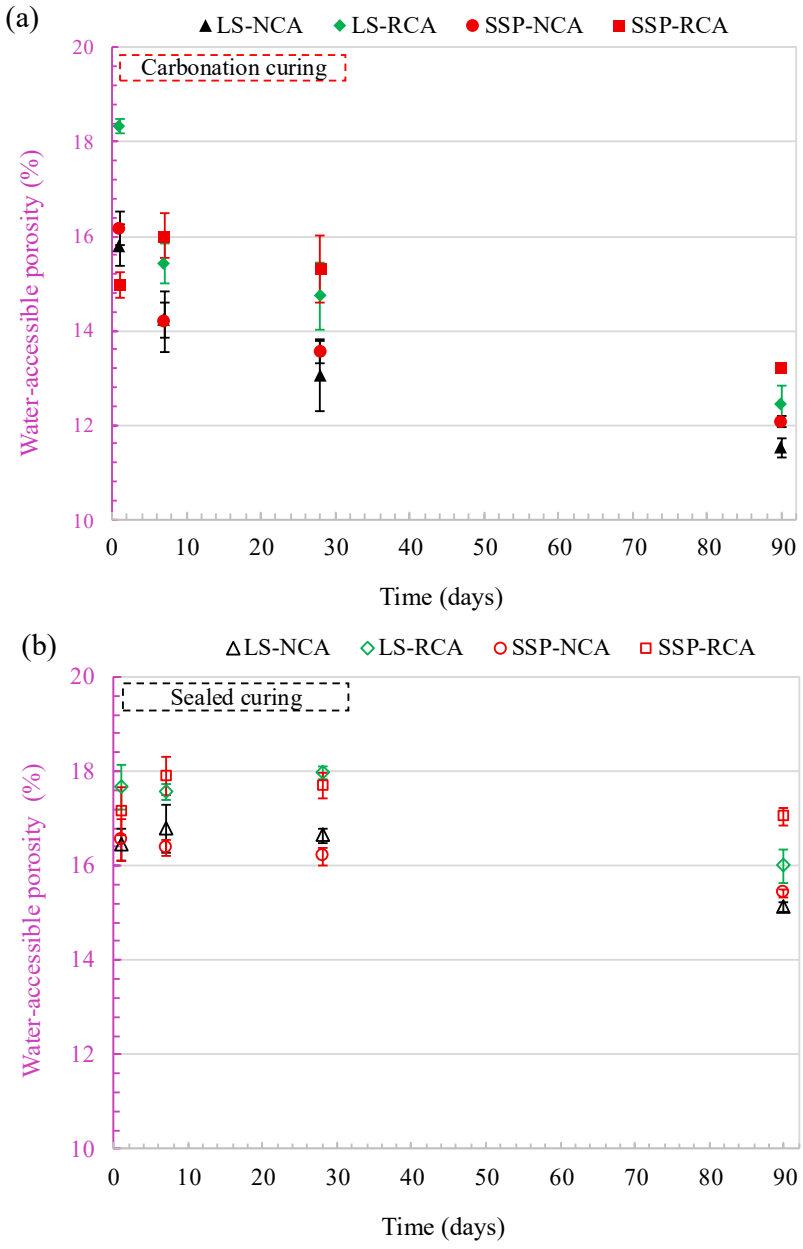

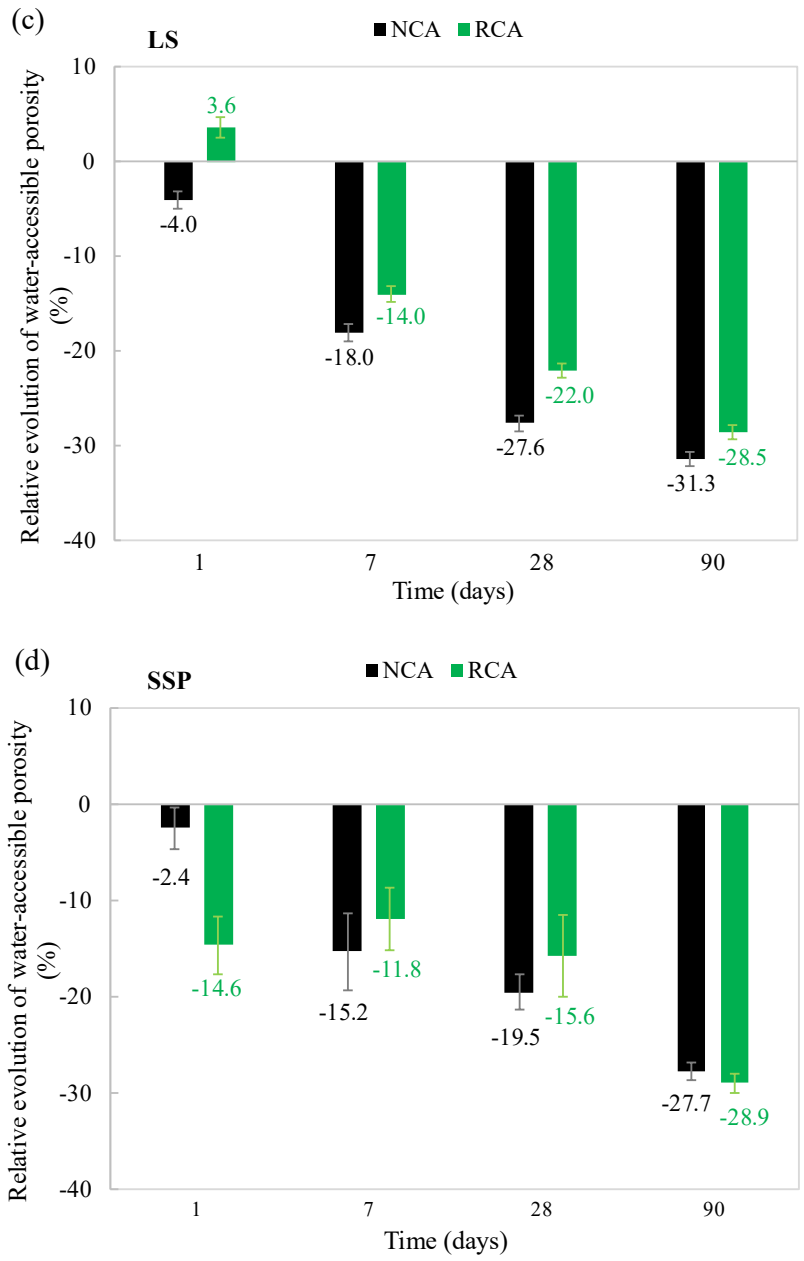

Figure V-7: Water-accessible porosity of SCC specimens: (a) Carbonation curing and (b) Sealed curing; (c-d) Relative water-accessible porosity evolution under carbonation curing compared to sealed curing for LS-based and SSP-based specimens.

Beyond the 7th day, all specimens exhibit a progressive decrease in porosity, albeit to varying extents (Figure V-7c and d). These variations are attributed to differences observed in the carbonation of $Ca(OH)_2$ and the subsequent decalcification of C-S-H, driven by the ongoing CO_2 diffusion into the inner layers of the specimens. This results from the varying precipitation of $CaCO_3$, which clogs the pores, thus redistributing porosity within the matrix [374,408,409].

As expected, LS-based specimens exhibit the most pronounced reduction in porosity during the initial 28 days of carbonation curing (Figure V-7c), followed by a decreasing trend comparable to that of their SSP-based counterparts by 90 days (Figure V-7d). These results are consistent with their compressive strength and bulk density testing. Notably, the slight increase in porosity observed in RCA-based specimens due to carbonation does not negatively impact their compressive strength.

Although carbonation governs the overall water-accessible porosity trend, the influence of the inherent characteristics of aggregates and cement precursors was already evident under the standard curing regime (Chapter III). Therefore, the higher water-accessible porosity of SSP-RCA specimens also reflects the higher porosity of RCA and SSP, whose organic content can trap air and increase accessible porosity.

2.1.4 Water absorption

As expected, the water absorption behavior of the four SCC mix design specimens closely reflects the trend observed in water-accessible porosity (Figure V-8). All specimens exhibit an overall reduction in water absorption under carbonation curing (Figure V-8a), compared to their sealed counterparts (Figure V-8b).

Among the NCA-based specimens, SSP-NCA and LS-NCA exhibit comparable water absorption values at early ages (Figure V-8a). As carbonation progresses, SSP-NCA specimens exhibit a less pronounced decrease in water absorption over time than LS-NCA (Figure V-8c and d). This behavior is attributed to microstructural differences, where the extent of pore refinement induced by carbonation varies between the two mixes [405].

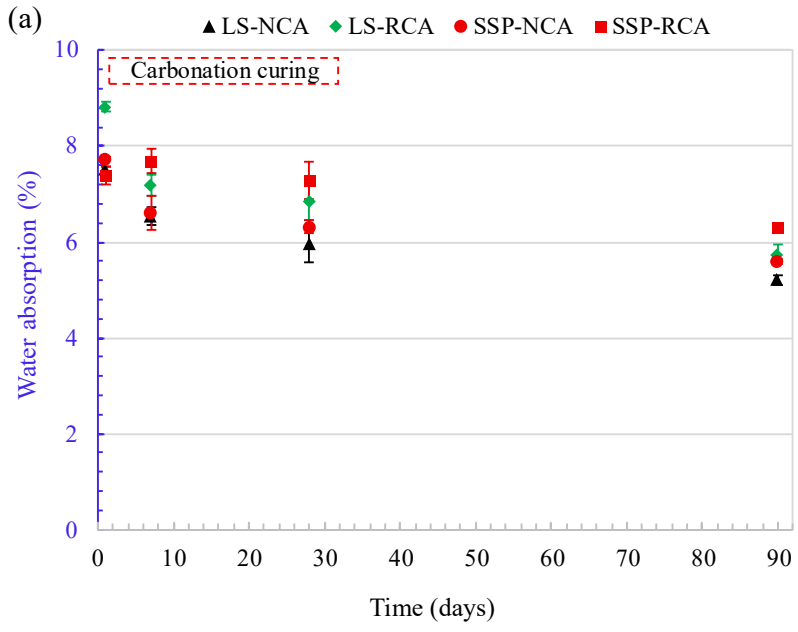

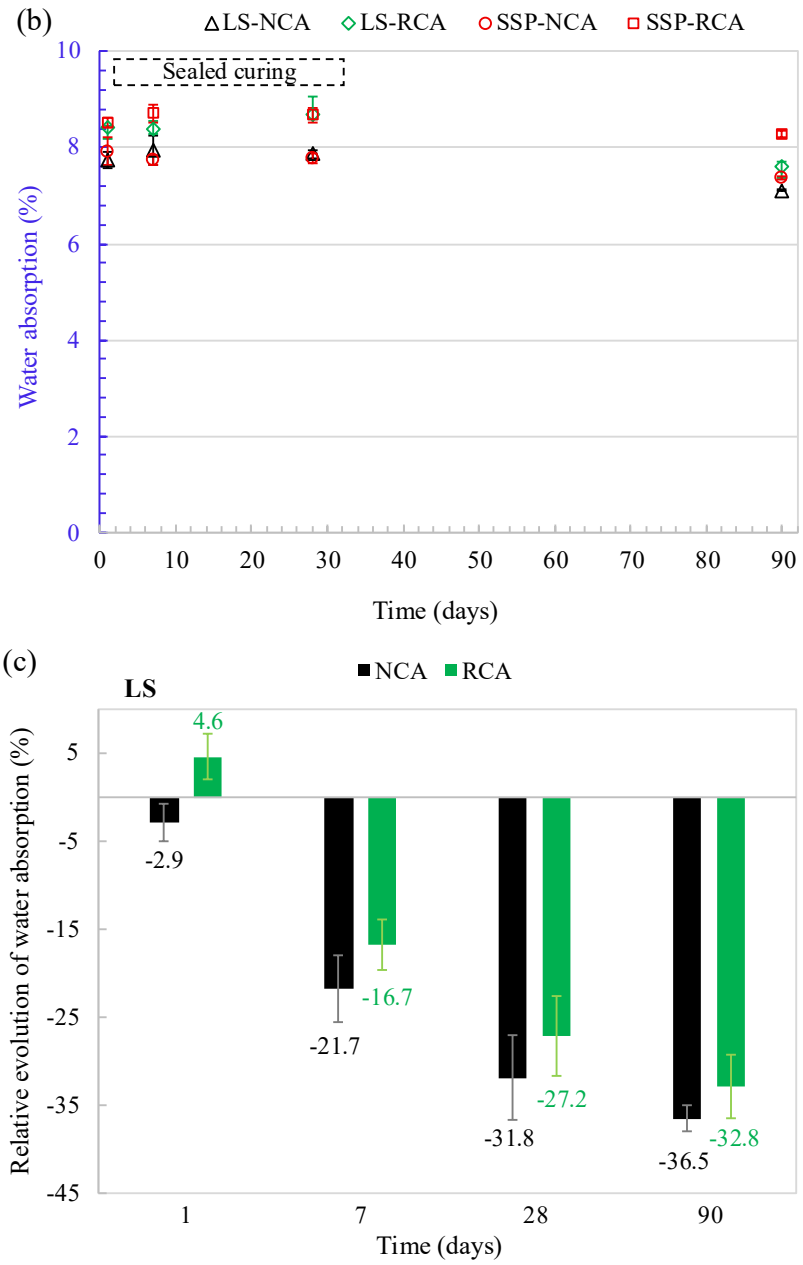
(b)
LS-NCA
LS-RCA
SSP-NCA
SSP-RCA
Sealed curing
Water absorption (%)
Time (days)
(c)
NCA
RCA
LS
Relative evolution of water absorption (%)
4.6
-2.9
-16.7
-21.7
-27.2
-31.8
-32.8
-36.5
Time (days)

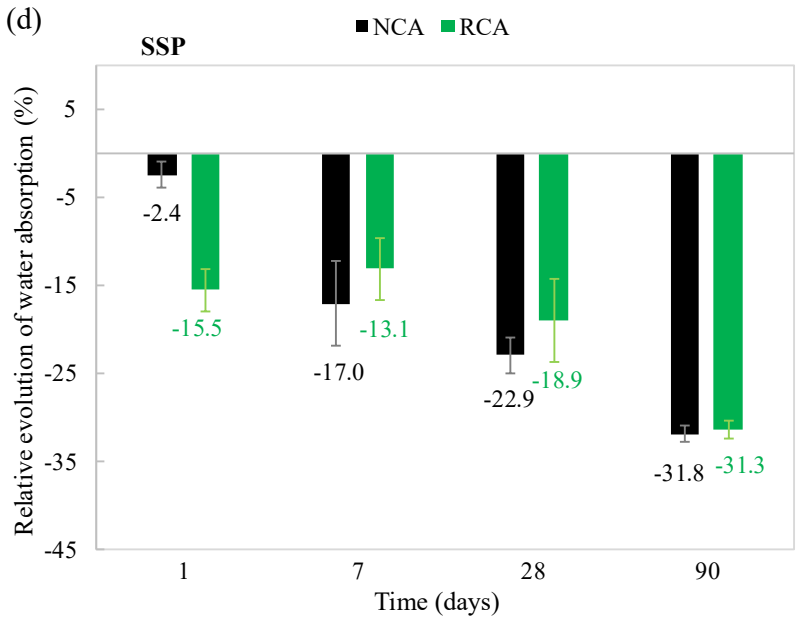

Figure V-8: Water absorption of SCC specimens: (a) Carbonation curing and (b) Sealed curing; (c-d) Relative water absorption evolution under carbonation curing for LS-based and SSP-based specimens.

Regarding RCA-based specimens, LS-RCA specimens (Figure V-8a) exhibit an increase of approximately 5% after 1 day (Figure V-8c), while SSP-RCA specimens exhibit a reduction of around 15% (Figure V-8d). These results are consistent with the corresponding porosity measurements, indicating that the early carbonation can either refine or destabilize the pore network depending on the initial microstructure. At later ages, however, the progressive filling of pores with $CaCO_3$ contributes to a further reduction in water absorption compared to their sealed-cured counterparts (Figure V-8b) [410].

Ren *et al.* [411] attributed the lower sensitivity of the pore structure to water regain to the nanostructure of C-S-H alteration gels caused by carbonation. In other words, when C-S-H undergoes decalcification during carbonation, its structure becomes more polymerized and silica-rich, which decreases its hygroscopic nature, making the pore structure less responsive to water absorption [412].

Even though both porosity (§ 2.1.3) and water absorption decrease over time, RCA- and SSP-based consistently demonstrate higher water absorption than their NCA- and LS-based counterparts, respectively. This distinction highlights the inherent influence of RCA and SSP on pore connectivity and transport properties.

The strong correlation between water absorption and water-accessible porosity (Figure V-9) confirms that both parameters are primarily governed by microstructural refinement rather than by the total pore volume alone. The moderate slope of 0.53 indicates that water absorption increases only partially with water-accessible porosity. This behavior is mainly controlled by pore connectivity, size,

and tortuosity, which are affected by the microstructural changes induced by carbonation in each mix design.

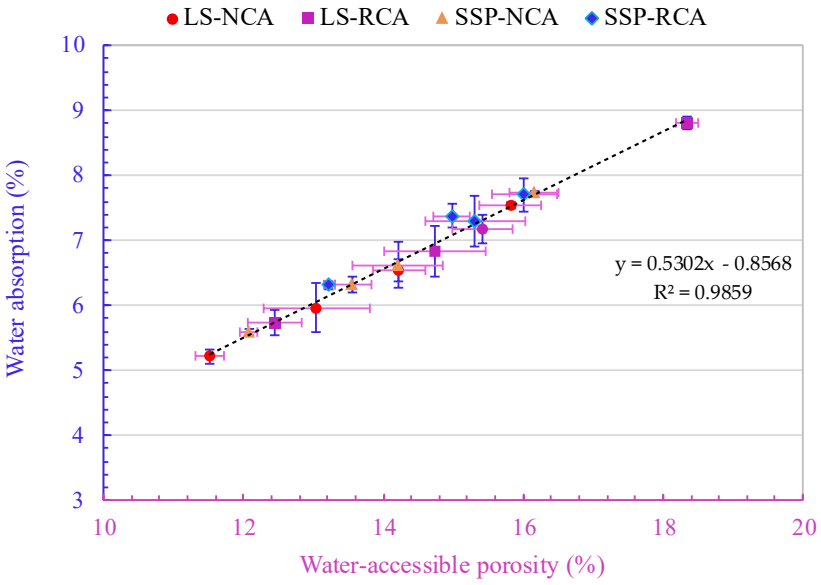

Figure V-9: Correlation between water absorption and water-accessible porosity to water in SCC specimens.

- **General observations**

Based on the analysis of how carbonation alters mechanical and physical properties, carbonation curing improves compressive strength and bulk density, while decreasing water-accessible porosity and water absorption. The extent of these improvements largely depends on: (i) the aggregates (RCA or NCA) and the cement precursors (SSP or LS) used; and (ii) the interplay between hydration and carbonation, which is initially influenced by the water content and the efficiency of CO_2 transport during the simultaneous progression of both mechanisms.

The behavior of the LS-NCA specimens demonstrates that the highest CO_2 uptake does not automatically lead to the best properties; rather, it is the balance between carbonation and hydration that drives the most significant improvements in macroscopic properties. However, estimating the relative extent of carbonation versus hydration is challenging, as this balance is dynamic rather than static, a limitation already highlighted in the literature (Chapter I). Similarly, RCA-based specimens provide evidence that the inherent characteristics of the aggregates directly influence the final mechanical and physical properties, regardless of their interference in the carbonation mechanism.

Although carbonation curing is an effective method for improving compressive strength, bulk density, accessible porosity, and water absorption, to the best of our knowledge, systematic studies on the carbonation curing behavior and these properties in SCC mixtures are lacking. Further research is needed to accurately determine the actual effects of the adopted protocol in this study.

2.2 pH

Carbonation is known to significantly decrease the pH of the cement-based materials, including the considered carbonation-cured SCC specimens (Figure V-10). After one day of carbonation curing, the pH decreases across all SCC specimens from an average of 12.43 to 10.61. This acidification of the pore solution arises mainly from the destabilization of $Ca(OH)_2$, which maintains the cement matrix alkalinity. As carbonation consumes the OH^- ions, the buffering capacity of the pore solution progressively diminishes, leading to the observed drop in pH. At this stage of the pH evolution, other cementitious phases are also destabilized by carbonation (Chapter I3.3.6), consistent with XRD results (Chapter IV4.3).

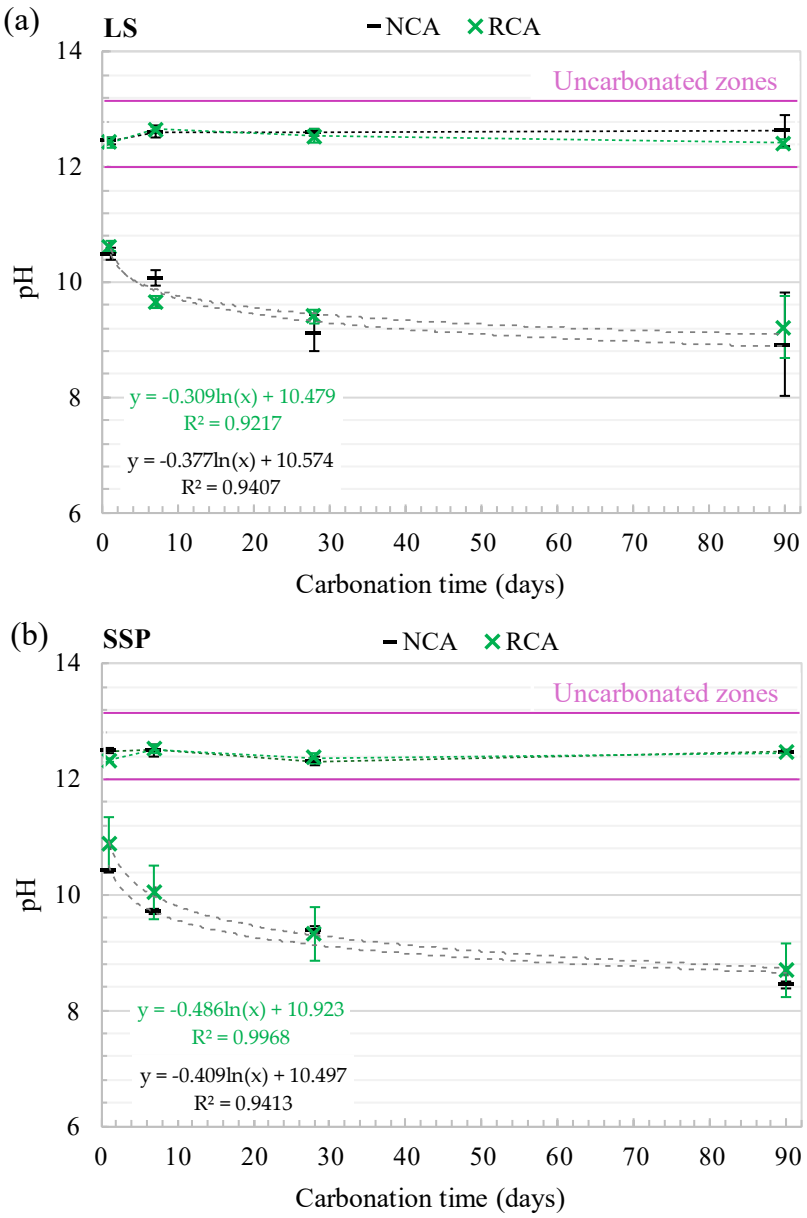

Figure V-10: Evolution of pH of SCC specimens at different carbonation curing ages.

After 7 days of carbonation curing, the pH further decreases but remains above 10 units in LS-NCA and SSP-RCA specimens, and reaches 9.65 and 9.72 in LS-RCA and SSP-NCA (Figure V-10a and b). Before the total consumption of $Ca(OH)_2$, the pH remains above 10.4; maintaining this level may indicate either incomplete $Ca(OH)_2$ consumption or the subsequent formation of hydrated products that buffer the pore solution, delaying further pH decrease [380]. In LS-NCA specimens, the delayed pH decrease is attributed to their higher $Ca(OH)_2$ content at this age, as confirmed by XRD analysis, compared to the other SCC mixes. As carbonation progresses deeper in the SCC specimens, the pH decreases continuously during the 28 days to reach final values at 90 days of 8.92, 8.45, 9.22, and 8.69 for LS-NCA, SSP-NCA, LS-RCA, and SSP-RCA, respectively. At 28 days, Rietveld quantification indicates that no residual $Ca(OH)_2$ remains in any of the specimens.

The progressive decrease in pore solution pH observed across all specimens can be described as a two-stage process. In the initial state, the pH begins to drop as H_2CO_3 forms, partially dissociates, and releases H_3O^+ ions. However, this release contributes minimally, as most H^+ ions are immediately neutralized by abundant OH^- ions present in the highly alkaline medium. Under these conditions, the $CaCO_3$ system is dominated by CO_3^{2-} ions (Chapter I). As $CaCO_3$ precipitates, CO_3^{2-} ions are removed from the solution. Consequently, Eq. V-1 shifts to the right to re-establish equilibrium, promoting further dissociation of HCO_3^- and H_2CO_3 to replenish CO_3^{2-} (Le Chatelier's principle). These reactions consume OH^- from $Ca(OH)_2$, resulting in an initial observed pH drop from approximately 12.4 to around 10.6 across all specimens [413,414].

$$CO_{2(g)} + H_2O \leftrightarrow H_2CO_{3(aq)} \leftrightarrow H^+_{(aq)} + HCO^-_{3(aq)} \leftrightarrow H^+_{(aq)} + CO^{2-}_{3(aq)} \quad \text{Eq. V-1}$$

Once $Ca(OH)_2$ is depleted at 28 days, a second stage begins in which the CO_3^{2-}/HCO_3^- equilibrium dominates the pore solution chemistry of SCC specimens. As CO_3^{2-} continues to be consumed through $CaCO_3$ precipitation, this equilibrium repeatedly shifts to the right, releasing additional H^+ ions and causing a gradual pH decrease, as long as Ca^{2+} (e.g., from the destabilization of other hydrates) and CO_3^{2-} ions remain available. When the pH approaches approximately 8, CO_3^{2-} ions are no longer stable in solution, and the carbonation process effectively stops, as observed after 90 days in the SCC specimens [158,413,415].

During this process, other factors may contribute to the observed pH fluctuations across the specimens. Alkali ions (Na^+, K^+) in the pore solution may be incorporated into the C-S-H structure as Ca^{2+} is leached, modifying local alkalinity. In SSP-based specimens, the decomposition of organic matter may also slightly increase local pH through the release of weakly basic organic compounds.

Therefore, the evolution of the pH of the pore solution during carbonation is governed not only by the consumption of $Ca(OH)_2$ (Eq. I-5), but also by intermediate buffering reactions and equilibrium processes that regulate the pore solution chemistry.

2.3 Microstructural analysis

2.3.1 Pore structure analysis: MIP testing

The effect of carbonation curing on the pore structure was evaluated using mercury intrusion porosimetry (MIP) at 1, 7, and 28 days of curing. The results (Figure V-11) reveal that carbonation curing could heterogeneously influence the pore network across the specimens. After 1 day of carbonation curing, LS-NCA specimens exhibit a total porosity of approximately 16%, with a dominant intrusion peak at the critical pore diameter (d_c) of around 350 nm (Figure V-11a). Around 60% of the pore network consists of pores larger than 20 nm, mainly in the 20–50 nm and 50–200 nm ranges (Figure V-11b). In comparison, SSP-NCA specimens show a slightly lower total porosity (≈3% less) and a flatter intrusion peak centered at $d_c \approx 220$ nm, although nearly 80% of their pores also exceed 20 nm within similar size ranges (Figure V-11b).

On the other hand, LS-RCA and SSP-RCA specimens exhibit higher total porosity of approximately 16% and 18%, respectively. The pore network in SSP-RCA is characterized by the sharpest and most pronounced intrusion peak at $d_c \approx 280$ nm, with roughly 80% of the pores exceeding 20 nm in diameter, mainly within the 50–200 nm range (Figure V-11a and b). In comparison, LS-RCA specimens exhibit a less intense dominant peak at $d_c \approx 500$ nm, with approximately 70% of pores larger than 20 nm, primarily concentrated within the 20–50 nm and 50–200 nm ranges.

At this early stage, it is difficult to directly evaluate the changes induced by carbonation, since MIP testing was not performed on the sealed-cured specimens to provide a baseline. However, the progressive changes in the pore network can be evaluated over the course of carbonation curing, although pore connectivity may partially influence CO_2 diffusion at later ages.

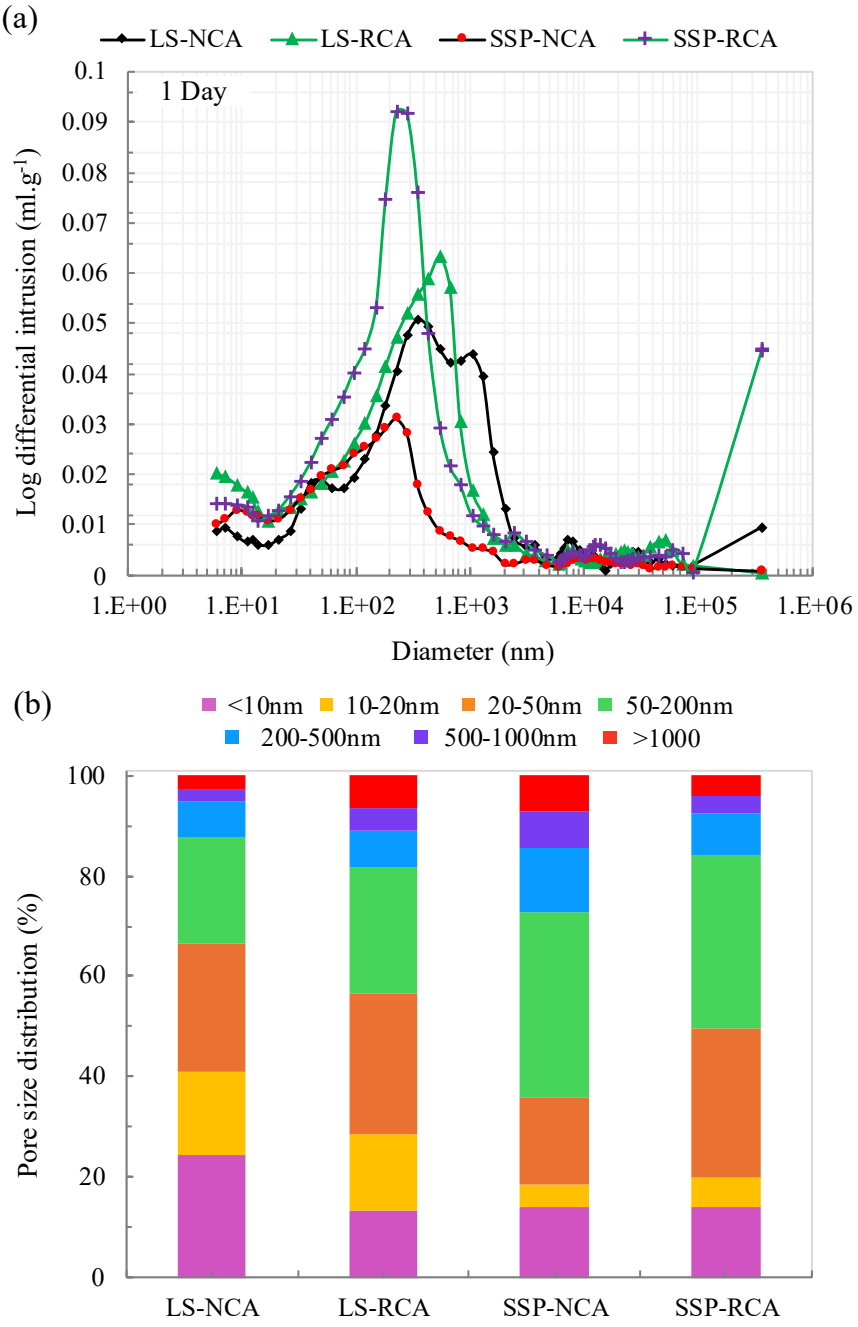

Figure V-11: MIP testing results of SCC specimens after 1 day of carbonation curing: (a) differential intrusion curves and (b) corresponding pore size distribution profiles.

As carbonation progresses to 7 days of curing (Figure V-12), the total porosity of LS-NCA specimens decreases to approximately 14%. The dominant peak, initially broad at 1 day, shifts toward smaller diameters, becoming sharper and more well-defined at $d_c \approx 77$ nm, accompanied by a secondary peak at approximately 450 nm (Figure V-12a). A slight increase in pores exceeding 1000 nm is observed, along with a more pronounced increase in the 50–200 nm range (Figure V-12b). The microstructure of SSP-NCA specimens, on the other hand, coarsens during carbonation, with an increase in total porosity

to approximately 13.5%. The dominant peak shifts toward larger pore diameters, with increased intensity at $d_c \approx 380$ nm, while an increase in pores within the 50–200 nm range and those larger than 1000 nm is also observed (Figure V-12a and b). These observations highlight the more uniform microstructure of LS-NCA specimens, supporting the physical and mechanical testing results. It is also important to note that the two cement precursors can partly influence the coarsening of the pore system. In contrast to LS, the porosity of SSP and its organic matter contribute to the formation of additional voids that may persist after carbonation, regardless of mix design or curing age.

Regarding RCA-based specimens (Figure V-12a and b), the total porosity decreases to 12% for LS-RCA and 14% for SSP-RCA specimens. The latter specimens remain slightly higher than SSP-NCA due to their initially more porous microstructure. In LS-RCA, the dominant intrusion peak becomes less intense and shifts to lower $d_c \approx 280$ nm, accompanied by a marked reduction in pores within the 20-50 nm range. By contrast, SSP-RCA specimens exhibit a slight decrease in peak intensity with the peak shifting to smaller pores at approximately 180 nm, while the pore network remains largely governed by pores in the 50-200 nm range. These results indicate progressive pore refinement in both mixes, but more pronounced in LS-RCA.

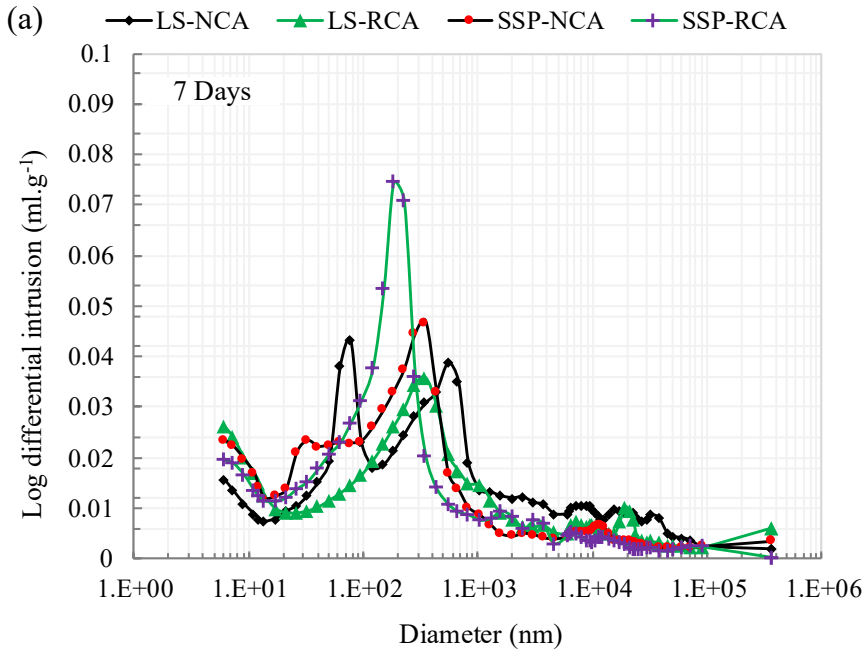

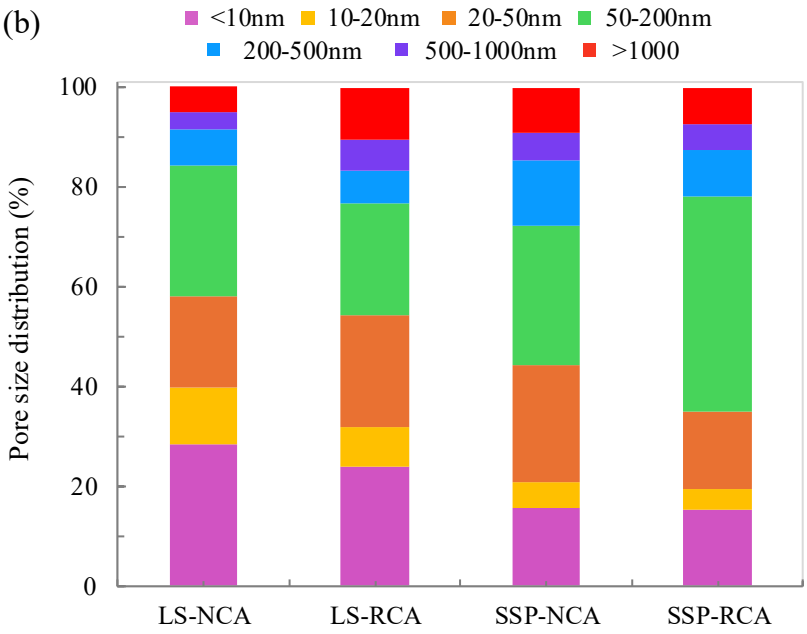

Figure V-12: MIP testing results of SCC specimens after 7 days of carbonation curing: (a) differential intrusion curves and (b) corresponding pore size distribution profiles.

After 28 days of carbonation curing (Figure V-13), the LS-NCA specimens exhibit a further reduction in total porosity (≈ 12%), while the SSP-NCA specimens show no significant change in total porosity. The pore structure of both specimens continues to evolve, as evidenced by the emergence of a sharper intrusion peak at $d_c \approx 32$ nm. However, the pore size distribution in SSP-NCA is dominated by pores in the 200–500 nm range (Figure V-13a and b). In LS-NCA specimens, the dominant intrusion peak broadens, with a more uniform pore distribution (Figure V-13a and b).

The RCA-based specimens, in turn, exhibit a further decrease in total porosity (≈ 11% for LS-RCA and ≈ 13% for SSP-RCA), reaching values comparable to their corresponding NCA specimens. A reduction in the intensity of the dominant intrusion peaks is observed, with the SSP-RCA specimens exhibiting a coarser pore structure, predominantly within the 50–200 nm range (Figure V-13b).

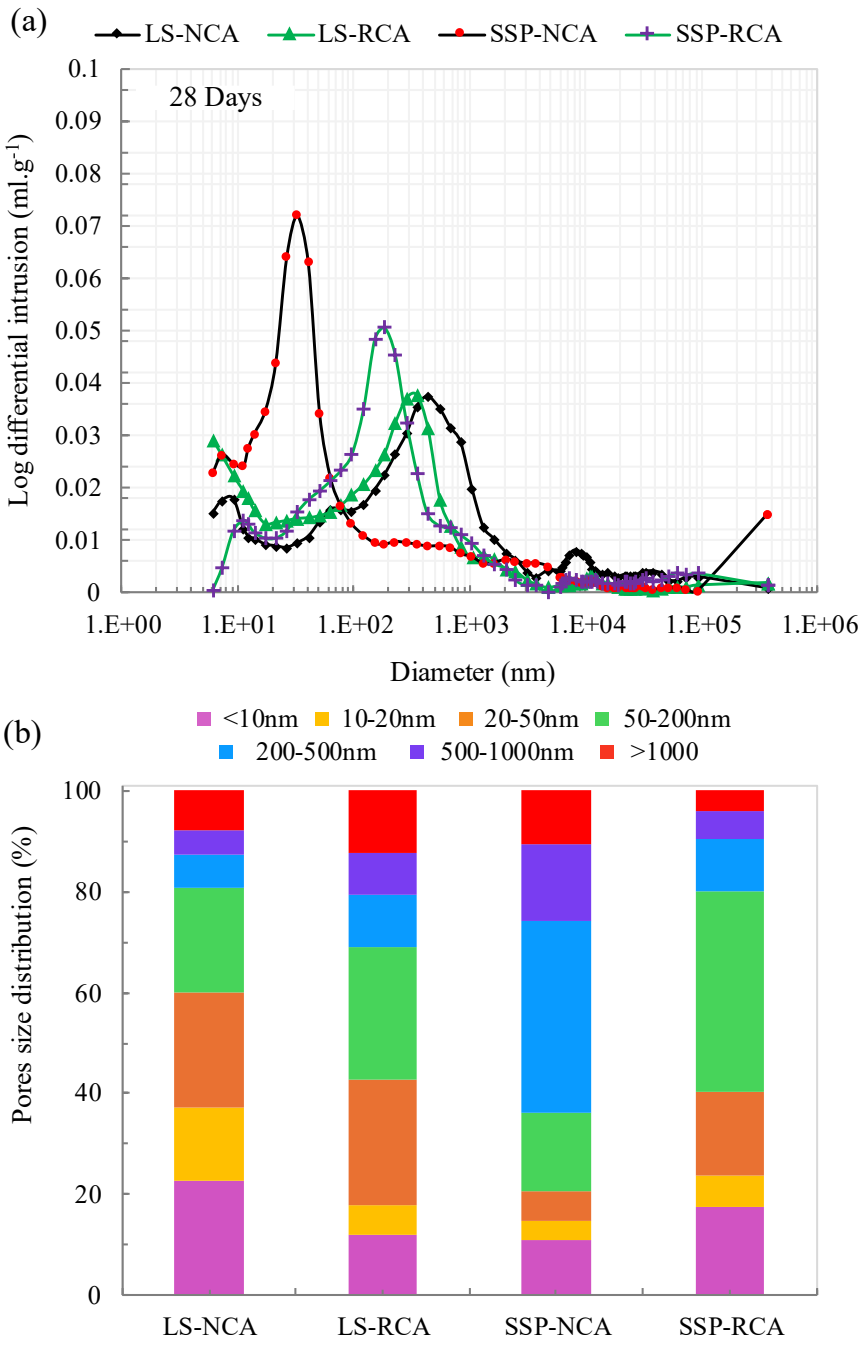

Figure V-13: MIP testing results of SCC specimens after 28 days of carbonation curing: (a) differential intrusion curves and (b) corresponding pore size distribution profiles.

Beyond the general observations, the precipitation of $CaCO_3$, typically occurring along the walls of capillary pores, increases the proportion of small capillary pores (<200 nm), thereby densifying the microstructure in most SCC specimens [190]. The increase in total porosity of SSP-NCA with further carbonation may reflect the progression of $Ca(OH)_2$ and C-S-H carbonation. Pham [410] noted that carbonation of $Ca(OH)_2$, characterized by the crystallization of calcite on portlandite platelets, increases

the pore surface area. Morales-Florez et al [416] reported that the carbonation of low-density C-S-H and the associated precipitation of porous silica gel contribute to an increase in total pore volume.

Furthermore, the relatively high proportion of gel porosity (<10 nm), which generally indicates a higher degree of hydration [190,417], observed in LS-NCA specimens during carbonation curing, suggests a more effective hydration process. However, it is worth noting that although C-S-H carbonation typically increases specific surface area by opening gel pores [185], this mechanism does not appear significant in these specimens, as they exhibited the lowest extent of C-S-H carbonation and still maintained higher compressive strength than the other specimens.

In RCA-based specimens, the carbonation process generally follows a similar pattern to that of their NCA-based counterparts, with slightly lower gel porosity and a marginal increase in coarse pore volume. These differences in porosity may be attributed to the lower effectiveness of carbonation, which could result from reduced CO_2 diffusion within the mixes (Chapter IV3) or the inherently higher initial porosity of the RCA specimens.

Overall, LS-based specimens benefit from more effective hydration and limited C-S-H carbonation, thereby maintaining a denser microstructure. In contrast, SSP-based specimens exhibit signs of over-carbonation, leading to increased porosity.

2.3.2 Microstructural observations

The microstructural observations from SEM images of carbonation-cured specimens, compared to their sealed-cured counterparts, were guided by the XRD and by the morphological characteristics reported in the literature [367–369,418]. The following analysis aims to highlight microstructural insights, particularly the distribution of $CaCO_3$ crystals, to explain the observed differences in the physical and mechanical properties of all specimens.

- **General SEM observation**

All carbonation-cured specimens exhibit a denser microstructure, which evolves with the duration of carbonation curing (Figure V-14), characterized by a substantial quantity of $CaCO_3$ crystals, which are less prominent in the sealed-cured specimens [219,377,419]. The three polymorphs detected in XRD analysis are visible in SEM images: spheroidal vaterite, rod-like aragonite crystallites, and calcite rhombs [377]. The morphology of calcite will be detailed in a dedicated section (Figure V-14b). In contrast, sealed-cured specimens exhibit a more pronounced presence of anhydrous cement grains and hydration products (Figure V-14a). See Appendix 2 for more SEM images.

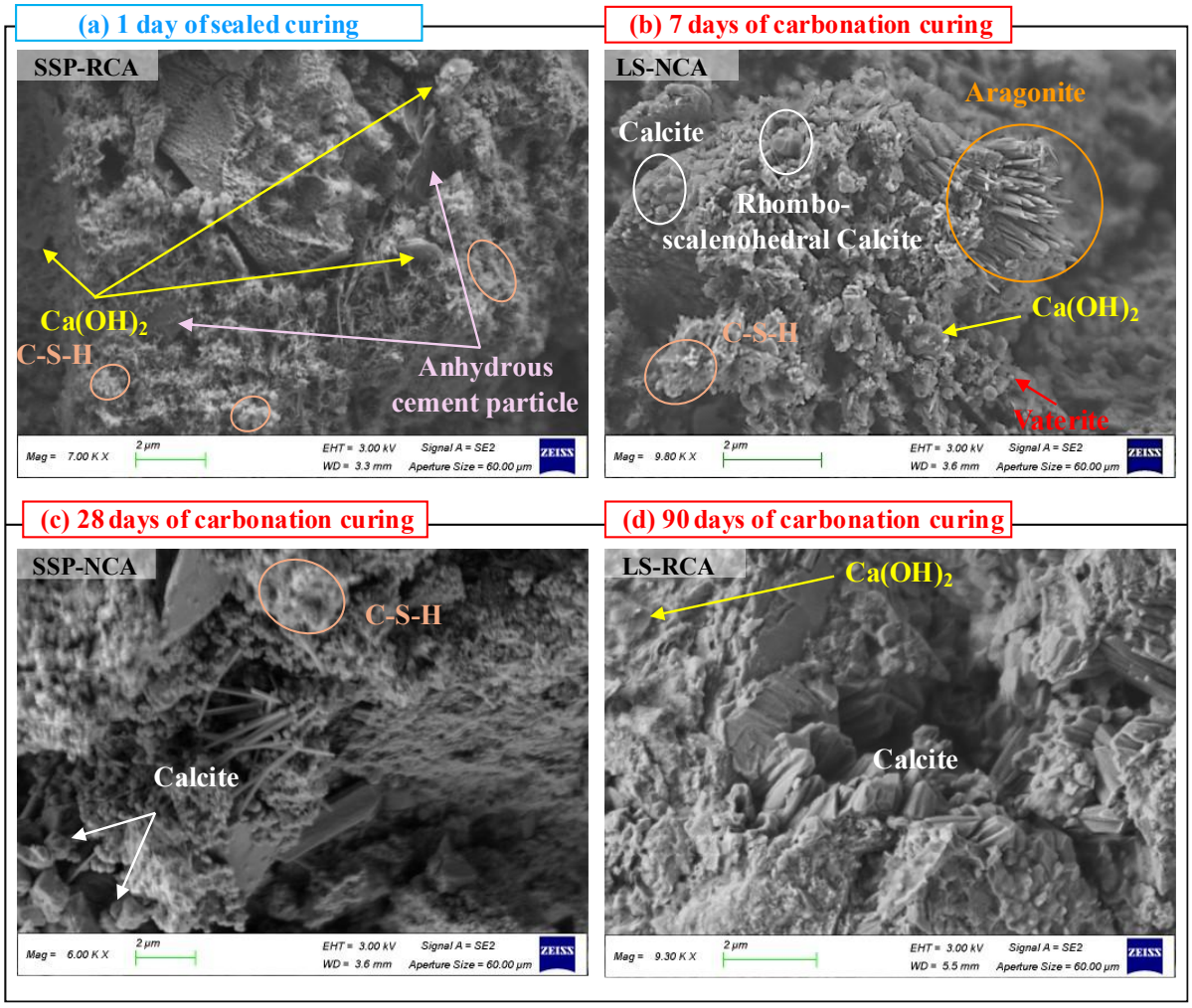

Figure V-14: SEM images showing the microstructural evolution from (a) sealed-cured specimens after 1 day to (b-d) carbonation-cured specimens at different ages for various mix designs.

Moreover, carbonation-cured specimens also exhibit a stronger bond between the aggregate and the cementitious matrix, as the precipitation of $CaCO_3$ crystals fills pores and microcracks within the ITZ, thereby reducing its thickness and defects [420]. These observations, as well as the evolution of the matrix, are evident in all specimens; for instance, in carbonation-cured SSP-based specimens (Figure V-15b) and sealed-cured LS-based specimens (Figure V-15a).

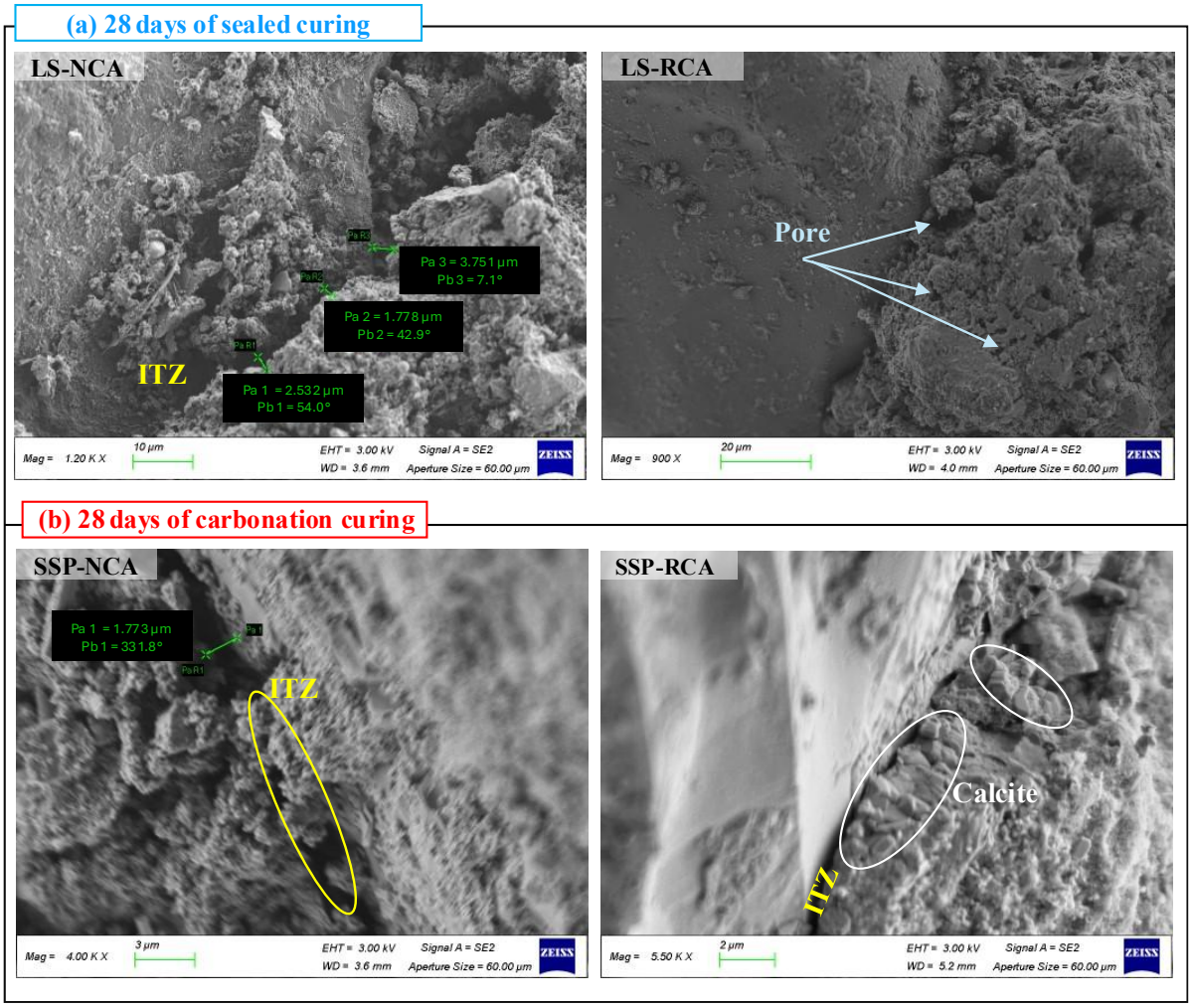

Figure V-15: SEM images of the ITZ and the adjacent matrix, shown as examples for (a) sealed-cured LS-based and (b) carbonation-cured SSP-based specimens at 28 days

- **SEM observations of NCA-based specimens**

Compared with the carbonation-cured SSP-NCA specimens, the spatial distribution of $CaCO_3$ crystals, particularly calcite, within the LS-NCA matrix shows notable differences across curing ages (Figure V-16). From 7 days onward, the LS-NCA specimens exhibit denser accumulations of finely dispersed calcite, often forming compact clusters predominantly located near the surface of the C-S-H gel (Figure V-16a). Individual calcite crystals are also observed either embedded in or located on the surface of C-S-H gel [420]. This distribution results in a strong bond between calcite crystals and C-S-H gel, thereby improving the mechanical properties and likely contributing to the higher compressive strength observed in the LS-NCA specimens [421]. Although calcite clusters are also present within the SSP-NCA specimens, they tend to be less densely packed. The C-S-H gel is less discernible in these specimens, likely due to its greater consumption during the carbonation process (Figure V-16b).

Consequently, C-S-H gel decalcification contributes to a less cohesive microstructure, which may explain the lower compressive strength observed in the SSP-NCA specimens [422].

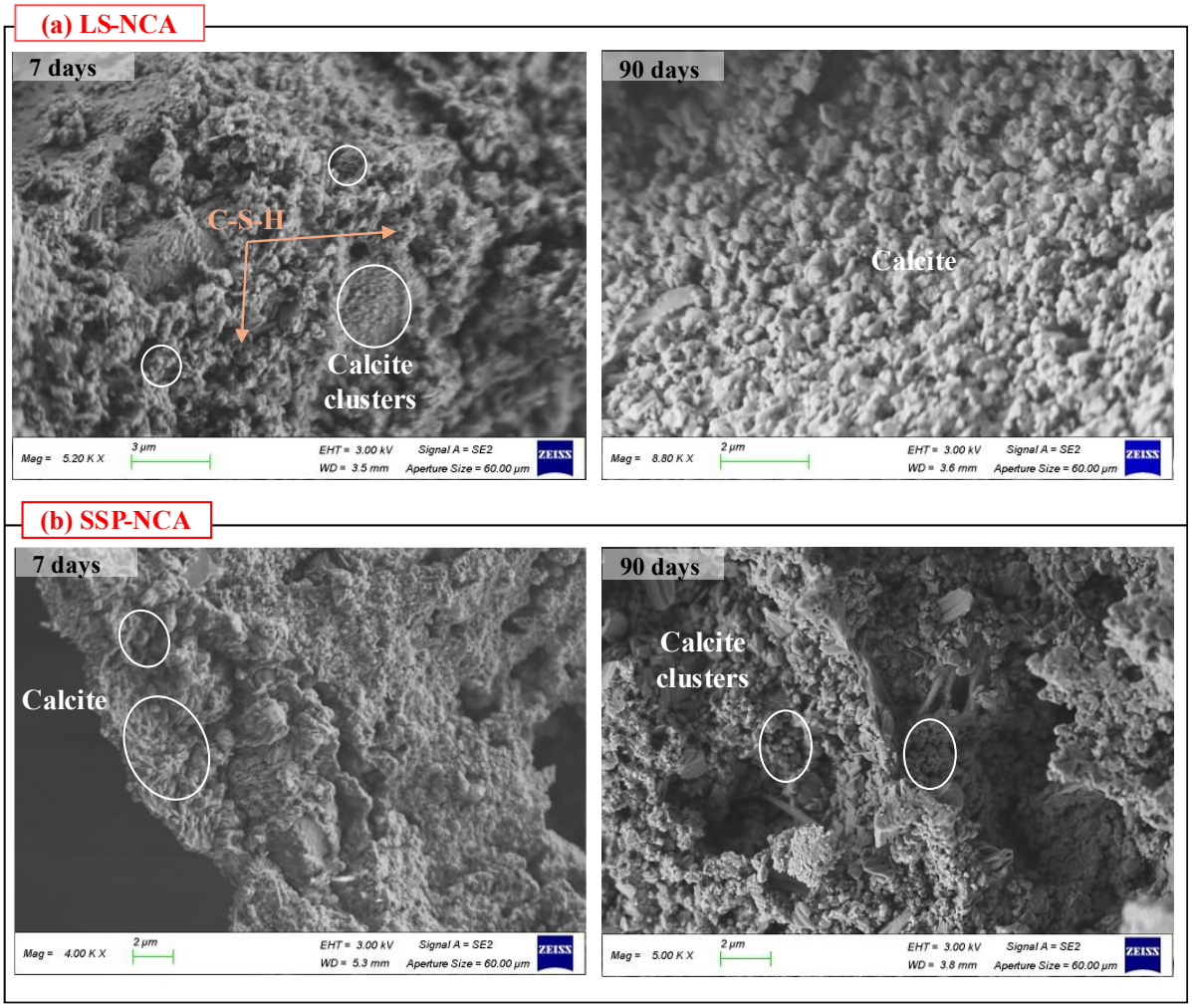

Figure V-16: SEM images showing the spatial distribution of $CaCO_3$ crystals within (a) LS-NCA and (b) SSP-NCA specimens after different carbonation curing ages.

- **SEM observations of RCA-based specimens**

Regarding the microstructure of the carbonation-cured RCA-based specimens, the morphology and size of the calcite crystals appear more heterogeneous (Figure V-17). Their distribution is more clustered within the ITZ, whereas in the bulk matrix, calcite tends to be more sparsely and irregularly dispersed. Additionally, microcracks are more prevalent and often remain partially unfilled, in contrast to their NCA-based counterparts (Figure V-16). These features may contribute to slightly lower mechanical performance and higher porosity in RCA-based specimens. Nevertheless, carbonation curing progressively improves the microstructure with increasing curing age, enhancing the bond between the aggregate and the matrix.

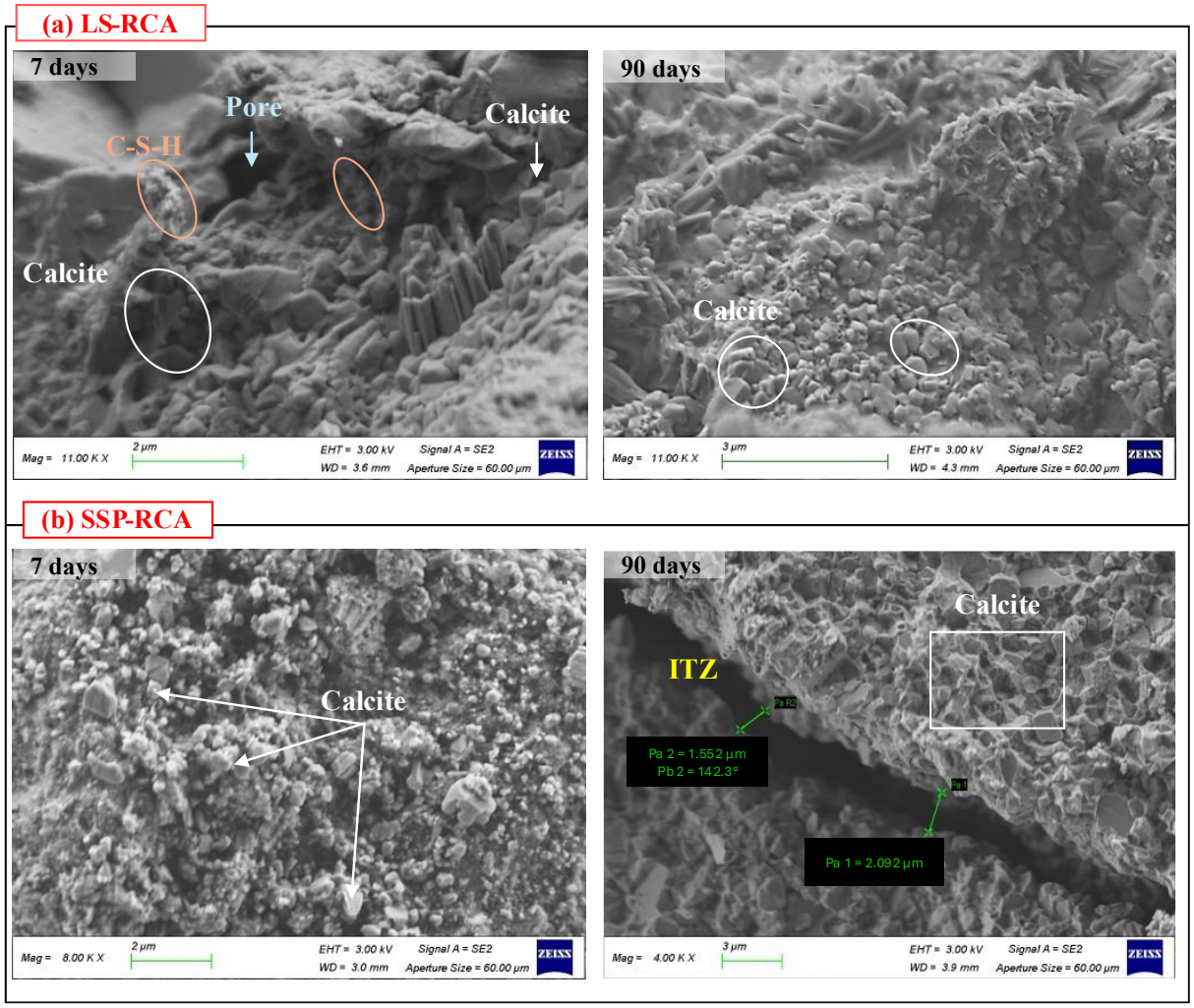

Figure V-17: SEM images showing the spatial distribution of $CaCO_3$ crystals within (a) LS-RCA and (b) SSP-RCA specimens after different carbonation curing ages.

- **Morphology evolution of calcite crystals**

During carbonation curing, the shape of calcite crystals changes over time as the chemical environment and pH evolve. On the first day, nanometer-sized rhombohedral crystals form (Figure V-18a) when rapid nucleation dominates. By around 7 days, the crystals grow into rhombo-scalenohedral (Figure V-18b) or scaleno-rhombohedral (Figure V-18c) as the pH drops to ~10, allowing more directional growth. At later stages, scalenohedral crystals (Figure V-18d) appear under lower pH, where slower growth and reduced supersaturation favor the development of larger, elongated crystals [248,423,424].

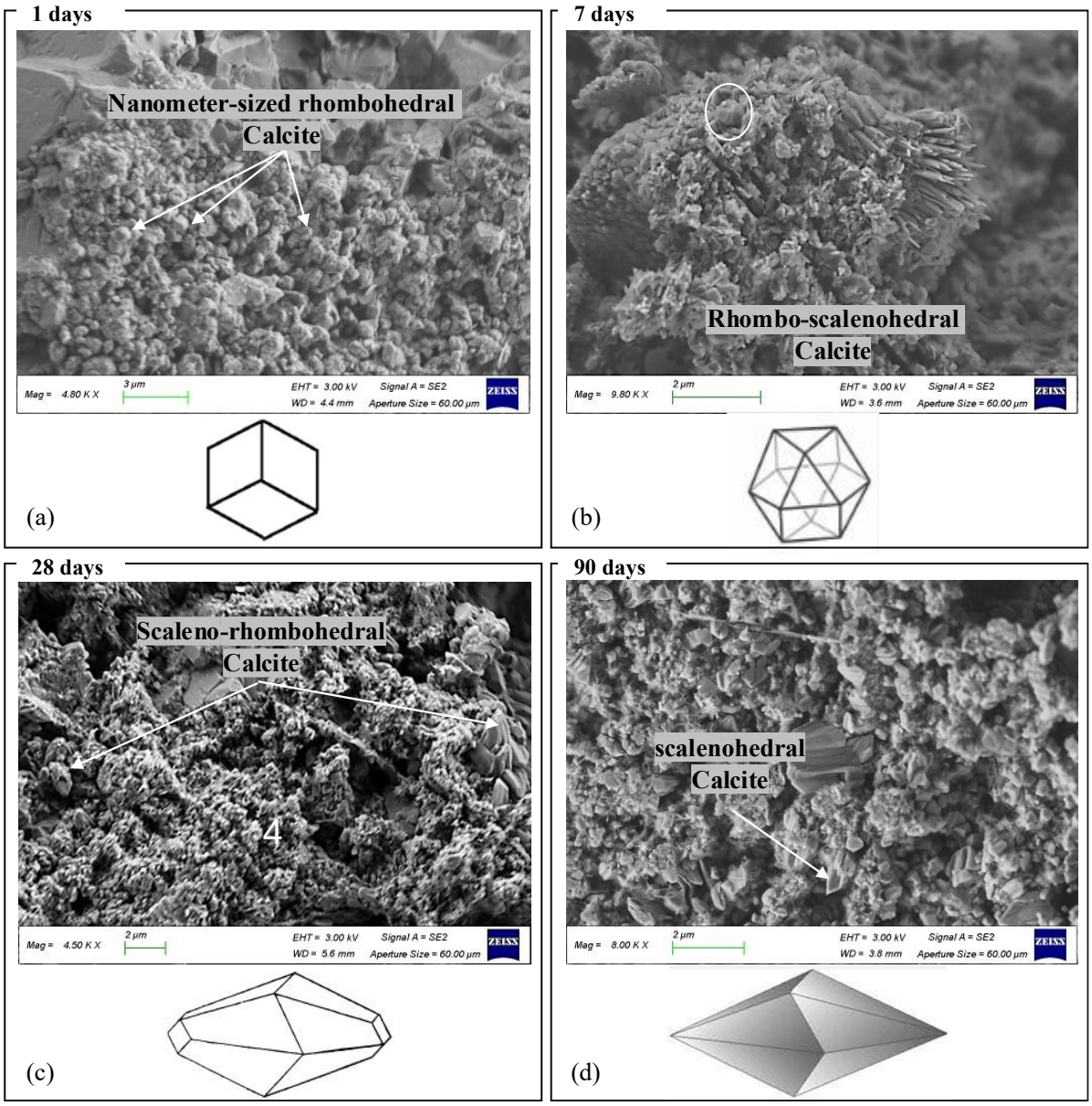

Figure V-18: SEM images showing the morphological evolution of $CaCO_3$ crystals during carbonation-induced pH drop.

3 Carbonation curing as a viable alternative to standard curing

3.1 Analysis of compressive strength in carbonation versus standard curing

The strengths achieved through carbonation curing remain lower than those attained in standard curing after 1 day across all specimens (Figure V-19). At this age, carbonation curing is not sufficiently effective to meet the performance of standard curing in terms of strength in all SCC specimens. In standard curing, continuous hydration in water rapidly develops C-S-H gel, providing early compressive

strength. In contrast, carbonation-cured specimens undergo a pre-conditioning step that includes heating, which initially limits hydration and leaves some newly generated pores unfilled by carbonation products.

By 7 days of carbonation curing, the strength evolution becomes notably more pronounced in LS-based specimens (Figure V-19a), with strength deficits of only around -1% and -3% observed for LS-NCA and LS-RCA, respectively, relative to their standard-cured counterparts. From the 7th day onward, the strength gain tends to stabilize, ultimately exceeding the compressive strength of standard-cured specimens by an average margin of approximately 4% at 90 days. Evidently, this improved performance is attributed to the refinement of the pore structure from calcite precipitation.

However, with SSP-RCA and SSP-NCA, the strength gap between the two regimes remains obvious even at 28 days, particularly in the SSP-NCA specimens (Figure V-19b). By 90 days, the performance gap reverses, with carbonation-cured specimens exceeding the compressive strength of their standard-cured counterparts by an average of 9.60% and compensating for the decreases in compressive strength observed with the standard-cured specimens (Chapter III4.1). These trends indicate that the ongoing hydration process plays a significant role in the development of compressive strength over time.

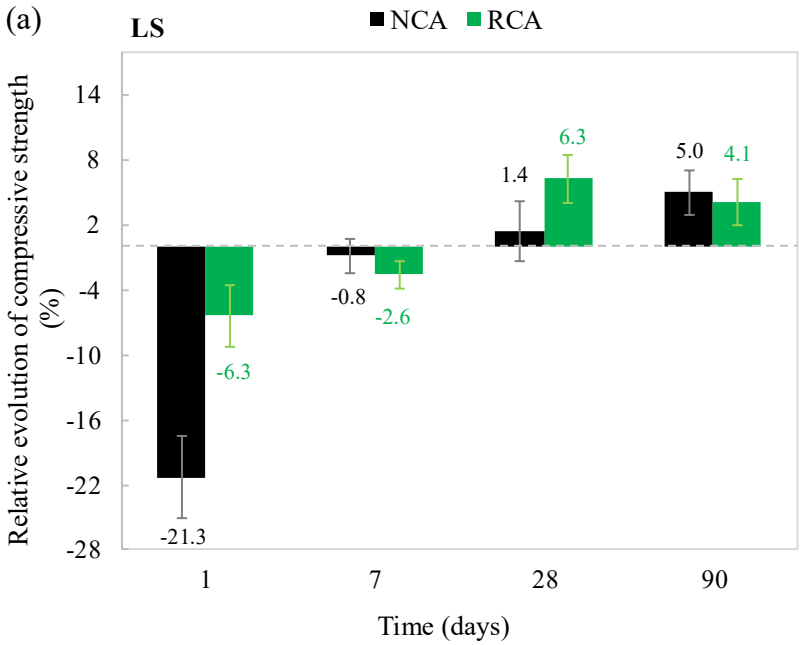

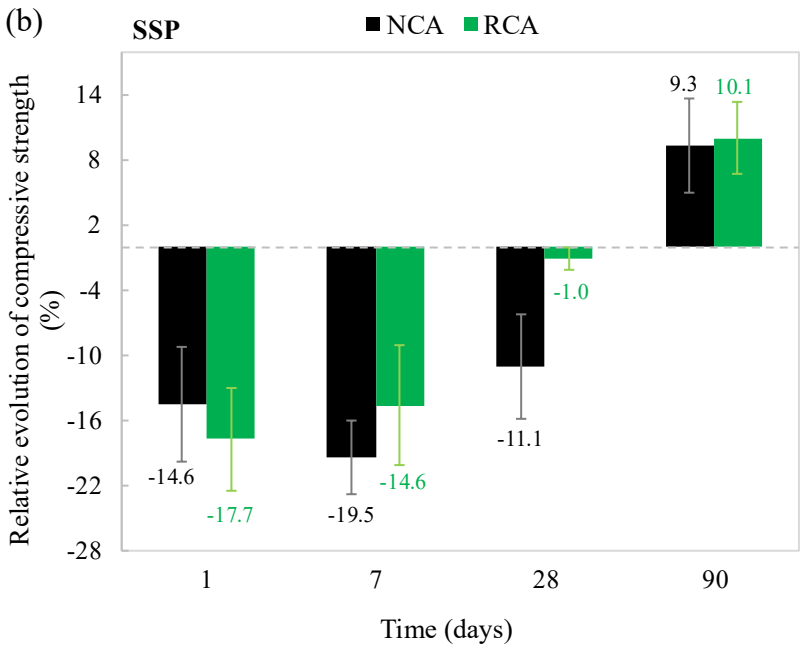

Figure V-19: Relative compressive strength evolution under carbonation curing compared to standard curing of (a) LS-based and (b) SSP-based specimens.

Overall, these results indicate that early-age compressive strength is primarily controlled by hydration, which is more effective in standard specimens. Over time, however, the carbonation-cured specimens benefit from calcite precipitation and continued hydration, particularly in LS-based specimens, ultimately achieving comparable or even higher long-term strength.

These results, however, contrast with trends reported in other studies, which show an average relative evolution of approximately 20 ± 4 % after 1 day, decreasing to around 15 ± 6 % at 28 days, with only marginal changes at 90 days compared to standard curing, depending on mix design and carbonation curing protocol [167,180,261,425]. The opposite trends observed in the SCC specimens were expected, primarily due to the pre-conditioning step, which may have limited early hydration and influenced subsequent strength development under carbonation curing, as noted above.

3.2 Bulk density, water-accessible porosity, and water absorption in carbonation versus standard curing

Carbonation curing has a positive effect on bulk density, water-accessible porosity, and water absorption across all SCC mixtures (Figure V-20). While the improvements are relatively moderate at early ages compared to the standard curing regime, their magnitude increases over time.

- **Bulk density**

After 1 day, the carbonation-cured SSP-based specimens exhibit a greater increase in bulk density (up to ≈ 3.5%) compared to their LS-based counterpart, relative to standard curing (Figure V-20a and b). SSP-based specimens already demonstrated higher CO_2 uptake than LS-based specimens. As previously noted, carbonation products occupy a larger molar volume than hydration products, particularly $Ca(OH)_2$, resulting in more pronounced matrix densification. Therefore, it is not surprising that these specimens exhibit higher bulk density. Moreover, the similar bulk densities observed in LS-based specimens under both curing regimes suggest that hydration remains dominant at early stages. As curing progresses, LS-NCA and LS-RCA specimens show steady and comparable improvements, ultimately exceeding the bulk density of their standard-cured counterparts. Therefore, carbonation curing clearly enhances densification relative to standard curing, though this does not necessarily translate into improved microstructural cohesion.

- **Water-accessible porosity**

In terms of porosity, carbonation curing consistently reduces the water-accessible porosity compared to standard curing across all specimens. LS-based specimens (Figure V-20c), particularly LS-NCA, exhibit a rapid and pronounced reduction in porosity up to 28 days compared to SSP-based specimens (Figure V-20d). This may be attributed to the fact that, although carbonation reduces the total porosity of SSP-based specimens, the resulting pore network is predominantly composed of larger-diameter pores, as will be discussed in the following section. Consequently, the reduction in water-accessible porosity appears to occur more rapidly in LS-based specimens than in SSP-NCA. However, by 90 days, the extent of improvement in porosity becomes comparable across all specimens, suggesting that the long-term impact of carbonation is broadly consistent regardless of the mix design.

- **Water absorption**

Following the same trend, water absorption also decreases more significantly under carbonation curing. A greater reduction in water absorption is observed up to 28 days for LS-based specimens (Figure V-20e) compared to their SSP-based counterpart (Figure V-20f). By 90 days, however, both LS- and SSP-based specimens converge to similar levels of water absorption reduction. The disparity in improvement between LS-based and SSP-based specimens is consistent with that observed for water-accessible porosity.

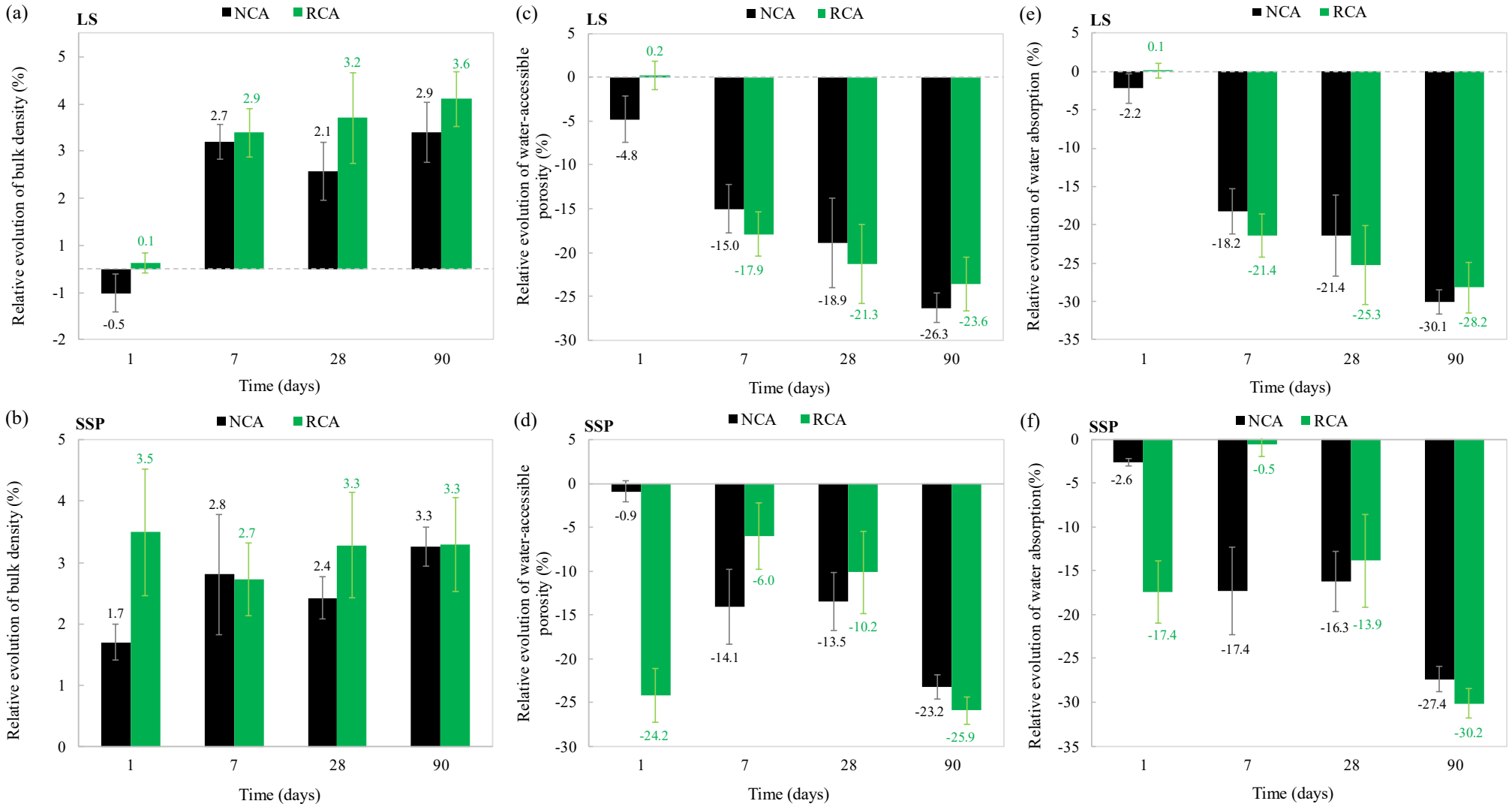

Figure V-20: (a-b) Bulk density, (c-d) porosity accessible to water, and (e-f) water absorption relative evolution under carbonation curing compared to standard curing of LS-based and SSP-based specimens.

Overall, carbonation curing produces a denser material with lower water absorption and reduced accessible porosity compared to standard curing. The effectiveness and evolution of SCC recovery from the pre-conditioning step are both strongly influenced by the mix design, as documented in the literature [426–428]. Although the improvements observed in this study are consistent with previous findings (Table V-1), a direct comparison remains challenging due to the limited number of comparable studies and variations in mixes' composition and curing conditions.

Table V-1: Physical property improvements of cement-based materials after carbonation curing.

Properties	Test samples	Carbonation conditions	Improvements	Ref
Bulk density	Concrete	21 ± 2 °C, 5% CO_2, 65 ± 10% RH	1% at 28 days	[429]
Bulk density	Mortar w/c=0.4	21 ± 1 °C 65% ± 10 RH, 5% CO_2	11% at 7 days	[430]
Water-accessible porosity	Mortar w/c=0.4	21 ± 1 °C,5% CO_2, 65% ± 10 RH	10.5% at 7 days	[430]
Open porosity	Concrete	6 h, 15 Psi, ≈ 99% CO_2, 25 ± 5 °C, ambient RH	50% at 28 days	[170]
Water absorption	PC mortar w/c=0.4	0.2 MPa, pure, 6h	32.4% at 1 day	[431]
Water absorption	PC mortar w/c = 0.4	0.2 MPa, pure, 6h	48.7% at 28 days	[432]
Water absorption	PC paste w/c = 0.35	21 ± 1 °C 65% RH, 20% CO_2	51% at 28 days	[433]

3.3 Pore size distribution: MIP testing

Based on MIP testing of standard- and carbonation-cured specimens, carbonation curing consistently increases total porosity over time across all specimens (Table V-2). This is once again due to the difference in molar volume between hydration and carbonation products. It is worth noting that this phenomenon increases the measured pore volume while reducing the connectivity of pores available for water transport, thereby remaining consistent with the observed decrease in water-accessible porosity.

Table V-2: Total porosity (%) of SCC mix specimens under carbonation and standard curing regimes.

SCC mix	1 day		7 days		28 days	
	Carbonation	Standard	Carbonation	Standard	Carbonation	Standard
LS-NCA	15.82	12.04	14.22	8.83	12.5	5.08
LS-RCA	16.39	13.7	12.13	11.85	11.33	8.80
SSP-NCA	10.07	15.21	13.48	9.06	13.26	7.70
SSP-RCA	18.84	16.35	14.1	10.42	12.67	9.80

Furthermore, the pore system is substantially altered by the curing regime. In carbonation curing (Figure V-21a, c, and e), the pore system exhibits an increase in the volume fraction of pores smaller than 50 nm alongside a simultaneous decrease in the volume fraction of pores larger than 200 nm compared to standard curing (Figure V-21b, d, and f). As previously noted, the increase in finer pores (<50 nm) is attributed to $CaCO_3$ precipitation within the capillary pore network, which subdivides existing larger pores into smaller domains, particularly at early ages, as commonly reported in the literature [219,434,435]. By 28 days (Figure V-21b e and f), the pore structure of carbonation-cured LS-based specimens closely resembles that of their standard-cured counterparts, consistent with their comparable compressive strengths.

In SSP-based systems, the pore structures of carbonation- and standard-cured RCA specimens converge over time. However, the carbonation-cured SSP-NCA specimens retain a higher fraction of large pores (>200 nm), a feature that aligns with the observed variability in the extent of compressive strength improvement (§ 3.1).

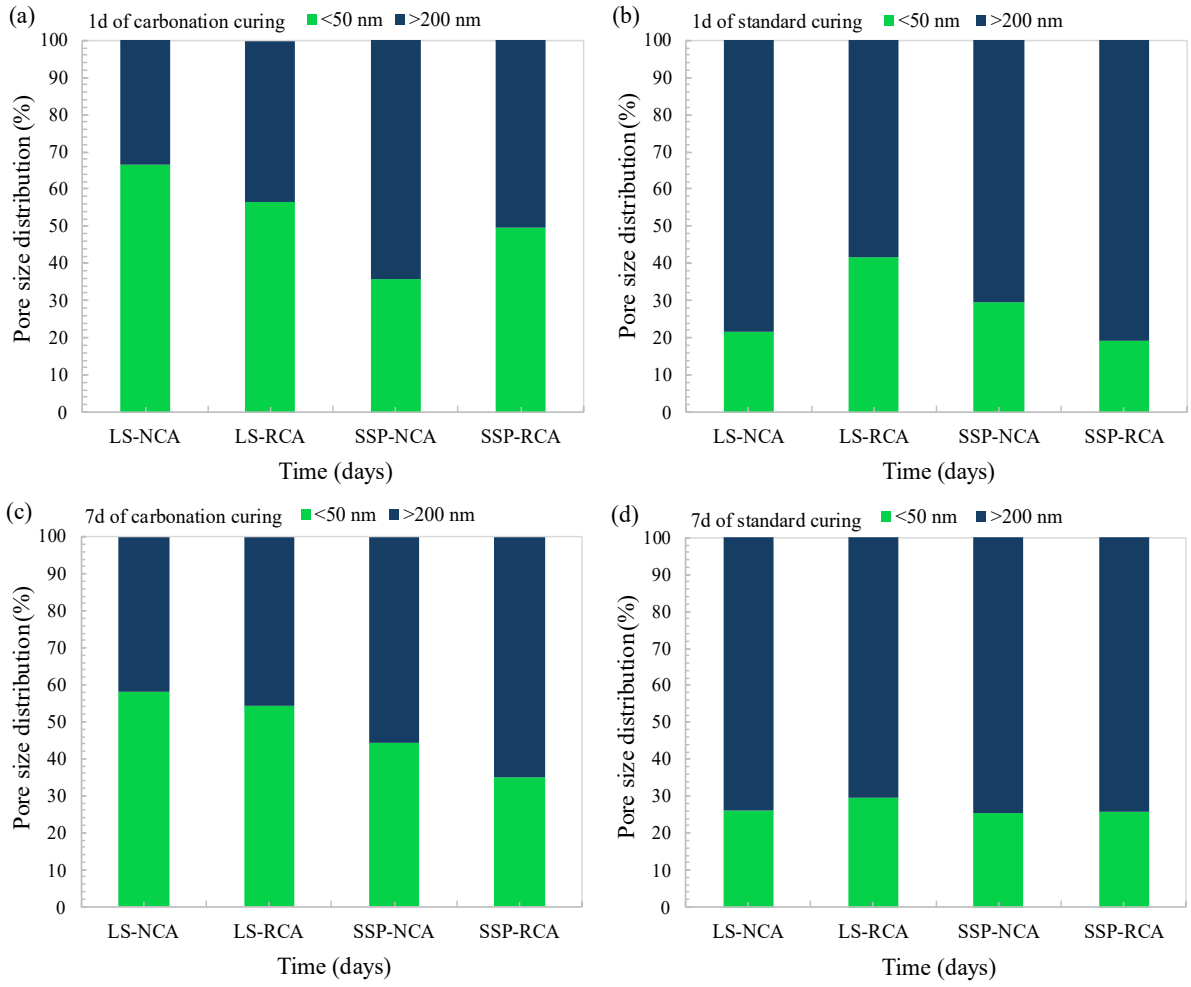

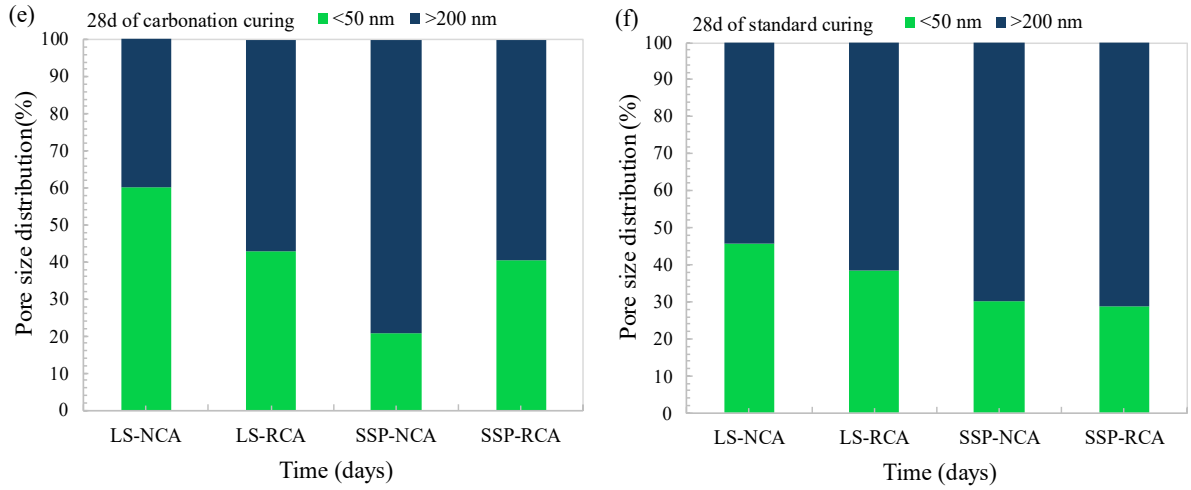

Figure V-21: Pore size distribution of SCC specimens under (a, c, and e) carbonation curing and (b, d, and f) standard curing.

3.4 CO_2 uptake as a potential added value of carbonation curing in SCC

a) Low-carbon contribution of scallop shell and limestone powders

It is worth mentioning that the SCC mix designs already contain 30% $CaCO_3$ by weight of cement, originating from LS and SSP. This $CaCO_3$ content represents CO_2 previously sequestered by these materials. In this context, SSP can be considered a dual carbon sink: (i) mineral, as mollusks biologically convert dissolved CO_2 from seawater into $CaCO_3$ for their shells, and (ii) organic, as part of the carbon is incorporated into the shell's organic matrix. In contrast, the CO_2 in LS originates primarily from the mineral fraction formed from skeletal remains of marine organisms and calcareous deposits, as any original organic carbon has long since decomposed and returned to the atmosphere. By incorporating LS and SSP, the SCC mixes inherently retain CO_2 and organic carbon from SSP. RCA also contributes additional $CaCO_3$ through the natural carbonation of the adherent mortar. These sources complement the additional CO_2 captured during the carbonation curing process.

b) Carbonation curing contribution

Compared with standard curing, carbonation curing of SCC enables an average of 45 kg CO_2/m^3 to be stored after just 24 h, increasing to an average of 106 kg CO_2/m^3 with prolonged curing of up to 90 days (Figure V-22). This value exceeds the CO_2 inherently stored within the mix constituents, estimated at approximately 60 kg CO_2/m^3 from the combined contribution of SSP and LS, with an additional 6 kg CO_2/m^3 provided by RCA [430], as indicated by the dashed lines.

Moreover, Rietveld refinement indicates that the relative $CaCO_3$ content evolves from a minimum average of approximately 8% in NCA-based specimens after 24h to a maximum average of 70% with longer curing times up to 28 days in RCA-based specimens. These results demonstrate that

carbonation curing is an effective method of CO_2 sequestration, in addition to its beneficial effects on the analyzed SCC's properties.

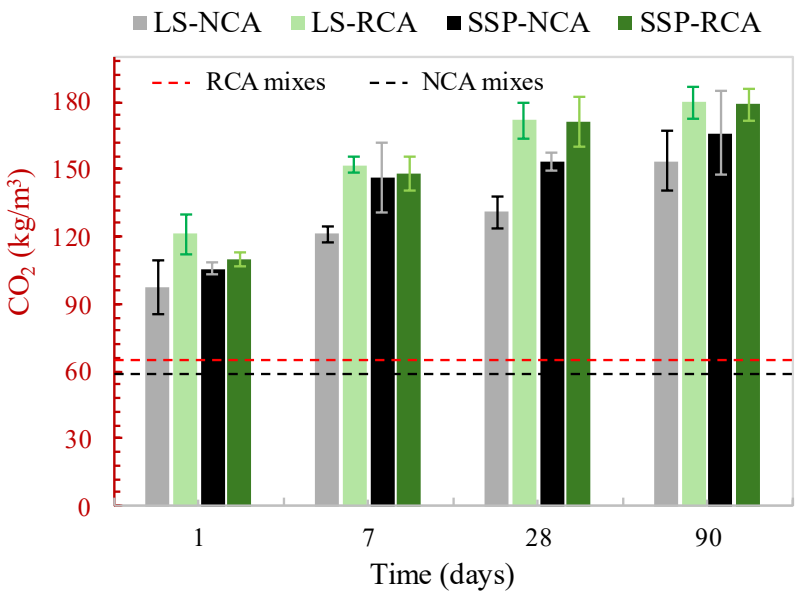

Figure V-22: CO_2 stored in SCC mix designs through carbonation curing, based on the mass loss method data.

4 Synthesis

The effect of carbonation curing on the properties of the SCC mix designs was systematically evaluated. The investigation focused on the development of compressive strength, bulk density, open porosity, water absorption, pore structure, and the spatial distribution of precipitated $CaCO_3$ within the cementitious matrix. The results obtained from carbonation curing were critically compared with those derived from standard curing conditions. The principal findings of this study are summarized as follows:

- **Carbonation curing versus sealed curing**

Compressive strength: The compressive strength of the carbonation-cured specimens exhibited an overall progressive increase with extended carbonation duration, rising from approximately 8%, 5%, 3%, and 4% at 1 day to 42%, 34%, 31%, and 22% at 90 days for LS-NCA, SSP-NCA, LS-RCA, and SSP-RCA, respectively. Overall, the compressive strength demonstrated a linear relationship with the CO_2 uptake within a given mix design. However, this relationship was not consistently observed across all specimens. Notably, the LS-NCA specimens achieved the highest compressive strength despite exhibiting the lowest CO_2 uptake among the investigated mixes.

Physical properties: Although the effect of carbonation curing was only moderately pronounced within the initial 24 h, extended carbonation led to a progressive and consistent increase in

bulk density, accompanied by a concomitant decrease in capillary water-accessible porosity and water absorption. The extent of these microstructural modifications was strongly dependent on the specific mix design, which is governed by the interplay between hydration and carbonation processes, as well as by the spatial distribution of carbonation products within the cementitious matrix.

Microstructure properties: The MIP results revealed that carbonation curing induced distinct, mix-dependent alterations in pore structure. LS-NCA specimens exhibited progressive microstructural refinement, whereas SSP-NCA specimens showed coarsening and an increase in total porosity of about 31.7% at 7 days, with no significant further decrease afterwards. RCA-based specimens followed the same trends as their counterparts, reaching comparable total porosity values by 28 days.

SEM observations revealed densification of the SCC microstructure. Pore filling was primarily due to calcite precipitation at all curing ages, with minor spherical vaterite and rod-shaped aragonite appearing only at early ages. The LS-NCA specimens' matrix contained compact calcite clusters interspersed with C-S-H gel, which explains their superior compressive strength. In contrast, the SSP-NCA specimens' matrix exhibited looser calcite packing and less C-S-H gel. RCA-based specimens displayed heterogeneous calcite distribution and persistent microcracks, though microstructure improved with extended carbonation.

Pore solution pH: carbonation curing, as expected, altered the alkalinity of the specimens, which decreased with progressive $Ca(OH)_2$ consumption and was later governed by the CO_3^{2-}/HCO_3^- equilibrium. Early-stage carbonation preserves the pH above 10.4, while extended curing gradually lowers it, with final values after 90 days ranging from 8.45 to 9.22.

- **Carbonation curing versus standard curing**

Compressive strength: Carbonation curing initially yielded lower compressive strengths across all SCC specimens. LS-based specimens exhibited accelerated strength development, surpassing the standard-cured counterparts by an average of approximately 4% at 90 days. In contrast, SSP-based specimens exhibited delayed early-age gains but ultimately exceeded standard curing by an average of around 9.6% at 90 days. Additionally, carbonation curing resulted in higher bulk density, lower water accessible porosity, and reduced water absorption over time. LS-based specimens demonstrate faster early improvements, though long-term effects are comparable across all mix design specimens.

Microstructure properties: The comparative MIP results of the specimens cured under the two regimes showed that carbonation curing modifies the pore structure by increasing the volume fraction of <50 nm pores and reducing that of coarse pores (>200 nm). The pore system of LS-based specimens cured under the two regimes converged over time, consistent with their comparable compressive strengths. In contrast, SSP-NCA specimens maintain a higher proportion of large pores, accounting for the observed variability in strength development.

CO_2 storage potential: Carbonation curing provided a promising environmental benefit, enabling the storage of 45 kg CO_2/m^3 within the SCC during the first day of the process. An approximate 140% increase was achieved with prolonged curing duration.

Conclusion and Perspectives

This doctoral research aimed to address the construction industry's contribution to global CO_2 emissions and its impact on climate change. Through our investigations, we have found that carbonation curing can be an effective solution, especially when combined with low-carbon alternative raw materials. This approach not only helps reduce emissions in the construction sector but also emphasizes the use of low-carbon impact raw materials, favoring alternatives such as SSP and RCA.

The journey to achieve the goal of this research, evaluating the CO_2 storage potential of SCC to mitigate emissions in the construction sector, started with a thorough examination of the SCC, incorporating the studied raw materials, aiming to understand its properties and how it could act as a CO_2 sink. From there, the focus shifted toward identifying the most effective approaches to maximize CO_2 storage. Guided by the literature, carbonation curing emerged as the most promising approach. Along the way, the literature highlighted several challenges and knowledge gaps, particularly concerning carbonation curing protocols optimization and the fundamental mechanisms of carbonation. The gaps then became the central targets of our investigation, shaping the research direction and guiding our efforts to provide meaningful answers.

In the first experimental work, the focus was on formulating a rheologically stable SCC with sufficient mechanical strength to promote its industrial application. The aim was to reduce the use of limestone (LS) and natural coarse aggregates (NCA) by valorizing alternative materials, namely ground seashells (scallop shell powder, SSP) and recycled coarse aggregates (RCA). This study demonstrated that these materials could serve as feasible substitutes. Compared to LS, SSP improved viscosity and segregation resistance with only minimal slump loss. However, a major concern with SSP is the presence of its intergranular organic matrix, which was observed to interfere with hydration mechanisms by blocking nucleation sites for hydrate growth. Another issue arose from the organic matrix trapping air, which partly coarsened the pore network. Combined with the delayed hydrate formation, this further contributed to pore coarsening and ultimately a moderate reduction in long-term compressive strength. Regarding the replacement of NCA, RCA reduced fresh density and limited workability retention to about 45 minutes. It also increased porosity and water absorption and decreased compressive strength by up to 11%. However, this reduction in compressive strength is considered moderate by the scientific community, particularly when compared to the more detrimental losses reported in other studies.

The second experimental campaign, dedicated to investigating the carbonation behavior and identifying the parameters influencing CO_2 uptake within each SCC matrix, provided valuable insights. To achieve this, the carbonation curing protocol was carefully adapted, starting from the preconditioning step to prepare the specimens to receive CO_2, to the selection of ideal environmental conditions to optimize CO_2 absorption. Although the type of precursor and coarse aggregate influenced CO_2 uptake to some extent, their effect was relatively minor compared to other factors. Instead, the initial water content and the interplay between hydration and carbonation emerged as the primary drivers of carbonation progression and CO_2 storage. RCA-based mixes showed higher CO_2 uptake, even though

with lower carbonation depths. SSP-NCA mixes achieved greater CO_2 storage than LS-NCA specimens, not because of the SSP reactivity, since XRD showed both SSP and LS had similar reactivity, but because the carbonation process was more favorable in these matrices.

Finally, the experiment concluded with an evaluation of carbonation curing as an alternative to standard curing, confirming its potential to improve both mechanical performance and CO_2 storage. Compared to sealed curing, carbonation curing generally increased bulk density, refined pore structure, and promoted microstructural densification through $CaCO_3$ precipitation. These improvements were moderate at early ages of carbonation and became more pronounced with extended curing. Importantly, the magnitude and nature of these enhancements remained strongly mix-dependent. The simultaneous occurrence of carbonation and hydration mechanisms, with hydration prevailing at early ages, together with the precipitation of calcite in dense clusters interspersed with C-S-H, led to the greater improvements recorded. These same parameters also influenced recovery time after the preconditioning step, ultimately affecting the ability of SCC specimens to regain similar performance to that achieved under standard curing.

Overall, this research demonstrates that integrating alternative raw materials with optimized carbonation protocols constitutes an encouraging approach for reducing the construction industry's carbon footprint. The use of SSP and RCA, combined with carbonation curing, demonstrates the potential of SCC to sequester CO_2 effectively while enhancing microstructural and mechanical properties. Moreover, this work advanced our understanding of the mechanisms that govern CO_2 storage and SCC performance. These findings contribute not only to scientific knowledge but also provide practical insights that may guide future strategies for sustainable construction.

Perspectives

It is worth noting, however, that some areas remain incomplete and require further exploration. These include (i) long-term strength loss in compressive strength with standard cured SSP-based specimens; (ii) absence of embedded sensors within the specimens during carbonation to monitor internal temperature and relative humidity, which would provide deeper insights into the reactional medium; (iii) divergent CO_2 uptake results from different techniques highlight challenges in accurate quantification; and (vi) omission of life cycle assessment (LCA), which limits the comprehensive evaluation of carbonation as a strategy for mitigating CO_2 emissions.

Therefore, the work presented opens multiple perspectives and avenues for further investigation. Future studies could focus on more in-depth analyses of the durability of carbonation-cured SCC, including long-term mechanical performance, resistance to freeze-thaw, and the stability of sequestered CO_2 over time.

Developing or combining complementary analytical techniques, such as in situ spectroscopy, advanced thermogravimetric methods, and mass spectrometry, to more accurately quantify CO_2 sequestration and improve the reliability of CO_2 uptake measurements.

Multi-scale modeling could provide valuable insights into understanding and optimizing CO_2 storage in these concretes. By combining molecular-level simulations of hydration and carbonation reactions with pore-network models, it would be possible to identify the most effective mix designs and predict how microstructural changes influence overall CO_2 sequestration. This approach could help bridge the gap between laboratory-scale experiments and practical industrial applications.

Including life cycle assessment (LCA) in future work would verify the effectiveness of carbonation curing for CO_2 storage. This would provide a quantitative evaluation of the environmental benefits of SCC production and identify potential trade-offs.

The encouraging outcomes of carbonation curing could extend beyond SCC to other materials with potential for CO_2 sequestration. Among the materials identified as having significant potential is bio-based concrete.

- C4 plants, such as miscanthus or sorghum, are particularly encouraged over C3 plants. The advantage of the C4 plants lies in their higher photosynthetic efficiency, which enables them to fix more CO_2 and produce greater biomass under similar conditions compared to C3 plants [436,437].
- Air lime is recommended for two reasons: first, it sets only by reacting with CO_2, and second, it provides greater control over the phases participating in the carbonation reaction.

This approach avoids the use of cementitious binders, whose strength contribution can rather be ensured through the precipitation of $CaCO_3$. Furthermore, the estimation of CO_2 stored by the material becomes more accurate, as the reactive phases are primarily $Ca(OH)_2$.

However, a major issue is the stability of the biomass cell wall chemistry, which may promote fungal growth under favorable conditions. In this case, the focus should be on identifying the optimal environmental conditions, particularly temperature and relative humidity, when conducting carbonation curing. Moreover, biomass is a limited resource with severe competing demands from food, energy, materials, and construction. This trade-off emphasizes the need to carefully select feedstocks and manage resources to balance CO_2 sequestration with broader societal priorities.

References

[1] M. Nieto, Whatever it takes to reach net zero emissions around 2050 and limit global warming to 1.5 °C: the cases of United States, China, European Union and Japan, BAFFI CAREFIN Centre Research Paper. (2022). https://doi.org/http://dx.doi.org/10.2139/ssrn.4007974.

[2] N. Scafetta, Impacts and risks of "realistic" global warming projections for the 21st century, Geoscience Frontiers. 15 (2024) 101774. https://doi.org/https://doi.org/10.1016/j.gsf.2023.101774.

[3] P.C. Change, Global warming of 1.5 C, World Meteorological Organization: Geneva, Switzerland (2018).

[4] L. Zhang, B. Liu, J. Du, C. Liu, H. Li, S. Wang, Internationalization trends of carbon emission linkages: A case study on the construction sector, J Clean Prod. 270 (2020) 122433. https://doi.org/https://doi.org/10.1016/j.jclepro.2020.122433.

[5] S.A. Miller, G. Habert, R.J. Myers, J.T. Harvey, Achieving net zero greenhouse gas emissions in the cement industry via value chain mitigation strategies, One Earth. 4 (2021) 1398–1411. https://doi.org/https://doi.org/10.1016/j.oneear.2021.09.011.

[6] Y. Guo, L. Luo, T. Liu, L. Hao, Y. Li, P. Liu, T. Zhu, A review of low-carbon technologies and projects for the global cement industry, J Environ Sci. 136 (2024) 682–697. https://doi.org/https://doi.org/10.1016/j.jes.2023.01.021.

[7] H. Dong, L. Zhang, Transition towards carbon neutrality: Forecasting Hong Kong's buildings carbon footprint by 2050 using a machine learning approach, Sustain Prod Consump. 35 (2023) 633–642. https://doi.org/https://doi.org/10.1016/j.spc.2022.12.014.

[8] MineralInfo, Careers in France, Https://Www.Mineralinfo.Fr/Fr/Ressources-Minerales-France-Gestion/Carrieres-France (2020).

[9] W. Xu, Y. Zhang, Y. Su, X. Zhu, L. Wang, D.C.W. Tsang, Using waste to improve the weak: Recycled seashell as an ideal way to regulate the interfacial transition zone in biochar-cement composites, Constr. Build. Mater. 444 (2024) 137765. https://doi.org/10.1016/j.conbuildmat.2024.137765.

[10] A. Diemer, C.E. Nedelciu, M.E. Morales, C. Batisse, C. Cantuarias-Villessuzanne, Waste Management and Circular Economy in the French Building and Construction Sector, Frontiers in Sustainability 3 (2022). https://doi.org/10.3389/frsus.2022.840091.

[11] K. Ozawa, K. Maekawa, H. Okamura, Development of high performance concrete, Journal of the Faculty of Engineering, University of Tokyo, Series B;(Japan) 41 (1992).

[12] S.C. Kou, C.S. Poon, Properties of self-compacting concrete prepared with coarse and fine recycled concrete aggregates, Cem. Concr. Compos. 31 (2009) 622–627. https://doi.org/10.1016/j.cemconcomp.2009.06.005.

[13] H. Okamura, M. Ouchi, Self-compacting high performance concrete, Progress in Structural Engineering and Materials 1 (1998) 378–383. https://doi.org/10.1002/pse.2260010406.

[14] K.H. Khayat, Workability, testing, and performance of self-consolidating concrete, Materials Journal 96 (1999) 346–353. https://doi.org/doi:10.14359/632.

[15] A. Singh, Introduction to self-compacting concrete, in: Alternative Cementitious Materials for Self-Compacting Concrete, Elsevier, 2024: pp. 1–33. https://doi.org/10.1016/B978-0-323-95139-5.00014-X.

[16] K.O. Naoki Nagamo, "Mixture Properties of Self-Compacting, High-Performance Concrete," in: "SP-172: High-Performance Concrete - Proceedings: ACI International Conference, Malaysia 1997," American Concrete Institute, 1999. https://doi.org/10.14359/6155.

[17] Ch.R. kumar Seshagiri Rao Boddu, Self-Compacting Concrete, Imperial Journal of Interdisciplinary Research 2 (2016). http://www.onlinejournal.in (accessed March 26, 2025).

[18] M. El Marzak, H. Karim Serroukh, M. Benaicha, O. Jalbaud, A. Hafidi Alaoui, Y. Burtschell, Rheological and mechanical analysis of self-compacting concrete incorporating rubber aggregates, Case Studies in Construction Materials 22 (2025) e04564. https://doi.org/10.1016/j.cscm.2025.e04564.

[19] G. De Schutter, P.J.M. Bartos, P. Domone, J. Gibbs, Self-compacting concrete, Whittles Publishing Caithness, 2008.

[20] NF EN 934-2+A1, dmixtures for concrete, mortar and grout — Part 2 : Concrete admixtures - Definitions, requirements, conformity, marking and labelling, (2012).

[21] R. Flatt, I. Schober, Superplasticizers and the rheology of concrete, in: Understanding the Rheology of Concrete, Elsevier, 2012: pp. 144–208. https://doi.org/10.1533/9780857095282.2.144.

[22] R. Dilawar Riaz, M. Usman, A. Ali, U. Majid, M. Faizan, U. Jalil Malik, Inclusive characterization of 3D printed concrete (3DPC) in additive manufacturing: A detailed review, Constr. Build. Mater. 394 (2023) 132229. https://doi.org/10.1016/j.conbuildmat.2023.132229.

[23] Y. Fang, X. Wang, L. Jia, C. Liu, Z. Zhao, C. Chen, Y. Zhang, Synergistic effect of polycarboxylate superplasticizer and silica fume on early properties of early high strength grouting material for semi-flexible pavement, Constr. Build. Mater. 319 (2022) 126065. https://doi.org/10.1016/j.conbuildmat.2021.126065.

[24] V.K. Singh, Portland cement additives, in: The Science and Technology of Cement and Other Hydraulic Binders, Elsevier, 2023: pp. 499–570. https://doi.org/10.1016/B978-0-323-95080-0.00014-5.

[25] R.B. Bian, C.W. Miao, J. Shen, Review of chemical structures and synthetic methods for polycarboxylate superplasticizers, Eighth CANMET International Conference. Sorrento, Italy (2006).

[26] B. Felekoğlu, H. Sarıkahya, Effect of chemical structure of polycarboxylate-based superplasticizers on workability retention of self-compacting concrete, Constr. Build. Mater. 22 (2008) 1972–1980. https://doi.org/10.1016/j.conbuildmat.2007.07.005.

[27] S. Sha, M. Wang, C. Shi, Y. Xiao, Influence of the structures of polycarboxylate superplasticizer on its performance in cement-based materials-A review, Constr. Build. Mater. 233 (2020) 117257. https://doi.org/10.1016/j.conbuildmat.2019.117257.

[28] Z. Chen, J. Qiao, X. Yang, Y. Sun, D. Sun, A review of grouting materials for pouring semi-flexible pavement: Materials, design and performance, Constr. Build. Mater. 379 (2023) 131235. https://doi.org/10.1016/j.conbuildmat.2023.131235.

[29] H.H.M. Darweesh, Black liquor waste as a cement admixture or cement and concrete admixtures, Biopolymers and Biotech Admixtures for Eco-Efficient Construction Materials (2016) 99–130. https://doi.org/10.1016/B978-0-08-100214-8.00006-3.

[30] C. Wang, O. Kayali, J.-L. Liow, The effectiveness and mechanisms of superplasticisers in dispersing class F fly ash pastes, Powder Technol. 392 (2021) 81–92. https://doi.org/10.1016/j.powtec.2021.06.054.

[31] S. Jiang, B.-G. Kim, P.-C. Aïtcin, Importance of adequate soluble alkali content to ensure cement/superplasticizer compatibility, Cem. Concr. Res. 29 (1999) 71–78. https://doi.org/10.1016/S0008-8846(98)00179-3.

[32] U. Pott, C. Jakob, D. Jansen, J. Neubauer, D. Stephan, Investigation of the Incompatibilities of Cement and Superplasticizers and Their Influence on the Rheological Behavior, Materials 13 (2020) 977. https://doi.org/10.3390/ma13040977.

[33] Nicolas Edwige, Compatibilités et incompatibilités liants cimentaires/superplastifiants, Université de Luxembourg, 2010. http://hdl.handle.net/10993/15617.

[34] R.J. Flatt, Y.F. Houst, A simplified view on chemical effects perturbing the action of superplasticizers, Cem. Concr. Res. 31 (2001) 1169–1176. https://doi.org/10.1016/S0008-8846(01)00534-8.

[35] T. Dorn, O. Blask, D. Stephan, Acceleration of cement hydration – A review of the working mechanisms, effects on setting time, and compressive strength development of accelerating admixtures, Constr. Build. Mater. 323 (2022) 126554. https://doi.org/10.1016/j.conbuildmat.2022.126554.

[36] V.H. Dodson, Set Accelerating Admixtures, in: Concrete Admixtures, Springer US, Boston, MA, 1990: pp. 73–102. https://doi.org/10.1007/978-1-4757-4843-7_4.

[37] W.-C. Wang, H.T.H. Duong, C.-H. Zhang, Influence of accelerating admixtures on high early strength cement performance using heat curing method, Case Studies in Construction Materials 18 (2023) e01746. https://doi.org/10.1016/j.cscm.2022.e01746.

[38] Z. Wan, T. He, Chemical admixtures for concrete: Effects of accelerators on the volume stability of cement-based materials, Mater. Today Commun. 35 (2023) 106256. https://doi.org/10.1016/j.mtcomm.2023.106256.

[39] B. Sukumar, K. Nagamani, R. Srinivasa Raghavan, Evaluation of strength at early ages of self-compacting concrete with high volume fly ash, Constr. Build. Mater. 22 (2008) 1394–1401. https://doi.org/10.1016/j.conbuildmat.2007.04.005.

[40] M.C.G. Juenger, R. Siddique, Recent advances in understanding the role of supplementary cementitious materials in concrete, Cem. Concr. Res. 78 (2015) 71–80. https://doi.org/10.1016/j.cemconres.2015.03.018.

[41] M.C.G. Juenger, R. Snellings, S.A. Bernal, Supplementary cementitious materials: New sources, characterization, and performance insights, Cem. Concr. Res. 122 (2019) 257–273. https://doi.org/10.1016/j.cemconres.2019.05.008.

[42] M.N.N. Khan, M. Jamil, M.R. Karim, M.F.M. Zain, A.B.M.A. Kaish, Filler effect of pozzolanic materials on the strength and microstructure development of mortar, KSCE Journal of Civil Engineering 21 (2017) 274–284. https://doi.org/10.1007/s12205-016-0737-5.

[43] K.H. Khayat, A.F. Omran, S. Naji, P. Billberg, A. Yahia, Field-oriented test methods to evaluate structural build-up at rest of flowable mortar and concrete, Mater. Struct. 45 (2012) 1547–1564. https://doi.org/10.1617/s11527-012-9856-8.

[44] M. Jalal, E. Mansouri, M. Sharifipour, A.R. Pouladkhan, Mechanical, rheological, durability and microstructural properties of high performance self-compacting concrete containing SiO_2 micro and nanoparticles, Mater. Des. 34 (2012) 389–400. https://doi.org/10.1016/J.MATDES.2011.08.037.

[45] G. Barluenga, I. Palomar, J. Puentes, Hardened properties and microstructure of SCC with mineral additions, Constr. Build. Mater. 94 (2015) 728–736. https://doi.org/10.1016/j.conbuildmat.2015.07.072.

[46] Md Sohel Rana, A review: Mechanical Properties of Self-Compacting Concrete (SCC) and Influential Factors, Engeneering Engrxiv Archive (2023). https://doi.org/10.31224/2935.

[47] M. Uysal, K. Yilmaz, M. Ipek, The effect of mineral admixtures on mechanical properties, chloride ion permeability and impermeability of self-compacting concrete, Constr. Build. Mater. 27 (2012) 263–270. https://doi.org/10.1016/j.conbuildmat.2011.07.049.

[48] H. Qasrawi, Fresh properties of green SCC made with recycled steel slag coarse aggregate under normal and hot weather, J. Clean. Prod. 204 (2018) 980–991. https://doi.org/10.1016/j.jclepro.2018.09.075.

[49] T. Ahmad Wani, S. Ganesh, Study on fresh properties, mechanical properties and microstructure behavior of fiber reinforced self compacting concrete: A review, Mater. Today Proc. 62 (2022) 6663–6670. https://doi.org/10.1016/J.MATPR.2022.04.666.

[50] Self-Compacting Concrete: Specification & Guidelines, (2002). https://studylib.net/doc/18555656/specification-and-guidelines-for-self-compacting-concrete (accessed October 7, 2025).

[51] F. Azarhomayun, M. Haji, M. Shekarchi, M. Kioumarsi, Investigating the Effectiveness of the Stable Measurement Tests of Self-Compacting Concrete, Constr. Build. Mater. 383 (2023) 131262. https://doi.org/10.1016/j.conbuildmat.2023.131262.

[52] N. Tregger, A. Gregori, L. Ferrara, S. Shah, Correlating dynamic segregation of self-consolidating concrete to the slump-flow test, Constr. Build. Mater. 28 (2012) 499–505. https://doi.org/10.1016/j.conbuildmat.2011.08.052.

[53] R. Raydan, F. Chamseddine, A. Jahami, O. Baalbaki, J. M. Khatib, A. Elkordi, Production of low-cost self-consolidating concrete (SCC) using manufactured aggregates, BAU Journal - Science and Technology 3 (2022). https://doi.org/10.54729/HKRO9755.

[54] P.L. Domone, A review of the hardened mechanical properties of self-compacting concrete, Cem. Concr. Compos. 29 (2007) 1–12. https://doi.org/10.1016/j.cemconcomp.2006.07.010.

[55] K. Holschemacher, Y. Klug, A database for the evaluation of hardened properties of SCC, Lacer 7 (2002) 124–134.

[56] H.A.F. Dehwah, Mechanical properties of self-compacting concrete incorporating quarry dust powder, silica fume or fly ash, Constr. Build. Mater. 26 (2012) 547–551. https://doi.org/10.1016/j.conbuildmat.2011.06.056.

[57] W. Sun, H. Yan, B. Zhan, Analysis of mechanism on water-reducing effect of fine ground slag, high-calcium fly ash, and low-calcium fly ash, Cem. Concr. Res. 33 (2003) 1119–1125. https://doi.org/10.1016/S0008-8846(03)00022-X.

[58] D. Youness, A. Mechaymech, R. Al Wardany, Flow assessment and development towards sustainable self-consolidating concrete using blended basalt and limestone-cement systems, J. Clean. Prod. 283 (2021) 124582. https://doi.org/10.1016/J.JCLEPRO.2020.124582.

[59] A. Yahia, M. Tanimura, Y. Shimoyama, Rheological properties of highly flowable mortar containing limestone filler-effect of powder content and W/C ratio, Cem. Concr. Res. 35 (2005) 532–539. https://doi.org/10.1016/J.CEMCONRES.2004.05.008.

[60] B. Felekoglu, Utilisation of high volumes of limestone quarry wastes in concrete industry (self-compacting concrete case), Resour. Conserv. Recycl. 51 (2007) 770–791. https://doi.org/10.1016/j.resconrec.2006.12.004.

[61] M.K. Mohammed, A.R. Dawson, N.H. Thom, Production, microstructure and hydration of sustainable self-compacting concrete with different types of filler, Constr. Build. Mater. 49 (2013) 84–92. https://doi.org/10.1016/j.conbuildmat.2013.07.107.

[62] H.T. Cam, N. Neithalath, Moisture and ionic transport in concretes containing coarse limestone powder, Cem. Concr. Compos. 32 (2010) 486–496. https://doi.org/10.1016/j.cemconcomp.2010.04.002.

[63] P. Thongsanitgarn, W. Wongkeo, A. Chaipanich, C.S. Poon, Heat of hydration of Portland high-calcium fly ash cement incorporating limestone powder: Effect of limestone particle size, Constr. Build. Mater. 66 (2014) 410–417. https://doi.org/10.1016/j.conbuildmat.2014.05.060.

[64] R. Bisai, S.K. Palaniappan, S.K. Pal, Effects of high-temperature heating and cryogenic quenching on the physico-mechanical properties of limestone, SN Appl. Sci. 2 (2020) 158. https://doi.org/10.1007/s42452-020-1944-8.

[65] G. Sua-iam, N. Makul, Use of increasing amounts of bagasse ash waste to produce self-compacting concrete by adding limestone powder waste, J. Clean. Prod. 57 (2013) 308–319. https://doi.org/10.1016/j.jclepro.2013.06.009.

[66] G. Sua-iam, N. Makul, Utilization of limestone powder to improve the properties of self-compacting concrete incorporating high volumes of untreated rice husk ash as fine aggregate, Constr. Build. Mater. 38 (2013) 455–464. https://doi.org/10.1016/j.conbuildmat.2012.08.016.

[67] G. Sua-iam, N. Makul, Use of limestone powder during incorporation of Pb-containing cathode ray tube waste in self-compacting concrete, J. Environ. Manage. 128 (2013) 931–940. https://doi.org/10.1016/j.jenvman.2013.06.031.

[68] Ma, K., Long, G., XIE, Y., & ZHU, R, Rheological Properties of Compound Pastes with Cement-Fly Ash-Limestone Powder, Journal of the Chinese Ceramic Society 41.5 (2013): 582-587. https://doi.org/10.7521/j.issn.0454–5648.2013.05.02.

[69] D. Wang, C. Shi, N. Farzadnia, Z. Shi, H. Jia, A review on effects of limestone powder on the properties of concrete, Constr. Build. Mater. 192 (2018) 153–166. https://doi.org/10.1016/j.conbuildmat.2018.10.119.

[70] K. Vance, A. Kumar, G. Sant, N. Neithalath, The rheological properties of ternary binders containing Portland cement, limestone, and metakaolin or fly ash, Cem. Concr. Res. 52 (2013) 196–207. https://doi.org/10.1016/j.cemconres.2013.07.007.

[71] C.F. Ferraris, K.H. Obla, R. Hill, The influence of mineral admixtures on the rheology of cement paste and concrete, Cem. Concr. Res. 31 (2001) 245–255. https://doi.org/10.1016/S0008-8846(00)00454-3.

[72] S. Yalcın, D. Chateigner, L. Le Pluart, S. Gascoin, S. Eve, Investigation of structural and mechanical properties of Bio$CaCO_3$-LDPE composites, Materials International 1 (2019) 29–43. https://doi.org/10.33263/Materials12.029043.

[73] J. Wang, E. Liu, Upcycling waste seashells with cement: Rheology and early-age properties of Portland cement paste, Resour. Conserv. Recycl. 155 (2020) 104680. https://doi.org/10.1016/J.RESCONREC.2020.104680.

[74] C. Martínez-García, B. González-Fonteboa, F. Martínez-Abella, D. Carro- López, Performance of mussel shell as aggregate in plain concrete, Constr. Build. Mater. 139 (2017) 570–583. https://doi.org/10.1016/J.CONBUILDMAT.2016.09.091.

[75] M. Zhou, J. Chen, W. Huang, H. Chao, L. Yu, X. Ma, X. Ouyang, Multiscale study on the effect of Seashell powder on rheology, hydration and strength development of cement paste, Constr. Build. Mater. 456 (2024) 139257. https://doi.org/10.1016/J.CONBUILDMAT.2024.139257.

[76] F. Debieb, S. Kenai, The use of coarse and fine crushed bricks as aggregate in concrete, Constr. Build. Mater. 22 (2008) 886–893. https://doi.org/10.1016/j.conbuildmat.2006.12.013.

[77] C.S. Poon, S.C. Kou, L. Lam, Influence of recycled aggregate on slump and bleeding of fresh concrete, Mater. Struct. 40 (2007) 981–988. https://doi.org/10.1617/s11527-006-9192-y.

[78] P. Gentilini, O. Yazoghli-Marzouk, V. Delmotte, Y. Descantes, Determination of the water content of fillerised fine aggregates in the saturated surface dry state, Constr. Build. Mater. 98 (2015) 662–670. https://doi.org/10.1016/J.CONBUILDMAT.2015.08.131.

[79] R.V. Silva, J. de Brito, R.K. Dhir, Fresh-state performance of recycled aggregate concrete: A review, Constr. Build. Mater. 178 (2018) 19–31. https://doi.org/10.1016/j.conbuildmat.2018.05.149.

[80] H. Mefteh, O. Kebaïli, H. Oucief, L. Berredjem, N. Arabi, Influence of moisture conditioning of recycled aggregates on the properties of fresh and hardened concrete, J. Clean. Prod. 54 (2013) 282–288. https://doi.org/10.1016/j.jclepro.2013.05.009.

[81] C.S. Poon, Z.H. Shui, L. Lam, Effect of microstructure of ITZ on compressive strength of concrete prepared with recycled aggregates, Constr. Build. Mater. 18 (2004) 461–468. https://doi.org/10.1016/j.conbuildmat.2004.03.005.

[82] N. Otsuki, S. Miyazato, W. Yodsudjai, Influence of Recycled Aggregate on Interfacial Transition Zone, Strength, Chloride Penetration and Carbonation of Concrete, Journal of Materials in Civil Engineering 15 (2003) 443–451. https://doi.org/10.1061/(ASCE)0899-1561(2003)15:5(443).

[83] A. Katz, Properties of concrete made with recycled aggregate from partially hydrated old concrete, Cem. Concr. Res. 33 (2003) 703–711. https://doi.org/10.1016/S0008-8846(02)01033-5.

[84] P.B. Cachim, Mechanical properties of brick aggregate concrete, Constr. Build. Mater. 23 (2009) 1292–1297. https://doi.org/10.1016/j.conbuildmat.2008.07.023.

[85] G. Kakali, S. Tsivilis, E. Aggeli, M. Bati, Hydration products of C_3A, C_3S and Portland cement in the presence of $CaCO_3$, Cem. Concr. Res. 30 (2000) 1073–1077. https://doi.org/10.1016/S0008-8846(00)00292-1.

[86] T. Oey, A. Kumar, J.W. Bullard, N. Neithalath, G. Sant, The Filler Effect: The Influence of Filler Content and Surface Area on Cementitious Reaction Rates, Journal of the American Ceramic Society 96 (2013) 1978–1990. https://doi.org/10.1111/jace.12264.

[87] Y. Briki, M. Zajac, M. Ben Haha, K. Scrivener, Impact of limestone fineness on cement hydration at early age, Cem. Concr. Res. 147 (2021) 106515. https://doi.org/10.1016/j.cemconres.2021.106515.

[88] E. Berodier, K. Scrivener, Understanding the Filler Effect on the Nucleation and Growth of C-S-H, Journal of the American Ceramic Society 97 (2014) 3764–3773. https://doi.org/10.1111/jace.13177.

[89] P. Juilland, A. Kumar, E. Gallucci, R.J. Flatt, K.L. Scrivener, Effect of mixing on the early hydration of alite and OPC systems, Cem. Concr. Res. 42 (2012) 1175–1188. https://doi.org/10.1016/J.CEMCONRES.2011.06.011.

[90] G. De Schutter, L. Taerwe, Fundamental and practical study of thermal stresses in hardening massive concrete elements, Doctoral Thesis, Magnel Laboratory for Concrete Research, Ghent University, Belgium (1996) 364.

[91] J. Bensted, Some applications of conduction calorimetry to cement hydration, Advances in Cement Research 1 (1987) 35–44. https://doi.org/10.1680/adcr.1987.1.1.35.

[92] B. Lothenbach, G. Le Saout, E. Gallucci, K. Scrivener, Influence of limestone on the hydration of Portland cements, Cem. Concr. Res. 38 (2008) 848–860. https://doi.org/10.1016/J.CEMCONRES.2008.01.002.

[93] K. De Weerdt, M. Ben Haha, G. Le Saout, K.O. Kjellsen, H. Justnes, B. Lothenbach, Hydration mechanisms of ternary Portland cements containing limestone powder and fly ash, Cem. Concr. Res. 41 (2011) 279–291. https://doi.org/10.1016/j.cemconres.2010.11.014.

[94] I. Kang, S. Shin, J. Kim, Optimal Limestone Content on Hydration Properties of Ordinary Portland Cement with 5% Ground Granulated Blast-Furnace Slag, Materials 17 (2024) 3255. https://doi.org/10.3390/ma17133255.

[95] Y. Dhandapani, M. Santhanam, G. Kaladharan, S. Ramanathan, Towards ternary binders involving limestone additions — A review, Cem. Concr. Res. 143 (2021) 106396. https://doi.org/10.1016/J.CEMCONRES.2021.106396.

[96] V.L. Bonavetti, V.F. Rahhal, E.F. Irassar, Studies on the carboaluminate formation in limestone filler-blended cements, Cem. Concr. Res. 31 (2001) 853–859. https://doi.org/10.1016/S0008-8846(01)00491-4.

[97] Chowaniec Olga, Limestone Addition in Cement, Ph.D.Thesis. École Polytechnique Fédérale de Lausanne (EPFL), 2012.

[98] G. Magnabosco, D. Giuri, A.P. Di Bisceglie, F. Scarpino, S. Fermani, C. Tomasini, G. Falini, New material perspective for waste seashells by covalent functionalization, ACS Sustain. Chem. Eng. 9 (2021) 6203–6208. https://doi.org/10.1021/acssuschemeng.1c01306.

[99] D.P. Bentz, A. Ardani, T. Barrett, S.Z. Jones, D. Lootens, M.A. Peltz, T. Sato, P.E. Stutzman, J. Tanesi, W.J. Weiss, Multi-scale investigation of the performance of limestone in concrete, Constr. Build. Mater. 75 (2015) 1–10. https://doi.org/10.1016/j.conbuildmat.2014.10.042.

[100] L. Li, M. Cao, H. Yin, Comparative roles between aragonite and calcite calcium carbonate whiskers in the hydration and strength of cement paste, Cem. Concr. Compos. 104 (2019) 103350. https://doi.org/10.1016/J.CEMCONCOMP.2019.103350.

[101] D. Zhao, J.M. Williams, Z. Li, A.-H.A. Park, A. Radlińska, P. Hou, S. Kawashima, Hydration of cement pastes with calcium carbonate polymorphs, Cem. Concr. Res. 173 (2023) 107270. https://doi.org/10.1016/j.cemconres.2023.107270.

[102] S. Rode, N. Oyabu, K. Kobayashi, H. Yamada, A. Kühnle, True Atomic-Resolution Imaging of ($10\bar{1}4$) Calcite in Aqueous Solution by Frequency Modulation Atomic Force Microscopy, Langmuir 25 (2009) 2850–2853. https://doi.org/10.1021/la803448v.

[103] D. Wang, C. Shi, N. Farzadnia, Z. Shi, H. Jia, Z. Ou, A review on use of limestone powder in cement-based materials: Mechanism, hydration and microstructures, Constr. Build. Mater. 181 (2018) 659–672. https://doi.org/10.1016/j.conbuildmat.2018.06.075.

[104] Y. Araki, K. Tsukamoto, N. Oyabu, K. Kobayashi, H. Yamada, Atomic-Resolution Imaging of Aragonite (001) Surface in Water by Frequency Modulation Atomic Force Microscopy, Jpn. J. Appl. Phys. 51 (2012) 08KB09. https://doi.org/10.1143/JJAP.51.08KB09.

[105] S. Gowthaman, M. Chen, K. Nakashima, S. Kawasaki, Effect of Scallop Powder Addition on MICP Treatment of Amorphous Peat, Front. Environ. Sci. 9 (2021). https://doi.org/10.3389/fenvs.2021.690376.

[106] M. Pepe, E.A.B. Koenders, C. Faella, E. Martinelli, Structural concrete made with recycled aggregates: Hydration process and compressive strength models, Mech. Res. Commun. 58 (2014) 139–145. https://doi.org/10.1016/J.MECHRESCOM.2014.02.001.

[107] E.A.B. Koenders, M. Pepe, E. Martinelli, Compressive strength and hydration processes of concrete with recycled aggregates, Cem. Concr. Res. 56 (2014) 203–212. https://doi.org/10.1016/j.cemconres.2013.11.012.

[108] M. Cyr, P. Lawrence, E. Ringot, Efficiency of mineral admixtures in mortars: Quantification of the physical and chemical effects of fine admixtures in relation with compressive strength, Cem. Concr. Res. 36 (2006) 264–277. https://doi.org/10.1016/J.CEMCONRES.2005.07.001.

[109] D. Chateigner, S. Ouhenia, C. Krauss, C. Hedegaard, O. Gil, M. Morales, L. Lutterotti, M. Rousseau, E. Lopez, Voyaging around nacre with the X-ray shuttle: From bio-mineralisation to prosthetics via mollusc phylogeny, Mater Sci Eng: A. 528 (2010) 37–51. https://doi.org/10.1016/j.msea.2010.07.032.

[110] W. Maherzi, M. Benzerzour, Y. Mamindy-Pajany, E. van Veen, M. Boutouil, N.E. Abriak, Beneficial reuse of Brest-Harbor (France)-dredged sediment as alternative material in road building: laboratory investigations, Environ. Technol. 39 (2018) 566–580. https://doi.org/10.1080/09593330.2017.1308440.

[111] M. Thomas, K. Folliard, T. Drimalas, T. Ramlochan, Diagnosing delayed ettringite formation in concrete structures, Cem. Concr. Res. 38 (2008) 841–847. https://doi.org/10.1016/j.cemconres.2008.01.003.

[112] C. Martínez-García, B. González-Fonteboa, D. Carro-López, F. Martínez-Abella, Impact of mussel shell aggregates on air lime mortars. Pore structure and carbonation, J. Clean. Prod. 215 (2019) 650–668. https://doi.org/10.1016/J.JCLEPRO.2019.01.121.

[113] Y. Zhu, D. Chen, X. Yu, R. Liu, Y. Liao, Properties of Cementitious Materials Utilizing Seashells as Aggregate or Cement: Prospects and Challenges, Materials 17 (2024) 1222. https://doi.org/10.3390/ma17051222.

[114] F. López Gayarre, C. López-Colina Pérez, M.A. Serrano López, A. Domingo Cabo, The effect of curing conditions on the compressive strength of recycled aggregate concrete, Constr. Build. Mater. 53 (2014) 260–266. https://doi.org/10.1016/J.CONBUILDMAT.2013.11.112.

[115] Y.-X. Liu, T.-C. Ling, K.-H. Mo, Progress in developing self-consolidating concrete (SCC) constituting recycled concrete aggregates: A review, International Journal of Minerals, Metallurgy and Materials 28 (2021) 522–537. https://doi.org/10.1007/s12613-020-2060-x.

[116] A.S. Brand, J.R. Roesler, A. Salas, Initial moisture and mixing effects on higher quality recycled coarse aggregate concrete, Constr. Build. Mater. 79 (2015) 83–89. https://doi.org/10.1016/j.conbuildmat.2015.01.047.

[117] G. Sua-iam, N. Makul, Self-compacting concrete produced with recycled concrete aggregate coated by a polymer-based agent: A case study, Case Studies in Construction Materials 19 (2023) e02351. https://doi.org/10.1016/J.CSCM.2023.E02351.

[118] R. Martínez-García, M.I. Guerra-Romero, J.M. Morán-del Pozo, J. de Brito, A. Juan-Valdés, Recycling Aggregates for Self-Compacting Concrete Production: A Feasible Option, Materials 13 (2020) 868. https://doi.org/10.3390/ma13040868.

[119] N. Singh, S.P. Singh, Carbonation and electrical resistance of self compacting concrete made with recycled concrete aggregates and metakaolin, Constr. Build. Mater. 121 (2016) 400–409. https://doi.org/10.1016/J.CONBUILDMAT.2016.06.009.

[120] N. Singh, M. M, S. Arya, Utilization of coal bottom ash in recycled concrete aggregates based self compacting concrete blended with metakaolin, Resour. Conserv. Recycl. 144 (2019) 240–251. https://doi.org/10.1016/J.RESCONREC.2019.01.044.

[121] K. Kapoor, S.P. Singh, B. Singh, P. Singh, Effect of recycled aggregates on fresh and hardened properties of self compacting concrete, Mater. Today Proc. 32 (2020) 600–607. https://doi.org/10.1016/J.MATPR.2020.02.753.

[122] Z.J. Grdic, G.A. Toplicic-Curcic, I.M. Despotovic, N.S. Ristic, Properties of self-compacting concrete prepared with coarse recycled concrete aggregate, Constr. Build. Mater. 24 (2010) 1129–1133. https://doi.org/10.1016/j.conbuildmat.2009.12.029.

[123] V. Revilla-Cuesta, V. Ortega-López, M. Skaf, J.M. Manso, Effect of fine recycled concrete aggregate on the mechanical behavior of self-compacting concrete, Constr. Build. Mater. 263 (2020) 120671. https://doi.org/10.1016/J.CONBUILDMAT.2020.120671.

[124] R.V. Silva, J. de Brito, R.K. Dhir, Tensile strength behaviour of recycled aggregate concrete, Constr. Build. Mater. 83 (2015) 108–118. https://doi.org/10.1016/j.conbuildmat.2015.03.034.

[125] R.V. Silva, J. de Brito, R.K. Dhir, Properties and composition of recycled aggregates from construction and demolition waste suitable for concrete production, Constr. Build. Mater. 65 (2014) 201–217. https://doi.org/10.1016/j.conbuildmat.2014.04.117.

[126] F. Fiol, C. Thomas, C. Muñoz, V. Ortega-López, J.M. Manso, The influence of recycled aggregates from precast elements on the mechanical properties of structural self-compacting concrete, Constr. Build. Mater. 182 (2018) 309–323. https://doi.org/10.1016/J.CONBUILDMAT.2018.06.132.

[127] L.A. Pereira-De-Oliveira, M.C.S. Nepomuceno, J.P. Castro-Gomes, M.F.C. Vila, Permeability properties of self-compacting concrete with coarse recycled aggregates, Constr. Build. Mater. 51 (2014) 113–120. https://doi.org/10.1016/J.CONBUILDMAT.2013.10.061.

[128] Y.J. Zrar, K.H. Younis, A.F.H. Sherwani, Properties of sustainable self-compacted concrete with recycled concrete and waste tire crumb rubber aggregates, Constr. Build. Mater. 407 (2023) 133524. https://doi.org/10.1016/J.CONBUILDMAT.2023.133524.

[129] Y.F. Silva, R.A. Robayo, P.E. Mattey, S. Delvasto, Properties of self-compacting concrete on fresh and hardened with residue of masonry and recycled concrete, Constr. Build. Mater. 124 (2016) 639–644. https://doi.org/10.1016/J.CONBUILDMAT.2016.07.057.

[130] H. Sasanipour, F. Aslani, J. Taherinezhad, Effect of silica fume on durability of self-compacting concrete made with waste recycled concrete aggregates, Constr. Build. Mater. 227 (2019) 116598. https://doi.org/10.1016/J.CONBUILDMAT.2019.07.324.

[131] N. Arabi, H. Meftah, H. Amara, O. Kebaïli, L. Berredjem, Valorization of recycled materials in development of self-compacting concrete: Mixing recycled concrete aggregates – Windshield waste glass aggregates, Constr. Build. Mater. 209 (2019) 364–376. https://doi.org/10.1016/J.CONBUILDMAT.2019.03.024.

[132] H.-J. Ho, A. Iizuka, Mineral carbonation using seawater for CO_2 sequestration and utilization: A review, Separ Purif Technol. (2022) 122855. https://doi.org/https://doi.org/10.1016/j.seppur.2022.122855.

[133] W. Liu, L. Teng, S. Rohani, Z. Qin, B. Zhao, C.C. Xu, S. Ren, Q. Liu, B. Liang, CO_2 mineral carbonation using industrial solid wastes: A review of recent developments, Chemical Engineering Journal. 416 (2021) 129093. https://doi.org/https://doi.org/10.1016/j.cej.2021.129093.

[134] C. Kunzler, N. Alves, E. Pereira, J. Nienczewski, R. Ligabue, S. Einloft, J. Dullius, CO_2 storage with indirect carbonation using industrial waste, Energy Procedia 4 (2011) 1010–1017. https://doi.org/10.1016/j.egypro.2011.01.149.

[135] D. Wolff-Boenisch, S.R. Gislason, E.H. Oelkers, The effect of crystallinity on dissolution rates and CO_2 consumption capacity of silicates, Geochim Cosmochim Acta. 70 (2006) 858–870. https://doi.org/https://doi.org/10.1016/j.gca.2005.10.016.

[136] J.M. Matter, P.B. Kelemen, Permanent storage of carbon dioxide in geological reservoirs by mineral carbonation, Nat Geosci. 2 (2009) 837–841. https://doi.org/https://doi.org/10.1038/ngeo683.

[137] S. Gudbrandsson, D. Wolff-Boenisch, S.R. Gislason, E.H. Oelkers, Experimental determination of plagioclase dissolution rates as a function of its composition and pH at 22 C, Geochim Cosmochim Acta. 139 (2014) 154–172. https://doi.org/https://doi.org/10.1016/j.gca.2014.04.028.

[138] S.Ó. Snæbjörnsdóttir, B. Sigfússon, C. Marieni, D. Goldberg, S.R. Gislason, E.H. Oelkers, Carbon dioxide storage through mineral carbonation, Nat Rev Earth Environ. 1 (2020) 90–102. https://doi.org/https://doi.org/10.1038/s43017-019-0011-8.

[139] A. Ben Ghacham, L.-C. Pasquier, E. Cecchi, J.-F. Blais, G. Mercier, Valorization of waste concrete through CO_2 mineral carbonation: Optimizing parameters and improving reactivity using concrete separation, J Clean Prod. 166 (2017) 869–878. https://doi.org/https://doi.org/10.1016/j.jclepro.2017.08.015.

[140] S.K. Kaliyavaradhan, L. Li, T.-C. Ling, Response surface methodology for the optimization of CO_2 uptake using waste concrete powder, Constr Build Mater. 340 (2022) 127758. https://doi.org/https://doi.org/10.1016/j.conbuildmat.2022.127758.

[141] N.L. Ukwattage, P.G. Ranjith, X. Li, Steel-making slag for mineral sequestration of carbon dioxide by accelerated carbonation, Measurement. 97 (2017) 15–22. https://doi.org/https://doi.org/10.1016/j.measurement.2016.10.057.

[142] M.H. Ibrahim, M.H. El-Naas, A. Benamor, S.S. Al-Sobhi, Z. Zhang, Carbon mineralization by reaction with steel-making waste: a review, Processes. 7 (2019) 115. https://doi.org/https://doi.org/10.3390/pr7020115.

[143] H.-J. Ho, A. Iizuka, H. Kubo, Direct aqueous carbonation of dephosphorization slag under mild conditions for CO_2 sequestration and utilization: Exploration of new dephosphorization slag utilization, Environ Technol Innov. 28 (2022) 102905. https://doi.org/https://doi.org/10.1016/j.eti.2022.102905.

[144] S.-Y. Pan, A. Chiang, E.E. Chang, Y.-P. Lin, H. Kim, P.-C. Chiang, An innovative approach to integrated carbon mineralization and waste utilization: A review, Aerosol Air Qual. Res. 15 (2015) 1072–1091. https://doi.org/https://doi.org/10.4209/aaqr.2014.10.0240.

[145] H.-J. Ho, A. Iizuka, E. Shibata, T. Ojumu, Circular indirect carbonation of coal fly ash for carbon dioxide capture and utilization, J Environl Chem Eng. 10 (2022) 108269. https://doi.org/https://doi.org/10.1016/j.jece.2022.108269.

[146] H.-J. Ho, A. Iizuka, E. Shibata, Utilization of low-calcium fly ash via direct aqueous carbonation with a low-energy input: Determination of carbonation reaction and evaluation of the potential for CO_2 sequestration and utilization, J Environ Manag. 288 (2021) 112411. https://doi.org/https://doi.org/10.1016/j.jenvman.2021.112411.

[147] H.-J. Ho, A. Iizuka, E. Shibata, H. Tomita, K. Takano, T. Endo, Utilization of CO_2 in direct aqueous carbonation of concrete fines generated from aggregate recycling: Influences of the solid–liquid ratio and CO_2 concentration, J Clean Prod. 312 (2021) 127832. https://doi.org/https://doi.org/10.1016/j.jclepro.2021.127832.

[148] H.-J. Ho, A. Iizuka, E. Shibata, H. Tomita, K. Takano, T. Endo, CO_2 utilization via direct aqueous carbonation of synthesized concrete fines under atmospheric pressure, ACS Omega 5 (2020) 15877–15890. https://doi.org/https://doi.org/10.1021/acsomega.0c00985.

[149] M.F. Bertos, S.J.R. Simons, C.D. Hills, P.J. Carey, A review of accelerated carbonation technology in the treatment of cement-based materials and sequestration of CO_2, J Hazard Mater. 112 (2004) 193–205. https://doi.org/https://doi.org/10.1016/j.jhazmat.2004.04.019.

[150] Z. He, Z. Li, Y. Shao, Effect of carbonation mixing on CO_2 uptake and strength gain in concrete, J Mater Civ Eng. 29 (2017) 04017176. https://doi.org/https://doi.org/10.1061/(ASCE)MT.1943-5533.0002031.

[151] S. Monkman, M. MacDonald, On carbon dioxide utilization as a means to improve the sustainability of ready-mixed concrete, J Clean Prod. 167 (2017) 365–375. https://doi.org/https://doi.org/10.1016/j.jclepro.2017.08.194.

[152] S.-Y. Pan, P.-C. Chiang, W. Pan, H. Kim, Advances in state-of-art valorization technologies for captured CO_2 toward sustainable carbon cycle, Crit. Rev. Environ. Sci. Technol. 48 (2018) 471–534. https://doi.org/https://doi.org/10.1080/10643389.2018.1469943.

[153] D. Zhang, Z. Ghouleh, Y. Shao, Review on carbonation curing of cement-based materials, J CO_2 Util. 21 (2017) 119–131. https://doi.org/https://doi.org/10.1016/j.jcou.2017.07.003.

[154] N. Lippiatt, T.-C. Ling, S. Eggermont, Combining hydration and carbonation of cement using super-saturated aqueous CO_2 solution, Constr. Build. Mater. 229 (2019) 116825. https://doi.org/https://doi.org/10.1016/j.conbuildmat.2019.116825.

[155] D. Suescum-Morales, J.M. Fernández-Rodríguez, J.R. Jiménez, Use of carbonated water to improve the mechanical properties and reduce the carbon footprint of cement-based materials with recycled aggregates, J CO_2 Util. 57 (2022) 101886. https://doi.org/https://doi.org/10.1016/j.jcou.2022.101886.

[156] S. Luo, M.-Z. Guo, T.-C. Ling, Modification of early-age microstructure and enhanced mechanical properties of cement paste via injecting low-dose CO_2 at fresh stage, Constr. Build. Mater. 438 (2024) 137284. https://doi.org/https://doi.org/10.1016/j.conbuildmat.2024.137284.

[157] V. Rostami, Y. Shao, A.J. Boyd, Carbonation Curing versus Steam Curing for Precast Concrete Production, Journal of Materials in Civil Engineering 24 (2012) 1221–1229. https://doi.org/10.1061/(ASCE)MT.1943-5533.0000462.

[158] D. Zhang, Y. Shao, Early age carbonation curing for precast reinforced concretes, Constr. Build. Mater. 113 (2016) 134–143. https://doi.org/https://doi.org/10.1016/j.conbuildmat.2016.03.048.

[159] C. Liang, B. Li, M.-Z. Guo, S. Hou, S. Wang, Y. Gao, X. Wang, Effects of early-age carbonation curing on the properties of cement-based materials: A review, J Build Eng. (2024) 108495. https://doi.org/https://doi.org/10.1016/j.jobe.2024.108495.

[160] Z. Liu, W. Meng, Fundamental understanding of carbonation curing and durability of carbonation-cured cement-based composites: A review, Journal of CO_2 Utilization 44 (2021) 101428. https://doi.org/10.1016/J.JCOU.2020.101428.

[161] V. Rostami, Y. Shao, A.J. Boyd, Durability of concrete pipes subjected to combined steam and carbonation curing, Constr. Build. Mater. 25 (2011) 3345–3355. https://doi.org/10.1016/J.CONBUILDMAT.2011.03.025.

[162] J.F. YOUNG, R.L. BERGER, J. BREESE, Accelerated Curing of Compacted Calcium Silicate Mortars on Exposure to CO_2, Journal of the American Ceramic Society 57 (1974) 394–397. https://doi.org/10.1111/j.1151-2916.1974.tb11420.x.

[163] W.A. Klemm, R.L. Berger, Accelerated curing of cementitious systems by carbon dioxide: Part I. Portland cement, Cem. Concr. Res. 2 (1972) 567–576. https://doi.org/10.1016/0008-8846(72)90111-1.

[164] H. El-Hassan, Y. Shao, Z. Ghouleh, Effect of Initial Curing on Carbonation of Lightweight Concrete Masonry Units., ACI Mater. J. 110 (2013). https://doi.org/10.14359/51685791.

[165] L. Mo, F. Zhang, M. Deng, Mechanical performance and microstructure of the calcium carbonate binders produced by carbonating steel slag paste under CO_2 curing, Cem. Concr. Res. 88 (2016) 217–226. https://doi.org/10.1016/j.cemconres.2016.05.013.

[166] P. He, C. Shi, Z. Tu, C.S. Poon, J. Zhang, Effect of further water curing on compressive strength and microstructure of CO_2-cured concrete, Cem. Concr. Compos. 72 (2016) 80–88. https://doi.org/10.1016/j.cemconcomp.2016.05.026.

[167] D. Zhang, X. Cai, Y. Shao, Carbonation Curing of Precast Fly Ash Concrete, Journal of Materials in Civil Engineering 28 (2016). https://doi.org/10.1061/(ASCE)MT.1943-5533.0001649.

[168] A. Neves Junior, R.D. Toledo Filho, E. de Moraes Rego Fairbairn, J. Dweck, The effects of the early carbonation curing on the mechanical and porosity properties of high initial strength Portland cement pastes, Constr. Build. Mater. 77 (2015) 448–454. https://doi.org/10.1016/j.conbuildmat.2014.12.072.

[169] Z. Tu, M. Guo, C.S. Poon, C. Shi, Effects of limestone powder on $CaCO_3$ precipitation in CO_2 cured cement pastes, Cem. Concr. Compos. 72 (2016) 9–16. https://doi.org/10.1016/j.cemconcomp.2016.05.019.

[170] N.Ap.M. Beltrame, R.L. Dias, F.B. Witzke, R.A. Medeiros-Junior, Effect of carbonation curing on the physical, mechanical, and microstructural properties of metakaolin-based geopolymer concrete, Constr. Build. Mater. 406 (2023) 133403. https://doi.org/10.1016/j.conbuildmat.2023.133403.

[171] W. Li, H. Wang, Z. Liu, N. Li, S. Zhao, S. Hu, Steel Slag Accelerated Carbonation Curing for High-Carbonation Precast Concrete Development, Materials 17 (2024) 2968. https://doi.org/10.3390/ma17122968.

[172] X. Pan, C. Shi, X. Hu, Z. Ou, Effects of CO_2 surface treatment on strength and permeability of one-day-aged cement mortar, Constr Build Mater. 154 (2017) 1087–1095. https://doi.org/https://doi.org/10.1016/j.conbuildmat.2017.07.216.

[173] D. Wang, T. Noguchi, T. Nozaki, Increasing efficiency of carbon dioxide sequestration through high temperature carbonation of cement-based materials, J. Clean. Prod. 238 (2019) 117980. https://doi.org/https://doi.org/10.1016/j.jclepro.2019.117980.

[174] S. Ouhenia, D. Chateigner, M.A. Belkhir, E. Guilmeau, C. Krauss, Synthesis of calcium carbonate polymorphs in the presence of polyacrylic acid, J Crystal Growth. 310 (2008) 2832–2841. https://doi.org/https://doi.org/10.1016/j.jcrysgro.2008.02.006.

[175] W. Wang, X. Wei, X. Cai, H. Deng, B. Li, Mechanical and Microstructural Characteristics of Calcium Sulfoaluminate Cement Exposed to Early-Age Carbonation Curing, Materials 14 (2021) 3515. https://doi.org/10.3390/ma14133515.

[176] A. Neves Junior, R.D.T. Filho, E. de M.R. Fairbairn, J. Dweck, A study of the carbonation profile of cement pastes by thermogravimetry and its effect on the compressive strength, J. Therm. Anal. Calorim. 116 (2014) 69–76. https://doi.org/10.1007/s10973-013-3556-7.

[177] L. Zhang, X. Zha, J. Ning, W. Li, Research Status on the Application Technology of Early Age Carbon Dioxide Curing, Buildings 13 (2023) 957. https://doi.org/10.3390/buildings13040957.

[178] I.-S. Yoon, O. Çopuroğlu, K.-B. Park, Effect of global climatic change on carbonation progress of concrete, Atmos. Environ. 41 (2007) 7274–7285. https://doi.org/10.1016/j.atmosenv.2007.05.028.

[179] J.-M. Torrenti, Résultats du projet national FastCarb: stockage de CO_2 par carbonatation accélérée du béton recyclé, in: NOMAD 2022-4e Conférence Internationale Francophone Nouveaux Matériaux et Durabilité, 2022.

[180] H. El-Hassan, Y. Shao, Early carbonation curing of concrete masonry units with Portland limestone cement, Cem. Concr. Compos. 62 (2015) 168–177. https://doi.org/https://doi.org/10.1016/j.cemconcomp.2015.07.004.

[181] Y. Pu, L. Li, X. Shi, Q. Wang, A. Abomohra, Recent advances in accelerated carbonation for improving cement-based materials and CO_2 mitigation from a life cycle perspective, Constr. Build. Mater. 388 (2023) 131695. https://doi.org/10.1016/j.conbuildmat.2023.131695.

[182] M.-Y. Xuan, H.-K. Cho, X.-Y. Wang, Performance improvement of waste oyster-shell powder–cement binary system via carbonation curing, J Build Eng. 70 (2023) 106336. https://doi.org/https://doi.org/10.1016/j.jobe.2023.106336.

[183] D. Xuan, B. Zhan, C.S. Poon, A maturity approach to estimate compressive strength development of CO_2-cured concrete blocks, Cem. Concr. Compos. 85 (2018) 153–160. https://doi.org/10.1016/j.cemconcomp.2017.10.005.

[184] A. Younsi, P. Turcry, E. Rozière, A. Aït-Mokhtar, A. Loukili, Performance-based design and carbonation of concrete with high fly ash content, Cem. Concr. Compos. 33 (2011) 993–1000. https://doi.org/https://doi.org/10.1016/j.cemconcomp.2011.07.005.

[185] Q.T. Phung, N. Maes, D. Jacques, E. Bruneel, I. Van Driessche, G. Ye, G. De Schutter, Effect of limestone fillers on microstructure and permeability due to carbonation of cement pastes under controlled CO_2 pressure conditions, Constr. Build. Mater. 82 (2015) 376–390. https://doi.org/10.1016/j.conbuildmat.2015.02.093.

[186] R.-S. Lin, X.-Y. Wang, Effects of cement types and addition of quartz and limestone on the normal and carbonation curing of cement paste, Constr. Build. Mater. 305 (2021) 124799. https://doi.org/10.1016/j.conbuildmat.2021.124799.

[187] W. Zuo, X. Zhao, J. Luo, Z. He, J. Zhao, Investigating the impact of carbonation curing concentrations on the mechanical properties and microstructure of recycled concrete, Journal of Building Engineering 96 (2024) 110465. https://doi.org/10.1016/J.JOBE.2024.110465.

[188] S. von Greve-Dierfeld, B. Lothenbach, A. Vollpracht, B. Wu, B. Huet, C. Andrade, C. Medina, C. Thiel, E. Gruyaert, H. Vanoutrive, Understanding the carbonation of concrete with supplementary cementitious materials: a critical review by RILEM TC 281-CCC, Mater Struct. 53 (2020) 136. https://doi.org/https://doi.org/10.1617/s11527-020-01558-w.

[189] L. Liu, Y. Liu, X. Tian, X. Chen, Superior CO_2 uptake and enhanced compressive strength for carbonation curing of cement-based materials via flue gas, Constr. Build. Mater. 346 (2022) 128364. https://doi.org/https://doi.org/10.1016/j.conbuildmat.2022.128364.

[190] T. Chen, X. Gao, Effect of carbonation curing regime on strength and microstructure of Portland cement paste, J CO_2 Util. 34 (2019) 74–86. https://doi.org/https://doi.org/10.1016/j.jcou.2019.05.034.

[191] L. Qin, X. Gao, T. Chen, Influence of mineral admixtures on carbonation curing of cement paste, Constr. Build. Mater. 212 (2019) 653–662. https://doi.org/https://doi.org/10.1016/j.conbuildmat.2019.04.033.

[192] T. Chen, M. Bai, X. Gao, Carbonation curing of cement mortars incorporating carbonated fly ash for performance improvement and CO_2 sequestration, Journal of CO_2 Utilization 51 (2021) 101633. https://doi.org/10.1016/j.jcou.2021.101633.

[193] D. Zhang, Y. Shao, Effect of early carbonation curing on chloride penetration and weathering carbonation in concrete, Constr. Build. Mater. 123 (2016) 516–526. https://doi.org/https://doi.org/10.1016/j.conbuildmat.2016.07.041.

[194] M. Castellote, L. Fernandez, C. Andrade, C. Alonso, Chemical changes and phase analysis of OPC pastes carbonated at different CO_2 concentrations, Mater Struct. 42 (2009) 515–525. https://doi.org/https://doi.org/10.1617/s11527-008-9399-1.

[195] M. Boumaaza, B. Huet, P. Turcry, A. Aït-Mokhtar, The CO_2-binding capacity of synthetic anhydrous and hydrates: Validation of a test method based on the instantaneous reaction rate, Cem. Concr. Res. 135 (2020) 106113. https://doi.org/https://doi.org/10.1016/j.cemconres.2020.106113.

[196] Q. Qiu, A state-of-the-art review on the carbonation process in cementitious materials: Fundamentals and characterization techniques, Constr Build Mater. 247 (2020) 118503. https://doi.org/https://doi.org/10.1016/j.conbuildmat.2020.118503.

[197] E. Mohammadian, F. Hadavimoghaddam, M. Kheirollahi, M. Jafari, X. Chenlu, B. Liu, Probing Solubility and pH of CO_2 in aqueous solutions: Implications for CO_2 injection into oceans, J CO_2 Util. 71 (2023) 102463. https://doi.org/https://doi.org/10.1016/j.jcou.2023.102463.

[198] A. Uliasz-Bocheńczyk, A Comprehensive Review of CO_2 Mineral Sequestration Methods Using Coal Fly Ash for Carbon Capture, Utilisation, and Storage (CCUS) Technology, Energies (Basel). 17 (2024) 5605. https://doi.org/10.3390/en17225605.

[199] C.A.J. Appelo, D. Postma, Geochemistry, Groundwater and Pollution, CRC Press, 2004. https://doi.org/10.1201/9781439833544.

[200] Y. Han, M.G. Ucak-Astarlioglu, J.F. Burroughs, J.W. Bullard, Calcium hydroxide dissolution rates: Dependence on temperature and saturation, Chemical Engineering Journal 515 (2025) 162484. https://doi.org/10.1016/J.CEJ.2025.162484.

[201] T. Ishida, K. Maekawa, Modeling of pH profile in pore water based on mass transport and chemical equilibrium theory, Doboku Gakkai Ronbunshu. 2000 (2000) 203–215. https://doi.org/https://doi.org/10.2208/jscej.2000.648_203.

[202] D.R. Moorehead, Cementation by the carbonation of hydrated lime, Cem. Concr. Res. 16 (1986) 700–708. https://doi.org/https://doi.org/10.1016/0008-8846(86)90044-X.

[203] I. Galan, F.P. Glasser, D. Baza, C. Andrade, Assessment of the protective effect of carbonation on portlandite crystals, Cem. Concr. Res. 74 (2015) 68–77. https://doi.org/https://doi.org/10.1016/j.cemconres.2015.04.001.

[204] E. Ruiz-Agudo, K. Kudłacz, C. V Putnis, A. Putnis, C. Rodriguez-Navarro, Dissolution and carbonation of portlandite ($Ca(OH)_2$) single crystals, Environ Sci Technol. 47 (2013) 11342–11349. https://doi.org/https://doi.org/10.1021/es402061c.

[205] Y.-B. Hu, M. Wolthers, D.A. Wolf-Gladrow, G. Nehrke, Effect of pH and phosphate on calcium carbonate polymorphs precipitated at near-freezing temperature, Cryst. Growth Des. 15 (2015) 1596–1601. https://doi.org/https://doi.org/10.1021/cg500829p.

[206] X. Xu, C. Qi, X.M. Aretxabaleta, C. Ma, D. Spagnoli, H. Manzano, The initial stages of cement hydration at the molecular level, Nat Commun. 15 (2024) 2731. https://doi.org/https://doi.org/10.1038/s41467-024-46962-w.

[207] A.E. Morandeau, C.E. White, In situ X-ray pair distribution function analysis of accelerated carbonation of a synthetic calcium–silicate–hydrate gel, J Mater Chem A. 3 (2015) 8597–8605. https://doi.org/https://doi.org/10.1039/C5TA00348B.

[208] J.F. Young, W. Hansen, Volume relationships for CSH formation based on hydration stoichiometries, MRS Online Proc Libr. 85 (1986) 313–322. https://doi.org/https://doi.org/10.1557/PROC-85-313.

[209] H.F.W. Taylor, Cement chemistry, Thomas Telford London, 1997.

[210] M. Yousuf, A. Mollah, T.R. Hess, Y.-N. Tsai, D.L. Cocke, An FTIR and XPS investigations of the effects of carbonation on the solidification/stabilization of cement based systems-Portland type V with zinc, Cem. Concr. Res. 23 (1993) 773–784. https://doi.org/https://doi.org/10.1016/0008-8846(93)90031-4.

[211] X. Liu, P. Feng, Y. Cai, X. Yu, C. Yu, Q. Ran, Carbonation behavior of calcium silicate hydrate (CSH): Its potential for CO_2 capture, Chemical Engineering Journal 431 (2022) 134243. https://doi.org/https://doi.org/10.1016/j.cej.2021.134243.

[212] G. Villain, M. Thiery, G. Platret, Measurement methods of carbonation profiles in concrete: Thermogravimetry, chemical analysis and gammadensimetry, Cem. Concr. Res. 37 (2007) 1182–1192. https://doi.org/10.1016/j.cemconres.2007.04.015.

[213] F.P. Glasser, T. Matschei, Interactions between Portland cement and carbon dioxide, in: Proceedings of the ICCC Conference., 2007.

[214] A. Morandeau, M. Thiery, P. Dangla, Investigation of the carbonation mechanism of CH and CSH in terms of kinetics, microstructure changes and moisture properties, Cem. Concr. Res. 56 (2014) 153–170. https://doi.org/https://doi.org/10.1016/j.cemconres.2013.11.015.

[215] T. Nishikawa, K. Suzuki, S. Ito, K. Sato, T. Takebe, Decomposition of synthesized ettringite by carbonation, Cem. Concr. Res. 22 (1992) 6–14. https://doi.org/https://doi.org/10.1016/0008-8846(92)90130-N.

[216] K. Ndiaye, M. Cyr, S. Ginestet, Durability and stability of an ettringite-based material for thermal energy storage at low temperature, Cem. Concr. Res. 99 (2017) 106–115. https://doi.org/https://doi.org/10.1016/j.cemconres.2017.05.001.

[217] C.W. Hargis, B. Lothenbach, C.J. Müller, F. Winnefeld, Carbonation of calcium sulfoaluminate mortars, Cem. Concr. Compos. 80 (2017) 123–134. https://doi.org/https://doi.org/10.1016/j.cemconcomp.2017.03.003.

[218] J. Seo, S. Kim, S. Park, H.N. Yoon, H.-K. Lee, Carbonation of calcium sulfoaluminate cement blended with blast furnace slag, Cem. Concr. Compos. 118 (2021) 103918. https://doi.org/https://doi.org/10.1016/j.cemconcomp.2020.103918.

[219] V. Shah, K. Scrivener, B. Bhattacharjee, S. Bishnoi, Changes in microstructure characteristics of cement paste on carbonation, Cem. Concr. Res. 109 (2018) 184–197. https://doi.org/https://doi.org/10.1016/j.cemconres.2018.04.016.

[220] T. Grounds, H.G. Midgley, D. V Novell, Carbonation of ettringite by atmospheric carbon dioxide, Thermochim. Acta 135 (1988) 347–352. https://doi.org/https://doi.org/10.1016/0040-6031(88)87407-0.

[221] M.-N. Brahim, J.-M. Mechling, S. Janvier-Badosa, M. Marchetti, Early stage ettringite and monosulfoaluminate carbonation investigated by in situ Raman spectroscopy coupled with principal component analysis, Mater Today Commun. 35 (2023) 105539. https://doi.org/https://doi.org/10.1016/j.mtcomm.2023.105539.

[222] Y. Li, J. Zhang, H. Zeng, H. Zhang, Ion association behaviors in the initial stage of calcium carbonate formation: An ab initio study, J Chem Phys. 161 (2024). https://doi.org/https://doi.org/10.1063/5.0206841.

[223] J.W. Morse, F.T. Mackenzie, The CO_2-carbonic acid system and solution chemistry, Geochem Sediment Carbonates: Developments in Sedimentology. 48 (1990) 1–38.

[224] J.J. Chen, J.J. Thomas, H.F.W. Taylor, H.M. Jennings, Solubility and structure of calcium silicate hydrate, Cem. Concr. Res. 34 (2004) 1499–1519. https://doi.org/10.1016/J.CEMCONRES.2004.04.034.

[225] B. Lagerblad, Carbon dioxide uptake during concrete life cycle, State of the Art, Swedish Cement and Concrete Research Institute-CBI, Www. Cbi. Se. (2005).

[226] Z. Shi, B. Lothenbach, M.R. Geiker, J. Kaufmann, A. Leemann, S. Ferreiro, J. Skibsted, Experimental studies and thermodynamic modeling of the carbonation of Portland cement, metakaolin and limestone mortars, Cem. Concr. Res. 88 (2016) 60–72. https://doi.org/10.1016/j.cemconres.2016.06.006.

[227] C.W. Hargis, B. Lothenbach, C.J. Müller, F. Winnefeld, Carbonation of calcium sulfoaluminate mortars, Cem. Concr. Compos. 80 (2017) 123–134. https://doi.org/10.1016/j.cemconcomp.2017.03.003.

[228] K. De Weerdt, G. Plusquellec, A. Belda Revert, M.R. Geiker, B. Lothenbach, Effect of carbonation on the pore solution of mortar, Cem. Concr. Res. 118 (2019) 38–56. https://doi.org/10.1016/j.cemconres.2019.02.004.

[229] J.-Y. Gal, J.-C. Bollinger, H. Tolosa, N. Gache, Calcium carbonate solubility: a reappraisal of scale formation and inhibition, Talanta 43 (1996) 1497–1509. https://doi.org/https://doi.org/10.1016/0039-9140(96)01925-X.

[230] Y.S. Han, G. Hadiko, M. Fuji, M. Takahashi, Effect of flow rate and CO_2 content on the phase and morphology of $CaCO_3$ prepared by bubbling method, J Crystal Growth. 276 (2005) 541–548. https://doi.org/https://doi.org/10.1016/j.jcrysgro.2004.11.408.

[231] S.R. Kamhi, On the structure of vaterite $CaCO_3$, Acta Crystallogr. 16 (1963) 770–772. https://doi.org/10.1107/S0365110X63002000.

[232] M. Arandigoyen, B. Bicer-Simsir, J.I. Alvarez, D.A. Lange, Variation of microstructure with carbonation in lime and blended pastes, Appl. Surf. Sci. 252 (2006) 7562–7571. https://doi.org/https://doi.org/10.1016/j.apsusc.2005.09.007.

[233] A. Declet, E. Reyes, O.M. Suárez, Calcium carbonate precipitation: a review of the carbonate crystallization process and applications in bioinspired composites., Rev Adv Mater Sci. 44 (2016).

[234] J.W. Morse, R.S. Arvidson, A. Lüttge, Calcium carbonate formation and dissolution, Chem. Rev. 107 (2007) 342–381. https://doi.org/https://doi.org/10.1021/cr050358j.

[235] Z. Hu, Y. Deng, Synthesis of needle-like aragonite from calcium chloride and sparingly soluble magnesium carbonate, Powder Technol. 140 (2004) 10–16. https://doi.org/https://doi.org/10.1016/j.powtec.2004.01.001.

[236] E. Ruiz-Agudo, C. V. Putnis, C. Jiménez-López, C. Rodriguez-Navarro, An atomic force microscopy study of calcite dissolution in saline solutions: The role of magnesium ions, Geochim. Cosmochim. Acta 73 (2009) 3201–3217. https://doi.org/10.1016/J.GCA.2009.03.016.

[237] N. Shifeta, S.L. Hamukwaya, Q. An, H. Hao, M. Mashingaidze, Layer-by-Layer Fabrication of PAH/PAMAM/Nano-$CaCO_3$ Composite Films and Characterization for Enhanced Biocompatibility, Int. J. Biomater. 2022 (2022) 1–14. https://doi.org/10.1155/2022/6331465.

[238] R. Ševčík, P. Šašek, A. Viani, Physical and nanomechanical properties of the synthetic anhydrous crystalline $CaCO_3$ polymorphs: vaterite, aragonite and calcite, J Mater Sci. 53 (2018). https://doi.org/10.1007/s10853-017-1884-x.

[239] S. Gopi, V.K. Subramanian, K. Palanisamy, Aragonite–calcite–vaterite: A temperature influenced sequential polymorphic transformation of $CaCO_3$ in the presence of DTPA, Mater. Res. Bull. 48 (2013) 1906–1912. https://doi.org/https://doi.org/10.1016/j.materresbull.2013.01.048.

[240] Y.S. Han, G. Hadiko, M. Fuji, M. Takahashi, Effect of flow rate and CO_2 content on the phase and morphology of $CaCO_3$ prepared by bubbling method, J. Cryst. Growth 276 (2005) 541–548. https://doi.org/10.1016/J.JCRYSGRO.2004.11.408.

[241] Y.S. Han, G. Hadiko, M. Fuji, M. Takahashi, Influence of initial $CaCl_2$ concentration on the phase and morphology of $CaCO_3$ prepared by carbonation, J Mater Sci. 41 (2006) 4663–4667. https://doi.org/https://doi.org/10.1007/s10853-006-0037-4.

[242] Z. Xiao, J. Zhang, X. Hu, A. Khaskhoussi, P. He, X. You, X. Su, W. Chen, C. Shi, An overview on polymorphs of calcium carbonate formed during carbon mineralization of cementitious materials, J. Sustain. Cem. Based. Mater. (2025) 1–23. https://doi.org/10.1080/21650373.2025.2471820.

[243] F. Liendo, M. Arduino, F.A. Deorsola, S. Bensaid, Factors controlling and influencing polymorphism, morphology and size of calcium carbonate synthesized through the carbonation route: A review, Powder Technol. 398 (2022) 117050. https://doi.org/https://doi.org/10.1016/j.powtec.2021.117050.

[244] F. Wu, X. You, M. Wang, T. Liu, B. Lu, G. Hou, R. Jiang, C. Shi, Increasing flexural strength of CO_2 cured cement paste by $CaCO_3$ polymorph control, Cem. Concr. Compos. 141 (2023) 105128. https://doi.org/https://doi.org/10.1016/j.cemconcomp.2023.105128.

[245] D. Ergenç, L.S. Gómez-Villalba, R. Fort, Crystal development during carbonation of lime-based mortars in different environmental conditions, Mater Char. 142 (2018) 276–288. https://doi.org/https://doi.org/10.1016/j.matchar.2018.05.043.

[246] J. Chang, Y. Fang, X. Shang, The role of β-C_2S and γ-C_2S in carbon capture and strength development, Mater Struct. 49 (2016) 4417–4424. https://doi.org/https://doi.org/10.1617/s11527-016-0797-5.

[247] W. Ashraf, J. Olek, Carbonation behavior of hydraulic and non-hydraulic calcium silicates: potential of utilizing low-lime calcium silicates in cement-based materials, J Mater Sci. 51 (2016) 6173–6191. https://doi.org/https://doi.org/10.1007/s10853-016-9909-4.

[248] Ö. Cizer, C. Rodriguez-Navarro, E. Ruiz-Agudo, J. Elsen, D. Van Gemert, K. Van Balen, Phase and morphology evolution of calcium carbonate precipitated by carbonation of hydrated lime, J Mater Sci. 47 (2012) 6151–6165. https://doi.org/https://doi.org/10.1007/s10853-012-6535-7.

[249] J. Ibáñez, L. Artús, R. Cuscó, Á. López, E. Menéndez, M.C. Andrade, Hydration and carbonation of monoclinic C_2S and C_2S studied by Raman spectroscopy, J Raman Spectrosc. 38 (2007) 61–67. https://doi.org/https://doi.org/10.1002/jrs.1599.

[250] J.M. Bukowski, R.L. Berger, Reactivity and strength development of CO_2 activated non-hydraulic calcium silicates, Cem. Concr. Res. 9 (1979) 57–68. https://doi.org/https://doi.org/10.1016/0008-8846(79)90095-4.

[251] Z. He, Y. Jia, S. Wang, M. Mahoutian, Y. Shao, Maximizing CO_2 sequestration in cement-bonded fiberboards through carbonation curing, Constr. Build. Mater. 213 (2019) 51–60. https://doi.org/https://doi.org/10.1016/j.conbuildmat.2019.04.042.

[252] D. Xuan, B. Zhan, C.S. Poon, A maturity approach to estimate compressive strength development of CO_2-cured concrete blocks, Cem. Concr. Compos. 85 (2018) 153–160. https://doi.org/10.1016/j.cemconcomp.2017.10.005.

[253] B. Zhan, C.S. Poon, Q. Liu, S. Kou, C. Shi, Experimental study on CO_2 curing for enhancement of recycled aggregate properties, Constr. Build. Mater. 67 (2014) 3–7. https://doi.org/https://doi.org/10.1016/j.conbuildmat.2013.09.008.

[254] A. Djerbi, M. Sereng, O.M. Othman, B. Cazacliu, G.S. dos Reis, Développement de procédés de carbonatation accélérée pour les granulats recyclés, (2021).

[255] S.O. Ekolu, Model for practical prediction of natural carbonation in reinforced concrete: Part 1-formulation, Cem. Concr. Compos. 86 (2018) 40–56. https://doi.org/10.1016/j.cemconcomp.2017.10.006.

[256] Q.T. Phung, N. Maes, D. Jacques, G. De Schutter, G. Ye, J. Perko, Modelling the carbonation of cement pastes under a CO_2 pressure gradient considering both diffusive and convective transport, Constr. Build. Mater. 114 (2016) 333–351. https://doi.org/10.1016/j.conbuildmat.2016.03.191.

[257] B. Šavija, M. Luković, Carbonation of cement paste: Understanding, challenges, and opportunities, Constr Build Mater. 117 (2016) 285–301. https://doi.org/10.1016/j.conbuildmat.2016.04.138.

[258] S. Kashef-Haghighi, S. Ghoshal, Physico–Chemical Processes Limiting CO_2 Uptake in Concrete during Accelerated Carbonation Curing, Ind. Eng. Chem. Res. 52 (2013) 5529–5537. https://doi.org/10.1021/ie303275e.

[259] J.H. Seo, S.M. Park, H.K. Lee, Evolution of the binder gel in carbonation-cured Portland cement in an acidic medium, Cem. Concr. Res. 109 (2018) 81–89. https://doi.org/10.1016/j.cemconres.2018.03.014.

[260] X. Xian, Y. Shao, Microstructure of cement paste subject to ambient pressure carbonation curing, Constr. Build. Mater. 296 (2021) 123652. https://doi.org/10.1016/j.conbuildmat.2021.123652.

[261] L. Jiang, Q. Wu, Z. Huo, Z. Zhu, F. Wu, B. Lu, An approach to improve compressive strength of cement paste at low temperature by carbonation curing, Constr. Build. Mater. 365 (2023) 130128. https://doi.org/https://doi.org/10.1016/j.conbuildmat.2022.130128.

[262] M. Mutti, S. Joseph, R. Snellings, Ö. Cizer, Effect of slag pre-carbonation on its early-age reactivity in alkali activated binder, Constr. Build. Mater. 411 (2024) 134413. https://doi.org/https://doi.org/10.1016/j.conbuildmat.2023.134413.

[263] G. Li, Z. Li, H. Ma, Synthesis of aragonite by carbonization from dolomite without any additives, Int. J. Miner. Process. 123 (2013) 25–31. https://doi.org/https://doi.org/10.1016/j.minpro.2013.03.006.

[264] R. Hay, B. Peng, K. Celik, Filler effects of $CaCO_3$ polymorphs derived from limestone and seashell on hydration and carbonation of reactive magnesium oxide (MgO) cement (RMC), Cem. Concr. Res. 164 (2023) 107040. https://doi.org/https://doi.org/10.1016/j.cemconres.2022.107040.

[265] T. Van Gerven, G. Cornelis, E. Vandoren, C. Vandecasteele, Effects of carbonation and leaching on porosity in cement-bound waste, Waste Management 27 (2007) 977–985. https://doi.org/10.1016/j.wasman.2006.05.008.

[266] R. Kumar, B. Bhattacharjee, Porosity, pore size distribution and in situ strength of concrete, Cem. Concr. Res. 33 (2003) 155–164. https://doi.org/10.1016/S0008-8846(02)00942-0.

[267] J.G. Jang, G.M. Kim, H.J. Kim, H.-K. Lee, Review on recent advances in CO_2 utilization and sequestration technologies in cement-based materials, Constr. Build. Mater. 127 (2016) 762–773. https://doi.org/https://doi.org/10.1016/j.conbuildmat.2016.10.017.

[268] M. Auroy, S. Poyet, P. Le Bescop, J.M. Torrenti, T. Charpentier, M. Moskura, X. Bourbon, Impact of carbonation on unsaturated water transport properties of cement-based materials, Cem. Concr. Res. 74 (2015) 44–58. https://doi.org/10.1016/J.CEMCONRES.2015.04.002.

[269] M.J. Miah, J. Pei, H. Kim, J.G. Jang, Flexural behavior, porosity, and water absorption of CO_2-cured amorphous metallic-fiber-reinforced belite-rich cement composites, Constr. Build. Mater. 387 (2023) 131668. https://doi.org/10.1016/J.CONBUILDMAT.2023.131668.

[270] S.T. Pham, W. Prince, Effects of Carbonation on the Microstructure of Cement Materials: Influence of Measuring Methods and of Types of Cement, Int. J. Concr. Struct. Mater. 8 (2014) 327–333. https://doi.org/10.1007/s40069-014-0079-y.

[271] H. Ostovari, A. Sternberg, A. Bardow, Rock 'n'use of CO_2: carbon footprint of carbon capture and utilization by mineralization, Sustain. Energy Fuels 4 (2020) 4482–4496. https://doi.org/10.1039/D0SE00190B.

[272] N. Thonemann, L. Zacharopoulos, F. Fromme, J. Nühlen, Environmental impacts of carbon capture and utilization by mineral carbonation: A systematic literature review and meta life cycle assessment, J. Clean. Prod. 332 (2022) 130067.

[273] D. Chateigner, C. Hedegaard, H.R. Wenk, Mollusc shell microstructures and crystallographic textures, J. Struct. Geol. 22 (2000) 1723–1735. https://doi.org/10.1016/S0191-8141(00)00088-2.

[274] L.P. Singh, A. Goel, S.K. Bhattachharyya, S. Ahalawat, U. Sharma, G. Mishra, Effect of Morphology and Dispersibility of Silica Nanoparticles on the Mechanical Behaviour of Cement Mortar, Int. J. Concr. Struct. Mater. 9 (2015) 207–217. https://doi.org/10.1007/s40069-015-0099-2.

[275] B. Pokroy, J.S. Fieramosca, R.B. Von Dreele, A.N. Fitch, E.N. Caspi, E. Zolotoyabko, Atomic Structure of Biogenic Aragonite, Chemistry of Materials 19 (2007) 3244–3251. https://doi.org/10.1021/cm070187u.

[276] S. Ouhenia, D. Chateigner, M.A. Belkhir, E. Guilmeau, Microstructure and crystallographic texture of Charonia lampas lampas shell, J. Struct. Biol. 163 (2008) 175–184. https://doi.org/10.1016/J.JSB.2008.05.005.

[277] B. Pokroy, A.N. Fitch, F. Marin, M. Kapon, N. Adir, E. Zolotoyabko, Anisotropic lattice distortions in biogenic calcite induced by intra-crystalline organic molecules, J. Struct. Biol. 155 (2006) 96–103. https://doi.org/10.1016/J.JSB.2006.03.008.

[278] NF EN 1097-7, Tests for mechanical and physical properties of aggregates - Part 7: Determination of the particle density of filler - Pyknometer method, (2022).

[279] NF EN 196-6, Methods of testing cement - Determination of fineness, (2018).

[280] ISO 9277, Determination of the specific surface area of solids by gas adsorption - BET method, (2022).

[281] NF EN 1097-4, Tests for mechanical and physical properties of aggregates - Part 4: Determination of the voids of dry compacted filler, (2008).

[282] NF ISO 13320-1, Particle size analysis - Laser diffraction methods - Part 1: General principle, (2000).

[283] NF EN 1097-6, Tests for mechanical and physical properties of aggregates - Part 6 : determination of particle density and water absorption, (2022).

[284] NF EN 933-1, Tests for geometrical properties of aggregates - Part 1: Determination of particle size distribution - Sieving method, (2012).

[285] NF EN 1097-1, Tests for mechanical and physical properties of aggregates - Part 1 : determination of the resistance to wear (micro-Deval), (2023).

[286] NF EN 1097-2, Tests for mechanical and physical properties of aggregates - Part 2: Methods for the determination of resistance to fragmentation, 2 (2020).

[287] NF EN 12350-8, Testing fresh concrete - Part 8: Self-compacting concrete - Slump-flow test, (2019).

[288] C. Pade, M. Guimaraes, The CO_2 uptake of concrete in a 100 year perspective, Cem. Concr. Res. 37 (2007) 1348–1356. https://doi.org/https://doi.org/10.1016/j.cemconres.2007.06.009.

[289] NF EN 12350-11, Testing fresh concrete - Part 11: Self-compacting concrete - Sieve segregation test, (2010).

[290] NF EN 12390-3, Testing hardened concrete - Part 3 : compressive strength of test specimens, (2019).

[291] NF P 18-459, Concrete - Testing hardened concrete - Density and porosity test, (2022).

[292] ISO 15901-1, Evaluation of pore size distribution and porosity of solid materials by mercury porosimetry and gas adsorption - Part 1: Mercury porosimetry, (2016).

[293] A. Le Bail, Modelling the silica glass structure by the Rietveld method, J. Non. Cryst. Solids 183 (1995) 39–42. https://doi.org/10.1016/0022-3093(94)00664-4.

[294] OSCARS | Fostering the uptake of Open Science in Europe, (2024). https://oscars-project.eu/ (accessed October 21, 2025).

[295] MAUD - Materials Analysis Using Diffraction (and more), (n.d.). https://luttero.github.io/maud/ (accessed October 21, 2025).

[296] L. Lutterotti, D. Chateigner, S. Ferrari, J. Ricote, Texture, residual stress and structural analysis of thin films using a combined X-ray analysis, Thin Solid Films 450 (2004) 34–41. https://doi.org/10.1016/J.TSF.2003.10.150.

[297] N.C. Popa, The (hkl) Dependence of Diffraction-Line Broadening Caused by Strain and Size for all Laue Groups in Rietveld Refinement, J. Appl. Crystallogr. 31 (1998) 176–180. https://doi.org/10.1107/S0021889897009795.

[298] NF EN 1097-5, Tests for mechanical and physical properties of aggregates -Part 5: Determination of the water content by drying in aventilated oven, (2008).

[299] M. Sakoparnig, I. Galan, B. Müller, F. Mittermayr, J. Juhart, C. Grengg, Optical pH imaging reveals what phenolphthalein conceals – A carbonation study on blended cements, Cem. Concr. Res. 186 (2024) 107681. https://doi.org/10.1016/j.cemconres.2024.107681.

[300] L. Mo, D.K. Panesar, Effects of accelerated carbonation on the microstructure of Portland cement pastes containing reactive MgO, Cem. Concr. Res. 42 (2012) 769–777. https://doi.org/10.1016/j.cemconres.2012.02.017.

[301] NF EN 12390-12, Testing hardened concrete - Part 12: Determination of the carbonation resistance of concrete - Accelerated carbonation method, (2020).

[302] H.M. Rietveld, A profile refinement method for nuclear and magnetic structures, Urn:Issn:0021-8898 2 (1969) 65–71. https://doi.org/10.1107/S0021889869006558.

[303] L.B. Mccusker, R.B. Von Dreele, D.E. Cox, D. Louër, P. Scardi, Rietveld refinement guidelines, Urn:Issn:0021-8898 32 (1999) 36–50. https://doi.org/10.1107/S0021889898009856.

[304] B. Maestracci, Nouvelle approche de mesures et analyses combinées XRF-XRD sur site pour la caractérisation géochimique, minéralogique et texturale : application à la verse de Nartau enrichie en arsenic, district aurifère de Salsigne, Aude (France), 2023. https://theses.fr/2023NORMC260 (accessed October 21, 2025).

[305] B.H. Toby, R factors in Rietveld analysis: How good is good enough?, Powder Diffr. 21 (2006) 67–70. https://doi.org/10.1154/1.2179804.

[306] S.T. Misture, R.L. Snyder, X-ray Diffraction, Encyclopedia of Materials: Science and Technology (2001) 9799–9808. https://doi.org/10.1016/B0-08-043152-6/01778-2.

[307] Crystallography Open Database, (n.d.). https://www.crystallography.net/cod/ (accessed October 21, 2025).

[308] L. Liu, P. Yang, C. Qi, B. Zhang, L. Guo, K.-I. Song, An experimental study on the early-age hydration kinetics of cemented paste backfill, Constr. Build. Mater. 212 (2019) 283–294. https://doi.org/10.1016/j.conbuildmat.2019.03.322.

[309] J.W. Bullard, H.M. Jennings, R.A. Livingston, A. Nonat, G.W. Scherer, J.S. Schweitzer, K.L. Scrivener, J.J. Thomas, Mechanisms of cement hydration, Cem. Concr. Res. 41 (2011) 1208–1223. https://doi.org/10.1016/j.cemconres.2010.09.011.

[310] M.M. Rusu, D. Faux, I. Ardelean, Monitoring the Effect of Calcium Nitrate on the Induction Period of Cement Hydration via Low-Field NMR Relaxometry, Molecules 28 (2023) 476. https://doi.org/10.3390/molecules28020476.

[311] P. Juilland, E. Gallucci, R. Flatt, K. Scrivener, Dissolution theory applied to the induction period in alite hydration, Cem. Concr. Res. 40 (2010) 831–844. https://doi.org/10.1016/j.cemconres.2010.01.012.

[312] P. Li, Z. Jiang, X. An, K. Maekawa, S. Du, Time-dependent retardation effect of epoxy latexes on cement hydration: Experiments and multi-component hydration model, Constr. Build. Mater. 320 (2022) 126282. https://doi.org/10.1016/j.conbuildmat.2021.126282.

[313] X. Pang, The effect of water-to-cement ratio on the hydration kinetics of Portland cement at different temperatures, in: Proceedings of the 14th International Congress on Cement Chemistry, 2015. https://doi.org/10.13140/RG.2.1.4526.2800.

[314] M.J. Ahmed, K. Lambrechts, X. Ling, K. Schollbach, H.J.H. Brouwers, Effect of hydroxide, carbonate, and sulphate anions on the β-dicalcium silicate hydration rate, Cem. Concr. Res. 173 (2023) 107302. https://doi.org/10.1016/J.CEMCONRES.2023.107302.

[315] X. Gu, B. Yang, Z. Li, B. Liu, J. Liu, Q. Wang, M.L. Nehdif, Elucidating the reaction of seashell powder within fly ash cement: A focus on hydration products, Constr. Build. Mater. 428 (2024) 136331. https://doi.org/10.1016/j.conbuildmat.2024.136331.

[316] B. Lothenbach, K. Scrivener, R.D. Hooton, Supplementary cementitious materials, Cem. Concr. Res. 41 (2011) 1244–1256. https://doi.org/10.1016/j.cemconres.2010.12.001.

[317] O. Oueslati, J. Duchesne, The effect of SCMs and curing time on resistance of mortars subjected to organic acids, Cem. Concr. Res. 42 (2012) 205–214. https://doi.org/10.1016/J.CEMCONRES.2011.09.017.

[318] S. Ge, Y. Pan, L. Zheng, X. Xie, Effects of organic matter components and incubation on the cement-based stabilization/solidification characteristics of lead-contaminated soil, Chemosphere 260 (2020) 127646. https://doi.org/10.1016/J.CHEMOSPHERE.2020.127646.

[319] E. Lipczynska-Kochany, Humic substances, their microbial interactions and effects on biological transformations of organic pollutants in water and soil: A review, Chemosphere 202 (2018) 420–437. https://doi.org/10.1016/J.CHEMOSPHERE.2018.03.104.

[320] T. Danner, H. Justnes, M. Geiker, R.A. Lauten, Early hydration of C_3A–gypsum pastes with Ca- and Na-lignosulfonate, Cem. Concr. Res. 79 (2016) 333–343. https://doi.org/10.1016/J.CEMCONRES.2015.10.008.

[321] C. Ma, B. Chen, L. Chen, Effect of organic matter on strength development of self-compacting earth-based construction stabilized with cement-based composites, Constr. Build. Mater. 123 (2016) 414–423. https://doi.org/10.1016/J.CONBUILDMAT.2016.07.018.

[322] B. Tripathi, Effects of Polymers on Cement Hydration and Properties of Concrete: A Review, ACS Omega 9 (2024) 2014–2021. https://doi.org/10.1021/acsomega.3c05914.

[323] M. Hadjadj, M. Guendouz, D. Boukhelkhal, The effect of using seashells as cementitious bio-material and granite industrial waste as fine aggregate on mechanical and durability properties of green flowable sand concrete, Journal of Building Engineering 87 (2024) 108968. https://doi.org/10.1016/j.jobe.2024.108968.

[324] Y. Wu, J. Lu, Y. Nie, W. He, Effect of seashell powder as binder material on the performance and microstructure of low-carbon sustainable alkali-activated concrete, Journal of Building Engineering 90 (2024) 109442. https://doi.org/10.1016/j.jobe.2024.109442.

[325] M. Tuyan, A. Mardani-Aghabaglou, K. Ramyar, Freeze–thaw resistance, mechanical and transport properties of self-consolidating concrete incorporating coarse recycled concrete aggregate, Mater. Des. 53 (2014) 983–991. https://doi.org/10.1016/j.matdes.2013.07.100.

[326] A.M. Zeyad, A. Almalki, Influence of mixing time and superplasticizer dosage on self-consolidating concrete properties, Journal of Materials Research and Technology 9 (2020) 6101–6115. https://doi.org/10.1016/J.JMRT.2020.04.013.

[327] Combined Effect of Polycarboxylate Ether and Phosphonated Superplasticizers in Limestone Calcined Clay Cement, in: SP-362: ICCM2024, American Concrete Institute, 2024. https://doi.org/10.14359/51741004.

[328] S. Moghul, F. Zunino, R.J. Flatt, Flow loss in superplasticized limestone calcined clay cement, Journal of the American Ceramic Society 108 (2025). https://doi.org/10.1111/jace.20344.

[329] Md.H.R. Sobuz, S.D. Datta, A.S.M. Akid, V.W.Y. Tam, S. Islam, Md.J. Rana, F. Aslani, Ç. Yalçınkaya, N.M. Sutan, Evaluating the effects of recycled concrete aggregate size and concentration on properties of

high-strength sustainable concrete, Journal of King Saud University - Engineering Sciences (2022). https://doi.org/10.1016/j.jksues.2022.04.004.

[330] J.J. Assaad, J. Harb, Formwork Pressure of Self-Consolidating Concrete Containing Recycled Coarse Aggregates, ACI Mater. J. 114 (2017). https://doi.org/10.14359/51689494.

[331] C.-C. Liao, A study of the effect of liquid viscosity on density-driven wet granular segregation in a rotating drum, Powder Technol. 325 (2018) 632–638. https://doi.org/10.1016/j.powtec.2017.11.004.

[332] E.W.C. Lim, Density segregation of dry and wet granular mixtures in vibrated beds, Advanced Powder Technology 27 (2016) 2478–2488. https://doi.org/10.1016/j.apt.2016.09.028.

[333] S. Bellara, W. Maherzi, S. Mezazigh, A. Senouci, Mineral waste valorization in road subgrade construction: Algerian case study based on technical and environmental features, Case Studies in Construction Materials 20 (2024) e02764. https://doi.org/10.1016/j.cscm.2023.e02764.

[334] E. Mahfoud, W. Maherzi, K. Ndiaye, M. Benzerzour, S. Aggoun, N.-E. Abriak, Mechanical and microstructural properties of just add water geopolymer cement comprised of Thermo-Mechanicalsynthesis Sediments-Fly ash mix, Constr. Build. Mater. 400 (2023) 132626. https://doi.org/10.1016/j.conbuildmat.2023.132626.

[335] A.D. Iams, M.Z. Gao, A. Shetty, T.A. Palmer, Influence of particle size on powder rheology and effects on mass flow during directed energy deposition additive manufacturing, Powder Technol. 396 (2022) 316–326. https://doi.org/10.1016/j.powtec.2021.10.059.

[336] P.L. Domone, Self-compacting concrete: An analysis of 11 years of case studies, Cem. Concr. Compos. 28 (2006) 197–208. https://doi.org/10.1016/j.cemconcomp.2005.10.003.

[337] A. Hasnaoui, A. Bourguiba, N. Sebaibi, M. Boutouil, Valorization of queen scallop shells in the preparation of metakaolin-based geopolymer mortars, Journal of Building Engineering 53 (2022) 104578. https://doi.org/10.1016/J.JOBE.2022.104578.

[338] B.A. Tayeh, M.W. Hasaniyah, A.M. Zeyad, M.M. Awad, A. Alaskar, A.M. Mohamed, R. Alyousef, Durability and mechanical properties of seashell partially-replaced cement, Journal of Building Engineering 31 (2020) 101328. https://doi.org/10.1016/J.JOBE.2020.101328.

[339] G. İnan Sezer, Compressive strength and sulfate resistance of limestone and/or silica fume mortars, Constr. Build. Mater. 26 (2012) 613–618. https://doi.org/10.1016/j.conbuildmat.2011.06.064.

[340] S.-H. Choi, S.-E. Oh, J. Won, S.-Y. Chung, Impact of cleaning methods on the properties of cement mortars with cockle shell fine aggregates, Case Studies in Construction Materials 23 (2025) e05143. https://doi.org/10.1016/J.CSCM.2025.E05143.

[341] M. Fujishima, T. Miura, Y. Kawabata, Stress-bearing Mechanism of Concrete Damaged by Delayed Ettringite Formation under Compressive Stress with Various Loading Patterns, Journal of Advanced Concrete Technology 21 (2023) 294–306. https://doi.org/10.3151/jact.21.294.

[342] Z. Zhang, Y. Hu, L. Xiong, G. Geng, The influence of portlandite, calcite, quartz and ettringite inclusions on the multiscale mechanical behaviors of C-S-H matrix, Cem. Concr. Res. 189 (2025) 107781. https://doi.org/10.1016/J.CEMCONRES.2024.107781.

[343] A.G. Khoshkenari, P. Shafigh, M. Moghimi, H. Bin Mahmud, The role of 0–2mm fine recycled concrete aggregate on the compressive and splitting tensile strengths of recycled concrete aggregate concrete, Mater. Des. 64 (2014) 345–354. https://doi.org/10.1016/j.matdes.2014.07.048.

[344] W.C. Tang, P.C. Ryan, H.Z. Cui, W. Liao, Properties of Self-Compacting Concrete with Recycled Coarse Aggregate, Advances in Materials Science and Engineering 2016 (2016) 1–11. https://doi.org/10.1155/2016/2761294.

[345] J. Li, T. Wang, J. Hong, S. Liu, C. Zheng, Y. Chi, Axial compressive performance of low-carbon high-strength recycled aggregate concrete, Low-Carbon Materials and Green Construction 2 (2024) 25. https://doi.org/10.1007/s44242-024-00058-2.

[346] C. Wu, Y. Shi, J. Xu, M. Luo, Y. Lu, D. Zhu, Experimental Study of Mechanical Properties and Theoretical Models for Recycled Fine and Coarse Aggregate Concrete with Steel Fibers, Materials 17 (2024) 2933. https://doi.org/10.3390/ma17122933.

[347] C. Wang, C. Chazallon, S. Braymand, P. Hornych, Thermogravimetric analysis (TGA) for characterization of self-cementation of recycled concrete aggregates in pavement, Thermochim. Acta 733 (2024) 179680. https://doi.org/10.1016/j.tca.2024.179680.

[348] D.K. Panesar, B. Shindman, The effect of segregation on transport and durability properties of self consolidating concrete, Cem. Concr. Res. 42 (2012) 252–264. https://doi.org/10.1016/j.cemconres.2011.09.011.

[349] Z. Zhou, Y. Wang, S. Sun, Y. Wang, L. Xu, Preparation of PVA/waste oyster shell powder composite as an efficient adsorbent of heavy metals from wastewater, Heliyon 8 (2022) e11938. https://doi.org/10.1016/J.HELIYON.2022.E11938.

[350] K. Wu, H. Shi, G. De Schutter, G. Ye, Y. Gao, Mechanism of microstructural modification of the interfacial transition zone by using blended materials, in: 14th International Congress on the Chemistry of Cement (ICCC2015), 2015: pp. 1–11.

[351] D. Wang, C. Lu, Z. Zhu, Z. Zhang, S. Liu, Y. Ji, Z. Xing, Mechanical performance of recycled aggregate concrete in green civil engineering: Review, Case Studies in Construction Materials 19 (2023) e02384. https://doi.org/10.1016/j.cscm.2023.e02384.

[352] F. Agrela, M. Sánchez de Juan, J. Ayuso, V.L. Geraldes, J.R. Jiménez, Limiting properties in the characterisation of mixed recycled aggregates for use in the manufacture of concrete, Constr. Build. Mater. 25 (2011) 3950–3955. https://doi.org/10.1016/j.conbuildmat.2011.04.027.

[353] Y.F. Silva, S. Delvasto, S. Izquierdo, G. Araya-Letelier, Short and long-term physical and mechanical characterization of self-compacting concrete made with masonry and concrete residue, Constr. Build. Mater. 312 (2021) 125382. https://doi.org/10.1016/j.conbuildmat.2021.125382.

[354] D. Chen, T. Pan, X. Yu, Y. Liao, H. Zhao, Properties of Hardened Mortars Containing Crushed Waste Oyster Shells, Environ. Eng. Sci. 36 (2019) 1079–1088. https://doi.org/10.1089/ees.2018.0465.

[355] R. Liu, J. Fan, X. Yu, Y. Zhu, D. Chen, Properties of mortar containing polyvinyl alcohol pretreated waste oyster shells with various concentrations, Constr. Build. Mater. 363 (2023) 129879. https://doi.org/10.1016/J.CONBUILDMAT.2022.129879.

[356] E. Baffoe, E. Dauer, A. Ghahremaninezhad, Effect of proteins on biocementation in construction materials, IScience 27 (2024) 108743. https://doi.org/10.1016/j.isci.2023.108743.

[357] B. El Moustapha, Effect of Metakaolin Addition on The Mechanical Performance and Durability of Granulated Blast Furnace Slag Based Geopolymer Mortar with Micro-Encapsulated Phase Change Materials, Journal of Cement Based Composites 2 (2021) 23–31. https://doi.org/10.36937/cebacom.2021.001.005.

[358] B. El Moustapha, Formulation et étude d'un géopolymère accumulateur d'énergie thermique dans le cadre de l'éco-construction des bâtiments - PASTEL - Thèses en ligne de ParisTech, (2023). https://pastel.hal.science/tel-03965505/ (accessed August 28, 2025).

[359] by Thomas Matschei Dipl, Thermodynamics of Cement Hydration, (2007).

[360] C. Li, L. Jiang, Utilization of limestone powder as an activator for early-age strength improvement of slag concrete, Constr. Build. Mater. 253 (2020) 119257. https://doi.org/10.1016/J.CONBUILDMAT.2020.119257.

[361] Y.-S. Wang, S.-H. Tae, R.-S. Lin, X.-Y. Wang, Effects of Na_2CO_3 on engineering properties of cement–limestone powder–slag ternary blends, Journal of Building Engineering 57 (2022) 104937. https://doi.org/10.1016/j.jobe.2022.104937.

[362] Z. Zhang, G. Geng, Measuring the surface cohesion of calcium silicate hydrate, Cem. Concr. Res. 175 (2024) 107369. https://doi.org/10.1016/J.CEMCONRES.2023.107369.

[363] R. Shahrin, C.P. Bobko, Micropillar compression investigation of size effect on microscale strength and failure mechanism of Calcium-Silicate-Hydrates (C-S-H) in cement paste, Cem. Concr. Res. 125 (2019) 105863. https://doi.org/10.1016/J.CEMCONRES.2019.105863.

[364] R. Alizadeh, J.J. Beaudoin, L. Raki, Mechanical properties of calcium silicate hydrates, Mater. Struct. 44 (2011) 13–28. https://doi.org/10.1617/s11527-010-9605-9.

[365] S. Zhang, R. Liu, C. Lu, Y. Gao, J. Xu, L. Yao, Y. Chen, Application of digital image correlation to study the influence of the water/cement ratio on the interfacial transition zone in cement-based materials, Constr. Build. Mater. 367 (2023) 130167. https://doi.org/10.1016/j.conbuildmat.2022.130167.

[366] S.-M. Kim, R.K. Abu Al-Rub, Meso-scale computational modeling of the plastic-damage response of cementitious composites, Cem. Concr. Res. 41 (2011) 339–358. https://doi.org/10.1016/j.cemconres.2010.12.002.

[367] A. Leemann, R. Loser, B. Münch, Influence of cement type on ITZ porosity and chloride resistance of self-compacting concrete, Cem. Concr. Compos. 32 (2010) 116–120. https://doi.org/10.1016/j.cemconcomp.2009.11.007.

[368] N.O. Emekli, M. Saydan, A. Ünal, Effect of hydration products on the mechanical behavior of reinforced concrete slabs made with ternary systems, Journal of Building Engineering 106 (2025) 112625. https://doi.org/10.1016/j.jobe.2025.112625.

[369] X. Feng, J. Li, Q. Chen, J. Xu, G. Chen, Y. Sun, Z. Jiang, H. Zhu, Effect of flowing water on the ettringite-induced healing of concrete cracks by electrodeposition: Experiments and molecular dynamics simulations, Constr. Build. Mater. 443 (2024) 137718. https://doi.org/10.1016/j.conbuildmat.2024.137718.

[370] Y. Chen, F. Al-Neshawy, J. Punkki, Investigation on the effect of entrained air on pore structure in hardened concrete using MIP, Constr. Build. Mater. 292 (2021) 123441. https://doi.org/10.1016/j.conbuildmat.2021.123441.

[371] S. Bellara, M. Hidjeb, W. Maherzi, S. Mezazigh, A. Senouci, Optimization of an Eco-Friendly Hydraulic Road Binders Comprising Clayey Dam Sediments and Ground Granulated Blast-Furnace Slag, Buildings 11 (2021) 443. https://doi.org/10.3390/buildings11100443.

[372] B. Liu, X. Gu, H. Wang, J. Liu, M.L. Nehdi, Y. Zhang, Study on the mechanism of early strength strengthening and hydration of LC3 raised by shell powder, Journal of Building Engineering 98 (2024) 111422. https://doi.org/10.1016/J.JOBE.2024.111422.

[373] H.-W. Song, S.-J. Kwon, K.-J. Byun, C.-K. Park, Predicting carbonation in early-aged cracked concrete, Cem. Concr. Res. 36 (2006) 979–989. https://doi.org/10.1016/j.cemconres.2005.12.019.

[374] R. Mi, K.M. Liew, G. Pan, New insights into diffusion and reaction of CO_2 gas in recycled aggregate concrete, Cem. Concr. Compos. 129 (2022) 104486. https://doi.org/10.1016/J.CEMCONCOMP.2022.104486.

[375] P.H.R. Borges, J.O. Costa, N.B. Milestone, C.J. Lynsdale, R.E. Streatfield, Carbonation of CH and C–S–H in composite cement pastes containing high amounts of BFS, Cem. Concr. Res. 40 (2010) 284–292. https://doi.org/10.1016/j.cemconres.2009.10.020.

[376] W. Ashraf, J. Olek, S. Sahu, Phase evolution and strength development during carbonation of low-lime calcium silicate cement (CSC), Constr. Build. Mater. 210 (2019) 473–482. https://doi.org/10.1016/J.CONBUILDMAT.2019.03.038.

[377] J. Liu, C. Zeng, Z. Li, G. Liu, W. Zhang, G. Xie, F. Xing, Carbonation of steel slag at low CO_2 concentrations: Novel biochar cold-bonded steel slag artificial aggregates, Science of The Total Environment 902 (2023) 166065. https://doi.org/10.1016/J.SCITOTENV.2023.166065.

[378] B. Lu, S. Drissi, J. Liu, X. Hu, B. Song, C. Shi, Effect of temperature on CO_2 curing, compressive strength and microstructure of cement paste, Cem. Concr. Res. 157 (2022) 106827. https://doi.org/10.1016/J.CEMCONRES.2022.106827.

[379] M. Liu, S. Hong, Y. Wang, J. Zhang, D. Hou, B. Dong, Compositions and microstructures of hardened cement paste with carbonation curing and further water curing, Constr. Build. Mater. 267 (2021) 121724. https://doi.org/10.1016/J.CONBUILDMAT.2020.121724.

[380] B. Lu, Z. Huo, Q. Xu, G. Hou, X. Wang, J. Liu, X. Hu, Characteristics of CSH under carbonation and its effects on the hydration and microstructure of cement paste, Constr. Build. Mater. 364 (2023) 129952. https://doi.org/https://doi.org/10.1016/j.conbuildmat.2022.129952.

[381] S.K. Saikia, A.S. Rajput, Effect of carbon sequestration methods on uptake potential and characteristics of ordinary portland cement-based concrete, Constr. Build. Mater. 418 (2024) 135330. https://doi.org/10.1016/J.CONBUILDMAT.2024.135330.

[382] S. Ahmad, R.A. Assaggaf, M. Maslehuddin, O.S.B. Al-Amoudi, S.K. Adekunle, S.I. Ali, Effects of carbonation pressure and duration on strength evolution of concrete subjected to accelerated carbonation curing, Constr. Build. Mater. 136 (2017) 565–573. https://doi.org/10.1016/J.CONBUILDMAT.2017.01.069.

[383] V. Rostami, Y. Shao, A.J. Boyd, Z. He, Microstructure of cement paste subject to early carbonation curing, Cem. Concr. Res. 42 (2012) 186–193. https://doi.org/10.1016/J.CEMCONRES.2011.09.010.

[384] W. bin Yuan, Y. Zheng, N. ting Yu, Y. Shen, X.K. Hao, Comparative analysis of time-dependent CO_2 uptake in cement and geopolymer concretes via diffusion-induced carbonation, Case Studies in Construction Materials 22 (2025) e04573. https://doi.org/10.1016/J.CSCM.2025.E04573.

[385] Y. Pu, L. Li, Q. Wang, X. Shi, C. Luan, G. Zhang, L. Fu, A. El-Fatah Abomohra, Accelerated carbonation technology for enhanced treatment of recycled concrete aggregates: A state-of-the-art review, Constr. Build. Mater. 282 (2021) 122671. https://doi.org/10.1016/J.CONBUILDMAT.2021.122671.

[386] S.A. Yaseen, G.A. Yiseen, Z. Li, Elucidation of Calcite Structure of Calcium Carbonate Formation Based on Hydrated Cement Mixed with Graphene Oxide and Reduced Graphene Oxide, ACS Omega 4 (2019) 10160–10170. https://doi.org/10.1021/acsomega.9b00042.

[387] L. Black, C. Breen, J. Yarwood, K. Garbev, P. Stemmermann, B. Gasharova, Structural Features of C–S–H(I) and Its Carbonation in Air—A Raman Spectroscopic Study. Part II: Carbonated Phases, Journal of the American Ceramic Society 90 (2007) 908–917. https://doi.org/10.1111/j.1551-2916.2006.01429.x.

[388] C. Rodriguez-Navarro, K. Kudłacz, Ö. Cizer, E. Ruiz-Agudo, Formation of amorphous calcium carbonate and its transformation into mesostructured calcite, CrystEngComm 17 (2015) 58–72. https://doi.org/10.1039/C4CE01562B.

[389] H. El-Hassan, Y. Shao, Z. Ghouleh, Reaction Products in Carbonation-Cured Lightweight Concrete, Journal of Materials in Civil Engineering 25 (2013) 799–809. https://doi.org/10.1061/(ASCE)MT.1943-5533.0000638.

[390] O. Shtepenko, C. Hills, A. Brough, M. Thomas, The effect of carbon dioxide on β-dicalcium silicate and Portland cement, Chemical Engineering Journal 118 (2006) 107–118. https://doi.org/10.1016/J.CEJ.2006.02.005.

[391] M. Castellote, C. Andrade, X. Turrillas, J. Campo, G.J. Cuello, Accelerated carbonation of cement pastes in situ monitored by neutron diffraction, Cem. Concr. Res. 38 (2008) 1365–1373. https://doi.org/10.1016/J.CEMCONRES.2008.07.002.

[392] D.C. Green, J. Ihli, P.D. Thornton, M.A. Holden, B. Marzec, Y.-Y. Kim, A.N. Kulak, M.A. Levenstein, C. Tang, C. Lynch, S.E.D. Webb, C.J. Tynan, F.C. Meldrum, 3D visualization of additive occlusion and tunable full-spectrum fluorescence in calcite, Nat. Commun. 7 (2016) 13524. https://doi.org/10.1038/ncomms13524.

[393] Y.-Q. Niu, J.-H. Liu, C. Aymonier, S. Fermani, D. Kralj, G. Falini, C.-H. Zhou, Calcium carbonate: controlled synthesis, surface functionalization, and nanostructured materials, Chem. Soc. Rev. 51 (2022) 7883–7943. https://doi.org/10.1039/D1CS00519G.

[394] L.S. Gomez-Villalba, P. López-Arce, M. Alvarez de Buergo, R. Fort, Atomic Defects and Their Relationship to Aragonite–Calcite Transformation in Portlandite Nanocrystal Carbonation, Cryst. Growth Des. 12 (2012) 4844–4852. https://doi.org/10.1021/cg300628m.

[395] Ö. Cizer, C. Rodriguez-Navarro, E. Ruiz-Agudo, J. Elsen, D. Van Gemert, K. Van Balen, Phase and morphology evolution of calcium carbonate precipitated by carbonation of hydrated lime, J. Mater. Sci. 47 (2012) 6151–6165. https://doi.org/10.1007/s10853-012-6535-7.

[396] J. Ibáñez, L. Artús, R. Cuscó, Á. López, E. Menéndez, M.C. Andrade, Hydration and carbonation of monoclinic C_2S and C_3S studied by Raman spectroscopy, Journal of Raman Spectroscopy 38 (2007) 61–67. https://doi.org/10.1002/JRS.1599.

[397] K.C. Reddy, N.S. Melaku, S. Park, Thermodynamic Modeling Study of Carbonation of Portland Cement, Materials 2022, Vol. 15, Page 5060 15 (2022) 5060. https://doi.org/10.3390/MA15145060.

[398] M. Takasaki, Y. Kezuka, M. Tajika, Y. Oaki, H. Imai, Evolution of Calcite Nanocrystals through Oriented Attachment and Fragmentation: Multistep Pathway Involving Bottom-Up and Break-Down Stages, ACS Omega 2 (2017) 8997–9001. https://doi.org/10.1021/acsomega.7b01487.

[399] C. Zhang, S. Liu, P. Tang, X. Guan, C. Shi, Enhancing the hardening properties and microstructure of magnesium slag blocks by carbonation-hydration sequential curing, Journal of Building Engineering 76 (2023) 107414. https://doi.org/10.1016/J.JOBE.2023.107414.

[400] D. Zhang, Y. Shao, Enhancing Chloride Corrosion Resistance of Precast Reinforced Concrete by Carbonation Curing., ACI Mater. J. 116 (2019). https://doi.org/10.14359/51714461.

[401] L. Han-Seung, X.Y. Wang, Evaluation of compressive strength development and carbonation depth of high volume slag-blended concrete, Constr. Build. Mater. 124 (2016) 45–54. https://doi.org/10.1016/J.CONBUILDMAT.2016.07.070.

[402] Y. Fang, J. Chang, Microstructure changes of waste hydrated cement paste induced by accelerated carbonation, Constr. Build. Mater. 76 (2015) 360–365. https://doi.org/10.1016/J.CONBUILDMAT.2014.12.017.

[403] M. Rabehi, B. Mezghiche, S. Guettala, Correlation between initial absorption of the cover concrete, the compressive strength and carbonation depth, Constr. Build. Mater. 45 (2013) 123–129. https://doi.org/10.1016/J.CONBUILDMAT.2013.03.074.

[404] J.M. Chi, R. Huang, C.C. Yang, Effects of Carbonation on Mechanical Properties and Durability of Concrete Using Accelerated Testing Method, J. Mar. Sci. Technol. 10 (2002). https://doi.org/10.51400/2709-6998.2296.

[405] E. Mahfoud, K. Ndiaye, W. Maherzi, S. Aggoun, N.E. Abriak, M. Benzerzour, Carbonation in just add water geopolymer based on fly ash and dredged sediments mix, Constr. Build. Mater. 452 (2024) 138959. https://doi.org/10.1016/J.CONBUILDMAT.2024.138959.

[406] A. Neves Junior, R.D. Toledo Filho, E. de Moraes Rego Fairbairn, J. Dweck, The effects of the early carbonation curing on the mechanical and porosity properties of high initial strength Portland cement pastes, Constr. Build. Mater. 77 (2015) 448–454. https://doi.org/10.1016/j.conbuildmat.2014.12.072.

[407] Y.S. Wang, S. Ishak, G.Z. Zhang, X.Y. Wang, Carbonation curing behavior and performance improvement of recycled coral waste concrete, Journal of Building Engineering 90 (2024) 109473. https://doi.org/10.1016/J.JOBE.2024.109473.

[408] Beneficial Use of Carbonation for Concrete, in: SP-235: Eighth CANMET/ACI International Conference on Recent Advances in Concrete Technology, American Concrete Institute, 2006. https://doi.org/10.14359/15861.

[409] M. Thiery, G. Villain, P. Dangla, G. Platret, Investigation of the carbonation front shape on cementitious materials: Effects of the chemical kinetics, Cem. Concr. Res. 37 (2007) 1047–1058. https://doi.org/10.1016/J.CEMCONRES.2007.04.002.

[410] C. Gervais, A.C. Garrabrants, F. Sanchez, R. Barna, P. Moszkowicz, D.S. Kosson, The effects of carbonation and drying during intermittent leaching on the release of inorganic constituents from a cement-based matrix, Cem. Concr. Res. 34 (2004) 119–131. https://doi.org/10.1016/S0008-8846(03)00248-5.

[411] S.T. Pham, Influence of Microstructural Changes on Some Macro Physical Properties of Cement Mortar during Accelerated Carbonation, Open Journal of Civil Engineering 04 (2014) 85–91. https://doi.org/10.4236/ojce.2014.42008.

[412] F. Ren, C. Zhou, Z. Zhang, C.H. Dreimol, U. Angst, Effect of accelerated carbonation on long-term water absorption behavior of cement-based materials, Mater. Struct. 58 (2025) 16. https://doi.org/10.1617/s11527-024-02533-5.

[413] N.M. Alderete, Y.A. Villagrán Zaccardi, N. De Belie, Physical evidence of swelling as the cause of anomalous capillary water uptake by cementitious materials, Cem. Concr. Res. 120 (2019) 256–266. https://doi.org/10.1016/J.CEMCONRES.2019.04.001.

[414] J.H.M. Visser, Influence of the carbon dioxide concentration on the resistance to carbonation of concrete, Constr. Build. Mater. 67 (2014) 8–13. https://doi.org/10.1016/J.CONBUILDMAT.2013.11.005.

[415] T. Nakagaki, I. Tanaka, Y. Furukawa, H. Sato, Y. Yamanaka, Experimental Evaluation of Effect of Oxidative Degradation of Aqueous Monoethanolamine on Heat of CO_2 Absorption, Vapor Liquid Equilibrium and CO_2 Absorption Rate, Energy Procedia 63 (2014) 2384–2393. https://doi.org/10.1016/J.EGYPRO.2014.11.260.

[416] K. Maekawa, T. Ishida, T. Kishi, Multi-scale Modeling of Concrete Performance Integrated Material and Structural Mechanics, Journal of Advanced Concrete Technology 1 (2003) 91–126.

[417] V. Morales-Florez, N. Findling, F. Brunet, Changes on the nanostructure of cementitius calcium silicate hydrates (C–S–H) induced by aqueous carbonation, J. Mater. Sci. 47 (2012) 764–771. https://doi.org/10.1007/s10853-011-5852-6.

[418] X. Kang, X. Zhu, J. Qian, J. Liu, Y. Huang, Effect of graphene oxide (GO) on hydration of tricalcium silicate (C_3S), Constr. Build. Mater. 203 (2019) 514–524. https://doi.org/10.1016/J.CONBUILDMAT.2019.01.117.

[419] X. Gu, B. Yang, Z. Li, B. Liu, J. Liu, Q. Wang, M.L. Nehdif, Elucidating the reaction of seashell powder within fly ash cement: A focus on hydration products, Constr. Build. Mater. 428 (2024) 136331. https://doi.org/10.1016/j.conbuildmat.2024.136331.

[420] H.K. Kim, S.J. Park, J.I. Han, H.K. Lee, Microbially mediated calcium carbonate precipitation on normal and lightweight concrete, Constr. Build. Mater. 38 (2013) 1073–1082. https://doi.org/10.1016/J.CONBUILDMAT.2012.07.040.

[421] B. Guo, G. Chu, R. Yu, Y. Wang, Q. Yu, D. Niu, Effects of sufficient carbonation on the strength and microstructure of CO_2-cured concrete, Journal of Building Engineering 76 (2023) 107311. https://doi.org/10.1016/J.JOBE.2023.107311.

[422] B.J. Zhan, D.X. Xuan, C.S. Poon, C.J. Shi, Mechanism for rapid hardening of cement pastes under coupled CO2-water curing regime, Cem. Concr. Compos. 97 (2019) 78–88. https://doi.org/10.1016/J.CEMCONCOMP.2018.12.021.

[423] J.G. Jang, G.M. Kim, H.J. Kim, H.K. Lee, Review on recent advances in CO_2 utilization and sequestration technologies in cement-based materials, Constr. Build. Mater. 127 (2016) 762–773. https://doi.org/10.1016/J.CONBUILDMAT.2016.10.017.

[424] J. García Carmona, J. Gómez Morales, R. Rodríguez Clemente, Rhombohedral–scalenohedral calcite transition produced by adjusting the solution electrical conductivity in the system $Ca(OH)_2$–CO_2–H_2O, J. Colloid Interface Sci. 261 (2003) 434–440. https://doi.org/10.1016/S0021-9797(03)00149-8.

[425] F. Liendo, M. Arduino, F.A. Deorsola, S. Bensaid, Factors controlling and influencing polymorphism, morphology and size of calcium carbonate synthesized through the carbonation route: A review, Powder Technol. 398 (2022) 117050. https://doi.org/10.1016/J.POWTEC.2021.117050.

[426] C. Liang, H. Chen, R. Li, W. Chi, S. Wang, S. Hou, Y. Gao, P. Zhang, Effect of additional water content and adding methods on the performance of recycled aggregate concrete, Constr. Build. Mater. 423 (2024) 135868. https://doi.org/10.1016/J.CONBUILDMAT.2024.135868.

[427] P. Turcry, L. Oksri-Nelfia, A. Younsi, A. Aït-Mokhtar, Analysis of an accelerated carbonation test with severe preconditioning, Cem. Concr. Res. 57 (2014) 70–78. https://doi.org/10.1016/J.CEMCONRES.2014.01.003.

[428] F. Xie, D. Zhou, M. Zhang, Research progress on carbon dioxide curing of cementitious materials: a review, Canadian Journal of Civil Engineering 52 (2025) 1045–1059. https://doi.org/10.1139/cjce-2024-0425.

[429] A. Padmalal, K. Kulkarni, P. Rawat, H. Sugandhini, Efficacy of Accelerated Carbonation Curing and Its Influence on the Strength Development of Concrete, Buildings 14 (2024) 2573. https://doi.org/10.3390/buildings14082573.

[430] A.M. Merino-Lechuga, Á. González-Caro, E. Fernández-Ledesma, J.R. Jiménez, J.M. Fernández-Rodríguez, D. Suescum-Morales, Accelerated Carbonation of Vibro-Compacted Porous Concrete for Eco-Friendly Precast Elements, Materials 2023, Vol. 16, Page 2995 16 (2023) 2995. https://doi.org/10.3390/MA16082995.

[431] D. Suescum-Morales, K. Kalinowska-Wichrowska, J.M. Fernández, J.R. Jiménez, Accelerated carbonation of fresh cement-based products containing recycled masonry aggregates for CO_2 sequestration, Journal of CO_2 Utilization 46 (2021) 101461. https://doi.org/10.1016/J.JCOU.2021.101461.

[432] X. Pan, C. Shi, X. Hu, Z. Ou, Effects of CO_2 surface treatment on strength and permeability of one-day-aged cement mortar, Constr. Build. Mater. 154 (2017) 1087–1095. https://doi.org/10.1016/J.CONBUILDMAT.2017.07.216.

[433] X. Pan, C. Shi, N. Farzadnia, X. Hu, J. Zheng, Properties and microstructure of CO_2 surface treated cement mortars with subsequent lime-saturated water curing, Cem. Concr. Compos. 99 (2019) 89–99. https://doi.org/10.1016/J.CEMCONCOMP.2019.03.006.

[434] X. Jia, T.C. Ling, H. Mehdizadeh, K.H. Mo, Impact of CO_2 curing on the microhardness and strength of 0.35 w/c cement paste: Comparative study of internal/surface layers, Journal of Materials Research and Technology 9 (2020) 11849–11860. https://doi.org/10.1016/J.JMRT.2020.08.051.

[435] M. Boumaaza, P. Turcry, B. Huet, A. Aït-Mokhtar, Influence of carbonation on the microstructure and the gas diffusivity of hardened cement pastes, Constr. Build. Mater. 253 (2020) 119227. https://doi.org/10.1016/J.CONBUILDMAT.2020.119227.

[436] Z. Zhang, U. Angst, Microstructure and moisture transport in carbonated cement-based materials incorporating cellulose nanofibrils, Cem. Concr. Res. 162 (2022) 106990. https://doi.org/10.1016/J.CEMCONRES.2022.106990.

[437] C. Wang, L. Guo, Y. Li, Z. Wang, Systematic Comparison of C3 and C4 Plants Based on Metabolic Network Analysis, BMC Syst. Biol. 6 (2012) S9. https://doi.org/10.1186/1752-0509-6-S2-S9.

[438] T. van der Weijde, O. Dolstra, R.G.F. Visser, L.M. Trindade, Stability of cell wall composition and saccharification efficiency in Miscanthus across diverse environments, Front. Plant Sci. 7 (2017) 231805. https://doi.org/10.3389/FPLS.2016.02004/BIBTE

Appendix

Appendix 1: Technical data sheet of raw materials

Direction Commerciale
Tour Alto
4 Place des Saisons
92400 Courbevoie
Tél : 01 40 89 51 00

Ciments Calcia
HEIDELBERGCEMENT Group

version du: 17/05/23
N° DoP : 0333-CPR-1609

Fiche produit	RANVILLE CEM II/A-LL 52,5 N CE PM-CP2 NF

Caractéristiques physiques et mécaniques

Compression en MPa				Eau pâte pure en %	Début de prise en mn	Stabilité en mm	Masse volumique en g/cm³	Surface Blaine en cm²/g	Chaleurs en J/g		L*
1j	2j	7j	28j						41h	120h	
25	37	51	60	30,1	3h15	1	3,11	4436	#N/A	-	59

Indice de concentration d'activité I	0,23

Composition élémentaire (%)	
Perte au feu	-
SiO_2	19
Al_2O_3	4,6
Fe_2O_3	3,7
TiO_2	-
MnO	-
CaO	63
MgO	1,0
SO_3	2,5
K_2O	0,96
Na_2O	0,06
P_2O_5	0,38
S--	0,05
Cl-	0,04
Insoluble	-
Na_2O eq.	0,73
Na_2O eq. Actif	0,71
C_3A	-
$C_3A+0.27xC_3S$	20
$C_4AF+2xC_3A$	-

Constituants (%)	
Principaux	
Clinker (K) RANVILLE (%)	90,0
Calcaire (LL) (%)	8,0
Secondaires	2,0
Laitier (S) (%)	
Cendres (V) (%)	
FDEC (%)	
Sulfate de calcium	
Gypse	2,4
Anhydrite	-
Additifs	
Agent de mouture	0,100
Agent réducteur de Cr VI	0,15

Etablissement	Vrac	Big bag	Sac 25 kg	Sac 35 kg
Usine de Ranville	Oui	Non	Non	Non

Caractéristiques des constituants

Nature	Caractéristiques		
			(K)
Clinker (K) RANVILLE (%)	CaO/SiO_2	-	3,1
	C_3S+C_2S (%)	-	77
	MgO (%)	-	1,1
	Al_2O_3 (%)	-	5,1
	C_3S (%)	-	68
	C_2S (%)	-	8,9
	C_3A (%)	-	6,9
	C_4AF (%)	-	12
Calcaire (L ou LL)	$CaCO_3$ (%)		93
	Vb (g/100g)		0,33
	TOC (%)		0,05
Laitier (S)	Laitier vitreux (%)		98
	$(CaO+MgO)/SiO_2$		1,3
	$CaO+MgO+SiO_2$ (%)		85
Cendres (V)	PF (%)		3,5
	CaO réactive (%)		<10
	SiO_2 réactive (%)		42
Fumées de silice (D)	SiO_2 amorphe (%)		-
	PF (%)		-
	Aire massique BET (m^2/kg)		-

Ces valeurs ne sont données qu'à titre indicatif. Les résultats d'auto-contrôle sont disponibles sur demande à la Direction Commerciale.

Appendix 1.1: CEMII/A-LL 52.5 N CE PM-CP2 NF.

Fiche technique

Omya International AG
P.O. Box 335
CH-4665 Oftringen
+41 62 789 29 29
+41 62 789 20 77
www.omya.com

Betocarb® HP - EN

SITE:	ENTRAINS, France (certifié ISO 9001, 14001 et OHSAS 18001)		
DESCRIPTION DU PRODUIT:	Addition calcaire de catégorie A-FM selon la norme NF P18-508 pour bétons hydrauliques. Utilisable en tant que filler pour bétons hydrauliques hautes performances (EN 12620+A1). Produit adapté aux bétons de parement et architectoniques (essai LG_007).		
COMPOSITION TYPE DE LA ROCHE:	$CaCO_3$	98.2	%
	Carbonates totaux	98.6	%
	Chlorures	0.003	%
	Sulfates	0.01	%
	Soufre total	0.01	%
	Matières organiques	0.01	%
	Essai au bleu de méthylène	0.4	g/kg
	Alcalins équivalents	0.01	%
	Silice totale	0.2	%
	Réactivité aux alcalins	NR	
CARACTERISTIQUES TYPES DU PRODUIT:	Granulométrie:		
	· Particules < 2 mm	100	%
	· Particules < 0.125 mm	98	%
	· Particules < 0.063 mm	90	%
	Surface spécifique Blaine (DIN 66126)	611	m^2/kg
	Blancheur :		
	. CIE L* (ISO 11664-4)	94	
	Indice d'activité à 28 jours	0.81	
	Taux d'humidité départ usine (ISO 787-2)	0.2	%
CARACTERISTIQUES GENERALES DU PRODUIT:	Densité (ISO 787-10)	2.7	g/ml
	Densité apparente tassée (ISO 787-11)	1.4	g/ml

APPLICATIONS PRINCIPALES:

Béton auto-plaçant
Béton prêt à l'emploi
Eléments préfabriqués architectoniques
Applications spéciales
- Béton projeté

REPARTITION GRANULOMETRIQUE (Malvern Mastersizer 2000):

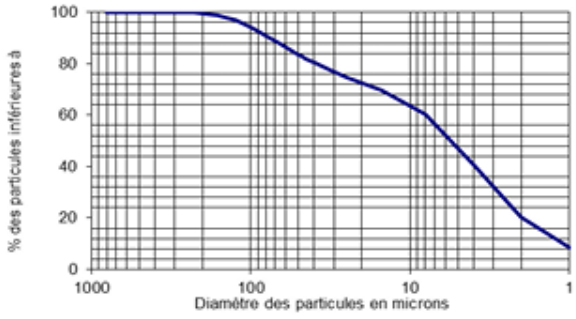

CONDITIONNEMENT STANDARD :

- VRAC

édition : 04.01.2018
Product information :

Appendix 1.2:OMYA Betocarb Limestone Filler.

CARRIERES STREF

LABORATOIRE
RD 321, 27340 Criquebeuf/Seine
tél:06.19.89.69.59

Fiche Technique de Produit
Engagement du 01/01/2021 au 30/06/2021

Page 1/1, imprimé le jeudi 17 décembre 2020

GRAVILLON 4/12.5

Producteur : SAS des carrières STREF & Cie (Jumièges)
Pétrographie : ALLUVION SILICO-CALCAIRE
Elaboration : SEMI-CONCASSE-LAVE

Fiche Technique selon NF P 18545-art 10 Critere F1

Partie contractuelle

Valeurs spécifiées sur lesquelles le producteur s'engage

Classe granulaire		Norme	Code
4	12.5	Norme NF P 18-545 Article 10	Code A

		d/2	d			D/1.4	D			1.4D	2D		
	0.063	2	4	6.3	8	9	12.5	14	16	18	25	f	Fl
Etendue e						30							
Incertitude U	0.3	1	5	6		6	5			1		0.3	4
V.S.S.+U	1.8	6.0	15.0			76.0	100.0					1.80	24.0
V.S.S.	1.5	5.0	10.0			70.0	99.0					1.50	20.0
V.S.I.			0.0			40.0	90.0			98.0	100.0		
V.S.I.-U			0.0			34.0	85.0			97.0			
Ecart-type max						9.09							
Valeur Type		0.4	3.5							100	100	0.2	19.62
LS	1.5	5.0	15.0			70.0	99.0					1.50	20.0
LI			0.0			25.0	90.0			98.0	100.0		

Partie informative

Résultats de production

	du 06/07/20 au 11/12/20												
	0.063	2	4	6.3	8	9	12.5	14	16	18	25	f	Fl
Maximum	0.4	0.9	6.8	37.2	57.5	68.2	97.3	99.6	100.0	100.0	100.0	0.43	19.6
Xi+1,25xEcart-types													
Moyenne Xi	0.1	0.5	4.6	27.8	48.4	61.3	94.9	99.1	100.0	100.0	100.0	0.13	18.2
Xi-1,25xEcart-types													
Minimum	0.0	0.3	2.7	14.7	33.4	49.7	90.3	97.7	100.0	100.0	100.0	0.01	17.1
Ecart-type	0.11	0.18	1.27	6.30	6.51	5.44	1.94	0.59	0.00	0.00	0.00	0.109	1.10
Nombre de résultats	10	10	10	10	10	10	10	10	10	10	10	10	3

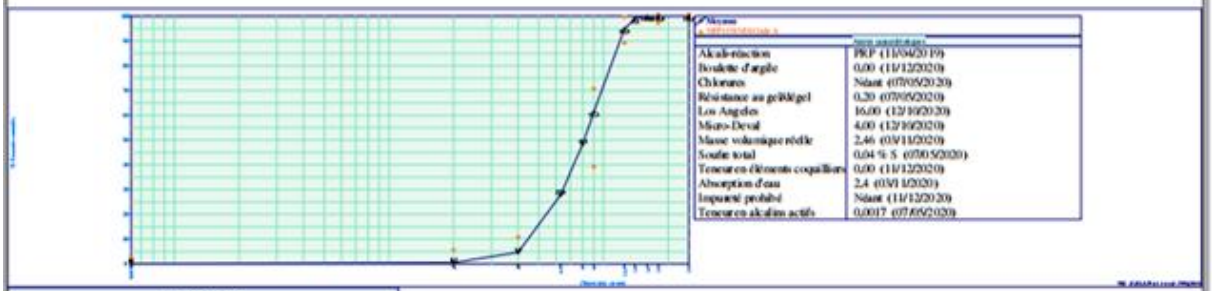

F.BOYER

Appendix 1.3: NCA 4/12.5.

CRB

CARRIERES DE LA ROCHE BLAIN
LE FIEF NOUVEL
14680 Fresney le Puceux
tel : 02.31.15.36.08 fax : 02.31.15.36.05

FICHE TECHNIQUE PRODUIT

Période de validé de l'engagement
Du : 01/11/2021
Au : 11/04/2022

Producteur : Carrières de la Roche Blain - Recyclage Blainville sur Orne
Granulat : Gravillon 4/14 Recyclé
Nature géologique : Recyclage
Type de gisement : Démolition

Partie normative
Valeurs spécifiées sur lesquelles le fournisseur s'engage

Classe Granulaire			Code
4	14	NF P 11-300 - F71	

	28	20	14	10	6,3	4	2	1	0,063	FI	MDE*	LA*	AS	W
Vss + u														
Vss														
Vsi														
Vsi - u														
sf Max														

(*) Sans application de la règle de compensation - Avec application intégrée de la règle de compensation (rayer la mention inutile)

Partie informative
Résultats des essais de fabrication : Période du 01/11/2021 au 30/11/2021
Résultats des autres essais : Période du 22/11/2020 au 22/11/2022

	28	20	14	10	6,3	4	2	1	0,063	FI	MDE	LA	AS	W
Maximum	100	100	96,3	45	25,9	6,8	5,7	4,5	1,6	16	28	32	0,17	5,9
Xf + 1.25 sf														
moyenne Xf	100	100	96,3	45	25,9	6,8	5,7	4,5	1,6	16	28	32	0,17	5,9
Xf - 1.25 sf														
Minimum	100	100	96,3	45	25,9	6,8	5,7	4,5	1,6	16	28	32	0,17	5,9
Ecart type sf														
Nbre résultats	1	1	1	1	1	1	1	1	1	1	1	1	1	1

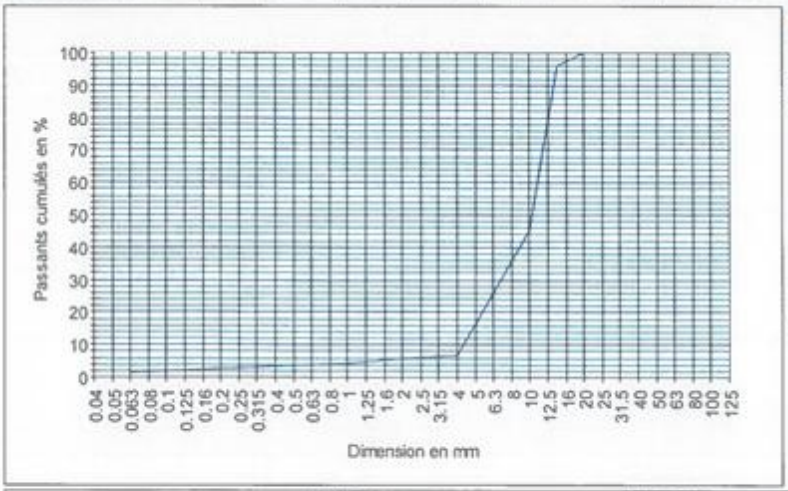

/ Moyenne
- - Fuseau fabrication
V Valeurs spécifiées

Essai(s) complémentaire(s)
- Classification des constituants de gravillons recyclés :
  Rcug = 86 % (08/11/2021)
- Classification des constituants de gravillons recyclés :
  X = 1 % (08/11/2021)
- Classification des constituants de gravillons recyclés :
  FL = 0 Cm³/Kg (08/11/2021)

Date :

Signature :

Acceptabilité environnementale de matériaux alternatifs en technique routière : Les usage de type 1 et 2 sont validés. "Voir page 2"

Appendix 1.4: RCA sieved to 4–12.5 mm.

OSCAR SAVREUX

Carrière de Saint Firmin

Lieu dit Mayocq BP 10, Saint Firmin les Crotoy
80550 Le Crotoy
Tel:03 22 27 34 34

Fiche Technique de Produit

Page 1/1, imprimé le jeudi 22 juin 2023

Granulats : **0/4 roulé lavé**
Pétrographie : alluvion siliceuse
Elaboration : Roulé

Utilisateur : **Controle Interne**

Partie normative

Valeurs spécifiées sur lesquelles le producteur s'engage

Classe granulaire : *0* / *4*

Norme : *Norme NF P 18-545 Article 10 - EN 12620*

Catégorie : *Code A*

	0.063	0.125	0.25	0.5	1	2	4	5.6	8	f	FM	MB	W
Etendue e	6		40		40		10			6	0.6		
Incertitude U	1		4		3		5	1		1	0.15	0.5	
V.S.S.+U	7.00		47.0		100.0		100.0			7.00	2.94	2.00	
V.S.S.	6.00		43.0		98.0		99.0			6.00	2.79	1.50	
V.S.I.			3.0		58.0		89.0	95.0	100.0	0.00	2.19		
V.S.I.-U			0.0		55.0		84.0	94.0		0.00	2.04		
Ecart-type max			12.12		12.12						0.18		

Partie informative

Résultats de production

du 28/11/22 au 12/06/23

	0.063	0.125	0.25	0.5	1	2	4	5.6	8	f	FM	MB	W
Maximum	1.44	6.5	36.8	77.1	83.5	88.6	97.0	99.9	100.0	1.44	2.48	0.60	6.85
Xf+1.25xEcart-types	1.18	5.3	34.7	76.5	83.3	88.1	96.3	100.0	100.0	1.18	2.42	0.48	6.23
Moyenne Xf	0.90	4.3	30.9	72.6	80.4	86.1	95.2	99.6	100.0	0.90	2.30	0.33	5.07
Xf-1.25xEcart-types	0.63	3.3	27.2	68.6	77.5	84.2	94.0	99.3	100.0	0.63	2.19	0.17	3.91
Minimum	0.63	3.5	25.3	66.1	75.5	82.7	93.8	98.8	100.0	0.63	2.20	0.25	3.69
Ecart-type	0.220	0.82	3.00	3.18	2.33	1.55	0.90	0.28	0.00	0.219	0.090	0.120	0.930
Nombre de résultats	15	15	15	15	15	15	15	15	15	15	15	15	15

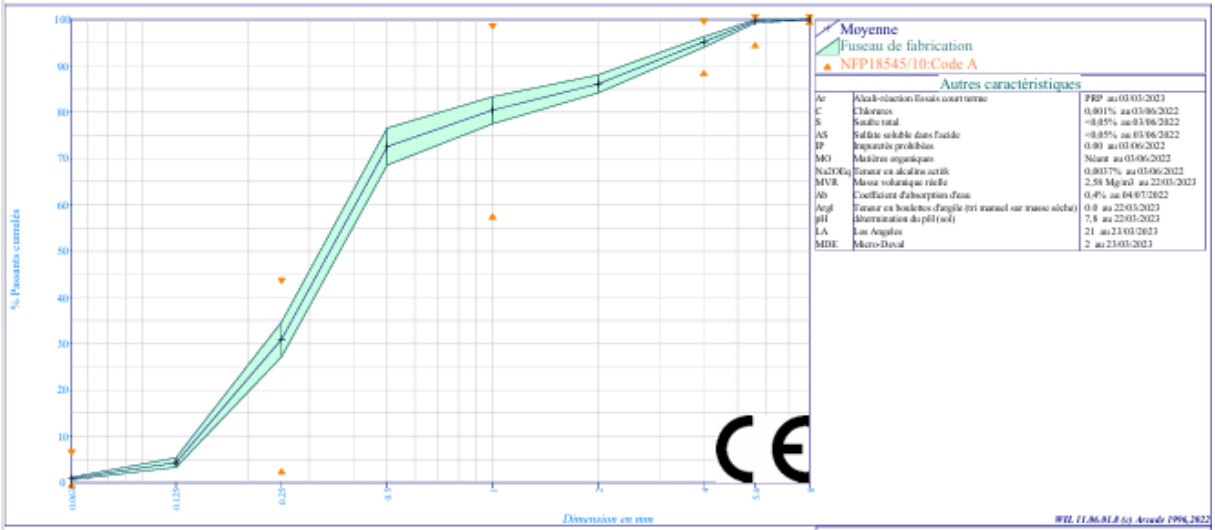

Responsable Qualité : Mohamed EDDAHABI

Appendix 1.5: Sand 0/4.

BASF
We create chemistry

MasterGlenium ACE 550

EN 934.2
Marque NF
cf. Rp NF 085

Superplastifiant pour bétons préfabriqués

Description

Le MasterGlenium ACE 550 est un Superplastifiant Haut Réducteur d'Eau non-chloré, basé sur la technologie des polycarboxylates, et développé pour l'industrie de la préfabrication, dans le cadre du concept Zero Energy System.

Zero Energy System

Le concept du Zero Energy System est de minimiser les dépenses énergétiques nécessaires à la production d'éléments en béton.
Les polycarboxylates innovants du MasterGlenium ACE 550 permettent donc aux préfabricants d'envisager une optimisation de la production.

La nouvelle chimie des MasterGlenium ACE

La configuration particulière des molécules du MasterGlenium ACE 550 accélère les processus d'hydratation à jeune âge. Les nouveaux principes d'adsorption du polymère, très rapide, combiné à un effet puissant de dispersion, permettent d'obtenir une défloculation forte des grains de ciment et une surface de contact avec l'eau plus grande pour chaque grain.
La structure des polymères constituant le MasterGlenium ACE 550 a été spécialement conçue pour améliorer le comportement dynamique et la mise en œuvre des bétons préfabriqués : ceux-ci présentent une haute fluidité et une excellente robustesse vis-à-vis des variations d'eau.

Domaines d'application

Le MasterGlenium ACE 550 est recommandé dans des bétons préfabriqués de consistance ferme à fluide, et dans les BFUHP. Il est particulièrement adapté aux bétons autoplaçants, leur conférant une très haute fluidité et une forte robustesse vis-à-vis des variations d'eau.

Le MasterGlenium ACE 550 facilite la mise en œuvre et assure une bonne qualité de parement.
Ces caractéristiques sont à associer à de hautes résistances mécaniques à court et long terme.

Propriétés

Le MasterGlenium ACE 550 offre les avantages suivants :

- Haute fluidité des bétons
- Bétons très souples, faciles à mettre en œuvre permettant un bon comportement sous vibration
- Excellente stabilité et grande résistance des bétons au ressuage et à la ségrégation
- Facilité de coulage
- Amélioration des parements

Mode d'emploi

L'effet optimal est généralement obtenu par incorporation du MasterGlenium ACE 550 dans le béton en différé, c'est-à-dire après l'addition de 70 % de l'eau de gâchage dans le malaxeur. Toutefois, il est possible d'incorporer le MasterGlenium ACE 550 dans l'eau de gâchage.

Compatibilité

Le MasterGlenium ACE 550 est compatible avec la majorité des ciments.
Pour une utilisation en synergie avec un autre adjuvant de la gamme Master Builders Solutions, consultez votre représentant local BASF France - Division Construction Chemicals.

Dosage

0,2 à 4,0 % de poids de ciment,
Soit 0,19 L à 3,77 L pour 100 Kg de ciment.

Caractéristiques	
Aspect	Liquide
Couleur	Blanchâtre à jaunâtre
Masse volumique à + 20° C	1,06 ± 0,03 g/cm³
Teneur en chlorure	< 0,10 %
Extrait sec	30,0 ± 1,5 %
Na2O eq	≤ 2,0 %
pH	5,5 ± 1,7
Transport	Non-classé
Etiquetage	Le MasterGlenium ACE 550 n'est pas soumis à étiquetage·
Stockage	
Durée de vie	12 mois à compter de la date de fabrication.
Stockage	Le MasterGlenium ACE 550 doit être conservé à une température comprise entre + 5° C et + 30° C.
Conditionnement	Bidon de 10 L, fût de 210 L, container de 1.000 L et vrac.

BASF France SAS - Division Construction Chemicals a couvert sa responsabilité civile tant en exploitation qu'après livraison de ses produits par une police d'assurance souscrite auprès de la Compagnie HDI Gerling France. Les garanties de cette police sont complétées par la police "parapluie" responsabilité civile du Groupe souscrite auprès de la société d'assurances HDI Gerling Allemagne.

BASF France SAS - Division Construction Chemicals

Z.I. Petite Montagne Sud - 10, rue des Cévennes - Lisses - 91017 Evry Cedex
Tél. : 01 69 47 50 00 Fax : 01 60 86 06 32
http://www.master-builders-solutions.basf.fr

Nos fiches techniques ont pour objectif de vous conseiller d'après nos connaissances les plus récentes. Nous nous réservons donc le droit de modifier à tout moment le contenu de celles-ci.
L'emploi des produits doit être adapté aux conditions spécifiques à chaque situation. Pour toute précision complémentaire, nous vous conseillons de prendre contact avec l'une de nos agences BASF France SAS - Division Construction Chemicals.

Conformément à la réglementation en vigueur, nos Fiches de Données de Sécurité (FDS) sont transmises automatiquement (par courrier postal ou électronique) aux clients livrés.
Pour toute question, veuillez contacter votre agence BASF France SAS - Division Construction Chemicals.

MASTER® BUILDERS SOLUTIONS

Appendix 1.6: Superplasticizer.

MasterSet AC 555

EN 934.2
Marque NF
cf. Rp NF 085

Accélérateur de prise sans chlore

Description
Le MasterSet AC 555 est un adjuvant liquide destiné à accélérer la prise du béton.
Il permet la fabrication d'un béton par faibles températures.

Domaines d'applications
Tous types de béton et plus précisément :
- Béton coulé par temps froid
- Béton de préfabrication avec ou sans étuvage
- Béton synergie

Propriétés
Le MasterSet AC 555 :
- **Augmente fortement les résistances mécaniques du béton au jeune âge même par basses températures**
- **Accélère le durcissement du béton**
- **Permet un décoffrage plus rapide**

Le MasterSet AC 555 est particulièrement recommandé pour accélérer la prise des ciments à base de laitier et de cendres volantes.

Mode d'emploi
Le MasterSet AC 555 peut être incorporé dans l'eau de gâchage du béton ou lorsque le béton est déjà mouillé (introduction différée dans le malaxeur).

Recommandations
En cas de gel, réchauffer le produit jusqu'à une température proche de + 30° C, et agiter mécaniquement.
Proscrire l'agitation par air comprimé.

Remarque
Une pellicule brunâtre peut se former en surface du produit.

Dosage
Plage d'utilisation
0,8 % à 2,6 % du poids de ciment, soit 0,57 à 1,84 L pour 100 kg de ciment.
Le dosage varie en fonction du ciment utilisé, du taux d'accélérateur souhaité et de la température ambiante.

Conditionnement
Le MasterSet 555 AC est disponible en bidon de 10 L, fût de 210 L, container de 1.000 L et vrac.

Durée de vie
Le MasterSet 555 AC a une durée de vie de 18 mois, à compter de la date de fabrication.

Stockage
Le MasterSet 555 AC doit être stocké à une température supérieure à + 5° C dans des cuves en plastique, fibres de verre ou acier inox. Proscrire les cuve en acier normal (risque de corrosion dû au pH).

Précaution d'emploi
Consulter la Fiche de Données de Sécurité.

V14 - Edition 11/2018 - Page 1/2

BASF
We create chemistry

MasterSet AC 555

Caractéristiques	
Aspect	Liquide
Couleur	Incolore à brun
Masse volumique à + 20° C	1,39 g/cm³ ± 0,030
Teneur en chlorure	< 0,1 %
Extrait sec dessicateur halogène	42,65 % ± 2,25 %
Na2O eq	≤ 2,5 %
pH	8,0 ± 2
Point de congélation	- 9° C
Etiquetage	

Appendix 1.7: Set accelerator.

Appendix 2: SEM images of carbonation- and sealed-cured samples

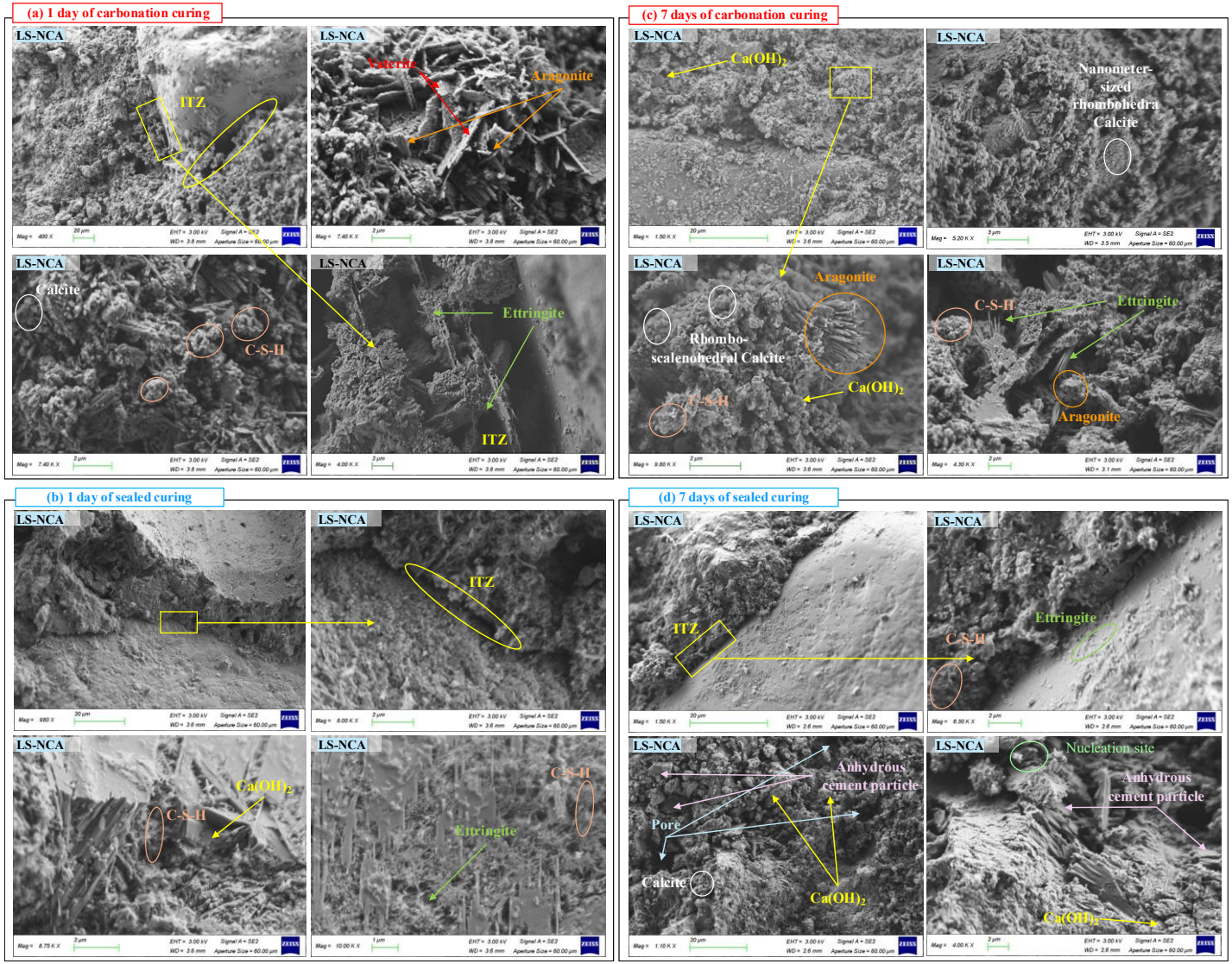

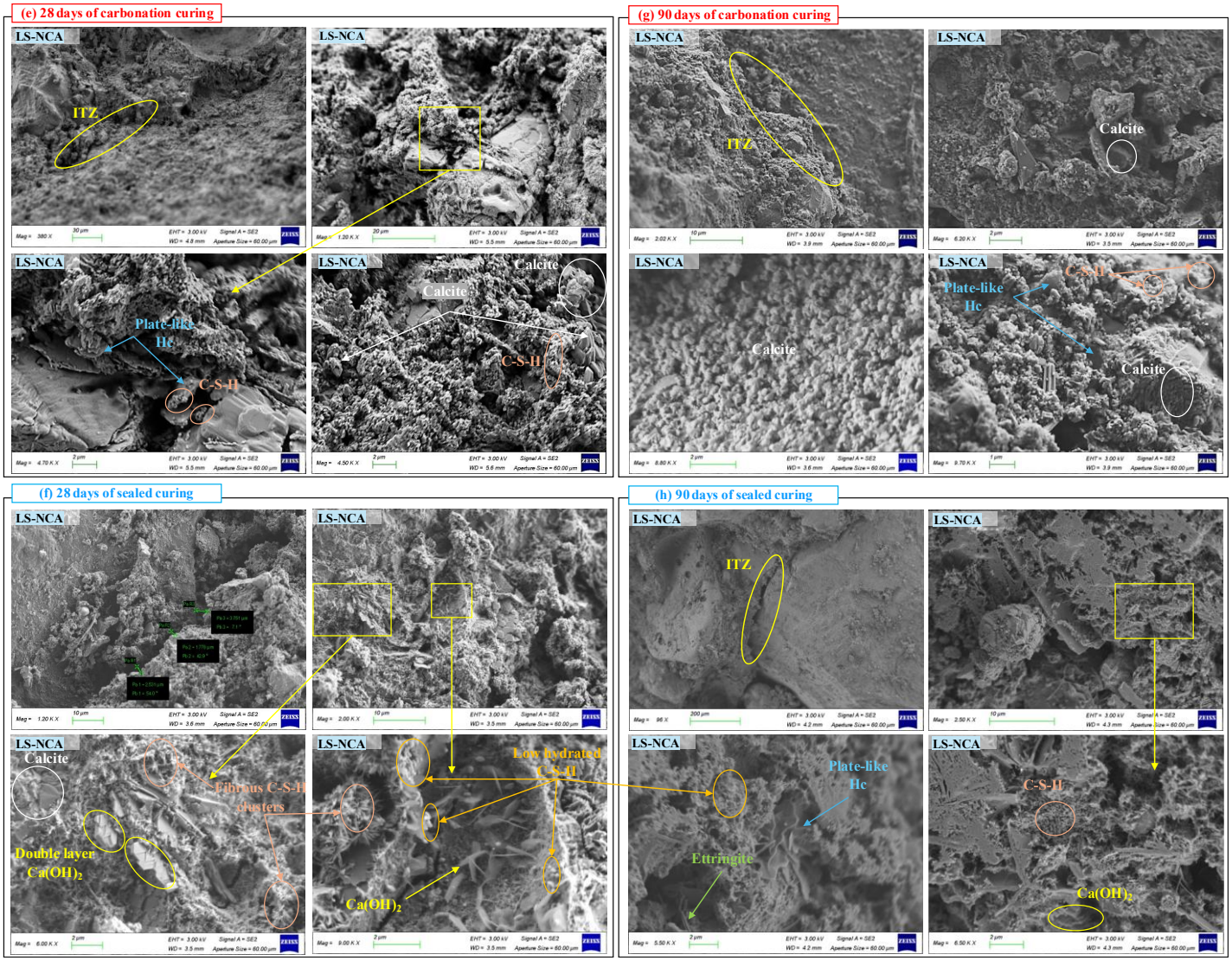

Appendix 2.1: SEM images of carbonated LS-NCA specimens (a, c, e, and g) and their sealed counterparts (b, d, f, and h) at different curing ages.

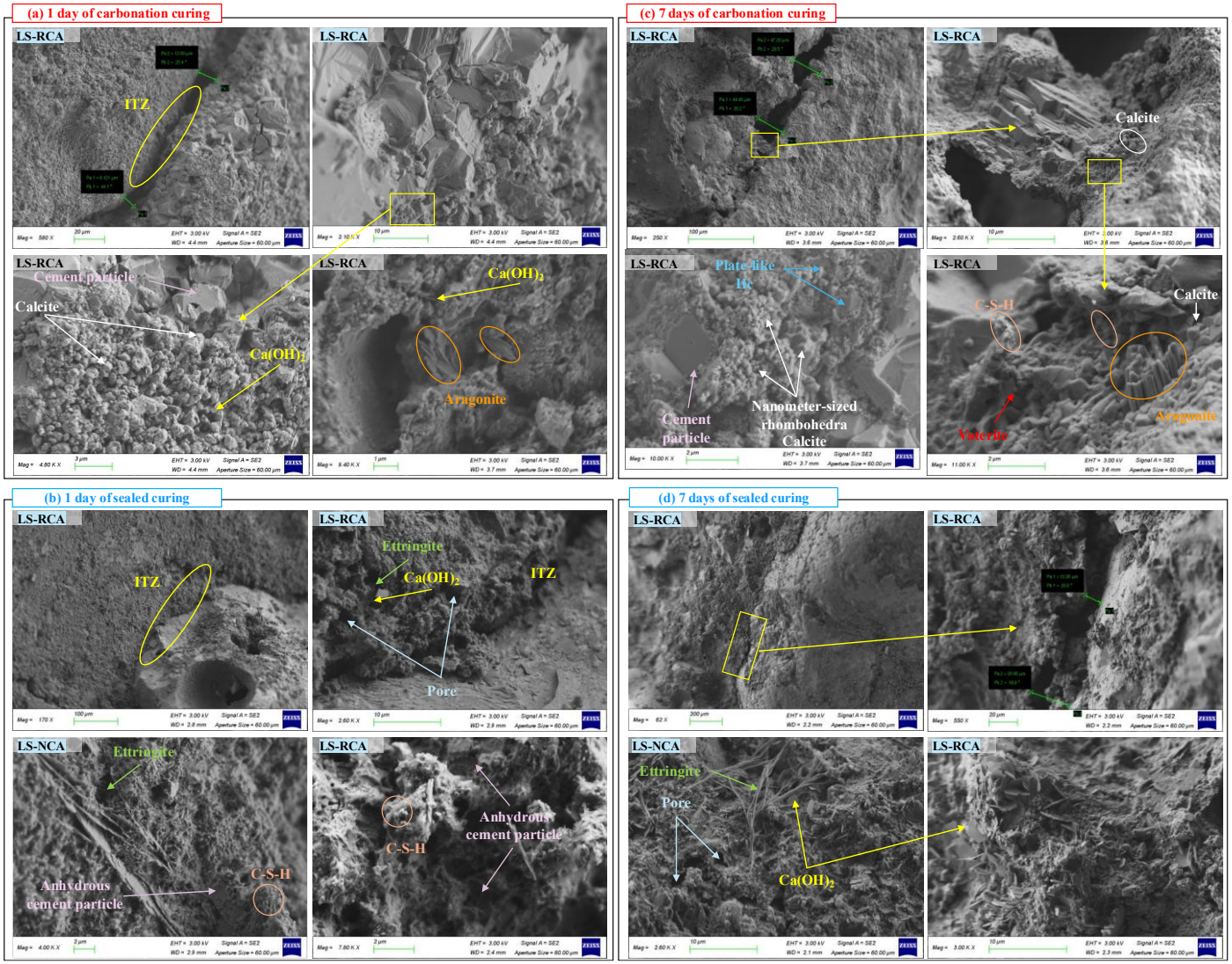
(a) 1 day of carbonation curing
LS-RCA
ITZ
LS-RCA
LS-RCA
Cement particle
Calcite
Ca(OH)2
LS-RCA
Ca(OH)2
Aragonite
(c) 7 days of carbonation curing
LS-RCA
LS-RCA
Calcite
LS-RCA
Plate-like
Ht
Cement
particle
Nanometer-sized
rhombohedra
Calcite
LS-RCA
C-S-H
Calcite
Aragonite
Vaterite
(b) 1 day of sealed curing
LS-RCA
ITZ
LS-RCA
Ettringite
Ca(OH)2
ITZ
Pore
LS-NCA
Ettringite
Anhydrous
cement particle
C-S-H
LS-RCA
C-S-H
Anhydrous
cement particle
(d) 7 days of sealed curing
LS-RCA
LS-RCA
LS-NCA
Ettringite
Pore
Ca(OH)2
LS-RCA

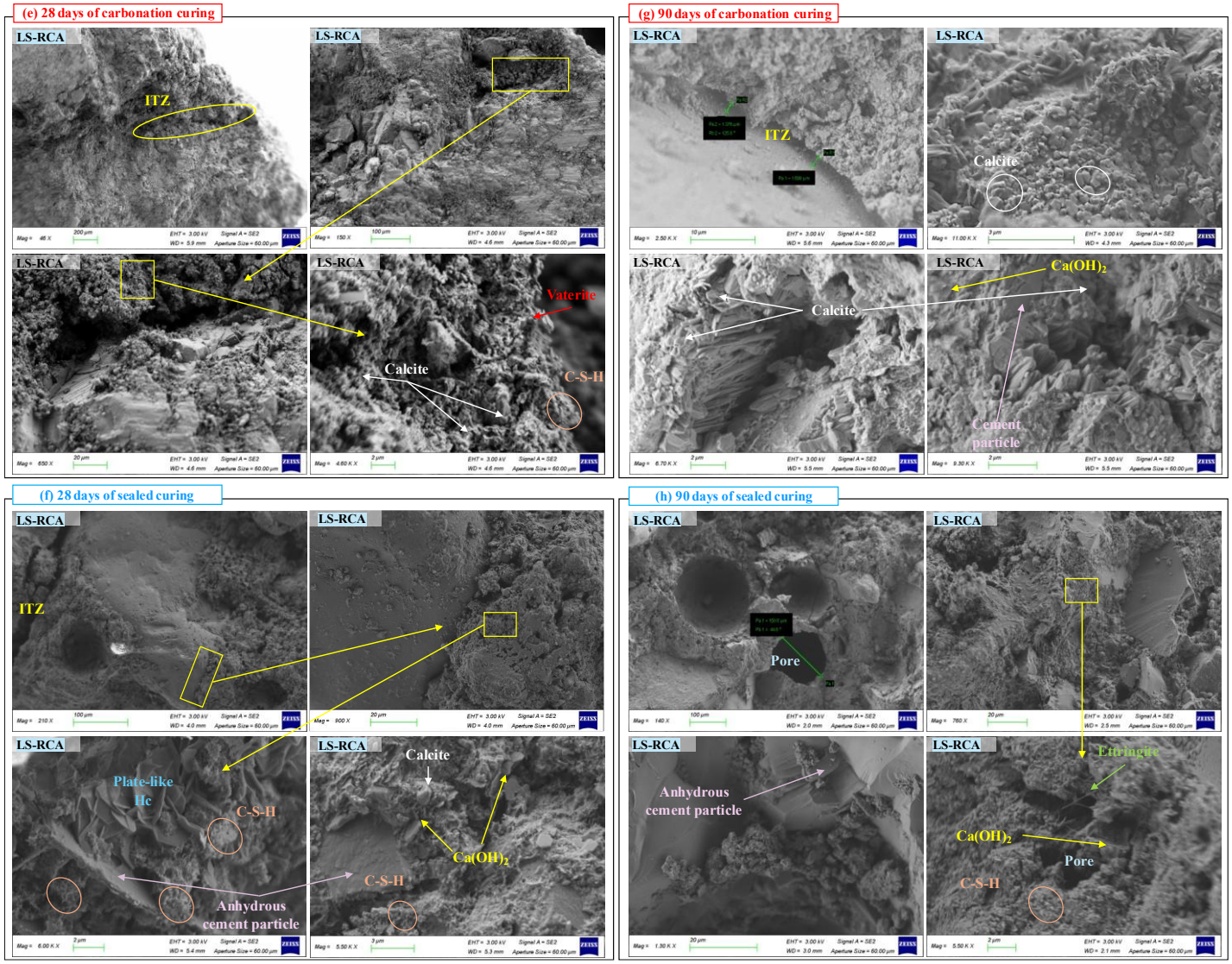

Appendix 2.2: SEM images of (a, c, e, and g) carbonated LS-RCA specimens and (b, d, f, and h) their sealed counterparts at different curing ages.

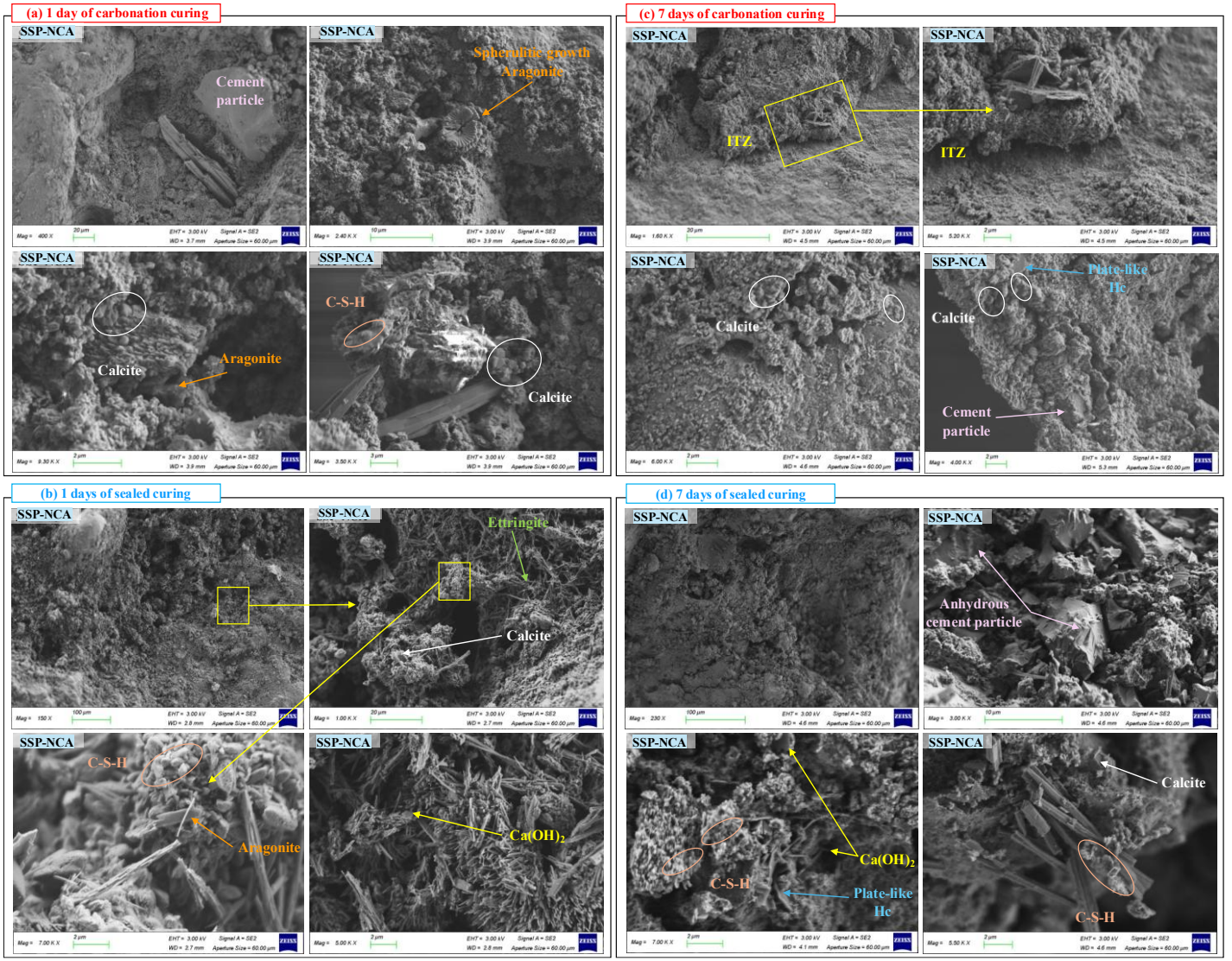
(a) 1 day of carbonation curing
SSP-NCA
Cement particle
SSP-NCA
Spherulitic growth Aragonite
SSP-NCA
Calcite
Aragonite
SSP-NCA
C-S-H
Calcite
(c) 7 days of carbonation curing
SSP-NCA
ITZ
SSP-NCA
ITZ
SSP-NCA
Calcite
SSP-NCA
Plate-like Hc
Calcite
Cement particle
(b) 1 days of sealed curing
SSP-NCA
SSP-NCA
Ettringite
Calcite
SSP-NCA
C-S-H
Aragonite
SSP-NCA
Ca(OH)2
(d) 7 days of sealed curing
SSP-NCA
SSP-NCA
Anhydrous cement particle
SSP-NCA
Ca(OH)2
C-S-H
Plate-like Hc
SSP-NCA
Calcite
C-S-H

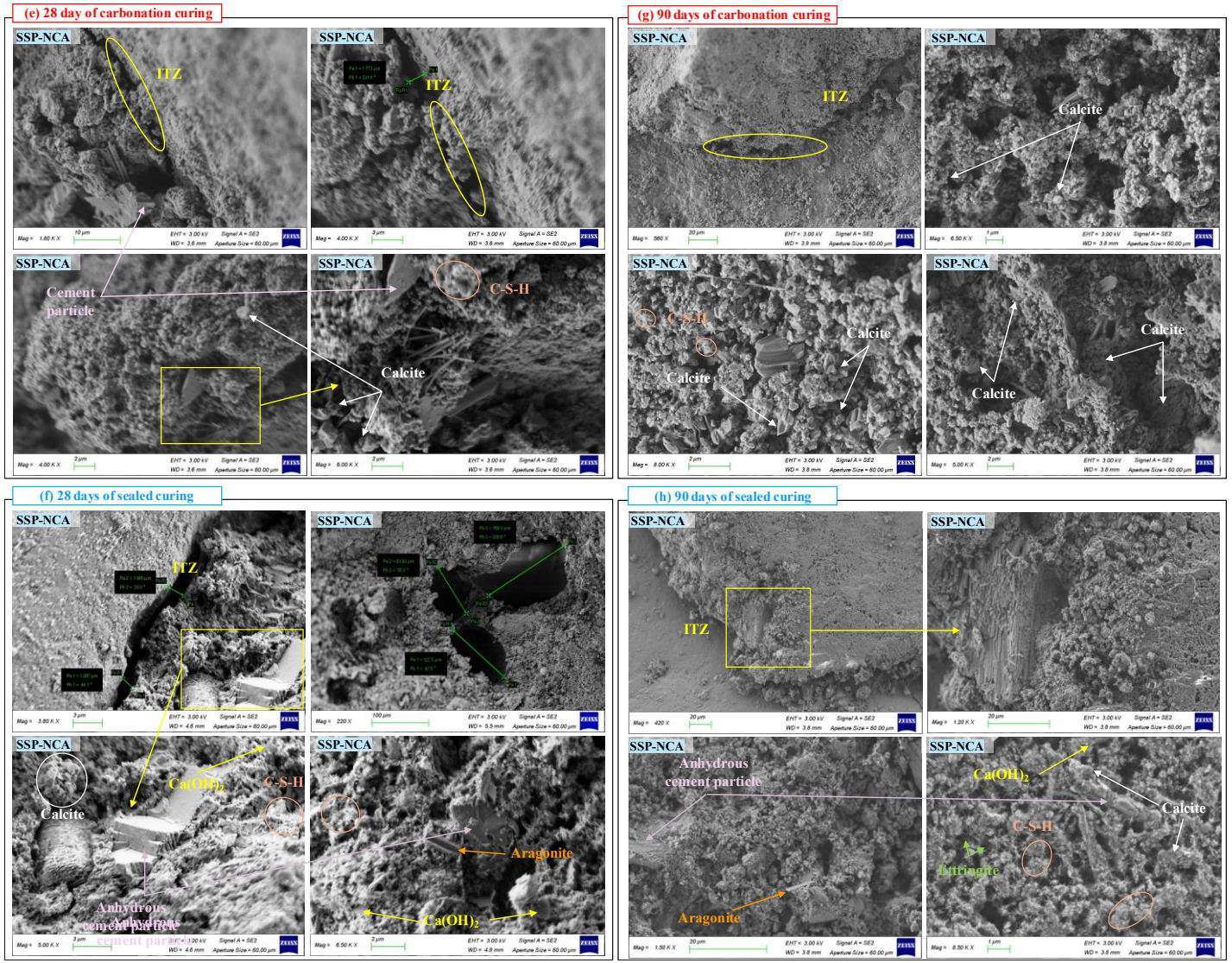

Appendix 2.3: SEM images of (a, c, e, and g) carbonated SSP-NCA specimens and (b, d, f, and h) their sealed counterparts at different curing ages.

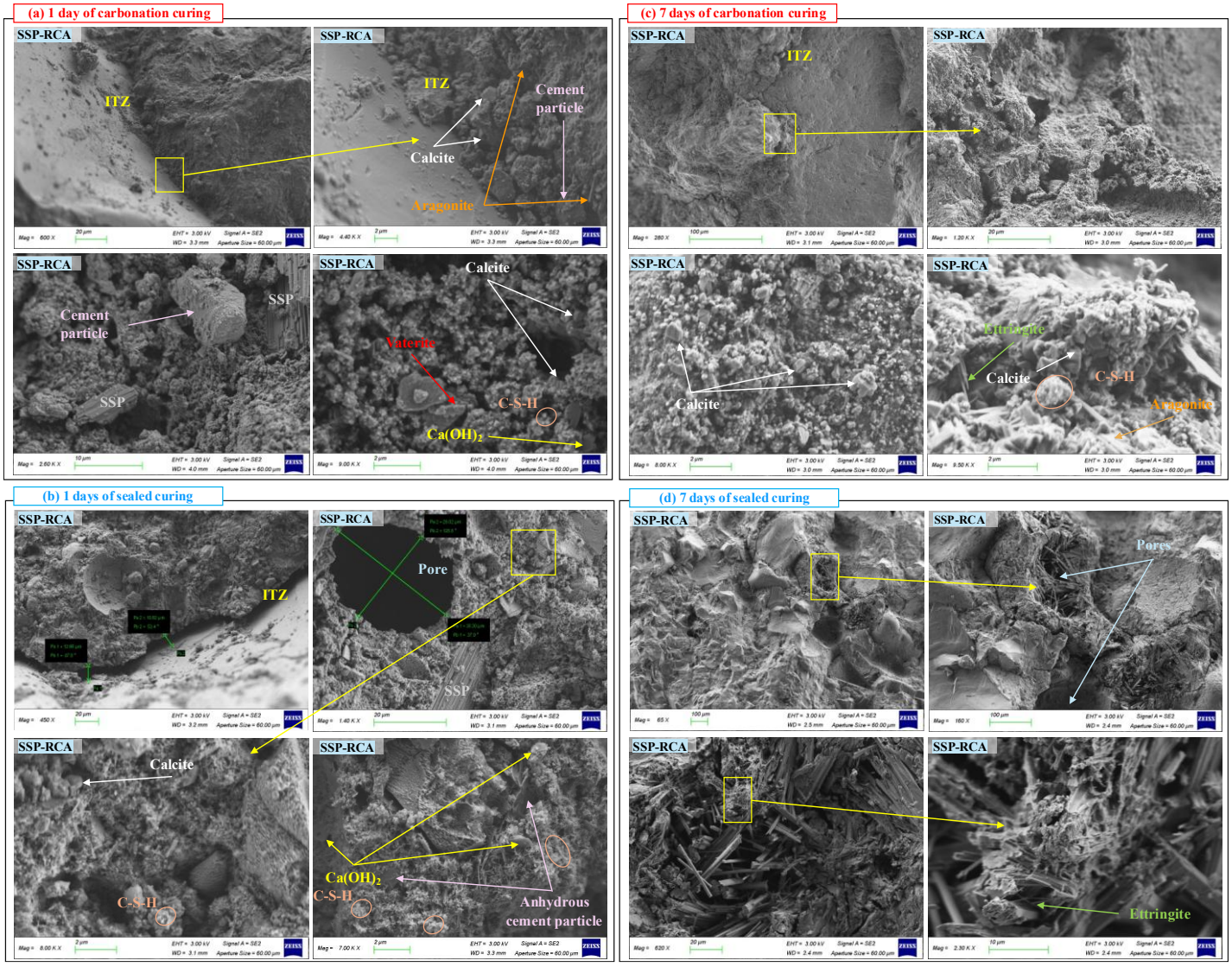
(a) 1 day of carbonation curing
SSP-RCA
ITZ
SSP-RCA
ITZ
Cement particle
Calcite
Aragonite
SSP-RCA
Cement particle
SSP
SSP
SSP-RCA
Calcite
Vaterite
C-S-H
Ca(OH)2
(c) 7 days of carbonation curing
SSP-RCA
ITZ
SSP-RCA
SSP-RCA
Calcite
SSP-RCA
Ettringite
Calcite
C-S-H
Aragonite
(b) 1 days of sealed curing
SSP-RCA
ITZ
SSP-RCA
Pore
SSP
SSP-RCA
Calcite
C-S-H
SSP-RCA
Ca(OH)2
C-S-H
Anhydrous cement particle
(d) 7 days of sealed curing
SSP-RCA
SSP-RCA
Pores
SSP-RCA
SSP-RCA
Ettringite

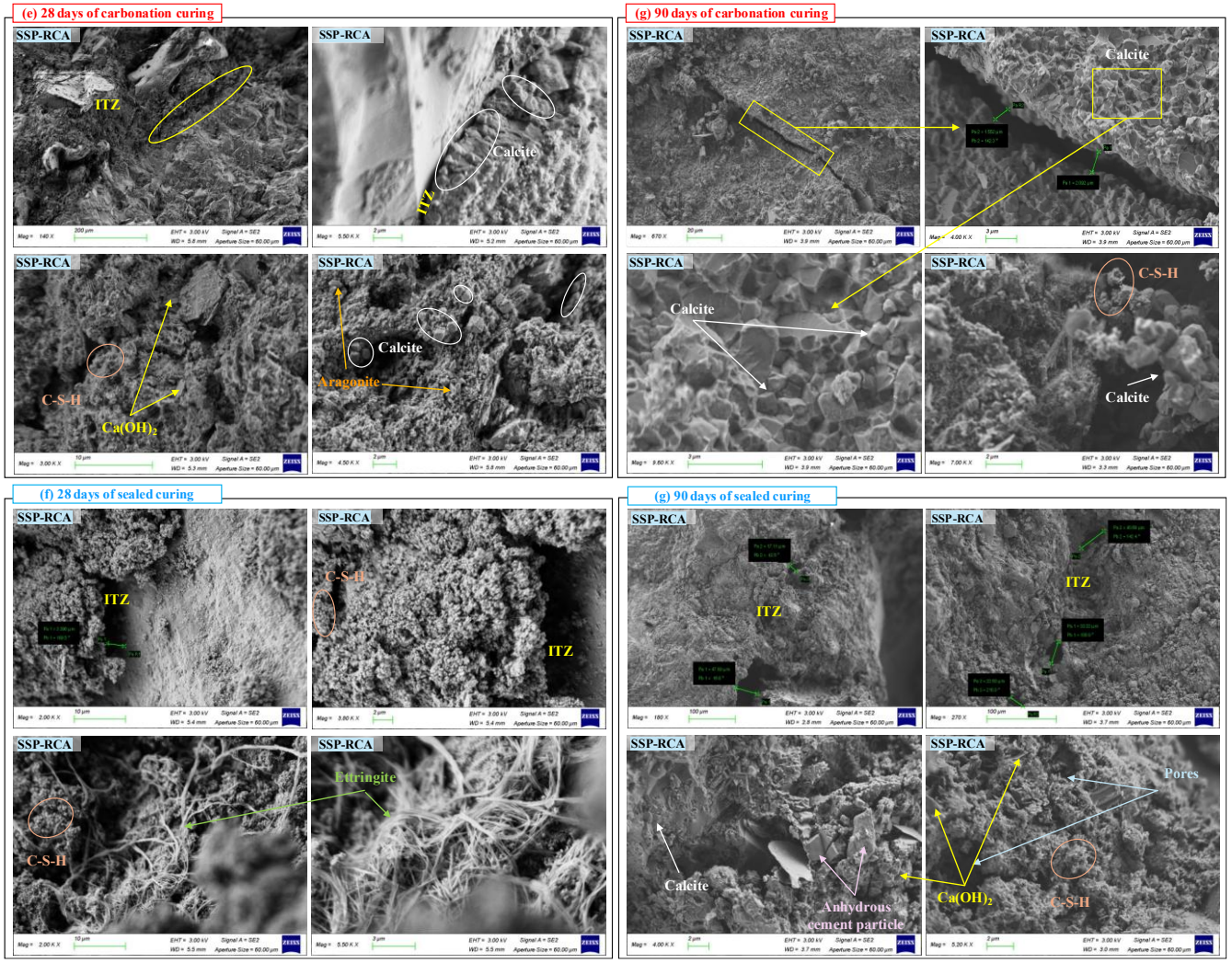

Appendix 2.4: SEM images of (a, c, e, and g) carbonated SSP-RCA specimens and (b, d, f, and h) their sealed counterparts at different curing ages.